CARBON GAIN AND RISK IN LEAF GAS EXCHANGE

by

Yujie Wang

A dissertation submitted to the faculty of
The University of Utah
in partial fulfillment of the requirements for the degree of

Doctor of Philosophy

School of Biological Sciences

The University of Utah

May 2020

The University of Utah Graduate School

STATEMENT OF DISSERTATION APPROVAL

The dissertation of **Yujie Wang**
has been approved by the following supervisory committee members:

John S. Sperry	, Chair	**12/03/2019** Date Approved
William Anderegg Love	, Member	**12/03/2019** Date Approved
Frederick R. Adler	, Member	**12/03/2019** Date Approved
David R. Bowling	, Member	**12/03/2019** Date Approved
James R. Ehleringer	, Member	**12/03/2019** Date Approved

and by **M. Denise Dearing**, Chair/Dean of
the Department/College/School of **Biological Sciences**
and by **David B. Kieda**, Dean of The Graduate School.

ABSTRACT

Modeling leaf gas exchange through the stomata is key to modeling the terrestrial carbon and water fluxes. However, there has been great uncertainty in the land surface models that tried to predict future carbon and water cycles due to the variability in (1) the environment and thus the plants' response to it and (2) plant functional traits both spatially and temporally. Previous attempts that have been devoted to address these issues showed great power in fitting existing data but little potential in predicting the future because the fitted parameters (1) have not been trained at novel environment and (2) lack physiological identities and thus have little potential to track the traits shift with space and time. These deficits, however, can be addressed by the optimality theory. The benefit of gas exchange through the leaf can be quantified by the instantaneous photosynthesis, and the risks associated potentially lie in damage to hydraulic transport and reduction of water supply. Mechanistically modeling the gain-risk optimization with plant functional traits allows for predicting the future stomatal behavior with confidence. Further, the embedded plant traits makes it possible to account for the trait variations.

This dissertation consists of works that aim to improve the modeling of leaf gas exchange by incorporating the gain versus risk optimality theory based on plant traits. The chapters include (1) a model that addresses the CO_2 and H_2O diffusion in anatomical scale to improve the calculation of carbon gain—photosynthesis, (2) a review that quantifies the sources for carbon risks in leaf gas exchange to guide how to define the risk, (3) an experimental verification of a trait-based gain versus risk model performance by examining whole tree level gas exchange in a growth chamber, and (4) a further development of the trait-based model that provides insights on how to track the trait changes spatially and temporally. Together these works have helped advance the modeling of gas exchange from the leaf level to ecosystem level.

CONTENTS

LIST OF TABLES

ACKNOWLEDGMENTS

At the University of Utah, I have had the opportunity to meet with lots of brilliant and kind people, who helped me through the doctoral study in a foreign country. I owe a special thanks to my adviser—John S. Sperry, one of the best architects in plant hydraulics, without whom this work would not have been possible. John has taught me a lot about how to logically design experiment, present data, and grasp the big picture of a study. Not only an excellent scientist, John is also an exceptional teacher as he have been dedicated to inspire the students during his "plant form and function" class. In John's class, he did not instill the students with knowledge but instead showed them how and why, and this further illuminated my passion for teaching. I am very lucky to be his student and honored to be the last graduate. I wish he has a wonderful retirement life with his wife Holly, enjoying hiking and camping in the beautiful mountains and canoeing in the gorgeous rivers.

I thank my supervisory committee members: Bill Anderegg, Dave Bowling, Fred Adler, and Jim Ehleringer. They have been great committee and provided priceless feedback and help. I would specially acknowledge Bill and Dave, who showed great appreciation over my work and recommended me for postdoc positions. I would also thank Tom Kursar, who had served in my committee and will live in my memory. David Love, Martin Venturas, Anna Trugman, Xiaonan Tai, and Kuliang Yu have been generous and helpful to me during my research and life. It is really great to have them as collaborators and more importantly as friends. I also thank Lynn Bohs, who always praises my cooking, good or bad.

Shannon Nielsen, the best graduate coordinator, helped me through the years at the University of Utah. Shannon is very responsible for us graduate students, and always has everything settled quickly. For example, during my first week here she carefully showed me what I should do to register, settle down, buy insurance, and etc. I also appreciate the precious help from April Mills, a big fan of my lovely daughter.

Jinyu Liu, wife of mine and mother of my kids, accompanied and supported me during these years. Without her encouragement, I will not be able to finish the study, or would I had

finished my master study several years ago. My lovely daughter Melanie, named by and after my master adviser Melvin Tyree, has make my life full of joy and happiness though she is naughty, too. My little son Jonathan, named by and after John, has not been able to delight my life yet but he contributes to my panda eyes. I would thank my parents-in-law who help with taking care of my kids. I owe special thanks to my grandparents, who brought me and my brothers up and supported us through high school and college. I am very grateful to my aunts, brothers, and cousins who take care of my grandparents while I am thousands of miles away from home. Melvin Tyree and Charleen Miles have been great friends of us and helped with our settlement in the first year in Utah as Charleen flew from Vermont to Salt Lake City. I wish they enjoy their countryside-style life in their farm and cheese factory.

CHAPTER 1

INTRODUCTION

Anthropogenic CO_2 emission has resulted in a significant increase of CO_2 concentration from about 270 ppm to 410 ppm since the first industrial revolution, and during the last 60 years the concentration increased by almost 100 ppm (NASA GISS). The accumulated greenhouse gas has led to increased mean annual temperature globally and hence unprecedented global climate change. Global warming has caused unpredicted drought stress to plants due to the increasing atmospheric demand for water and thus tree mortality across the globe (Allen et al., 2010; Anderegg et al., 2016; Hartmann et al., 2015; McDowell & Allen, 2015; Mcdowell et al., 2016). The rapidly changing environment and plants make it extremely difficult to project the impacts on carbon and water cycles and forest health from global climate change due to the elusive understanding of (1) how plants respond to the changing environment and (2) how plants and forests change spatially and temporally.

The key to the first problem is the stomata on leaves, where gas exchange occurs. The leaf diffusive conductances to H_2O and CO_2 are usually dynamically regulated via the stomata to respond to the environmental cues, such as atmospheric humidity, soil moisture, light, and atmospheric [CO_2]. However, the complexity of stomatal control has been a great challenge for modeler. One practical approach is to deduce empirical rules from empirical observations (Ball et al., 1987; Leuning, 1995; Medlyn et al., 2011). This approach, though fits well the existing data, shows little promise in predicting the future because the fitted parameters (1) have not been validated in novel environment and (2) have no physiological identities and thus cannot track the plant and forest level trait shifts. Another option is to model the stomatal control mechanistically (i.e., modeling the guard cell behavior at cell level). However, the qualitative mechanism remains unsettled (Chen et al., 2012; Hills et al., 2012) and is impractical and too computational expensive for ecological studies (Buckley & Mott, 2013).

Potentially the most powerful solution is to derive the goal-oriented solution for optimal stomatal behavior (e.g., assuming that plants optimize the water loss and carbon gain). Instead of modeling the cell level mechanism, the goal-oriented solution aims towards the evolutionary driver of stomatal behavior to ask why and how the plants regulate the stomata. Therefore, the mystery of stomatal control mechanism is upscaled to the concern of how to find the evolutionary driver. There have been many optimization models with different optimization criteria since the first optimization model of Cowan & Farquhar (1977). However, the optimization theory has not been improved much until a carbon maximization hypothesis (Wolf et al., 2016), which explicitly posits plants maximize difference of the carbon gain and carbon risk associated with stomatal opening. Models based on the carbon maximization theory over compete the traditionally used Cowan and Farquhar model and also showed equal or better prediction power compared to the empirical approach, which curve fits the data (Anderegg et al., 2018; Venturas et al., 2018; Wang et al., 2019). Despite the successful trials, it remains unclear in theory why or why not the models work, and there are many important issues that are typically neglected (e.g., mesophyll conductance inside the leaf).

Key to the second problem is to model how the plant functional traits are optimized. Fortunately, this is doable with the trait-based optimization models, which have interfaces to different traits from leaf level such as photosynthetic capacity and leaf anatomy, to tree level such as leaf area and biomass allocation to root and shoot, and to ecosystem level such as tree density and forest composition. However, little is known about how these traits coordinate with each other or how they will change. Thus, a mechanistic model of how the trait coordination and shift influence the future water and carbon cycles is at demand.

1.1 The Chapters

This dissertation aims to provide answers to the two problems from both theoretical and experimental works. In Chapter 2, a 3-dimensional gas exchange model is presented to simulate the different diffusions of water vapor from the wet cell surfaces to the atmosphere and of CO_2 from the atmosphere to the palisade for typical hypostomatous leaves. The gas-phase mesophyll conductance in the intercellular airspace is numerically computed with the model and further summarized to analytical equations. The simplified computation

of gas-phase mesophyll conductance allows for accounting for the variable total mesophyll conductance and hence improve the accuracy of photosynthesis calculations.

In Chapter 3, a review of carbon gain and risk optimization models is made. In this review, the carbon gain is defined as the instantaneous photosynthetic rate, which benefits from the model in Chapter 2; the carbon risk associated is theorized to the risk in xylem transport and in water supply. By quantitatively integrating the total loss of hydraulic conductivity along the tree and computing the deficit of carbon for a given transpiration rate, seven fundamental requirements for the defining the total risk are presented, answering why and why not the optimization models work. The optimization models are further tested with existing datasets to compare how each model performs. The review also highlights how the plants ought to weight the risks in xylem transport and water supply depending on the environment. With the carbon gain improved by incorporating variable mesophyll conductance in Chapter 2 and the carbon risk improved by following the seven requirements, the optimization theory holds promise to improve the land surface models.

Not only being able to predict the realistic trend, the optimization model should also predict the stomatal performance with accuracy. Therefore, Chapter 4 describes an experiment that has been conducted in a growth chamber to examine how stomata behave when the tree is exposed to changing atmospheric [CO_2], humidity, and soil drought. The leaf level and tree level responses including leaf photosynthesis (A), whole tree transpiration (E), and canopy leaf xylem pressure (P) were measured and compared to a trait-based optimization model prediction. The mean absolute percentage error for combined A, E, and P is 26.8% compared with the 37.5% for a standard empirical model. The good performance of the trait-based model without curve fitting the data itself highlights the promise of trait-based optimization models.

Equally important as the model performance with known traits, the ability to track the change of traits is key to predict how water and carbon cycles and forest health are influenced by the environment change. Therefore, Chapter 5 presents a higher-level optimization of canopy leaf area and photosynthetic capacity based on an optimal stomatal control model. The optimization is to spontaneously optimize leaf area and photosynthetic capacity that maximize the return on investment of leaves. In brief, the benefit of the investment is cumulative photosynthesis throughout the growing season whereas the cost

of the investment is cumulative respiration from the leaves plus an one-time construction cost of the leaves. Both the intrinsic traits such as vulnerability curves and construction cost ratios, and the environmental cues such as soil water supply and atmospheric [CO_2] are varied from low to high values to examine how sensitive the optimal investment is to these stimuli. Model simulations suggest the optimal investment is sensitive to environmental cues include soil water supply, atmospheric [CO_2], and atmospheric humidity. However, the optimal investment is only sensitive to leaf-level traits including construction costs but not sensitive to other intrinsic traits such as drought resistance and hydraulic transport efficiency. The model simulations also suggest the ratio between internal [CO_2] and atmospheric [CO_2] is conservative in the range from 0.6–0.8, and the ratio varies with the environment and plant functional traits. The optimal leaf investment model highlights the key plant traits that influence significantly the optimal leaf area and photosynthetic capacity, helping prevent blind shoot over understanding the leaf investment strategy.

1.2 References

Allen, C. D., Macalady, A. K., Chenchouni, H., Bachelet, D., McDowell, N., Vennetier, M., … Cobb, N. (2010). A global overview of drought and heat-induced tree mortality reveals emerging climate change risks for forests. *Forest Ecology and Management*, *259*(4), 660–684.

Anderegg, W. R. L., Klein, T., Bartlett, M., Sack, L., Pellegrini, A. F. A., Choat, B., & Jansen, S. (2016). Meta-analysis reveals that hydraulic traits explain cross-species patterns of drought-induced tree mortality across the globe. *Proceedings of the National Academy of Sciences*, *113*(18), 5024–5029.

Anderegg, W. R. L., Wolf, A., Arango-Velez, A., Choat, B., Chmura, D. J., Jansen, S., … Pacala, S. (2018). Woody plants optimise stomatal behaviour relative to hydraulic risk. *Ecology Letters*, *21*(7), 968–977.

Ball, J. T., Woodrow, I. E., & Berry, J. A. (1987). A model predicting stomatal conductance and its contribution to the control of photosynthesis under different environmental conditions. In *Progress in photosynthesis research* (pp. 221–224). Springer.

Buckley, T. N., & Mott, K. A. (2013). Modelling stomatal conductance in response to environmental factors. *Plant, Cell & Environment*, *36*(9), 1691–1699.

Chen, Z.-H., Hills, A., Bätz, U., Amtmann, A., Lew, V. L., & Blatt, M. R. (2012). Systems dynamic modeling of the stomatal guard cell predicts emergent behaviors in transport, signaling, and volume control. *Plant Physiology*, *159*(3), 1235–1251.

Cowan, I. R., & Farquhar, G. D. (1977). Stomatal function in relation to leaf metabolism and environment. *Symposia of the Society for Experimental Biology*, *31*, 471–505.

Hartmann, H., Adams, H. D., Anderegg, W. R. L., Jansen, S., & Zeppel, M. J. B. (2015). Research frontiers in drought-induced tree mortality: Crossing scales and disciplines. *New Phytologist*, *205*(3), 965–969.

Hills, A., Chen, Z.-H., Amtmann, A., Blatt, M. R., & Lew, V. L. (2012). OnGuard, a computational platform for quantitative kinetic modeling of guard cell physiology. *Plant Physiology*, *159*(3), 1026–1042.

Leuning, R. (1995). A critical appraisal of a combined stomatal-photosynthesis model for C_3 plants. *Plant, Cell & Environment*, *18*(4), 339–355.

McDowell, N. G., & Allen, C. D. (2015). Darcy's law predicts widespread forest mortality under climate warming. *Nature Climate Change*, *5*(7), 669.

Mcdowell, N. G., Williams, A. P., Xu, C., Pockman, W. T., Dickman, L. T., Sevanto, S., … Koven, C. (2016). Multi-scale predictions of massive conifer mortality due to chronic temperature rise. *Nature Climate Change*, *6*(3), 295.

Medlyn, B. E., Duursma, R. A., Eamus, D., Ellsworth, D. S., Prentice, I. C., Barton, C. V. M., … Wingate, L. (2011). Reconciling the optimal and empirical approaches to modelling stomatal conductance. *Global Change Biology*, *17*(6), 2134–2144.

Venturas, M. D., Sperry, J. S., Love, D. M., Frehner, E. H., Allred, M. G., Wang, Y., & Anderegg, W. R. L. (2018). A stomatal control model based on optimization of carbon gain versus hydraulic risk predicts aspen sapling responses to drought. *New Phytologist*, *220*(3), 836–850.

Wang, Y., Sperry, J. S., Venturas, M. D., Trugman, A. T., Love, D. M., & Anderegg, W. R. L. (2019). The stomatal response to rising CO_2 concentration and drought is predicted by a hydraulic trait-based optimization model. *Tree Physiology*, *39*, 1416–1427.

Wolf, A., Anderegg, W. R. L., & Pacala, S. W. (2016). Optimal stomatal behavior with competition for water and risk of hydraulic impairment. *Proceedings of the National Academy of Sciences*, *113*(46), E7222–E7230.

CHAPTER 2

STOMATAL APERTURE AND LEAF ANATOMY DRIVE VARIATION IN INTERCELLULAR LIMITATION TO PHOTOSYNTHESIS

2.1 Summary

Plants uptake atmospheric CO_2 for photosynthesis through adjustable stomatal pores on the leaf surface, losing water by transpiration in the process. The diffusive conductance of the stomatal pores to CO_2 (G_{SC}) is readily estimated from transpiration measurements. However, the additional CO_2 diffusive conductance through leaf mesophyll tissue to the chloroplasts (G_M) is difficult to measure and even more challenging to partition into its intercellular gas-phase component (G_{ias}) versus its intracellular liquid-phase component (G_{liq}). We modeled gas-phase diffusion and derived an equation to calculate G_{ias} for hypostomatous leaves from readily measurable leaf anatomical traits. The gas-phase G_{ias} limitation relative to the stomatal limitation (G_{SC}/G_{ias}), increased with stomatal aperture, stomatal frequency, spongy mesophyll thickness, and spongy mesophyll cellular density. The G_{ias} decreased with stomatal closure, a result that provided an alternative explanation for the widely observed decline in G_M with stomatal closure which has been previously attributed to G_{liq} rather than G_{ias}. The gas-phase limitation of G_M (G_M/G_{ias}) averaged 0.59, suggesting an important G_{ias} limitation on G_M and photosynthesis. Better estimates of G_{ias} will advance the understanding and modeling of leaf gas exchange and plant physiology.

• **Keywords:** CO_2 diffusion; gas exchange; intercellular limitation; mesophyll conductance; stomatal aperture

2.2 Introduction

Vascular plants exchange H_2O for CO_2 through stomata to photosynthesize. Within the leaf, water can evaporate from any free cell wall surface that lacks a cuticle. In contrast, the major sink for gas-phase CO_2 in a typical C_3 hypostomatous leaf is the palisade mesophyll,

where the bulk of chloroplasts are located and more than 80% of photosynthesis occurs (Smith et al., 1997). While both H_2O and CO_2 share the same diffusion path through the boundary layer and stoma (captured by a stomatal conductance term, G_S), most CO_2 has to diffuse further through an intercellular gas-phase space to the palisade cell walls before moving through a liquid-phase intracellular layer to the chloroplasts. The extra gas-phase intercellular conductance for CO_2 (G_{ias}) and liquid-phase intracellular conductance for CO_2 (G_{liq}) are generally lumped together in a mesophyll conductance term (G_M, Berghuijs et al., 2016; Flexas et al., 2008). Although G_M can be examined experimentally (Ethier & Livingston, 2004; Ethier et al., 2006; Evans, 1989; Harley et al., 1992; Lloyd et al., 1992), it is neglected in most gas-exchange models (Ball et al., 1987; Cowan & Farquhar, 1977; Leuning, 1995; Love et al., 2019; Mackay et al., 2015; Medlyn et al., 2011; Sperry et al., 2017; Venturas et al., 2018; Wang et al., 2019; Wolf et al., 2016) due to measurement challenges and a lack of understanding of how and why G_M responds to the environment (Carriquí et al., 2019; Flexas et al., 2012; Flexas, Diaz-Espejo, et al., 2007). In this paper, we focus on the gas-phase G_{ias} limitation to CO_2 diffusion, and assess its magnitude, dynamics, and importance for modeling leaf gas exchange.

A number of studies have shown that G_M may limit photosynthesis both theoretically (Aalto et al., 1999; Parkhurst, 1977, 1994; Parkhurst et al., 1988) and experimentally (Berghuijs et al., 2016; Evans et al., 2009; Flexas et al., 2012; Mott & Peak, 2011; Tosens et al., 2012). In addition, experiments have shown that G_M varies with the environment (e.g., G_M decreases with rising CO_2 concentration; Berghuijs et al., 2016; Carriquí et al., 2019; Flexas et al., 2012; Flexas, Diaz-Espejo, et al., 2007; Flexas et al., 2008), further complicating the modeling of leaf gas exchange. Given that G_M integrates both the gas- and liquid-phase components (G_{ias} and G_{liq}) and that the two components involve different mechanisms of responding to changing environmental drivers, a mechanistic understanding of how G_M responds to the environment requires partitioning G_{ias} and G_{liq}.

Previous attempts to quantify G_{ias} differ in results. Experimentally measuring G_M separately in air and helox (air with N_2 replaced by helium), Parkhurst & Mott (1990) found G_{ias} limitation to be significant in thick, hypostomatous leaves but low in amphistomatous leaves. Yet, Genty et al. (1998) found nondetectable G_{ias} limitation in *Rosa rubiginosa* L. (hypostomatous) and *Populus koreana*×*trichocarpa* cv. "Peace" (amphistomatous) with the

same experimental setup. Due to the difficulty of isolating G_{ias} from G_M and the fact that G_{ias} limitation is low for amphistomatous and some hypostomatous species, a G_{ias} limitation to photosynthesis has been assumed to be nonsignificant. However, Parkhurst modeled the 3-dimensional (3D) diffusion and found that G_{ias} was limiting in some circumstances, and varied with stomatal aperture (Parkhurst, 1977, 1994; Parkhurst et al., 1988), which is further supported by another 3D model (Aalto & Juurola, 2002; Aalto et al., 1999). In contrast, 1-dimensional models suggest a constant G_{ias} independent of stomatal closure (Syvertsen et al., 1995; Terashima, 1995). Therefore, a more in-depth analysis is needed to quantify the magnitude of G_{ias}, understand how G_{ias} varies with stomatal aperture, and propagate the impact of G_{ias} on total mesophyll conductance.

Here, we develop a 3D model that simulates the gas-phase diffusion of H_2O and CO_2 for typical hypostomatous leaf anatomy including the boundary layer, which is neglected by other diffusion models. Modeling the gas-phase diffusion of H_2O and CO_2 also allows us to link G_{ias} directly to the commonly measured stomatal conductance. The present study aims to (1) develop a simple and accurate method to estimate G_{ias} from readily measurable anatomical traits, (2) determine how G_{ias} limitation varies with leaf anatomy and stomatal aperture, and (3) evaluate how G_{ias} limitation could influence the response of G_M to the environment.

2.3 Model Description

2.3.1 The theory

The total gas-phase conductance for CO_2 from the air to the palisade layer (G_{TC}) equals the stomatal conductance for CO_2 (G_{SC}, including boundary layer and spongy layer diffusion) and G_{ias} in series:

$$\frac{1}{G_{TC}} = \frac{1}{G_{SC}} + \frac{1}{G_{ias}}. \tag{2.1}$$

Solving for G_{ias} yields

$$G_{ias} = \frac{G_{TC} \cdot G_{SC}}{G_{SC} - G_{TC}}. \tag{2.2}$$

In terms of the diffusive resistance, intercellular resistance ($R_{ias} = 1/G_{ias}$) is the difference of total gas-phase resistance ($R_{TC} = 1/G_{TC}$) and stomatal resistance ($R_{SC} = 1/G_{SC}$):

$$R_{ias} = R_{TC} - R_{SC} = \frac{1}{G_{TC}} - \frac{1}{G_{SC}}. \quad (2.3)$$

The G_{SC} can be calculated from measurements of the stomatal conductance to H_2O (G_{SW}, including boundary layer and spongy layer diffusion): $G_{SC} = G_{SW}/1.6$, where the constant factor 1.6 is derived from the molar conversion of diffusive coefficients of H_2O and CO_2 in air. The G_{SW} is typically calculated from measurements of leaf transpiration rate (E) and the vapor mole fraction difference between leaf (w_{leaf}) and air (w_{air}):

$$G_{SW} = \frac{E}{w_{leaf} - w_{air}}. \quad (2.4)$$

The w_{leaf} is estimated as the saturated vapor mole fraction at leaf temperature, and it also declines with more negative leaf water potential according to the Kelvin equation (Buckley & Sack, 2019; Vesala et al., 2017).

The G_{TC} cannot be measured or calculated directly due to the inability of measuring internal CO_2 concentration gradients. Therefore, we modeled G_{SW} and G_{TC} from 3D diffusion of H_2O and CO_2 for a hypostomatous leaf. The G_{SW} (= 1.6 G_{SC}) was computed from equation 2.4 for steady-state diffusion of water vapor, assuming water could evaporate from all internal cell wall surfaces. The G_{TC} was modeled assuming all CO_2 was absorbed at the boundary between palisade and spongy mesophyll. The G_{ias} was computed from G_{TC} and G_{SC} (equation 2.2).

2.3.2 Diffusion model

Our 3D model resembles those developed by Parkhurst in treating the gas diffusion in a finite mesh defined by a series of three cylinders centered on a stomatal pore (Parkhurst, 1977, 1994; Parkhurst et al., 1988). The external cylinder represents the boundary layer, the central cylinder is the stomatal pore, and the internal cylinder is the spongy mesophyll (Fig. 2.1). Diffusion across the cuticle was assumed to be negligible under physiologically active situations. Discretizing the cylinder gas volume allowed us to model diffusion in three dimensions: normal to the leaf surface as well as laterally in all planes within the boundary layer and spongy air space (Fig. 2.1). The diffusive conductance of each cylinder was modeled separately and combined in series to give G_{SW}, G_{SC}, and G_{TC}. Diffusive conductance is defined as the steady state molar diffusion rate per leaf area per mole

fraction difference between source and sink (conductance unit: mol s^{-1} m^{-2} leaf area). The modeled diffusive conductance does not depend on the mole fraction difference or the direction of diffusion. Model code (Python 3.7.2, Python Software Foundation) is available at https://github.com/Yujie-WANG/Published-Codes-Yujie-WANG. Model variables, default values, and ranges tested in the sensitivity analysis are listed in Table 2.1.

2.3.2.1 Boundary layer

The boundary layer cylinder has an equivalent radius (R_{bd}) for a circle with the average leaf area per stoma and a length of boundary layer thickness (L_{bd}). The R_{bd} is a function of stomatal frequency. The L_{bd} (unit: m) varies with leaf width (lw, unit: m) and wind speed (ws, unit: m s-1): $L_{bd} = 0.004 \times \sqrt{lw/ws}$ (Nobel, 2009). We modeled the boundary layer diffusive conductance for H_2O ($G_{H,bd}$) by setting the plane opening of the stomatal cylinder as the diffusion source and the atmospheric end of the boundary layer cylinder as the diffusion sink (Fig. 2.1b). We divided the boundary cylinder into 11–12 cylindrical shells in the radial direction and 20 equally thick layers in the axial direction (Fig. 2.1a). If the stomatal pore radius (R_{st}) was 5 μm or less, only one shell was added to the innermost cylinder with radius of R_{st}; otherwise, two evenly thick shells were added to the innermost cylinder. The rest of the cylinder from R_{st} to R_{bd} was divided into ten equally thick shells with the thickness of (R_{bd}–R_{st})/10. For each shell, the geometrical radius was computed as $r = \sqrt{(r_{out}^2 + r_{in}^2)/2}$, where r_{out} and r_{in} were the radii of the outer and inner shell boundary, respectively.

The diffusive conductance is independent of the source-to-sink mole fraction difference, which we set to 1 (source = 1, sink = 0). We set the initial vapor fraction to 0 for each element in the boundary cylinder. Within a small time interval (Δt), we modeled the simultaneous diffusion for each element from the vapor fraction difference at time $t - \Delta t$. In this framework, it is necessary to maintain a sufficiently small Δt to ensure the vapor fraction in each element does not exceed the permissible range from 0 to 1. In each iteration, the radial diffusion rate between adjacent rings in the same layer was calculated using $J = 2\pi \cdot D \cdot \Delta C / \ln\left(\frac{r_2}{r_1}\right)$, where ΔC is the mole fraction difference, and r_2 and r_1 are the geometric radii of the adjacent ring elements (Crank, 1975; Wang et al., 2015). The axial diffusion rate between adjacent layers in the same shell was calculated using $J = D \cdot \Delta C / \Delta L$,

where ΔL is the average distance from two adjacent layers. Then vapor fraction was updated for each element based on diffusion during Δt. We ran the diffusion model until it reached steady-state (when the diffusion rate from the source equaled that to the sink), and calculated $G_{H,bd}$ as the diffusion rate of H_2O at steady state per mole fraction difference per leaf area. The boundary layer conductance for CO_2 ($G_{C,bd}$) was computed as $G_{H,bd}/1.6$ because the diffusion paths for the two gasses were the same in the boundary layer.

2.3.2.2 Stomatal pore

The stomatal cylinder has an equivalent radius for the stomatal pore aperture (namely R_{st}) and a length of stomatal pore depth represented by abaxial epidermis thickness (L_{st}). Variation in the R_{st} setting accounts for both the anatomical differences among species-specific maximal stomatal radius ($R_{st,max}$) and the stomatal aperture changes as the guard cells open and close ($R_{st} \leq R_{st,max}$). We modeled the stomatal pore conductance for H_2O ($G_{H,st}$) by setting the inside face of the cylinder as diffusion source and the outside face as the sink (Fig. 2.1c). The simple stomatal pore geometry allows for an analytical solution of $G_{H,st}$ from the Fick's first law (derived in supporting information, Note 2.7.1):

$$G_{H,st} = D \cdot \frac{P_{atm}}{RT} \cdot \frac{1}{L_{st}} \cdot \frac{R_{st}^2}{R_{bd}^2}, \tag{2.5}$$

where D is the diffusion coefficient of water vapor in the air (unit: $m^2\ s^{-1}$), R is the gas constant (8.314 Pa $m^3\ K^{-1}\ mol^{-1}$), T is the temperature in K, and P_{atm} is the atmospheric pressure in Pa. Here we used P_{atm} = 101325 Pa, and T = 298.15 K (25 °C). The stomatal pore conductance for CO_2 ($G_{C,st}$) was calculated as

$$G_{C,st} = \frac{G_{H,st}}{1.6}, \tag{2.6}$$

because the diffusion path for the two gasses are the same across the stomata. Note that $G_{H,st}$ and $G_{C,st}$ are different from G_{SW} and G_{SC}, which include boundary layer and spongy mesophyll components.

2.3.2.3 Spongy mesophyll

The spongy cylinder has a radius of R_{sp} (equals to R_{bd}) and a length (L_{sp}) set to the thickness of the spongy mesophyll. By default, the spongy cylinder is assumed to be empty with no mesophyll cells, and the impact of adding cells to this volume was evaluated by

the intercellular air fraction (f_{ias}, see below and Discussion). We meshed the spongy layer into 11–12 shells and 20 layers as for the boundary layer and used the same equations for running the diffusion model. The source and sink locations depended on whether G_{SW} or G_{TC} was modeled. For G_{SW}, we modeled the spongy layer conductance for H_2O ($G^{\varnothing}_{H,sp}$, where $\varnothing$ denoted that the spongy mesophyll cylinder was completely gas filled) assuming all interior surfaces as potential sources and the inner face of the stomatal cylinder as the sink (Fig. 2.1d). For G_{TC}, we modeled the spongy layer conductance for CO_2 ($G^{\varnothing}_{C,sp}$) assuming the inner face of the stomatal cylinder as the source and the spongy-palisade boundary as the gas-phase CO_2 sink.

The assumption of an empty spongy cylinder underestimates the $G_{H,sp}$ but overestimates $G_{C,sp}$. Adding cells to the spongy cylinder facilitates H_2O diffusion by adding more wet cell walls closer to the stomata, and obstructs and contorts the CO_2 diffusion to the palisade layer. We assumed that on average, adding spongy cells shortened the H_2O diffusion path by a factor of f_{ias} and lengthened the CO_2 diffusion path by a factor of $1/f_{ias}$. This assumption holds true for randomly distributed spongy cells.

2.3.2.4 Empirical equations for spongy and boundary layer conductances

Running the model to reach steady-state for boundary and spongy layer diffusion was time-consuming, limiting the model's utility. Thus, we summarized the modeled boundary and spongy layer conductances in analytically tractable solutions. We ran the finite mesh model described above to make 1000 estimates of the $G_{H,bd}$, $G^{\varnothing}_{H,sp}$, and $G^{\varnothing}_{C,sp}$ by varying the $R_{bd} = R_{sp}$ from 16.11 to 141.04 μm in 10 steps, and L_{bd} and L_{sp} from 21.50 to 435.00 μm in 10 steps. At each given $R_{bd} = R_{sp}$, maximal stomatal pore radius $R_{st,max}$ was computed by assuming stomatal pores occupy 2.5% leaf area, and R_{st} was ranged from $0.3R_{st,max}$ to $R_{st,max}$ in 10 steps. The minimal and maximal values for the anatomical traits were based on observations from a literature survey of 384 observations from 293 hypostomatous broad-leaf species (Ashton & Berlyn, 1992, 1994; Buckley et al., 2017; Earles et al., 2018; Franks & Beerling, 2009; Wylie, 1951, 1954).

The $G_{H,bd}$, $G^{\varnothing}_{H,sp}$, and $G^{\varnothing}_{C,sp}$ were all predictable from three key parameters: R_{st}, R_{bd} (equals R_{sp}), and L_{bd} or L_{sp}. The 1000 modeled conductances were each fitted with the following empirical relationships:

$$G_{\mathrm{H,bd}} = R_{\mathrm{st}}^{k_{\mathrm{st,bd}}\cdot\ln(R_{\mathrm{bd}})+k_{\mathrm{st,l}}\cdot L_{\mathrm{bd}}+l_{\mathtt{st}}} \cdot R_{\mathrm{bd}}^{k_{\mathrm{bd,st}}\cdot\ln(R_{\mathrm{st}})+k_{\mathrm{bd,l}}\cdot L_{\mathrm{bd}}+l_{\mathtt{bd}}} \cdot e^{(k_{\mathrm{l,st}}\cdot\ln(R_{\mathrm{st}})+k_{\mathrm{l,bd}}\cdot\ln(R_{\mathrm{bd}}))\cdot L_{\mathrm{bd}}+l_{\mathrm{l}}}, \quad (2.7)$$

$$G_{\mathrm{H,sp}} = \frac{1}{f_{\mathrm{ias}}} \cdot R_{\mathrm{st}}^{k_{\mathrm{st,sp}}\cdot\ln(R_{\mathrm{sp}})+k_{\mathrm{st,l}}\cdot L_{\mathrm{sp}}+l_{\mathtt{st}}} \cdot R_{\mathrm{sp}}^{k_{\mathrm{sp,st}}\cdot\ln(R_{\mathrm{st}})+k_{\mathrm{sp,l}}\cdot L_{\mathrm{sp}}+l_{\mathtt{sp}}} \cdot e^{(k_{\mathrm{l,st}}\cdot\ln(R_{\mathrm{st}})+k_{\mathrm{l,sp}}\cdot\ln(R_{\mathrm{sp}}))\cdot L_{\mathrm{sp}}+l_{\mathrm{l}}}, \quad (2.8)$$

$$G_{\mathrm{C,sp}} = f_{\mathrm{ias}} \cdot R_{\mathrm{st}}^{k_{\mathrm{st,sp}}\cdot\ln(R_{\mathrm{sp}})+k_{\mathrm{st,l}}\cdot L_{\mathrm{sp}}+l_{\mathtt{st}}} \cdot R_{\mathrm{sp}}^{k_{\mathrm{sp,st}}\cdot\ln(R_{\mathrm{st}})+k_{\mathrm{sp,l}}\cdot L_{\mathrm{sp}}+l_{\mathtt{sp}}} \cdot e^{(k_{\mathrm{l,st}}\cdot\ln(R_{\mathrm{st}})+k_{\mathrm{l,sp}}\cdot\ln(R_{\mathrm{sp}}))\cdot L_{\mathrm{sp}}+l_{\mathrm{l}}}, \quad (2.9)$$

where e is the natural logarithm base, and k and l with subscripts are fitting parameters (Table 2.2). With the analytical solutions for boundary layer, stomatal pore, and spongy layer conductances (equations 2.5–2.9), G_{SW} was solved using $1/G_{\mathrm{SW}} = 1/G_{\mathrm{H,bd}} + 1/G_{\mathrm{H,st}} + 1/G_{\mathrm{H,sp}}$, G_{SC} was computed using $G_{\mathrm{SC}} = G_{\mathrm{SW}}/1.6$, and G_{TC} was solved using $1/G_{\mathrm{TC}} = 1/G_{\mathrm{C,bd}} + 1/G_{\mathrm{C,st}} + 1/G_{\mathrm{C,sp}}$. The G_{ias} was then computed from equation 2.2.

2.3.3 Sensitivity analysis

A sensitivity analysis was used to determine G_{ias} and its importance relative to G_{SC} ($G_{\mathrm{SC}}/G_{\mathrm{ias}}$) as a function of major model inputs. Inputs were tested one at a time, varying over the observed anatomical range (Table 2.1) while holding all other parameters constant at default settings fixed at mean anatomical values. To estimate G_{ias} for an average hypostomatous species, species-specific parameters were fixed at default settings (mean $R_{\mathrm{st,max}}$, R_{bd}, R_{sp}, L_{sp}, L_{st}, f_{ias}), and stomatal aperture alone was varied (via R_{st}) at the default L_{bd}. The mean species-specific traits were the following: $R_{\mathrm{st,max}}$ = 6.35 μm (N = 274), $R_{\mathrm{bd}} = R_{\mathrm{sp}}$ = 38.89 μm (N = 295, stomatal frequency = 327.68 mm^{-2}), L_{sp} = 123.43 μm (N = 104), L_{st} = 14.06 μm (N= 97), and f_{ias} = 0.38 (N = 21). To test how anatomical traits impact the correlation between $G_{\mathrm{SC}}/G_{\mathrm{ias}}$ and G_{SW}, we varied each of L_{sp}, L_{st}, R_{sp} (a measure of stomatal frequency), and f_{ias} across the test range while holding other traits at their default values. We also tested the range of G_{ias} limitation in 14 species for which all traits except stomatal frequency (the R_{sp} setting) had been reported (Buckley et al., 2017); the R_{sp} for the 14 species was set to the mean value from the anatomical literature survey.

2.3.4 Implications for mesophyll conductance

Responses of G_{M} to the environment or experimental manipulations are generally assumed to result from changes in G_{liq} rather than in G_{ias}, although direct evidence is

usually lacking. We surveyed the literature on how G_M responds to different stimuli from gene and cell levels to tree and ecosystem levels (Table 2.3), and we used our model to estimate the G_{ias} component of the G_M response. We chose the studies that reported both G_M and G_{SW} (labeled with "*" in Table 2.3). From the reported G_{SW}, we calculated the G_{ias} based on average leaf anatomy (Table 2.1) because the actual anatomy of the species in question was generally not reported. The G_{ias} and the reported G_M allowed us to estimate G_{liq} using the equation for conductances in series: $1/G_M = 1/G_{ias} + 1/G_{liq}$. We computed the fractional gas-phase limitation of G_M as G_M/G_{ias}, which is the portion of the total mesophyll diffusive resistance ($1/G_M$) that is accounted for by the intercellular gas-phase resistance ($1/G_{ias}$).

2.4 Results

2.4.1 Empirical calculation of spongy and boundary layer conductances

The empirical equations used to summarize the 3D model (equations 2.7–2.9, Table 2.2) performed well in fitting the modeled conductances for the cylindrical components: $G_{H,bd}$ (y = 1.013x – 0.018, R^2 = 0.992, Fig. 2.2a), $G^{\varnothing}_{H,sp}$ (y = 1.003x – 0.006, R^2 = 0.994, Fig. 2.2b), and $G^{\varnothing}_{C,sp}$ (y = 1.013x – 0.011, R^2 = 0.992, Fig. 2.2c). These equations can be used to rapidly estimate G_{ias} from a few parameters. For example, a leaf with an effective leaf width of 5.0 cm in a wind speed of 4.0 m s^{-1} (L_{bd} = 447 μm), R_{bd} = 56.4 μm (= stomatal frequency of 100 mm^{-2}), L_{st} = 20 μm, R_{st} = 8 μm, L_{sp} = 100 μm, R_{sp} = R_{bd} = 56.4 μm, and f_{ias} = 0.4 would have G_{ias} = 0.568 mol m^{-2} s^{-1} (G_{SC}/G_{ias} = 0.374).

2.4.2 Sensitivity analysis

The G_{SC}/G_{ias} ratio indicates how limiting the intercellular airspace is to CO_2 uptake, rising from zero as G_{ias} becomes increasingly important relative to the stomatal G_{SC} component (a ratio of 0 indicates no limitation from G_{ias} and a ratio of 1 indicates equal limitation as G_{SC}). Bigger stomatal pores (higher R_{st}) and higher stomatal frequency (lower R_{sp}) both increased the intercellular limitation because the G_{SC} component increased faster than G_{ias} (Fig. 2.3a). A smaller volume fraction of intercellular airspace (higher cellular density and lower f_{ias}) increased the intercellular limitation because G_{SC} increased (equation 2.8b) while G_{ias} decreased (Fig. 2.3b). A thicker spongy mesophyll layer (larger

L_{sp}) also increased the intercellular limitation, chiefly by lowering G_{ias} (Fig. 2.3b). A thinner boundary layer (smaller L_{bd}) or thinner epidermis (smaller L_{st}) did not impact the G_{ias} but increased the intercellular limitation via increasing G_{SC}.

When parameters were fixed at mean values for the average hypostomatous leaf (Table 2.1), the G_{SC}/G_{ias} was influenced only by changes in stomatal aperture as simulated by allowing only $R_{st}$to vary. The G_{SC}/G_{ias} limitation increased roughly as a power function of G_{SW} (thick solid curve in Fig. 2.4a–e) with a scaling exponent of 0.30. This scaling exponent was not strongly dependent on leaf anatomical traits, ranging in 0.30–0.37, 0.25–0.33, 0.27–0.35, and 0.29–0.39 while varying each of L_{sp}, L_{st}, R_{sp}, and f_{ias} in its test range, respectively. The average exponent was 0.32, 0.31, 0.32, and 0.32 for each variable in the sensitivity analysis.

A similar scaling was observed across the 14 species with different reported trait combinations. For 13 species, the exponent averaged 0.30 and ranged from 0.27 to 0.35. One species was an outlier at 0.41, which resulted from a thick spongy layer of 236.4 μm and high f_{ias} of 0.60 (Fig. 2.4). The overall average scaling exponent across all 14 species (0.31) was not different from the 0.30 exponent obtained for the average hypostomatous leaf (P = 0.23).

2.4.3 Implications for mesophyll conductance

From the literature survey, G_M (black symbols in Fig. 2.5a) increased with stomatal conductance (slope = 0.58, $P < 0.001$), as did the corresponding G_{ias} calculated from our diffusion model assuming an average hypostomatous leaf (Fig. 2.5a, red symbols). The residual G_{liq} (computed from G_M and G_{ias}) showed no correlation with stomatal conductance (Fig. 2.5a, blue symbols; slope = 2.29, P = 0.343). The gas-phase G_{ias} limitation on mesophyll conductance, (i.e., G_M/G_{ias}), ranged from 0 (no G_{ias} influence) to 1 (no G_{liq} influence) with an average of 0.59 (N = 326, Fig. 2.5b, red symbols). The G_M/G_{ias} increased with stomatal conductance, G_{SW}, across the dataset (Fig. 2.5b, slope = 0.18, P = 0.002). In some cases (not shown in Fig. 2.5b) the calculated G_{ias} was less than G_M (58 out of 384 observations), which is physically impossible and may result from calculating G_{ias} from average leaf anatomy rather than the actual anatomy of the species in question.

2.5 Discussion

2.5.1 Can G_{ias} be neglected?

Gas exchange models have tended to neglect the G_{ias} due to the lack of (a) easy ways to estimate G_{ias} from simple gas exchange measurements, (b) mechanistic understanding of how G_{ias} varies with the environmental cues, and (c) understanding of the consequences of neglecting variable G_{ias}. We filled these knowledge gaps by modeling the 3D gas diffusion of H_2O and CO_2, and summarizing the 3D model using empirical equations for analytically computing G_{ias} (and the G_{SC}/G_{ias} ratio) from readily measurable traits. Compared with previous 3D diffusion models, we also included a boundary layer component, which allowed us to link G_{ias} to stomatal conductance. We evaluated how G_{ias} and G_{SC}/G_{ias} varied with leaf anatomical traits, and found the intercellular limitation scales with stomatal conductance for a given leaf anatomy. Given that G_{ias} can now be easily estimated, and that G_{ias} varies with stomatal closure, it may be less justifiable to neglect the G_{ias} or treat G_{ias} as a constant in future gas exchange modeling studies.

Despite these mechanistic improvements, our model includes some necessary simplifications. Specifically, we assume a single value for saturated vapor pressure as is typically done when measuring G_{SW} (equation 2.4). This in turn assumes an isothermal mesophyll with equal cell wall water potential. The magnitude of spatial gradients in temperature and water potential within the leaf mesophyll have not been directly measured. Significant temperature and water potential gradients would complicate the estimation and interpretation of G_{SW}, G_{SC}, and related diffusive conductances including G_{ias} (Buckley et al., 2015; Mott & Peak, 2011; Rockwell & Holbrook, 2017; Tyree & Yianoulis, 1980; Yianoulis & Tyree, 1984). Better experimental resolution of tissue-scale gradients in water potential and temperature is needed to determine the importance in understanding all aspects of leaf-level gas exchange.

Another simplification we make is that palisade is the sole sink for CO_2 for typical hypostomatous leaf. This assumption holds true for most hypostomatous species as a result of high CO_2 sink strength in the palisade (Smith et al., 1997). However, for an atypical hypostomatous leaf where significant amount of CO_2 is absorbed by the spongy mesophyll, the intercellular limitation ought to decrease because CO_2 diffusion path is shortened (as if the spongy layer was thinner in our representation). Similarly, the amphistomatous leaf may

have a lower G_{ias} limitation as each leaf side can be treated as an atypical hypostomatous leaf. Variation in leaf anatomy, however, does not alter the result that G_{ias} will decrease with stomatal closure for a given leaf.

2.5.2 G_{ias} and stomatal conductance

Our 3D model indicated that G_{ias} scales with G_{SW} (Fig. 2.4), supporting and simplifying Parkhurst's and Aalto's model result that the intercellular limitation depends on stomatal aperture (Aalto & Juurola, 2002; Aalto et al., 1999; Parkhurst, 1984, 1994). The simplified correlation makes it possible to incorporate mesophyll conductance limitation in higher level models (e.g., land surface models). According to our model (Fig. 2.4),

$$G_{ias} = G_0 \cdot G_{SW}^{pow}, \tag{2.10}$$

whereG_0 is the G_{ias} when G_{SW} = 1.0 mol m^{-2} s^{-1}, and pow is the scaling factor (pow $\approx$ 0.7 for the average hypostomatous leaf, consistent with Fig. 2.4). Our model differs from the simple 1D gas-phase conductance calculated in many studies:

$$G_{ias} = \frac{D_C \cdot f_{ias}}{L_{sp} \cdot \zeta} \cdot \frac{P_{atm}}{RT}, \tag{2.11}$$

where D_C is the diffusion coefficient of CO_2 in air (1/1.6 times that of H_2O in air: $D_C = D/1.6$), ζ is the diffusion path tortuosity (Syvertsen et al., 1995; Terashima, 1995; Tosens et al., 2012), and P_{atm}/RT converts the unit from m s^{-1} to mol m^{-2} s^{-1}. We account for the intercellular air fraction differently from equation 2.11 (see equations 2.7–2.10). The differences are (1) we use f_{ias} to correct the CO_2 and H_2O diffusion in the spongy layer ($G_{H,sp}$ and $G_{C,sp}$) separately, whereas equation 2.11 makes correction to the final product, G_{ias}; (2) we simulate the 3D diffusion from a tiny pore to a broad flat surface (palisade), whereas equation 2.11 treats the diffusion as 1D plane diffusion from leaf surface to the palisade.

Though equation 2.11 provides a qualitative understanding of how G_{ias} varies with f_{ias} and L_{sp}, this formulation does not allow conductance to change with the stomatal aperture or frequency as the present 3D model indicates (Fig. 2.3, 2.4). As a result, the G_{ias} calculated from equation 2.11 cannot capture the variable G_{ias} caused by changes in stomatal aperture and is much higher than using equation 2.10 (Fig. 2.5a, red horizontal line). Thus, the

intercellular resistance partition (i.e., G_M/G_{ias}) computed from the 1D equation estimates a G_{ias} resistance partition of less than 0.4 (gray "×" in Fig. 2.5b) compared to the average of 0.59 based on our 3D diffusion model and an average hypostomatous leaf (red "+" in Fig. 2.5b). Although G_{ias} is sensitive to leaf anatomy (Fig. 2.4), for a given leaf the 3D G_{ias} will always be lower than the 1D G_{ias} and scale with stomatal aperture.

The reason why G_{ias} declines with stomatal aperture involves the geometry of the 3D diffusion front as defined by contours in CO_2 concentration (Fig. 2.6). As defined by equations 2.1–2.3, the fact that G_{ias} declines with stomatal aperture means that the total gas-phase resistance to CO_2, R_{TC}, increases more with stomatal closure than the stomatal resistance, R_{SC}. The stomatal component is based on water vapor diffusion in reverse (G_{SC} = $G_{SW}/1.6$), and in this case the diffusion front quickly grows from the narrow confines of the stomatal aperture into a spherical shape of increasing surface area (Fig. 2.6a). The spherical geometry dampens the impact of a narrower aperture on the overall increase in diffusive resistance, R_{SC}. In the case of total gas-phase diffusion, however, the initial spherical expansion from the stomatal pore dissipates to a planer diffusion geometry as CO_2 moves to the distant sink at the palisade boundary (Fig. 2.6b). The limited expansion of the diffusion front increases the impact of a narrower stomatal aperture on the overall increase of resistance, R_{TC}. The result is that R_{TC} increases more for a given reduction in stomatal aperture than R_{SC} (Fig. 2.6, R_{SC} increases by 8.84 m^2 s mol^{-1} CO_2, R_{TC} rises by 9.01 m^2 s mol^{-1} CO_2, and R_{ias} rises by 0.17 m^2 s mol^{-1} CO_2, for a given reduction in stomatal aperture). In terms of conductances, the G_{ias} declines as stomata close.

2.5.3 G_{ias} and mesophyll conductance

Despite considerable effort to document and explain variation in mesophyll conductance (Flexas et al., 2012, 2018, 2008, also Table 2.3), a mechanistic understanding is still elusive. Our literature survey showed that the G_M response to the environment within an individual, and G_M variation across individuals (within and across species), was usually accompanied by a similar trend in G_{SW} (Fig. 2.5a; Table 2.3). Our model indicated that the gas-phase portion of G_M (i.e., G_{ias}) also scales with G_{SW} and that the G_{ias} is low enough to significantly limit G_M (accounting for an average of 59% of the mesophyll diffusive resistance). The covariation of G_{ias} and G_{SW} predicted by our model provides a potential explanation for

why G_M varies with G_{SW} regardless of whether the underlying stimulus involved changes in gene expression, chemical treatment, differences in leaf traits and species, or environmental cues (Table 2.3). Although we did not directly model the liquid-phase component of G_M (i.e., G_{liq}), we found no evidence that it scaled with G_{SW} (Fig. 2.5). However, G_{ias} cannot be the only driver for G_M variation because G_{ias} alone cannot explain those situations where G_M responded independently of G_{SW} (Table 2.3), as in the case of stimulation by ABA (Vrábl et al., 2009), blue light (Loreto et al., 2009), and temperature (Evans & von Caemmerer, 2013; Scafaro et al., 2011; von Caemmerer & Evans, 2015). Therefore, a mechanistic understanding of G_{liq} is also important, though it may be challenging to isolate from what we predict to be a dynamic and limiting G_{ias} component.

The observation of reduced G_M during drought is often interpreted as evidence for a "non-stomatal limitation" to photosynthesis (Dewar et al., 2018; Drake et al., 2017; Zhou et al., 2013, 2014), caused by lowered photosynthetic capacity and liquid-phase mesophyll conductance. However, the magnitude of the "non-stomatal" limitation needs to be carefully examined by isolating G_{liq} from the dynamics of G_{ias} as stomatal aperture changes. Though it remains unclear how G_{liq} changes with the environment, the correlation between G_M and G_{SW} can be generally accounted for by the scaling between G_{ias} and G_{SW}. The total gas-phase conductance to CO_2, including G_{SC} and G_{ias} in series, can be readily calculated:

$$G_{TC} = \frac{G_{SW}}{1.6 \cdot \dfrac{G_{SC}}{G_{ias}}} = \frac{G_{SW}}{1.6 \cdot con \cdot G_{SW}^{pow}}, \tag{2.12}$$

where con and pow are species-specific constants. Substituting G_{TC} for G_{SC} in gas exchange models will help predict more accurate photosynthetic rates under drought.

2.5.4 Conclusion

The spatial difference between H_2O evaporation source and gas-phase CO_2 sink inside the leaf results in a potentially limiting intercellular CO_2 conductance, G_{ias}, which is experimentally difficult to quantify. We present a numerical 3D diffusion model to compute G_{ias} and summarize the mechanistic model using analytical equations to help account for intercellular CO_2 diffusion. We further simplify the G_{ias} limitation within a species as a power function of stomatal conductance to water vapor, G_{SW}. The simplified analytical solution for G_{ias} advances the understanding and modeling of gas exchange inside the leaf

by demonstrating the dependence of G_{ias} on leaf anatomical traits and stomatal aperture.

2.6 References

Aalto, T., & Juurola, E. (2002). A three-dimensional model of CO_2 transport in airspaces and mesophyll cells of a silver birch leaf. *Plant, Cell & Environment*, *25*(11), 1399–1409.

Aalto, T., Vesala, T., Mattila, T., Simbierowicz, P., & Hari, P. (1999). A three-dimensional stomatal CO_2 exchange model including gaseous phase and leaf mesophyll separated by irregular interface. *Journal of Theoretical Biology*, *196*(1), 115–128.

Ashton, P. M. S., & Berlyn, G. P. (1992). Leaf adaptations of some *Shorea* species to sun and shade. *New Phytologist*, *121*(4), 587–596.

Ashton, P. M. S., & Berlyn, G. P. (1994). A comparison of leaf physiology and anatomy of *Quercus* (section *Erythrobalanus-Fagaceae*) species in different light environments. *American Journal of Botany*, *81*(5), 589–597.

Ball, J. T., Woodrow, I. E., & Berry, J. A. (1987). A model predicting stomatal conductance and its contribution to the control of photosynthesis under different environmental conditions. In *Progress in photosynthesis research* (pp. 221–224). Springer.

Barbour, M. M., Evans, J. R., Simonin, K. A., & von Caemmerer, S. (2016). Online CO_2 and H_2O oxygen isotope fractionation allows estimation of mesophyll conductance in C_4 plants, and reveals that mesophyll conductance decreases as leaves age in both C_4 and C_3 plants. *New Phytologist*, *210*(3), 875–889.

Barbour, M. M., & Kaiser, B. N. (2016). The response of mesophyll conductance to nitrogen and water availability differs between wheat genotypes. *Plant Science*, *251*, 119–127.

Barbour, M. M., Warren, C. R., Farquhar, G. D., Forrester, G. U. Y., & Brown, H. (2010). Variability in mesophyll conductance between barley genotypes, and effects on transpiration efficiency and carbon isotope discrimination. *Plant, Cell & Environment*, *33*(7), 1176–1185.

Berghuijs, H. N. C., Yin, X., Ho, Q. T., Driever, S. M., Retta, M. A., Nicolaï, B. M., & Struik, P. C. (2016). Mesophyll conductance and reaction-diffusion models for CO_2 transport in C_3 leaves; needs, opportunities and challenges. *Plant Science*, *252*, 62–75.

Bickford, C. P., Hanson, D. T., & McDowell, N. G. (2010). Influence of diurnal variation in mesophyll conductance on modelled ^{13}C discrimination: Results from a field study. *Journal of Experimental Botany*, *61*(12), 3223–3233.

Brilli, F., Tsonev, T., Mahmood, T., Velikova, V., Loreto, F., & Centritto, M. (2013). Ultradian variation of isoprene emission, photosynthesis, mesophyll conductance, and optimum temperature sensitivity for isoprene emission in water-stressed *Eucalyptus citriodora* saplings. *Journal of Experimental Botany*, *64*(2), 519–528.

Buckley, T. N., John, G. P., Scoffoni, C., & Sack, L. (2015). How does leaf anatomy influence water transport outside the xylem? *Plant Physiology*, *168*(4), 1616–1635.

Buckley, T. N., John, G. P., Scoffoni, C., & Sack, L. (2017). The sites of evaporation within

leaves. *Plant Physiology*, *173*(3), 1763–1782.

Buckley, T. N., & Sack, L. (2019). The humidity inside leaves and why you should care: Implications of unsaturation of leaf intercellular airspaces. *American Journal of Botany*, *106*(5), 618–621.

Campany, C. E., Tjoelker, M. G., von Caemmerer, S., & Duursma, R. A. (2016). Coupled response of stomatal and mesophyll conductance to light enhances photosynthesis of shade leaves under sunflecks. *Plant, Cell & Environment*, *39*(12), 2762–2773.

Cano, F. J., López, R., & Warren, C. R. (2014). Implications of the mesophyll conductance to CO_2 for photosynthesis and water-use efficiency during long-term water stress and recovery in two contrasting *Eucalyptus* species. *Plant, Cell & Environment*, *37*(11), 2470–2490.

Cano, F. J., Sánchez-Gómez, D., Rodríguez-Calcerrada, J., Warren, C. R., Gil, L., & Aranda, I. (2013). Effects of drought on mesophyll conductance and photosynthetic limitations at different tree canopy layers. *Plant, Cell & Environment*, *36*(11), 1961–1980.

Carriquí, M., Douthe, C., Molins, A., & Flexas, J. (2019). Leaf anatomy does not explain apparent short-term responses of mesophyll conductance to light and CO_2 in tobacco. *Physiologia Plantarum*, *165*(3), 604–618.

Cowan, I. R., & Farquhar, G. D. (1977). Stomatal function in relation to leaf metabolism and environment. *Symposia of the Society for Experimental Biology*, *31*, 471–505.

Crank, J. (1975). *The mathematics of diffusion*. Clarendon Press.

De Lucia, E. H., Whitehead, D., & Clearwater, M. J. (2003). The relative limitation of photosynthesis by mesophyll conductance in co-occurring species in a temperate rainforest dominated by the conifer *Dacrydium cupressinum*. *Functional Plant Biology*, *30*(12), 1197–1204.

Delfine, S., Alvino, A., Villani, M. C., & Loreto, F. (1999). Restrictions to carbon dioxide conductance and photosynthesis in spinach leaves recovering from salt stress. *Plant Physiology*, *119*(3), 1101–1106.

Delfine, S., Alvino, A., Zacchini, M., & Loreto, F. (1998). Consequences of salt stress on conductance to CO_2 diffusion, Rubisco characteristics and anatomy of spinach leaves. *Functional Plant Biology*, *25*(3), 395–402.

Dewar, R., Mauranen, A., Mäkelä, A., Hölttä, T., Medlyn, B., & Vesala, T. (2018). New insights into the covariation of stomatal, mesophyll and hydraulic conductances from optimization models incorporating nonstomatal limitations to photosynthesis. *New Phytologist*, *217*(2), 571–585.

Ding, L., Gao, L., Liu, W., Wang, M., Gu, M., Ren, B., … Guo, S. (2016). Aquaporin plays an important role in mediating chloroplastic CO_2 concentration under high-N supply in rice (*Oryza sativa*) plants. *Physiologia Plantarum*, *156*(2), 215–226.

Douthe, C., Dreyer, E., Epron, D., & Warren, C. R. (2011). Mesophyll conductance to CO_2, assessed from online TDL-AS records of $^{13}CO_2$ discrimination, displays small but significant short-term responses to CO_2 and irradiance in *Eucalyptus* seedlings. *Journal of*

Experimental Botany, *62*(15), 5335–5346.

Drake, J. E., Power, S. A., Duursma, R. A., Medlyn, B. E., Aspinwall, M. J., Choat, B., … Tissue, D. T. (2017). Stomatal and non-stomatal limitations of photosynthesis for four tree species under drought: A comparison of model formulations. *Agricultural and Forest Meteorology*, *247*, 454–466.

Earles, J. M., Theroux-Rancourt, G., Roddy, A. B., Gilbert, M. E., McElrone, A. J., & Brodersen, C. R. (2018). Beyond porosity: 3D leaf intercellular airspace traits that impact mesophyll conductance. *Plant Physiology*, *178*(1), 148–162.

Ethier, G. J., & Livingston, N. J. (2004). On the need to incorporate sensitivity to CO_2 transfer conductance into the Farquhar–von Caemmerer–Berry leaf photosynthesis model. *Plant, Cell & Environment*, *27*(2), 137–153.

Ethier, G. J., Livingston, N. J., Harrison, D. L., Black, T. A., & Moran, J. A. (2006). Low stomatal and internal conductance to CO_2 versus Rubisco deactivation as determinants of the photosynthetic decline of ageing evergreen leaves. *Plant, Cell & Environment*, *29*(12), 2168–2184.

Evans, J. R. (1989). Photosynthesis and nitrogen relationships in leaves of C_3 plants. *Oecologia*, *78*(1), 9–19.

Evans, J. R., Kaldenhoff, R., Genty, B., & Terashima, I. (2009). Resistances along the CO_2 diffusion pathway inside leaves. *Journal of Experimental Botany*, *60*(8), 2235–2248.

Evans, J. R., & von Caemmerer, S. (2013). Temperature response of carbon isotope discrimination and mesophyll conductance in tobacco. *Plant, Cell & Environment*, *36*(4), 745–756.

Ferrio, J. P., Pou, A., Florez-Sarasa, I., Gessler, A., Kodama, N., Flexas, J., & Ribas-Carbó, M. (2012). The Péclet effect on leaf water enrichment correlates with leaf hydraulic conductance and mesophyll conductance for CO_2. *Plant, Cell & Environment*, *35*(3), 611–625.

Flexas, J., Barbour, M. M., Brendel, O., Cabrera, H. M., Carriquí, M., Díaz-Espejo, A., … Warren, C. R. (2012). Mesophyll diffusion conductance to CO_2: An unappreciated central player in photosynthesis. *Plant Science*, *193*, 70–84.

Flexas, J., Carriquí, M., & Nadal, M. (2018). Gas exchange and hydraulics during drought in crops: Who drives whom? *Journal of Experimental Botany*, *69*(16), 3791–3795.

Flexas, J., Diaz-Espejo, A., Galmes, J., Kaldenhoff, R., Medrano, H., & Ribas-Carbo, M. (2007). Rapid variations of mesophyll conductance in response to changes in CO_2 concentration around leaves. *Plant, Cell & Environment*, *30*(10), 1284–1298.

Flexas, J., Ortuño, M. F., Ribas-Carbo, M., Diaz-Espejo, A., Florez-Sarasa, I. D., & Medrano, H. (2007). Mesophyll conductance to CO_2 in *Arabidopsis thaliana*. *New Phytologist*, *175*(3), 501–511.

Flexas, J., Ribas-Carbo, M., Diaz-Espejo, A., Galmes, J., & Medrano, H. (2008). Mesophyll conductance to CO_2: Current knowledge and future prospects. *Plant, Cell & Environment*, *31*(5), 602–621.

Flexas, J., Ribas-Carbó, M., Hanson, D. T., Bota, J., Otto, B., Cifre, J., ... Kaldenhoff, R. (2006). Tobacco aquaporin *NtAQP1* is involved in mesophyll conductance to CO_2 in vivo. *The Plant Journal*, *48*(3), 427–439.

Franks, P. J., & Beerling, D. J. (2009). Maximum leaf conductance driven by CO_2 effects on stomatal size and density over geologic time. *Proceedings of the National Academy of Sciences*, *106*(25), 10343–10347.

Galle, A., Florez-Sarasa, I., Tomas, M., Pou, A., Medrano, H., Ribas-Carbo, M., & Flexas, J. (2009). The role of mesophyll conductance during water stress and recovery in tobacco (*Nicotiana sylvestris*): Acclimation or limitation? *Journal of Experimental Botany*, *60*(8), 2379–2390.

Galle, A., Lautner, S., Flexas, J., Ribas-Carbo, M., Hanson, D., Roesgen, J., & Fromm, J. (2013). Photosynthetic responses of soybean (*Glycine max* L.) to heat-induced electrical signalling are predominantly governed by modifications of mesophyll conductance for CO_2. *Plant, Cell & Environment*, *36*(3), 542–552.

Genty, B., Meyer, S., Piel, C., Badeck, F., & Liozon, R. (1998). CO_2 diffusion inside leaf mesophyll of ligneous plants. In *Photosynthesis: Mechanisms and effects* (pp. 3961–3966). Springer.

Gilbert, M. E., Pou, A., Zwieniecki, M. A., & Holbrook, N. M. (2011). On measuring the response of mesophyll conductance to carbon dioxide with the variable *J* method. *Journal of Experimental Botany*, *63*(1), 413–425.

Gillon, J. S., & Yakir, D. (2000). Internal conductance to CO_2 diffusion and $C^{18}OO$ discrimination in C_3 leaves. *Plant Physiology*, *123*(1), 201–214.

Gong, H. Y., Li, Y., Fang, G., Hu, D. H., Jin, W. B., Wang, Z. H., & Li, Y. S. (2015). Transgenic rice expressing *Ictb* and *FBP/Sbpase* derived from cyanobacteria exhibits enhanced photosynthesis and mesophyll conductance to CO_2. *PLoS One*, *10*(10), e0140928.

Han, J.-M., Meng, H.-F., Wang, S.-Y., Jiang, C.-D., Liu, F., Zhang, W.-F., & Zhang, Y.-L. (2016). Variability of mesophyll conductance and its relationship with water use efficiency in cotton leaves under drought pretreatment. *Journal of Plant Physiology*, *194*, 61–71.

Han, Q. (2011). Height-related decreases in mesophyll conductance, leaf photosynthesis and compensating adjustments associated with leaf nitrogen concentrations in *Pinus densiflora*. *Tree Physiology*, *31*(9), 976–984.

Harley, P. C., Loreto, F., Di Marco, G., & Sharkey, T. D. (1992). Theoretical considerations when estimating the mesophyll conductance to CO_2 flux by analysis of the response of photosynthesis to CO_2. *Plant Physiology*, *98*(4), 1429–1436.

Hassiotou, F., Ludwig, M., Renton, M., Veneklaas, E. J., & Evans, J. R. (2009). Influence of leaf dry mass per area, CO_2, and irradiance on mesophyll conductance in sclerophylls. *Journal of Experimental Botany*, *60*(8), 2303–2314.

Hu, L., Wang, Z., & Huang, B. (2010). Diffusion limitations and metabolic factors associated with inhibition and recovery of photosynthesis from drought stress in a C_3 perennial grass species. *Physiologia Plantarum*, *139*(1), 93–106.

Jin, S. H., Huang, J. Q., Li, X. Q., Zheng, B. S., Wu, J. S., Wang, Z. J., … Chen, M. (2011). Effects of potassium supply on limitations of photosynthesis by mesophyll diffusion conductance in *Carya cathayensis*. *Tree Physiology*, *31*(10), 1142–1151.

Kodama, N., Cousins, A., Tu, K. P., & Barbour, M. M. (2011). Spatial variation in photosynthetic CO_2 carbon and oxygen isotope discrimination along leaves of the monocot triticale (*Triticum*×*Secale*) relates to mesophyll conductance and the Péclet effect. *Plant, Cell & Environment*, *34*(9), 1548–1562.

Lauteri, M., Scartazza, A., Guido, M. C., & Brugnoli, E. (1997). Genetic variation in photosynthetic capacity, carbon isotope discrimination and mesophyll conductance in provenances of *Castanea sativa* adapted to different environments. *Functional Ecology*, *11*(6), 675–683.

Leuning, R. (1995). A critical appraisal of a combined stomatal-photosynthesis model for C_3 plants. *Plant, Cell & Environment*, *18*(4), 339–355.

Lloyd, J., Syvertsen, J. P., Kriedemann, P. E., & Farquhar, G. D. (1992). Low conductances for CO_2 diffusion from stomata to the sites of carboxylation in leaves of woody species. *Plant, Cell & Environment*, *15*(8), 873–899.

Loreto, F., Harley, P. C., Di Marco, G., & Sharkey, T. D. (1992). Estimation of mesophyll conductance to CO_2 flux by three different methods. *Plant Physiology*, *98*(4), 1437–1443.

Loreto, F., Tsonev, T., & Centritto, M. (2009). The impact of blue light on leaf mesophyll conductance. *Journal of Experimental Botany*, *60*(8), 2283–2290.

Love, D. M., Venturas, M. D., Sperry, J. S., Brooks, P. D., Pettit, J. L., Wang, Y., … Mackay, D. S. (2019). Dependence of aspen stands on a subsurface water subsidy: Implications for climate change impacts. *Water Resources Research*, *55*(3), 1833–1848.

Lu, Z., Lu, J., Pan, Y., Lu, P., Li, X., Cong, R., & Ren, T. (2016). Anatomical variation of mesophyll conductance under potassium deficiency has a vital role in determining leaf photosynthesis. *Plant, Cell & Environment*, *39*(11), 2428–2439.

Mackay, D. S., Roberts, D. E., Ewers, B. E., Sperry, J. S., McDowell, N. G., & Pockman, W. T. (2015). Interdependence of chronic hydraulic dysfunction and canopy processes can improve integrated models of tree response to drought. *Water Resources Research*, *51*(8), 6156–6176.

Martins, S. C. V., Galmés, J., Molins, A., & DaMatta, F. M. (2013). Improving the estimation of mesophyll conductance to CO_2: On the role of electron transport rate correction and respiration. *Journal of Experimental Botany*, *64*(11), 3285–3298.

Medeiros, D. B., Martins, S. C. V., Cavalcanti, J. H. F., Daloso, D. M., Martinoia, E., Nunes-Nesi, A., … Araújo, W. L. (2016). Enhanced photosynthesis and growth in *atquac1* knockout mutants are due to altered organic acid accumulation and an increase in both stomatal and mesophyll conductance. *Plant Physiology*, *170*(1), 86–101.

Medlyn, B. E., Duursma, R. A., Eamus, D., Ellsworth, D. S., Prentice, I. C., Barton, C. V. M., … Wingate, L. (2011). Reconciling the optimal and empirical approaches to modelling stomatal conductance. *Global Change Biology*, *17*(6), 2134–2144.

Miyazawa, S.-I., Yoshimura, S., Shinzaki, Y., Maeshima, M., & Miyake, C. (2008). Deactivation of aquaporins decreases internal conductance to CO_2 diffusion in tobacco leaves grown under long-term drought. *Functional Plant Biology*, *35*(7), 553–564.

Mizokami, Y., Noguchi, K. O., Kojima, M., Sakakibara, H., & Terashima, I. (2015). Mesophyll conductance decreases in the wild type but not in an ABA-deficient mutant (aba1) of *Nicotiana plumbaginifolia* under drought conditions. *Plant, Cell & Environment*, *38*(3), 388–398.

Momayyezi, M., & Guy, R. D. (2017). Substantial role for carbonic anhydrase in latitudinal variation in mesophyll conductance of *Populus trichocarpa* Torr. & Gray. *Plant, Cell & Environment*, *40*(1), 138–149.

Mott, K. A., & Peak, D. (2011). Alternative perspective on the control of transpiration by radiation. *Proceedings of the National Academy of Sciences*, *108*(49), 19820–19823.

Nobel, P. S. (2009). *Physicochemical and environmental plant physiology*. Academic Press.

Olsovska, K., Kovar, M., Brestic, M., Zivcak, M., Slamka, P., & Shao, H. B. (2016). Genotypically identifying wheat mesophyll conductance regulation under progressive drought stress. *Frontiers in Plant Science*, *7*, 1111.

Ouyang, W., Struik, P. C., Yin, X., & Yang, J. (2017). Stomatal conductance, mesophyll conductance, and transpiration efficiency in relation to leaf anatomy in rice and wheat genotypes under drought. *Journal of Experimental Botany*, *68*(18), 5191–5205.

Pallozzi, E., Tsonev, T., Marino, G., Copolovici, L., Niinemets, U., Loreto, F., & Centritto, M. (2013). Isoprenoid emissions, photosynthesis and mesophyll diffusion conductance in response to blue light. *Environmental and Experimental Botany*, *95*, 50–58.

Parkhurst, D. F. (1977). A three-dimensional model for CO_2 uptake by continuously distributed mesophyll in leaves. *Journal of Theoretical Biology*, *67*(3), 471–488.

Parkhurst, D. F. (1984). Mesophyll resistance to photosynthetic carbon dioxide uptake in leaves: Dependence upon stomatal aperture. *Canadian Journal of Botany*, *62*(1), 163–165.

Parkhurst, D. F. (1994). Diffusion of CO_2 and other gases inside leaves. *New Phytologist*, *126*(3), 449–479.

Parkhurst, D. F., & Mott, K. A. (1990). Intercellular diffusion limits to CO_2 uptake in leaves: Studies in air and helox. *Plant Physiology*, *94*(3), 1024–1032.

Parkhurst, D. F., Wong, S.-C., Farquhar, G. D., & Cowan, I. R. (1988). Gradients of intercellular CO_2 levels across the leaf mesophyll. *Plant Physiology*, *86*(4), 1032–1037.

Peguero-Pina, J. J., Sisó, S., Flexas, J., Galmés, J., García-Nogales, A., Niinemets, U., … Gil-Pelegrín, E. (2017). Cell-level anatomical characteristics explain high mesophyll conductance and photosynthetic capacity in sclerophyllous Mediterranean oaks. *New Phytologist*, *214*(2), 585–596.

Perez-Martin, A., Flexas, J., Ribas-Carbó, M., Bota, J., Tomàs, M., Infante, J. M., & Diaz-Espejo, A. (2009). Interactive effects of soil water deficit and air vapour pressure deficit on mesophyll conductance to CO_2 in *Vitis vinifera* and *Olea europaea*. *Journal of Experimental*

Botany, *60*(8), 2391–2405.

Perez-Martin, A., Michelazzo, C., Torres-Ruiz, J. M., Flexas, J., Fernández, J. E., Sebastiani, L., & Diaz-Espejo, A. (2014). Regulation of photosynthesis and stomatal and mesophyll conductance under water stress and recovery in olive trees: Correlation with gene expression of carbonic anhydrase and aquaporins. *Journal of Experimental Botany*, *65*(12), 3143–3156.

Piel, C., Frak, E., Le Roux, X., & Genty, B. (2002). Effect of local irradiance on CO_2 transfer conductance of mesophyll in walnut. *Journal of Experimental Botany*, *53*(379), 2423–2430.

Rancourt, G. T., Éthier, G., & Pepin, S. (2015). Greater efficiency of water use in poplar clones having a delayed response of mesophyll conductance to drought. *Tree Physiology*, *35*(2), 172–184.

Rockwell, F. E., & Holbrook, N. M. (2017). Leaf hydraulic architecture and stomatal conductance: A functional perspective. *Plant Physiology*, *174*(4), 1996–2007.

Sade, N., Gallé, A., Flexas, J., Lerner, S., Peleg, G., Yaaran, A., & Moshelion, M. (2014). Differential tissue-specific expression of *NtAQP1* in *Arabidopsis thaliana* reveals a role for this protein in stomatal and mesophyll conductance of CO_2 under standard and salt-stress conditions. *Planta*, *239*(2), 357–366.

Sagardoy, R., Vázquez, S., Florez-Sarasa, I. D., Albacete, A., Ribas-Carbó, M., Flexas, J., … Morales, F. (2010). Stomatal and mesophyll conductances to CO_2 are the main limitations to photosynthesis in sugar beet (*Beta vulgaris*) plants grown with excess zinc. *New Phytologist*, *187*(1), 145–158.

Scafaro, A. P., von Caemmerer, S., Evans, J. R., & Atwell, B. J. (2011). Temperature response of mesophyll conductance in cultivated and wild *Oryza* species with contrasting mesophyll cell wall thickness. *Plant, Cell & Environment*, *34*(11), 1999–2008.

Schaeufele, R., Santrucek, J., & Schnyder, H. (2011). Dynamic changes of canopy-scale mesophyll conductance to CO_2 diffusion of sunflower as affected by CO_2 concentration and abscisic acid. *Plant, Cell & Environment*, *34*(1), 127–136.

Smith, W. K., Vogelmann, T. C., DeLucia, E. H., Bell, D. T., & Shepherd, K. A. (1997). Leaf form and photosynthesis: Do leaf structure and orientation interact to regulate internal light and carbon dioxide? *Bioscience*, *47*(11), 785–793.

Sorrentino, G., Haworth, M., Wahbi, S., Mahmood, T., Zuomin, S., & Centritto, M. (2016). Abscisic acid induces rapid reductions in mesophyll conductance to carbon dioxide. *PLoS One*, *11*(2), e0148554.

Sperry, J. S., Venturas, M. D., Anderegg, W. R. L., Mencuccini, M., Mackay, D. S., Wang, Y., & Love, D. M. (2017). Predicting stomatal responses to the environment from the optimization of photosynthetic gain and hydraulic cost. *Plant, Cell & Environment*, *40*(6), 816–830.

Stangl, Z. R., Tarvainen, L., Wallin, G., Ubierna, N., Räntfors, M., & Marshall, J. D. (2019). Diurnal variation in mesophyll conductance and its influence on modelled water-use efficiency in a mature boreal *Pinus sylvestris* stand. *Photosynthesis Research*, *141*, 53–63.

Syvertsen, J. P., Lloyd, J., McConchie, C., Kriedemann, P. E., & Farquhar, G. D. (1995). On the relationship between leaf anatomy and CO_2 diffusion through the mesophyll of hypostomatous leaves. *Plant, Cell & Environment*, *18*(2), 149–157.

Tazoe, Y., von Caemmerer, S., Badger, M. R., & Evans, J. R. (2009). Light and CO_2 do not affect the mesophyll conductance to CO_2 diffusion in wheat leaves. *Journal of Experimental Botany*, *60*(8), 2291–2301.

Tazoe, Y., von Caemmerer, S., Estavillo, G. M., & Evans, J. R. (2011). Using tunable diode laser spectroscopy to measure carbon isotope discrimination and mesophyll conductance to CO_2 diffusion dynamically at different CO_2 concentrations. *Plant, Cell & Environment*, *34*(4), 580–591.

Terashima, I. (1995). Three resistances to CO_2 diffusion: Leaf-surface water, intercellular spaces and mesophyll cells. In *Photosynthesis: From light to biosphere* (pp. 537–542). Kluwer Academic Publishers.

Tomeo, N. J., & Rosenthal, D. M. (2017). Variable mesophyll conductance among soybean cultivars sets a tradeoff between photosynthesis and water-use-efficiency. *Plant Physiology*, *174*(1), 241–257.

Tomás, M., Medrano, H., Brugnoli, E., Escalona, J. M., Martorell, S., Pou, A., … Flexas, J. (2014). Variability of mesophyll conductance in grapevine cultivars under water stress conditions in relation to leaf anatomy and water use efficiency. *Australian Journal of Grape and Wine Research*, *20*(2), 272–280.

Tosens, T., Niinemets, U., Vislap, V., Eichelmann, H., & Castro-Diez, P. (2012). Developmental changes in mesophyll diffusion conductance and photosynthetic capacity under different light and water availabilities in *Populus tremula*: How structure constrains function. *Plant, Cell & Environment*, *35*(5), 839–856.

Tyree, M. T., & Yianoulis, P. (1980). The site of water evaporation from sub-stomatal cavities, liquid path resistances and hydroactive stomatal closure. *Annals of Botany*, *46*(2), 175–193.

Velikova, V., Tsonev, T., Loreto, F., & Centritto, M. (2011). Changes in photosynthesis, mesophyll conductance to CO_2, and isoprenoid emissions in *Populus nigra* plants exposed to excess nickel. *Environmental Pollution*, *159*(5), 1058–1066.

Venturas, M. D., Sperry, J. S., Love, D. M., Frehner, E. H., Allred, M. G., Wang, Y., & Anderegg, W. R. L. (2018). A stomatal control model based on optimization of carbon gain versus hydraulic risk predicts aspen sapling responses to drought. *New Phytologist*, *220*(3), 836–850.

Vesala, T., Sevanto, S., Grönholm, T., Salmon, Y., Nikinmaa, E., Hari, P., & Hölttä, T. (2017). Effect of leaf water potential on internal humidity and CO_2 dissolution: Reverse transpiration and improved water use efficiency under negative pressure. *Frontiers in Plant Science*, *8*, 54.

von Caemmerer, S., & Evans, J. R. (2015). Temperature responses of mesophyll conductance differ greatly between species. *Plant, Cell & Environment*, *38*(4), 629–637.

Vrábl, D., Vašková, M., Hronková, M., Flexas, J., & Šantrůček, J. (2009). Mesophyll

conductance to CO_2 transport estimated by two independent methods: Effect of variable CO_2 concentration and abscisic acid. *Journal of Experimental Botany*, *60*(8), 2315–2323.

Wang, Y., Pan, R., & Tyree, M. T. (2015). Studies on the tempo of bubble formation in recently cavitated vessels: A model to predict the pressure of air bubbles. *Plant Physiology*, *168*(2), 521–531.

Wang, Y., Sperry, J. S., Venturas, M. D., Trugman, A. T., Love, D. M., & Anderegg, W. R. L. (2019). The stomatal response to rising CO_2 concentration and drought is predicted by a hydraulic trait-based optimization model. *Tree Physiology*, *39*, 1416–1427.

Wolf, A., Anderegg, W. R. L., & Pacala, S. W. (2016). Optimal stomatal behavior with competition for water and risk of hydraulic impairment. *Proceedings of the National Academy of Sciences*, *113*(46), E7222–E7230.

Wylie, R. B. (1951). Principles of foliar organization shown by sun-shade leaves from ten species of deciduous dicotyledonous trees. *American Journal of Botany*, *38*(5), 355–361.

Wylie, R. B. (1954). Leaf organization of some woody dicotyledons from New Zealand. *American Journal of Botany*, *41*(3), 186–191.

Xiong, D., Douthe, C., & Flexas, J. (2018). Differential coordination of stomatal conductance, mesophyll conductance, and leaf hydraulic conductance in response to changing light across species. *Plant, Cell & Environment*, *41*(2), 436–450.

Xiong, D., Flexas, J., Yu, T., Peng, S., & Huang, J. (2017). Leaf anatomy mediates coordination of leaf hydraulic conductance and mesophyll conductance to CO_2 in *Oryza*. *New Phytologist*, *213*(2), 572–583.

Xiong, D., Liu, X., Liu, L., Douthe, C., Li, Y., Peng, S., & Huang, J. (2015). Rapid responses of mesophyll conductance to changes of CO_2 concentration, temperature and irradiance are affected by N supplements in rice. *Plant, Cell & Environment*, *38*(12), 2541–2550.

Yianoulis, P., & Tyree, M. T. (1984). A model to investigate the effect of evaporative cooling on the pattern of evaporation in sub-stomatal cavities. *Annals of Botany*, *53*(2), 189–206.

Zhou, S., Duursma, R. A., Medlyn, B. E., Kelly, J. W. G., & Prentice, I. C. (2013). How should we model plant responses to drought? An analysis of stomatal and non-stomatal responses to water stress. *Agricultural and Forest Meteorology*, *182*, 204–214.

Zhou, S., Medlyn, B., Sabaté, S., Sperlich, D., & Prentice, I. C. (2014). Short-term water stress impacts on stomatal, mesophyll and biochemical limitations to photosynthesis differ consistently among tree species from contrasting climates. *Tree Physiology*, *34*(10), 1035–1046.

Table 2.1: List of variables used in this study with their symbols, descriptions, default values, units, and test ranges for the sensitivity analysis. The default and test range of species-specific anatomical traits are average and minimal–maximal values from the literature.

Symbol	Description	Default (unit)	Test range
	Species-specific anatomical traits		
L_{sp}	Spongy mesophyll thickness	123.43 (μm)	21.50–435.00
L_{st}	Stomatal pore depth, equals the abaxial epidermis thickness	14.06 (μm)	6.00–34.10
R_{bd}	Radius of the boundary layer cylinder	38.89 (μm)	16.12–141.05
R_{sp}	Radius of the spongy layer cylinder, $R_{sp} = R_{bd}$	38.89 (μm)	16.12–141.05
$R_{st,max}$	Maximal equivalent radius of a stoma	6.35 (μm)	1.51–21.26
f_{ias}	Intercellular air fraction in the spongy layer	0.38	0.10–0.73
	Non species-specific anatomical traits		
L_{bd}	Boundary layer thickness	200.00 (μm)	21.50–435.00
R_{st}	Equivalent radius of a stoma, $R_{st} \leq R_{st,max}$	5.00 (μm)	1.51–21.26
	Leaf diffusive conductance (gas-phase unless noted)		
$G_{C,bd}$	Diffusive conductance for CO_2 in the boundary layer	(mol m^{-2} s^{-1})	
$G_{C,sp}$	Diffusive conductance for CO_2 per leaf area in the spongy layer	(mol m^{-2} s^{-1})	
$G^{\varnothing}_{C,sp}$	$G_{C,sp}$ when there are no cells in the spongy layer	(mol m^{-2} s^{-1})	
$G_{C,st}$	Diffusive conductance for CO_2 per leaf area through stomata	(mol m^{-2} s^{-1})	
$G_{H,bd}$	Diffusive conductance for H_2O in the boundary layer	(mol m^{-2} s^{-1})	
$G_{H,sp}$	Diffusive conductance for H_2O per leaf area in the spongy layer	(mol m^{-2} s^{-1})	
$G^{\varnothing}_{H,sp}$	$G_{H,sp}$ when there are no cells in the spongy layer	(mol m^{-2} s^{-1})	
$G_{H,st}$	Diffusive conductance for H_2O per leaf area through stomata	(mol m^{-2} s^{-1})	
G_{ias}	Diffusive conductance for CO_2 in the intercellular airspace	(mol m^{-2} s^{-1})	
G_{liq}	Liquid-phase conductance for CO_2 from cell wall to chloroplasts	(mol m^{-2} s^{-1})	
G_{SC}	Diffusive conductance for CO_2 per leaf area, $G_{SC} = G_{SW}/1.6$	(mol m^{-2} s^{-1})	
G_{SW}	Diffusive conductance for H_2O per leaf area	(mol m^{-2} s^{-1})	0.00–0.50
G_{TC}	Total diffusive conductance for CO_2 per leaf area	(mol m^{-2} s^{-1})	

Table 2.2: Fitting parameters for equations 2.7–2.9 for boundary and spongy layer conductances (symbols defined in Table 2.1 and equations 2.7–2.9).

	$G_{H,bd}$	$G_{H,sp}$	$G_{C,sp}$
$k_{st,sp}$ or $k_{st,bd}$	-1.915731	-14.226819	9.820652
$k_{st,l}$	0.074672	0.014643	0.147947
l_{st}	1.559147	1.899844	1.559149
$k_{sp,st}$ or $k_{bd,st}$	1.833096	14.060909	-9.903288
$k_{sp,l}$ or $k_{bd,l}$	-0.200440	-0.111787	-0.263997
l_{bd} or l_{sp}	-1.870286	-1.806674	-1.870287
$k_{l,st}$	-0.074407	-0.012719	-0.147682
$k_{l,bd}$ or $k_{l,sp}$	0.202129	0.112050	0.265686
l_{d}	-0.010803	-0.007752	-0.010803
l_{l}	6.360923	6.417760	6.360925

Table 2.3: Literature survey of whether G_M and G_{SW} change in the same direction in response to manipulations of an independent variable at levels from the gene to the environment. Of the 62 studies cited, 57 reported a positive correlation between G_M and G_{SW}, whereas five did not support the covariation. Asterisked references were sources of the G_M and G_{SW} data plotted in Fig. 2.5.

Level	Independent variable	G_M and G_{SW} change in same direction		Reference
		Yes	No	
Gene	*NtDAQ1*	✓		(Flexas et al., 2006)*
		✓		(Sade et al., 2014)
	Ictb	✓		(Gong et al., 2015)
	FBP/Sbpase	✓		(Gong et al., 2015)
	Atquac1	✓		(Medeiros et al., 2016)
	OsPIP	✓		(Ding et al., 2016)
Cell	$HgCl_2$	✓		(Miyazawa et al., 2008)
	Acetazolamide	✓		(Momayyezi & Guy, 2017)
	Abscisic acid		✓	(Vrábl et al., 2009)*
		✓		(Mizokami et al., 2015)
		✓		(Sorrentino et al., 2016)
Leaf	Age	✓		(Flexas, Ortuño, et al., 2007)*
		✓		(Barbour et al., 2016)
	Geometry	✓		(Kodama et al., 2011)*
	Hydraulics	✓		(Xiong et al., 2018)
	G_{SW}	✓		(Bickford et al., 2010)*
		✓		(Ferrio et al., 2012)*
		✓		(Rancourt et al., 2015)
		✓		(Barbour & Kaiser, 2016)
		✓		(J.-M. Han et al., 2016)
		✓		(Tomeo & Rosenthal, 2017)
		✓		(Stangl et al., 2019)
	Height	✓		(Q. Han, 2011)*
Air	Vapor pressure deficit	✓		(Perez-Martin et al., 2009)*
	Heat Pulse	✓		(Galle et al., 2013)
	$[CO_2]$	✓		(Loreto et al., 1992)*
		✓		(Flexas, Diaz-Espejo, et al., 2007)*
		✓		(Hassiotou et al., 2009)*
		✓		(Tazoe et al., 2009)*
		✓		(Vrábl et al., 2009)*
		✓		(Douthe et al., 2011)*
		✓		(Schaeufele et al., 2011)
		✓		(Tazoe et al., 2011)*
		✓		(Gilbert et al., 2011)
		✓		(Galle et al., 2013)
		✓		(Martins et al., 2013)

Table 2.3: continued

Level	Independent variable	G_M and G_{SW} change in same direction		Reference
		Yes	No	
		✓		(Xiong et al., 2015)
		✓		(Olsovska et al., 2016)
	Light	✓		(Piel et al., 2002)*
		✓		(Hassiotou et al., 2009)*
		✓		(Tazoe et al., 2009)*
		✓		(Bickford et al., 2010)*
		✓		(Cano et al., 2013)
		✓		(Pallozzi et al., 2013)
		✓		(Xiong et al., 2015)
		✓		(Campany et al., 2016)
		✓		(Xiong et al., 2018)
	Blue light		✓	(Loreto et al., 2009)*
		✓		(Pallozzi et al., 2013)
	Temperature		✓	(Scafaro et al., 2011)
			✓	(Evans & von Caemmerer, 2013)
			✓	(von Caemmerer & Evans, 2015)
		✓		(Xiong et al., 2015)
Soil	Drought	✓		(Lauteri et al., 1997)*
		✓		(Delfine et al., 1999)*
		✓		(Galle et al., 2009)*
		✓		(Perez-Martin et al., 2009)
		✓		(Hu et al., 2010)*
		✓		(Brilli et al., 2013)
		✓		(Cano et al., 2014)
		✓		(Perez-Martin et al., 2014)
		✓		(Mizokami et al., 2015)
		✓		(Rancourt et al., 2015)
		✓		(Barbour et al., 2016)
		✓		(J.-M. Han et al., 2016)
		✓		(Olsovska et al., 2016)
		✓		(Ouyang et al., 2017)
	Salt Stress	✓		(Delfine et al., 1998)*
		✓		(Delfine et al., 1999)*
	Nitrogen	✓		(Xiong et al., 2015)
	Potassium	✓		(Jin et al., 2011)*
		✓		(Lu et al., 2016)
	Zinc	✓		(Sagardoy et al., 2010)*
	Nickel	✓		(Velikova et al., 2011)*
Tree	Genotype	✓		(Barbour et al., 2010)*
		✓		(Tomás et al., 2014)
		✓		(Xiong et al., 2017)
	Species	✓		(Gillon & Yakir, 2000)*

Table 2.3: continued

Level	Independent variable	G_M and G_{SW} change in same direction		Reference
		Yes	No	
		✓		(De Lucia et al., 2003)*
		✓		(Peguero-Pina et al., 2017)
Ecosystem	Latitude	✓		(Momayyezi & Guy, 2017)
Summary		57	5	

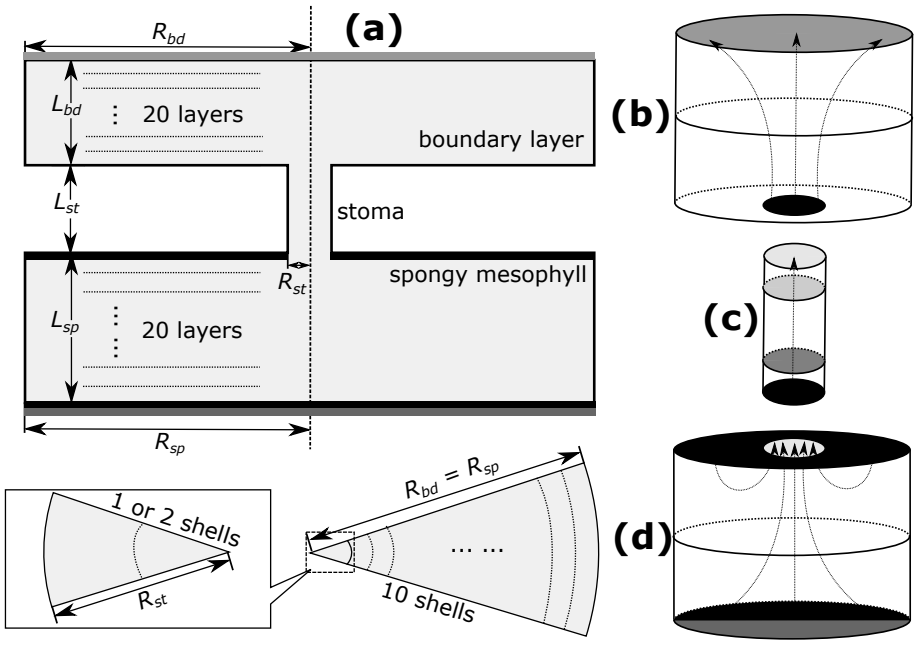

Figure 2.1: The leaf diffusion model. (a) Gas diffusion was divided in a series of three cylindrical units: boundary layer, stomatal pore, and spongy mesophyll (not drawn to scale). (b) In the boundary layer, H_2O diffuses from the stomatal pore opening to the atmospheric boundary as labeled with arrows, and CO_2 diffuses in the reverse direction. (c) In the stomatal pore, CO_2 and H_2O diffuse in plane diffusion in opposite directions. (d) In the spongy layer, H_2O diffuses from all internal surfaces as labeled with black to the stomatal pore as labeled with arrows, whereas CO_2 diffuses from the stomatal pore opening to the palisade boundary as labeled with dark gray.

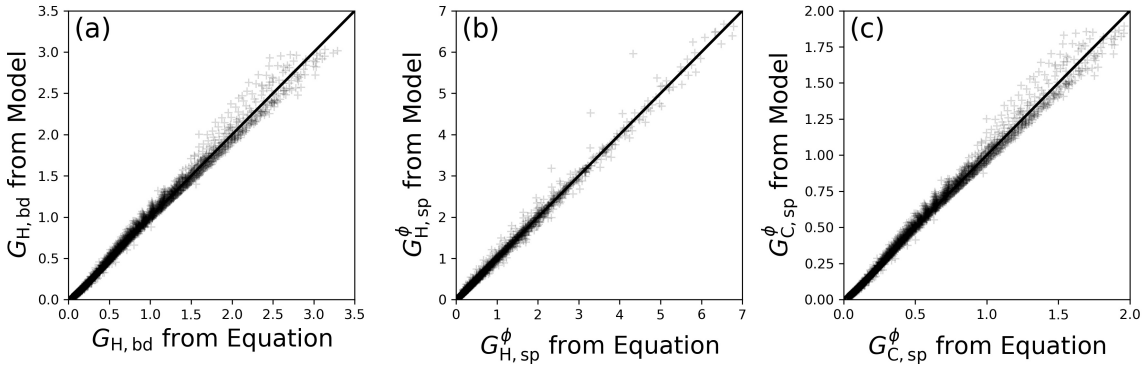

Figure 2.2: Comparison of numerically modeled and empirically fitted diffusive conductance. The y-axis plots the diffusive conductance obtained from the 3D numerical model simulation and the x-axis plots those fitted by the empirical functions in equation 3. Solid black in each panel indicates the 1:1 line. (a) Boundary layer conductance to H_2O ($G_{H,bd}$, mol m^{-2} s^{-1}). (b) Spongy layer conductance to H_2O ($G^{\varnothing}_{H,sp}$, mol m^{-2} s^{-1}). (c) Spongy layer conductance to CO_2 ($G^{\varnothing}_{C,sp}$, mol m^{-2} s^{-1}).

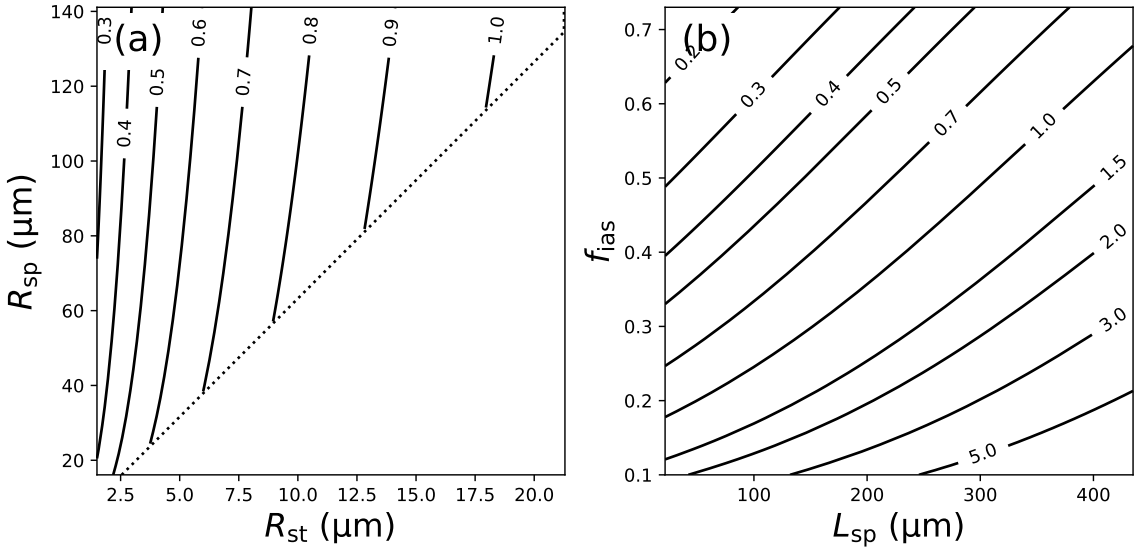

Figure 2.3: Sensitivity of G_{SC}/G_{ias} (labeled contours) to leaf anatomy. Indicated traits were varied over the reported range while holding other parameters constant at default (mean) values (Table 2.1). (a) Sensitivity to stomatal pore radius (R_{st}) and spongy layer radius (R_{sp}). White space below dotted line indicates limit to stomatal opening. (b) Sensitivity to spongy layer air fraction (f_{ias}) and spongy layer thickness (L_{sp}).

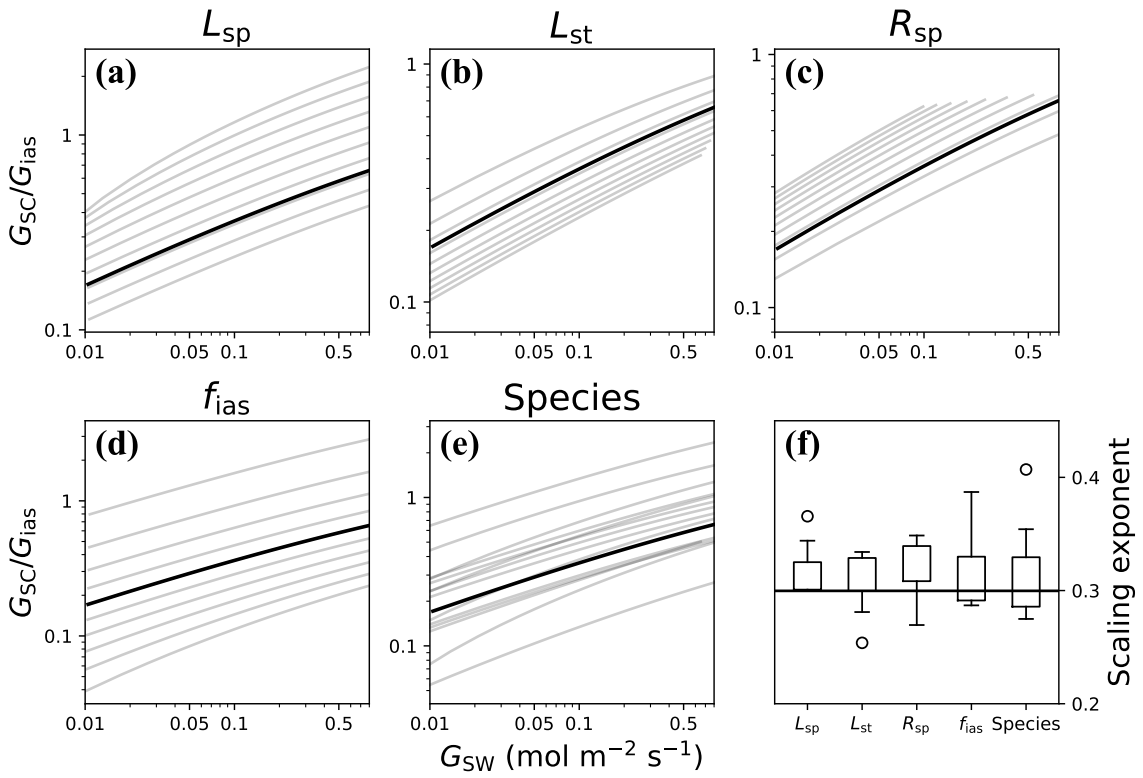

Figure 2.4: The G_{SC}/G_{ias} associated with stomatal closure in the C_3 hypostomatous leaf. For each curve in (a)–(e), diffusive conductance to water vapor (G_{SW}) was altered by altering stomatal pore area (via reducing R_{st} from maximal $R_{st,max}$) with other parameters constant. Solid curve is for the average hypostomatous leaf. (a) Gray curves plot the G_{SC}/G_{ias} versus G_{SW} at different spongy layer thickness (L_{sp}). The 10 gray curves from bottom to top are for increasing L_{sp} across its test range (evenly partitioned, same for (b)–(d)). (b) The G_{SC}/G_{ias} versus G_{SW} at different stomatal pore depth (L_{st}); curves from top to bottom are for increasing L_{st} across its test range. (c) The G_{SC}/G_{ias} versus G_{SW} at different spongy cylinder radius (R_{sp}); curves from top to bottom are for decreasing R_{sp} (increasing stomatal frequency). (d) The G_{SC}/G_{ias} versus G_{SW} at different intercellular air fraction (f_{ias}); curves from top to bottom are for increasing f_{ias}. (e) The G_{SC}/G_{ias} versus G_{SW} for different species, one gray curve per species. (f) Box plot of the scaling exponents for the gray curves in (a)–(e), with the horizontal line indicating the exponent (0.30) of the average leaf.

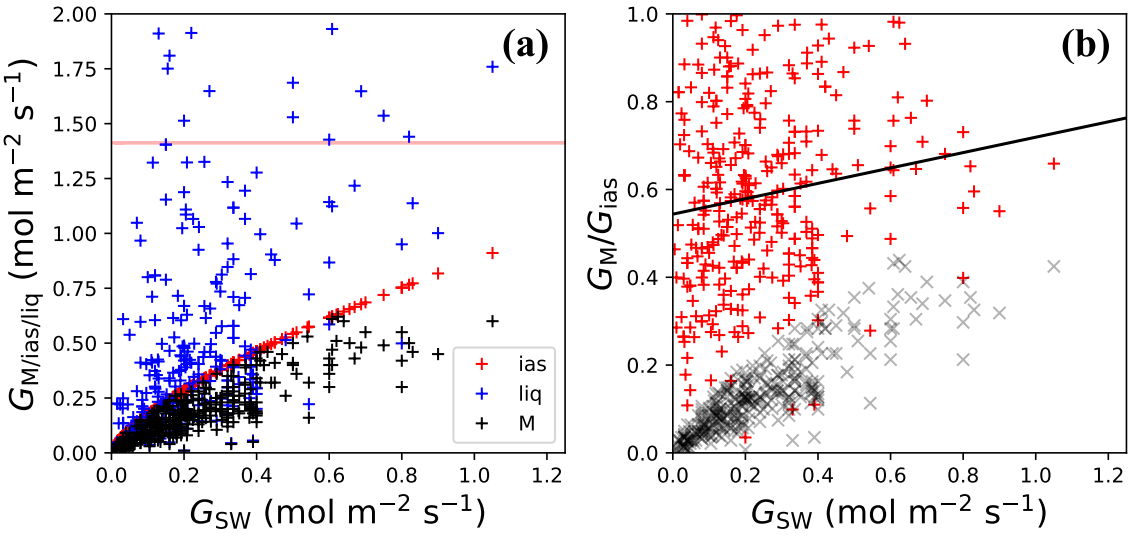

Figure 2.5: Partitioning mesophyll conductance to CO_2 (G_M; values from asterisked sources in Table 2.3) into gas-phase intercellular conductance (G_{ias}) and liquid-phase intracellular conductance (G_{liq}) as a function of stomatal diffusive conductance to water vapor (G_{SW}). (a) The G_{ias} (red "+") was estimated from G_{SW} with our 3D diffusion model for average hypostomatous leaf, and the residual of G_M (black "+") and G_{ias} was G_{liq} (blue "+"). The light red line represents the G_{ias} computed from the 1D diffusion equation 2.11. (b) The G_M/G_{ias}, which indicates the fraction of total diffusive mesophyll resistance ($1/G_M$) attributable to the intercellular gas diffusion. Red "+" with the solid regression line (P = 0.002) plot our 3D diffusion model, and gray "×" are based on equation 2.11.

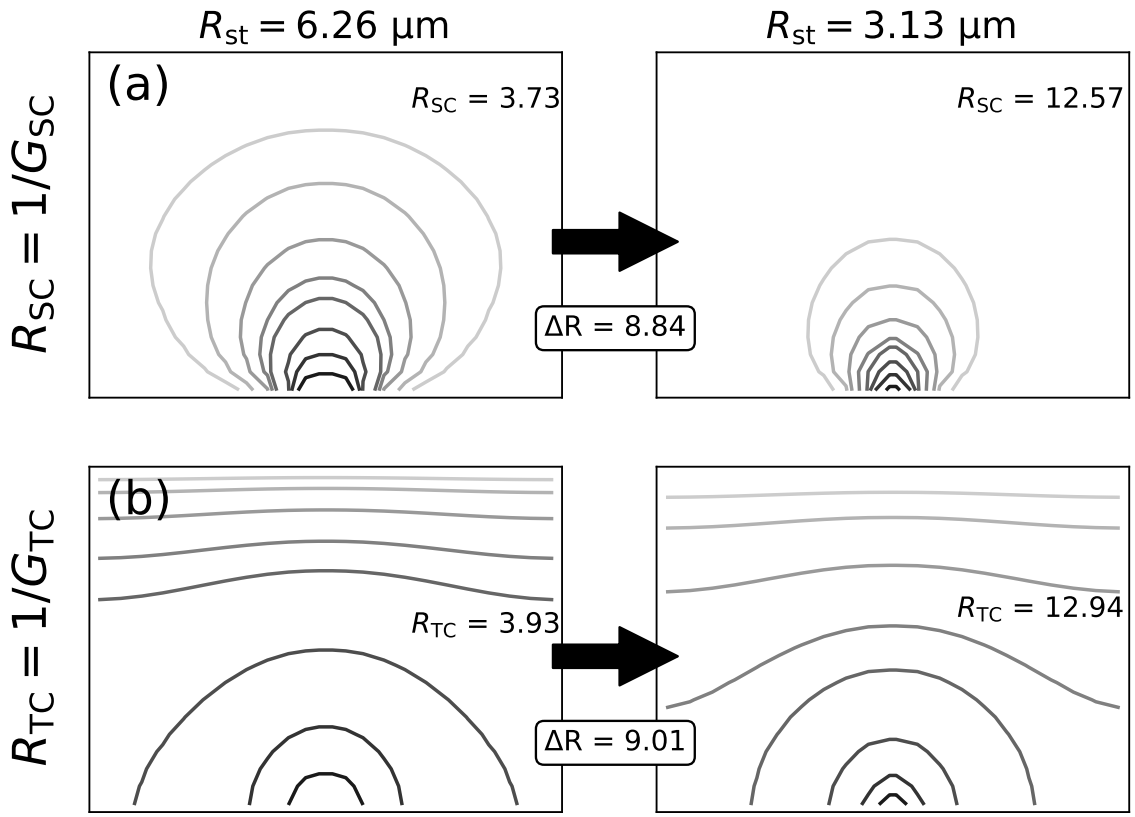

Figure 2.6: Geometry of the diffusion gradient as stomata adjust from wide open (left, R_{st} = 6.26 µm) to partially closed (right, R_{st} = 3.13 µm) for the average hypostomatous leaf (Table 2.1). The x axis represents the diameter and y axis plots the thickness of the spongy mesophyll cylinder. The stomatal pore is at the center of the bottom axis, and the palisade boundary is the top axis. Gray curves from top to bottom represent partial pressure contours of CO_2 at 0.5%, 1%, 2%, 3.5%, 5%, 10%, 20%, and 40% of the total pressure difference from the palisade to the stomatal pore. (a) The spherical geometry of stomatal diffusive conductance to CO_2 (G_{SC}), which is based on the diffusion of water vapor from internal wet surfaces. The reduction in stomatal aperture caused the resistance to stomatal diffusion to CO_2 ($R_{SC} = 1/G_{SC}$) to increase by ΔR = 8.84 m^2 s mol^{-1} CO_2. (b) The spherical-to-planar geometry of total gas-phase diffusive conductance to CO_2 (G_{TC}), which is based on CO_2 diffusion to the palisade. The reduction in stomatal aperture caused the total resistance to CO_2 diffusion ($R_{TC} = 1/G_{TC}$) to increase by ΔR = 9.01 m^2 s mol^{-1} CO_2, a greater increase than for R_{SC}. Note here that ΔR comprises increasing resistances in all the boundary layer, stomatal pore, and spongy mesophyll. The intercellular resistance ($R_{ias} = 1/G_{ias}$) is the difference between R_{TC} and R_{SC} (equation 2.3), and it increases by 0.17 m^2 s mol^{-1} CO_2 with stomatal closure.

2.7 Supporting Information

2.7.1 Derivation of equation 2.5

Diffusive conductance to water vapor is defined as the molar diffusion rate per leaf area per second. According to the Fick's First Law, the plane diffusion rate per plane area (J in mol m^{-2} s^{-1}) is proportional to the concentration gradient, that is,

$$J = D \cdot \frac{\Delta C}{\Delta L}, \tag{2.13}$$

where D is the diffusion coefficient of water vapor in air (m^2 s^{-1}), ΔC is the concentration difference (mol m^{-3}), and ΔL is the distance between the source and sink planes (m). The total diffusion rate of the stomatal pore per leaf area J_{st} is

$$J_{st} = D \cdot \frac{\Delta C}{\Delta L} \cdot \frac{\pi R_{st}^2}{\pi R_{bd}^2}, \tag{2.14}$$

where R_{st} is the stomatal pore radius and R_{bd} is the boundary layer cylinder radius. According to the Ideal Gas Law, ΔC can be computed from

$$\Delta C = \frac{\Delta P}{RT}, \tag{2.15}$$

where ΔP is the vapor pressure drop along the stomatal pore cylinder, R is the gas constant and T is the Kelvin temperature. The stomatal pore conductance is

$$G_{H,st} = \frac{J_{st}}{\mu_w}, \tag{2.16}$$

where μ_w is the vapor pressure fraction difference along the stomatal pore: $\mu_w = \Delta P / P_{atm}$ (P_{atm} is the atmospheric pressure).

Combining equations 2.13–2.16, the stomatal pore conductance is

$$G_{H,st} = D \cdot \frac{P_{atm}}{RT} \cdot \frac{1}{L_{st}} \cdot \frac{R_{st}^2}{R_{bd}^2} \tag{2.17}$$

where L_{st} is the length of stomatal pore cylinder (namely the abaxial epidermis thickness).

2.7.2 Sensitivity analyses of G_{ias} limitation

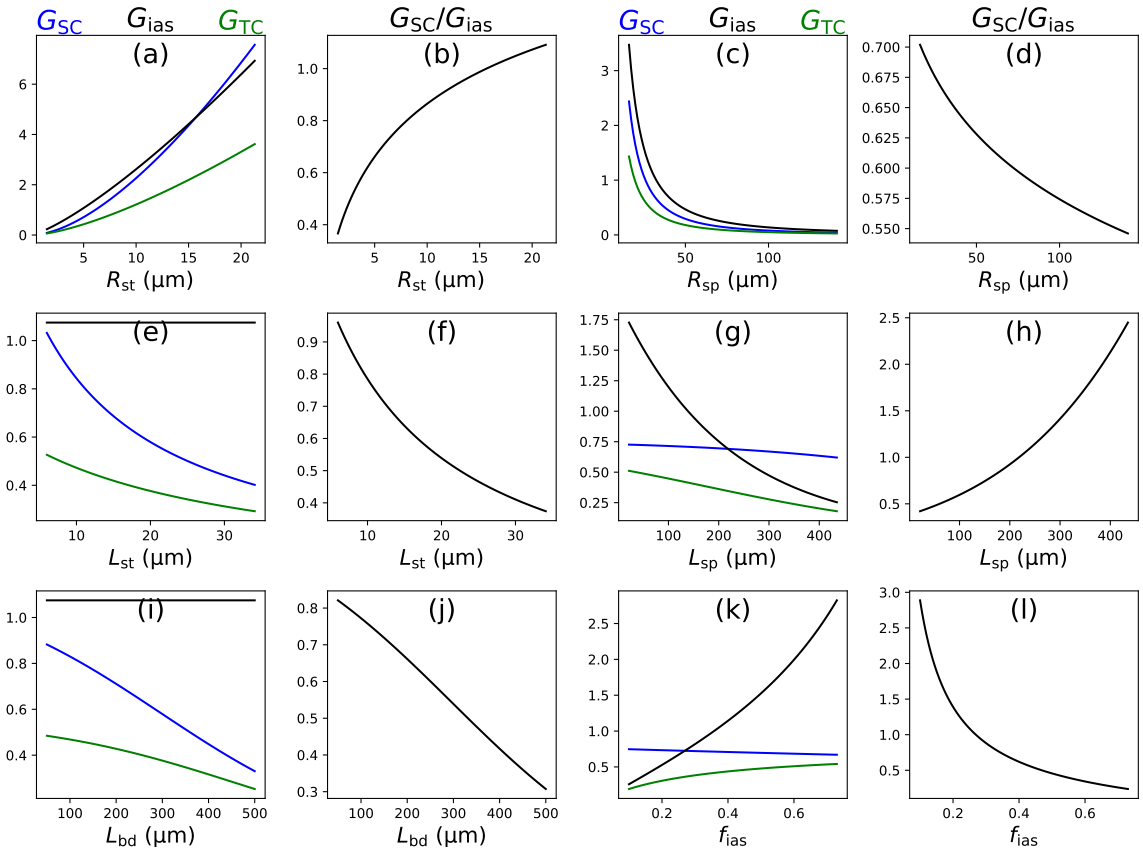

Figure 2.S1: Sensitivity analyses of G_{SC} (blue lines in column 1 and 3), G_{TC} (green lines in column 1 and 3), G_{ias} (black lines in column 1 and 3), and G_{SC}/G_{ias} (black lines in column 2 and 4) versus R_{st}, R_{sp}, L_{st}, L_{sp}, L_{bd}, and f_{ias}. The units for G_{SC}, G_{TC}, and G_{ias} are mol m^{-2} s^{-1}. The analyses were done by varying each of R_{st}, R_{sp}, L_{st}, L_{sp}, L_{bd}, and f_{ias} in the test range while holding the rest parameters at default value (Table 2.1 in the main text).

2.7.3 Leaf diffusive conductances versus stomatal pore aperture

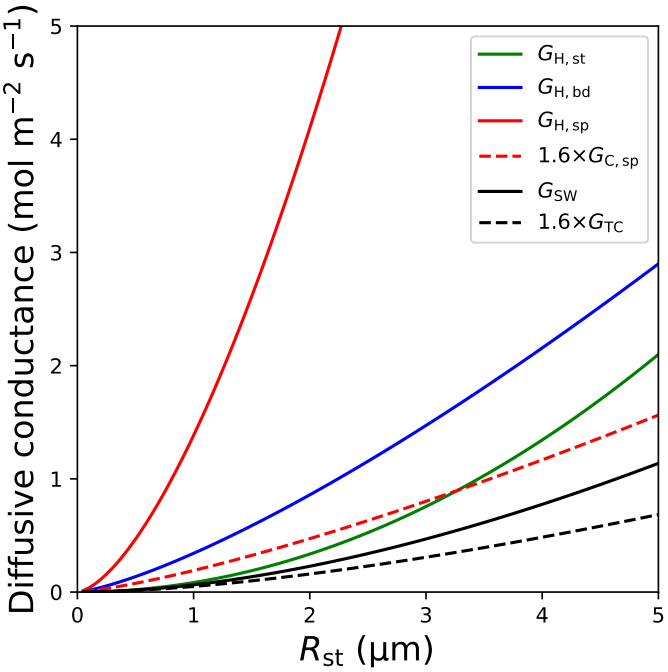

Figure 2.S2: Leaf diffusive conductances scale with stomatal pore aperture. In the simulation, leaf anatomical traits are set to default values (Table 2.1) and the stomatal pore radius (R_{st}) ranges from 0 to 5 μm. The diffusive conductance symbols ($G_{H,st}$, $G_{H,bd}$, $G_{H,sp}$, $G_{C,sp}$, G_{SW}, and G_{TC}) are defined in Table 2.1. The $G_{C,sp}$, and G_{TC} are converted to equivalent conductance for H_2O by multiplying a molar conversion factor 1.6 to scale with the $G_{H,st}$, $G_{H,bd}$, $G_{H,sp}$, and G_{SW} (mol m^{-2} s^{-1}).

CHAPTER 3

A THEORETICAL AND EMPIRICAL ASSESSMENT OF STOMATAL OPTIMIZATION MODELING

3.1 Summary

Optimal stomatal control models have shown great potential in predicting stomatal behavior and improving carbon cycle modeling. Basic stomatal optimality theory posits that stomatal regulation maximizes the carbon gain relative to a penalty of stomatal opening. All models take a similar approach to calculate instantaneous carbon gain from stomatal opening (the gain function). Where the models diverge is in how they calculate the corresponding penalty (the penalty function). In this review, we compare and evaluate nine different optimization models in how they quantify the penalty and how well they predict stomatal responses to the environment. We propose that the penalty function must meet seven basic criteria to produce a unique and realistic solution. We evaluate whether the models meet these criteria and further test them against multiple leaf gas exchange datasets. The optimization models with better predictive skills have penalty functions that meet our seven criteria and fitting parameters that are both few in number and physiology-based. The best performing models are those with a penalty function based on stress-induced hydraulic failure. We propose a new model that has a hydraulics-based penalty function which meets all seven criteria and demonstrates a highly predictive skill against our test datasets.

• **Keywords:** carbon gain, carbon penalty, gas exchange, hydraulics, optimization model, stomatal control, trade-off

3.2 Introduction

Trees balance CO_2 uptake and water loss by regulating the aperture of tiny pores in the leaf epidermis called stomata. The benefit of opening the stomata is CO_2 uptake that fuels photosynthesis. The fact that stomata often restrict photosynthesis by failing to open

maximally suggests there is also an inherent and unavoidable disadvantage or "penalty" for stomatal opening in certain environmental conditions. Penalties are numerous and can include consequences of transpiration such as running out of soil water, suffering excess xylem cavitation due to negative xylem pressure, and experiencing stress-induced non-stomatal limitation to photosynthesis (NSL; Dewar et al., 2018; Flexas et al., 2012). Basic optimization theory suggests that stomatal regulation ought to maximize the difference between the carbon gain and the penalty. While the carbon gain from stomatal opening is easily quantified, a fundamental challenge for optimization models is quantifying the penalty from potentially diverse sources and mechanisms over a range of timescales, and expressing it on equal terms with instantaneous photosynthesis.

The evolution of stomatal regulation presumably involves coordinated adjustments in almost all aspects of plant performance. Attempting to quantify the penalty from all such sources is, however, not realistic because (1) the suite of chosen physiological processes will likely be incomplete, (2) not all processes can be quantitatively represented due to insufficient mechanistic understanding, (3) parameterization would be extremely difficult, and (4) it would be computationally expensive to run such a multidimensional optimization model at the tree-level or beyond (Chen et al., 2012; Hills et al., 2012). Instead, optimization models have typically focused on a single candidate penalty as an implicit proxy for what, in reality, must be much more complex. From this practical standpoint, a successful penalty function is an algorithm that is readily parameterized from measurable physiological data or functional traits, and works in reproducing stomatal responses to changing environmental conditions.

Over the years, many such optimization models have been proposed, differing mainly in what process they choose to represent as the penalty of water use. Many of these are elaborations of the original Cowan & Farquhar (1977) assumption that a plant ought to maximize the cumulative photosynthesis while using a given amount of water in a given time (Buckley et al., 2017; Buckley & Schymanski, 2014; Katul et al., 2010, 2009; Manzoni et al., 2013; Medlyn et al., 2011). The original Cowan-Farquhar framework links the penalty to running out of water, but does not explicitly consider stress-induced damage to the vascular system or NSL. Other models use different penalty criteria, often explicitly incorporating the risk of vascular damage (Anderegg et al., 2018; Eller et al., 2018; Sperry et al., 2017; Wolf

et al., 2016) and/or NSL (Dewar et al., 2018; Hölttä et al., 2017).

In this review, we examine and compare several optimization formulations concerning their ability to predict stomatal behavior and analyze what makes some models more successful than others. We first develop seven fundamental criteria for how the penalty function must behave mathematically to predict the widely observed stomatal responses to environmental cues. Second, we review nine optimization models that captures diverse set of penalty function, and compare them against our seven fundamental criteria. Third, we test how the models perform against several datasets. Finally, to illustrate how our results can help further develop optimization models, we present and evaluate a new model that meets all seven criteria.

3.3 A Generic Optimization Equation

In our framing of basic optimization theory, stomatal opening (x) is optimized when the instantaneous $A - \Theta$ is maximized, where A is the current net photosynthetic rate, and Θ is the penalty (both in μmol CO_2 s^{-1} m^{-2} leaf area; list of symbols and units in Table 3.1). This optimization is obtained when the marginal photosynthetic gain (dA/dx) equals the marginal penalty ($d\Theta/dx$). The measure of stomatal opening, x, can be stomatal conductance for H_2O , transpiration rate (E_{leaf}), or leaf xylem pressure (P); we use $x = E_{\text{leaf}}$ in this review because the marginal gain (dA/dE) represents marginal water use efficiency. Thus, we have

$$\max(A - \Theta) \equiv \frac{dA}{dE} = \frac{d\Theta}{dE}, \tag{3.1}$$

To facilitate model comparison, we express all nine models in terms of equation 3.1. Most models interpret Θ as a "shadow cost" or "risk" to future plant performance, which leaves the current instantaneous A unchanged. The exception are models that assume the penalty is from NSL. In these models, Θ (distinguished as Θ', herein) represents the downregulation in instantaneous photosynthesis from its nonstressed, well-watered rate (distinguished as A_{ww}), and the difference is the actual instantaneous A ($A = A_{\text{ww}} - \Theta'$; these models maximize $A_{\text{ww}} - \Theta'$). We use A and Θ by default in this review except for the NSL models, where we use A_{ww} and Θ' instead.

3.3.1 The carbon gain calculation, A

All models are in basic agreement in using established photosynthesis models for calculating the instantaneous A from stomatal opening, photosynthetic capacity (V_{cmax} and J_{max}, where V_{cmax} is the maximal carboxylation rate and J_{max} is the maximal electron transport), and environmental conditions (including solar radiation, atmospheric vapor pressure deficit (VPD), atmospheric [CO_2] (C_a), and air temperature). In this review, we use the Farquhar et al. (1980) model to compute A, but add a correction for finite mesophyll conductance (G_M). With stomatal closure, G_M decreases, and this reduces A more than if G_M is ignored (Flexas et al., 2012). We highlight and include the mesophyll limitation to photosynthesis because the correction for G_M limitation improves the accuracy of A and dA/dE. Due to the elusive mechanistic understanding of how G_M responds to the environment, however, we assume the liquid-phase component of G_M is constant, and the gas-phase component scales with stomatal conductance as shown elsewhere (Chapter 2; Wang et al., in review). Hence, in our treatment, the decline in G_M under stress is part of the stomatal limitation on A rather than an independent NSL as is often hypothesized. Any other causes of a true NSL (e.g., a stress-induced decline in photosynthetic capacity) are quantified in the penalty function (i.e., as Θ') in this framework.

For any constant set of environmental conditions, as E_{leaf} increases, the A increases, and dA/dE decreases (Fig. 3.1). Different conditions, however, influence the absolute value of A at a given E_{leaf}. Higher VPD decreases A, and higher C_a increases A (Fig. 3.1, "+VPD" and "+C_a"). Soil drought has no effect on A or dA/dE as a function of E_{leaf}, except to limit the physiological range of E_{leaf}. This assumes that any true NSL is expressed in the penalty function (as Θ').

3.3.2 Seven criteria for a successful penalty calculation, Θ

Each of the nine models evaluated differs in how the carbon penalty, Θ, is calculated as a function of E_{leaf} (see Section 3.4). Here we define seven criteria for a mathematically and biologically successful $\Theta(E_{leaf})$ function. The first three criteria are based on the mathematical demand for a unique solution for $dA/dE = d\Theta/dE$ as defined by equation 3.1. The final four criteria are required to obtain biologically realistic stomatal responses to major environmental cues.

I. The $\mathrm{d}\Theta/\mathrm{d}E > 0$ when $E_{\mathrm{leaf}} > 0$. Opening the stomata must result in a positive penalty and marginal penalty to the plant, because A and $\mathrm{d}A/\mathrm{d}E$ is similarly positive.

II. The $\mathrm{d}\Theta/\mathrm{d}E$ is a monotonically increasing function of E_{leaf}. This ensures a single intersection with the monotonic decline in $\mathrm{d}A/\mathrm{d}E$ (Fig. 3.1). This necessarily requires that Θ is a concave-up function of E_{leaf} (Wolf et al., 2016).

III. The $\mathrm{d}\Theta/\mathrm{d}E < \mathrm{d}A/\mathrm{d}E$ when $E_{\mathrm{leaf}} = 0$. Criteria I and II ensure that $\mathrm{d}\Theta/\mathrm{d}E$ is positive and monotonically increases with E_{leaf}. Criterion III ensures that $\mathrm{d}\Theta/\mathrm{d}E$ starts out below $\mathrm{d}A/\mathrm{d}E$ to ensure the two functions intersect. Note that the initial $\mathrm{d}A/\mathrm{d}E$ at $E_{\mathrm{leaf}} = 0$ is $\dfrac{C_{\mathrm{a}} - \Gamma}{1.6 \cdot D}$, where Γ is the CO_2 compensation point with the presence of dark respiration, D is the leaf-to-air vapor pressure deficit relative to atmospheric pressure, and 1.6 is the molar conversion factor for diffusive coefficient of H_2O to CO_2 in air (derivation in 3.8.1). Thus, criterion III is equivalent to $\dfrac{\mathrm{d}\Theta}{\mathrm{d}E} < \dfrac{C_{\mathrm{a}} - \Gamma}{1.6 \cdot D}$ at $E_{\mathrm{leaf}} = 0$.

IV. The $\mathrm{d}\Theta/\mathrm{d}E$ is a monotonically decreasing function of VPD for a given E_{leaf}. This criterion is required to capture the typical stomatal closure response to rising VPD (holding other conditions constant), which causes E_{leaf} to either saturate or rise slowly (Ball et al., 1987; Leuning, 1995). Rising VPD typically causes $\mathrm{d}A/\mathrm{d}E$ to decrease (when $E_{\mathrm{leaf}} < 1.7$ mmol H_2O m^{-2} s^{-1} in Fig. 3.2a, shift of green $\mathrm{d}A/\mathrm{d}E$ curves from dotted to solid). Therefore, to obtain a realistic stomatal response to VPD where E_{leaf} is saturated or increasing (Fig. 3.2a, the thickened "solution" band on the solid green $\mathrm{d}A/\mathrm{d}E$ curve), the $\mathrm{d}\Theta/\mathrm{d}E$ must also decrease with VPD (Fig. 3.2a, shift from red dotted $\mathrm{d}\Theta/\mathrm{d}E$ curve to the shaded red region).

V. The $\mathrm{d}\Theta/\mathrm{d}E$ is a monotonically increasing function of C_{a} for a given E_{leaf}. This criterion is required to capture the typical stomatal closure response to rising C_{a} (holding other conditions constant), which causes E_{leaf} to decrease and A to increase (Ball et al., 1987; Medlyn et al., 2011). Rising C_{a} typically causes $\mathrm{d}A/\mathrm{d}E$ to increase (when $E_{\mathrm{leaf}} < 1.2$ mmol H_2O m^{-2} s^{-1} in Fig. 3.2b, shift of green $\mathrm{d}A/\mathrm{d}E$ curves from dotted to solid). Therefore, to obtain a realistic stomatal response to C_{a} where E_{leaf} decreases and A increases (Fig. 3.2b, the thickened "solution" band on the solid green $\mathrm{d}A/\mathrm{d}E$ curve), the $\mathrm{d}\Theta/\mathrm{d}E$ must also increase with C_{a} (Fig. 3.2b, shift from red

dotted $\mathrm{d}\Theta/\mathrm{d}E$ curve to the shaded red region).

VI. The $\mathrm{d}\Theta/\mathrm{d}E$ is a monotonically increasing function of soil drought for a given E_{leaf}. This criterion is required to capture the typical stomatal closure response to soil drought (holding other conditions constant), which causes E_{leaf} to decrease (Venturas et al., 2018). Soil drought can be assumed to not affect $\mathrm{d}A/\mathrm{d}E$ curve in the absence of NSL (Fig. 3.2c, dotted green $\mathrm{d}A/\mathrm{d}E$ curve). Therefore, to obtain a realistic stomatal response to soil drought where E_{leaf} decreases (Fig. 3.2c, the thickened "solution" band on the dotted green $\mathrm{d}A/\mathrm{d}E$ curve), the $\mathrm{d}\Theta/\mathrm{d}E$ must increase with soil drought (Fig. 3.2c, shift from red dotted $\mathrm{d}\Theta/\mathrm{d}E$ curve to the shaded red region).

VII. The $\mathrm{d}\Theta/\mathrm{d}E$ is a monotonically increasing function of prior loss of hydraulic conductivity for a given E_{leaf}. This criterion is required to capture the typical stomatal response to reduced plant hydraulic conductance from prior drought (holding other conditions constant), which generally causes E_{leaf} to decrease (Venturas et al., 2018; Yin & Bauerle, 2017). Loss of plant hydraulic conductance can be assumed to not affect the $\mathrm{d}A/\mathrm{d}E$ curve in the absence of NSL (Fig. 3.2c, dotted green $\mathrm{d}A/\mathrm{d}E$ curve). Therefore, to obtain a realistic stomatal response to reduced hydraulic conductance where E_{leaf} decreases (Fig. 3.2c, thickened "solution" band on the dotted green $\mathrm{d}A/\mathrm{d}E$ curve), the $\mathrm{d}\Theta/\mathrm{d}E$ must increase with reduced hydraulic conductance associated with more severe drought history (Fig. 3.2c, shift from red dotted $\mathrm{d}\Theta/\mathrm{d}E$ curve to the shaded red region).

3.4 Nine Optimization Models

In this section, we analyze how nine representative optimal stomatal control models define their penalty functions by setting a uniform gain function to all the models (i.e., gain is A, and marginal gain is $\mathrm{d}A/\mathrm{d}E$). We categorize the models by type of carbon penalty based primarily on (a) water supply, (b) xylem transport, and (c) NSL. At the end of this section, we compare each models' performance against several datasets that include stomatal responses to VPD, C_{a}, and soil drought.

3.4.1 Models with a penalty based on water supply

3.4.1.1 The Cowan-Farquhar model (1977)

Pioneering gas exchange optimization theory, Cowan & Farquhar (1977) modeled the penalty only in terms of optimal use of a finite soil water supply. The Cowan-Farquhar model posits that a plant maximizes the cumulative photosynthesis for an unspecified given amount of water (E_{total}) within an unspecified given amount of time (t_{total}):

$$\max\left(\int_0^{t_{\text{total}}} A \cdot \mathrm{d}t\right) \text{ while } \int_0^{t_{\text{total}}} E_{\text{leaf}} \cdot \mathrm{d}t = E_{\text{total}}. \tag{3.2}$$

The optimal solution for equation 3.2 requires that (1) the plant can roughly target the optimal trajectory based on the climate of the given site as if the plant "knows" the environmental conditions and E_{total} in the given t_{total} and (2) the plant can control water use freely at any time instant. Any deviation from the optima results in a decline in cumulative photosynthesis over the time period. The Cowan-Farquhar model solution is

$$\frac{\mathrm{d}A}{\mathrm{d}E} = \frac{1}{\lambda} \text{ when } E_{\text{leaf}} > 0, \tag{3.3}$$

$$\frac{\mathrm{d}A}{\mathrm{d}E} < \frac{1}{\lambda} \text{ when } E_{\text{leaf}} = 0, \tag{3.4}$$

where $1/\lambda$ is the optimal marginal water use efficiency, which is constant over the time period. The Cowan-Farquhar model can also be written as $\max(\lambda A - E_{\text{leaf}})$ or $\max(A - E_{\text{leaf}}/\lambda)$.

Converting the Cowan-Farquhar model to the gain-penalty format (i.e., $\max(A - \Theta)$), the penalty and marginal penalty at the optimum are

$$\Theta = \frac{E_{\text{leaf}}}{\lambda}, \tag{3.5}$$

$$\frac{\mathrm{d}\Theta}{\mathrm{d}E} = \frac{1}{\lambda}. \tag{3.6}$$

Thus, $\frac{\mathrm{d}\Theta}{\mathrm{d}E} = \frac{\mathrm{d}A}{\mathrm{d}E} = \frac{1}{\lambda}$ at the stomatal optimum (Table 3.2 summarizes all model penalty functions). Note that the Cowan-Farquhar model only specifies the optimal penalty in equations 3.5 and 3.6, not the entire instantaneous $\Theta(E_{\text{leaf}})$ function. The model also does not provide the calculation of λ or the time frame over which λ is constant.

The Cowan-Farquhar model is moot regarding meeting criteria I–III which concern

the behavior of $\Theta(E_{\text{leaf}})$ for a given instant in time, because the overall $\Theta(E_{\text{leaf}})$ function is not specified. However, criteria I–III are implicit in the model's assumption that there is a unique solution for $\frac{d\Theta}{dE} = \frac{dA}{dE} = \frac{1}{\lambda}$. The Cowan-Farquhar model as initially specified does not meet criteria IV–VII for realistic stomatal responses to VPD, C_a, soil moisture, and loss of plant hydraulic conductance (but see advances of the Cowan-Farquhar model below). This is because the optimal dA/dE is constant at $1/\lambda$ and cannot respond to these cues within the time period when λ is constant. As pointed out previously (Buckley, 2017; Buckley et al., 2017; Katul et al., 2010), the actual outcome for VPD and C_a responses depends on the particular value chosen for λ. A constant λ may produce a realistic VPD response when $1/\lambda$ is low (e.g., when $1/\lambda < 3.5$ μmol CO_2 mmol^{-1} H_2O in Fig. 3.2a). However, a problem will arise for the VPD response when $1/\lambda$ is too high (optimal E_{leaf} is lower, for example, during a drought period). Regarding C_a, an unrealistic response is also produced when $1/\lambda$ is too high (e.g., $1/\lambda > 5.2$ μmol CO_2 mmol^{-1} H_2O; Fig. 3.2b). A final shortcoming of the Cowan-Farquhar model is that λ cannot be determined a priori, and thus implementing the model predictively converts λ into a post hoc fitting parameter over an ambiguous time frame, which limits the model's predictive power.

3.4.1.2 The Manzoni model (2013)

There has been a considerable effort to extend the Cowan-Farquhar model, especially how to define a variable λ based on the environment (Buckley et al., 2017; Buckley & Schymanski, 2014; Hari et al., 1999; Katul et al., 2010, 2009; Manzoni et al., 2013; Novick et al., 2016; Vico et al., 2013). These advances to the Cowan-Farquhar model tend to assume a constant λ over a short time (e.g., daily) and adopt a variable λ over longer periods. Though a variable λ may help resolve the problems with stomatal response to long-term Ca change (Katul et al., 2010) and soil drought (Novick et al., 2016), it does not address unrealistic stomatal responses in the short time frame where λ is constant. Moreover, the long-term variable λ often cannot capture all the stomatal responses. For example, the Katul et al. (2010) and Buckley et al. (2017) models do not allow λ to vary with soil drought, and the Novick et al. (2016) model does not allow λ to vary with $C_a$or VPD.

The Manzoni model is an example of these efforts to develop the Cowan-Farquhar model (Katul et al., 2010, 2009; Manzoni et al., 2013). The Manzoni model assumes a plant

maximizes the sum of cumulative photosynthesis with a given amount of water in a given time plus an unknown additional carbon gain from using the water remaining in the soil:

$$\max\left(\int_0^{t_{\text{total}}} A \cdot \mathrm{d}t + \frac{1}{\Lambda} \cdot E_{\text{remain}}\right) \text{ while } \int_0^{t_{\text{total}}} E_{\text{leaf}} \cdot \mathrm{d}t = E_{\text{total}}. \tag{3.7}$$

where Λ is a proportionality constant for the additional carbon gain, and E_{remain} is the soil water at the end of the given time. Adding this additional carbon gain makes it possible to optimize E_{total} for the given time. As both the cumulative and additional carbon gains are functions of E_{total}, the Manzoni model is optimized when

$$\frac{\mathrm{d}(\int A \cdot \mathrm{d}t)}{\mathrm{d}E_{\text{total}}} + \frac{\mathrm{d}(E_{\text{remain}}/\Lambda)}{\mathrm{d}E_{\text{total}}} = 0. \tag{3.8}$$

Given that $\mathrm{d}E_{\text{total}}$ is infinitesimal and $\mathrm{d}E_{\text{total}} = -\mathrm{d}E_{\text{remain}}$, $\mathrm{d}(\int A \cdot dt)/\mathrm{d}E_{\text{total}}$ equals $1/\lambda$ and $\mathrm{d}(E_{\text{remain}}/\Lambda)/\mathrm{d}E_{\text{total}}$ equals $-1/\Lambda$ (derivation in 3.8.2). Therefore, the Manzoni model is optimized when $\lambda = \Lambda$.

The penalty and marginal penalty of the Manzoni model at the optimum are defined as

$$\Theta = \frac{E_{\text{leaf}}}{\Lambda}, \tag{3.9}$$

$$\frac{\mathrm{d}\Theta}{\mathrm{d}E} = \frac{1}{\Lambda}. \tag{3.10}$$

Although the Manzoni model resembles the Cowan-Farquhar model in form, the differences between the two models are the following: (1) the Manzoni model allows E_{total} to be defined and (2) Λ (and hence λ) is a preset constant in the Manzoni model, whereas λ in the Cowan-Farquhar model is an unknown constant whose value is often assigned from post hoc fitting.

Like the Cowan-Farquhar model, the Manzoni model is moot with regards to meeting criteria I–III, because the overall $\Theta(E_{\text{leaf}})$ function is not specified. However, these criteria are implicit in the model's assumption that there is a unique solution for $\frac{\mathrm{d}\Theta}{\mathrm{d}E} = \frac{\mathrm{d}A}{\mathrm{d}E} = \frac{1}{\Lambda}$. Likewise, the Manzoni model does not meet criteria IV–VII for consistently realistic stomatal responses to VPD, C_a, soil moisture, and loss of plant hydraulic conductance. This is because the optimal $\mathrm{d}A/\mathrm{d}E$ is constant at $1/\Lambda$ and does not respond to these cues within the time period when Λ applies, although the authors claimed otherwise (potentially due to a mathematical oversight, see 3.8.2). Qualitatively, however, the authors came to the correct

conclusion that $1/\lambda$ must increase with drought, a conclusion further developed by Novick et al. (2016). Future attempts to develop the Cowan-Farquhar approach could be guided by the need to define a variable λ as required by criteria IV–VII.

3.4.1.3 The Prentice model (2014)

The Prentice model is a minimal cost model that assumes a plant acts to minimize the maintenance costs of evaporation and photosynthetic capacity relative to the photosynthetic rate (Prentice et al., 2014). Mathematically, the Prentice model also fits the general gain-penalty framework as the model is equivalent to maximize the difference between the photosynthesis and maintenance costs:

$$\min\left(\frac{c_{\mathrm{E}}E_{\mathrm{leaf}}+c_{\mathrm{V}}V_{\mathrm{cmax}}}{A}\right)\equiv\max\left(\frac{A}{c_{\mathrm{E}}E_{\mathrm{leaf}}+c_{\mathrm{V}}V_{\mathrm{cmax}}}\right), \tag{3.11}$$

where c_{E} is the unit cost of maintaining E_{leaf}, and c_{V} is the unit cost of maintaining photosynthetic capacity (measured by V_{cmax}). Therefore, the Prentice model defines the penalty as

$$\Theta = A\cdot\left(1-\frac{1}{c_{\mathrm{E}}E_{\mathrm{leaf}}+c_{\mathrm{V}}V_{\mathrm{cmax}}}\right). \tag{3.12}$$

In their equation 1, Prentice et al. (2014) differentiated equation 3.11 and claimed the model was optimized when

$$c_{\mathrm{E}}\cdot\mathrm{d}\left(\frac{E_{\mathrm{leaf}}}{A}\right)+c_{\mathrm{V}}\cdot\mathrm{d}\left(\frac{V_{\mathrm{cmax}}}{A}\right)=0, \tag{3.13}$$

Equation 3.13 holds true when c_{E} and c_{V} are independent of stomatal opening as measured by E_{leaf}. However, in their equation 11, Prentice et al. (2014) made another assumption that

$$c_{\mathrm{E}}=\frac{\text{constant}}{E_{\mathrm{leaf}}}, \tag{3.14}$$

which violates the assumption of constant c_{E} made in equation 3.13. Therefore, only one of equations 3.13 and 3.14 can be correct for the Prentice model.

Here, we assume that equation 3.13 is correct, and it was the intent of Prentice et al. (2014) to make c_{E} independent of E_{leaf} (see 3.8.3 for discussion of the less realistic alternative that 3.14 is correct). In this case, the Prentice model is optimized when

$$\frac{\mathrm{d}A}{\mathrm{d}E}=\frac{A}{E+\dfrac{c_{\mathrm{V}}}{c_{\mathrm{E}}}\cdot V_{\mathrm{cmax}}}. \tag{3.15}$$

Therefore, the marginal penalty of the Prentice model is equivalent to

$$\frac{\mathrm{d}\Theta}{\mathrm{d}E} = \frac{A}{E_{\mathrm{leaf}} + \dfrac{c_{\mathrm{V}}}{c_{\mathrm{E}}} V_{\mathrm{cmax}}}. \tag{3.16}$$

Note that here equation 3.16 is not exactly the derivative of equation 3.12, which contains $\mathrm{d}A/\mathrm{d}E$ term in the equation, and we obtain equation 3.16 by rearranging the equations (derivation in 3.8.3).

This version of the Prentice model defines the entire $\Theta(E_{\mathrm{leaf}})$ function (equation 3.12) and meets criteria I and III. However, it fails to meet criterion II for being concave up with a monotonic increase in $\mathrm{d}\Theta/\mathrm{d}E$ because c_{E} and c_{V} are independent of E_{leaf}. Therefore, depending on the values of c_{E} and c_{V}, there could be multiple solutions for equation 3.1. In terms of how $\mathrm{d}\Theta/\mathrm{d}E$ (equation 3.16) responds to environmental cues, it satisfies criteria IV and V, thus potentially predicting realistic responses to VPD and C_{a}. However, the $\mathrm{d}\Theta/\mathrm{d}E$ does not respond to soil drought or plant hydraulic conductance, thus violating criteria VI and VII.

3.4.1.4 The Lu model (2016)

The Lu model assumes a plant maximizes the mean A (Lu et al., 2016) in a given t_{total}:

$$\max\left(\int_0^{P_{\mathrm{crit}}} f(P_{\mathrm{soil}}) \cdot A(P_{\mathrm{soil}}) \cdot \mathrm{d}P_{\mathrm{soil}}\right), \tag{3.17}$$

where $f(P_{\mathrm{soil}})$ is the probability density function of soil water potential (P_{soil}), $A(P_{\mathrm{soil}})$ is the photosynthetic rate at given soil water potential, and P_{crit} is the critical leaf xylem pressure beyond which plant desiccates (Sperry & Love, 2015). The optimization criterion is problematic because the Lu model assumes $A(P_{\mathrm{soil}})$ is solely a function of P_{soil} regardless of other environmental cues such as VPD and solar radiation. A broader and more accurate optimization criterion for the Lu model would take the form:

$$\max\left(\sum f(\mathrm{envir}) \cdot A(\mathrm{envir})\right), \tag{3.18}$$

where $f(\mathrm{envir})$ is the probability of the given combination of environmental cues, and $A(\mathrm{envir})$ is the photosynthetic rate at the given combination of environmental cues. Mathematically, equation 3.18 is equivalent to equation 3.2 (the Cowan-Farquhar model) for a given t_{total} and E_{total} because maximizing mean A during a period means maximizing

the cumulative A. Thus, the Lu model is identical to the Cowan-Farquhar model and its optimal stomatal conductance solution is questionable (see Section 3.8.4 for additional mathematical questions concerning the Lu model).

3.4.2 Models with a penalty based on xylem vulnerability to cavitation

Water transport along the xylem makes the xylem water pressure more and more negative due to gravity and friction in the xylem conduits, and the negative xylem pressure could result in cavitation (Sperry & Tyree, 1988). The more the plant uses water, the more likely the xylem gets cavitated, and the more energy it requires to refill the cavitated conduits or regrow new xylem to restore the lost hydraulic conductivity. The "vulnerability curves" that measure the loss of hydraulic conductance as a function of xylem pressure are available for a number of species, and form the basis for penalty functions in several model formulations.

3.4.2.1 The Wolf-Anderegg model (2016)

The Wolf-Anderegg model weighs the penalty on xylem cavitation and its consequences. Wolf et al. (2016) first proposed the penalty for opening the stomata includes direct, indirect, and opportunity components, including the risk of xylem cavitation. Wolf et al. (2016) further argued that the penalty function ought to be a concave-up function (criterion II) though did not specify the exact equation for the penalty. Anderegg et al. (2018), which tested the Wolf et al. (2016) approach against 34 species that span global forest biomes, assumed that the penalty is a quadratic function of leaf xylem pressure (note here that P is in $-$MPa so that P is a positive number). The plant-hydraulics-based penalty function significantly improved gas exchange modeling predictive ability relative to the Cowan-Farquhar approach, particularly during periods of water stress. The Wolf-Anderegg model defines the penalty function as

$$\Theta = aP^2(E_{\text{leaf}}) + bP(E_{\text{leaf}}) + c, \tag{3.19}$$

where a, b, and c are fitting constants that make Θ a concave-up function of E_{leaf}. The xylem pressure, P, is a function of E_{leaf} based on a hydraulic submodel. The marginal penalty of the Wolf-Anderegg model is

$$\frac{\mathrm{d}\Theta}{\mathrm{d}E} = \frac{2aP(E_{\mathrm{leaf}}) + b}{K}, \tag{3.20}$$

where K is the soil-plant hydraulic conductance at the canopy xylem pressure (i.e., $\mathrm{d}E/\mathrm{d}P$). The optimal $\mathrm{d}\Theta/\mathrm{d}E$ is determined numerically as the unique point where $\mathrm{d}\Theta/\mathrm{d}E = \mathrm{d}A/\mathrm{d}E$.

The marginal penalty of the Wolf-Anderegg model (equation 3.20) meets criteria I and II. However, the positive constants a and b do not guarantee criterion III. In terms of responses to environmental cues, the $\mathrm{d}\Theta/\mathrm{d}E$ described by constant a and b does not respond to C_{a} or VPD, thus not meeting criteria IV and V and making the model unable to always produce realistic response to C_{a} or VPD. Note that constant a and b may produce realistic C_{a} and VPD responses when optimal E_{leaf} is high (similar to the Cowan-Farquhar model). The model, however, does incorporate the K and its sensitivity to drought, hence meeting criteria VI and VII, and potentially predicting realistic responses to drought and drought history. The Wolf-Anderegg model relies on curve fitting two parameters (a and b), which limits its application in projecting stomatal behavior under novel conditions.

3.4.2.2 The Sperry model (2017)

The Sperry model (Sperry et al., 2017) was built from earlier versions of hydraulic models, which explicitly modeled gas exchange from vulnerability curves (Sperry et al., 1998; Sperry & Love, 2015; Sperry et al., 2016). Inspired by the Wolf-Anderegg model, the Sperry model assumes a plant maximizes the difference between relative gain and relative hydraulic risk, both of which are standardized to 0–1 for each moment in time (Sperry et al., 2017). The relative gain is defined as A/A_{max}, where A_{max} is the maximal achievable photosynthetic rate while leaf diffusive conductance ranges from 0 to maximum (A_{max} is not always at maximal transpiration rate, E_{crit}, because of the leaf cooling). The relative hydraulic risk is defined as $1 - K/K_{\mathrm{max}}$, where K_{max} is the maximal K when $E_{\mathrm{leaf}} = 0$. The Sperry model posits

$$\max\left(\frac{A}{A_{\mathrm{max}}} - 1 + \frac{K}{K_{\mathrm{max}}}\right) = \max\left(A - A_{\mathrm{max}} \cdot \left(1 - \frac{K}{K_{\mathrm{max}}}\right)\right). \tag{3.21}$$

$$\Theta = A_{\mathrm{max}} \cdot \left(1 - \frac{K}{K_{\mathrm{max}}}\right), \tag{3.22}$$

$$\frac{\mathrm{d}\Theta}{\mathrm{d}E} = -\frac{\mathrm{d}K}{\mathrm{d}E} \cdot \frac{A_{\mathrm{max}}}{K_{\mathrm{max}}}, \tag{3.23}$$

where equations 3.22 and 3.23 are for the complete penalty function. Like the Wolf-Anderegg model, the optimal solution ($\mathrm{d}\Theta/\mathrm{d}E = \mathrm{d}A/\mathrm{d}E$) is solved numerically.

The marginal penalty of the Sperry model (equation 3.23) meets criteria I–III and can be calculated from hydraulic trait data without requiring undefined fitting parameters. Because $A_{\max}$ increases with rising C_a and decreasing VPD, the Sperry model meets criteria IV and V. Because $\mathrm{d}K/\mathrm{d}E$ also increases with E_{leaf} before the plant desiccates, the Sperry model meets criterion VI. However, equation 3.23 predicts a marginal penalty of 0 when there is no new cavitation in the xylem, which can lead to unrealistic postdrought predictions when xylem has already been cavitated, in violation of criterion VII. To handle this problem, the Sperry model specifies that the leaf water potential after a drought equals that when there is no drought history to account for the drought history response (Venturas et al., 2018) and thereby satisfies criterion VII.

The Sperry model is the first model to define a penalty function without curve fitting parameters in the optimization criteria, and it performs equally well in an open garden experiment and better in a growth chamber experiment compared to the traditional empirical approach which relies on curve fitting the data (Venturas et al., 2018; Wang et al., 2019). The success of the Sperry model suggests the penalty of stomatal opening can be explained by the need to protect hydraulic integrity. Also, the Sperry model suggests that the penalty should not only be measured in terms of xylem transport but also weighted by the potential for photosynthesis (i.e., $A_{\max}$). The penalty to xylem cavitation is amplified by $A_{\max}$ when conditions are more favorable, and this weighting strategy allows the Sperry model to meet criteria III–V.

3.4.2.3 The Eller model (2018)

Inspired by the Sperry model, the Eller model maximizes the product of photosynthetic rate and a correction factor, $K/K_{\max,0}$, where $K_{\max,0}$ is the maximal marginal hydraulic conductance when there is no cavitation (Eller et al., 2018). Translated to the gain versus penalty model format, the optimization criterion and Θ are

$$\max\left(A \cdot \frac{K}{K_{\max,0}}\right) = \max\left(A - A \cdot \left(1 - \frac{K}{K_{\max,0}}\right)\right) \equiv \max(A \cdot K), \tag{3.24}$$

$$\Theta = A \cdot \left(1 - \frac{K}{K_{\max,0}}\right). \tag{3.25}$$

Directly differentiating equation 3.25, we have

$$\frac{\mathrm{d}\Theta}{\mathrm{d}E} = \frac{\mathrm{d}A}{\mathrm{d}E} \cdot \left(1 - \frac{K}{K_{\max,0}}\right) - \frac{\mathrm{d}K}{\mathrm{d}E} \cdot \frac{A}{K_{\max,0}}. \tag{3.26}$$

The Eller model is optimized when $\mathrm{d}A/\mathrm{d}E \times K + \mathrm{d}K/\mathrm{d}E \times A = 0$. Thus, the marginal penalty of the Eller model is equivalent to

$$\frac{\mathrm{d}\Theta}{\mathrm{d}E} = -\frac{\mathrm{d}K}{\mathrm{d}E} \cdot \frac{A}{K}, \tag{3.27}$$

which resembles the marginal penalty of the Sperry model (equation 3.23).

Like the Sperry model, the Eller model meets I–III. Due to the term "A/K", the Eller model can also predict realistic stomatal responses to VPD (IV), C_a (V), and P_soil (VI). However, it predicts a marginal penalty of 0 when there is no new cavitation in the xylem, thus not satisfying criterion VII. Unlike the Sperry model, the Eller model does not specify how the model deals with the postdrought response.

3.4.3 Models with a penalty based on non-stomatal limitation to photosynthesis

The penalty in NSL is different from those in water supply and xylem transport. Unlike water supply and xylem transport issues that represent future "shadow costs" or risks to future plant function, NSL acts by decreasing the instantaneous photosynthetic rate independently of stomatal behavior (hence the "non-stomatal limitation" terminology). Potential mechanisms for NSL include photosynthetic inhibition by accumulated photosynthate (Hölttä et al., 2017, 2009), decreasing photosynthetic capacity related to drought (Dewar et al., 2018; Drake et al., 2017), and decreasing liquid-phase mesophyll conductance (not including the gas-phase mesophyll conductance, which we assume is stomatal dependent; Wang et al., in review). Mathematically, NSL could be directly incorporated into the carbon gain function. However, as most of the NSL models did originally, we treat NSL as part of the penalty function in this review, denoting the penalty as Θ' to signal the distinction. Biologically, the difference is that NSL causes the computed instantaneous photosynthetic rate to be lower for the same E_leaf compared to the seven models listed above.

3.4.3.1 The Hölttä model (2017)

This model is based on coordination between sugar metabolism and phloem transport (Hölttä et al., 2017). If the leaf photosynthesizes more than the leaf can metabolize or transport out (Hölttä et al., 2009), photosynthesis might be inhibited by the high sugar concentration in the mesophyll cells. This negative feedback is the source of NSL in the Hölttä model. Based on the assumption that leaf photosynthesis metabolism decreases linearly as sugar concentration builds up, the Hölttä model posits that leaves maximize the instantaneous A, which is the difference of A_{ww} and Θ':

$$\max\left(A_{\mathrm{ww}} \cdot \left(1 - \frac{\mathrm{SC}}{\mathrm{SC}_{\mathrm{max}}}\right)\right), \tag{3.28}$$

where SC is the sugar concentration in the mesophyll cells, and $\mathrm{SC}_{\mathrm{max}}$ is the maximal sugar concentration at which photosynthesis is fully inhibited. Transforming the Hölttä model to the gain versus penalty model format assuming a penalty caused by the increasing sugar concentration, the NSL penalty (i.e., Θ') is

$$\Theta' = A_{\mathrm{ww}} \cdot \frac{\mathrm{SC}}{\mathrm{SC}_{\mathrm{max}}}, \tag{3.29}$$

Again, the symbol $'$ means the penalty reduces the computed instantaneous photosynthetic rate.

Taking the first-order derivative of equation 3.29, the marginal penalty is

$$\frac{\mathrm{d}\Theta'}{\mathrm{d}E} = \frac{1}{\mathrm{SC}_{\mathrm{max}}} \cdot \left(\mathrm{SC} \cdot \frac{\mathrm{d}A_{\mathrm{ww}}}{\mathrm{d}E} + A_{\mathrm{ww}} \cdot \frac{\mathrm{dSC}}{\mathrm{d}E}\right), \tag{3.30}$$

The Hölttä model is optimized when $\mathrm{d}(A_{\mathrm{ww}} \times [\mathrm{SC}_{\mathrm{max}} - \mathrm{SC}])/\mathrm{d}E = 0$, and thus the marginal penalty for the Hölttä model is equivalent to

$$\frac{\mathrm{d}\Theta'}{\mathrm{d}E} = \frac{A}{\mathrm{SC}_{\mathrm{max}} - \mathrm{SC}} \cdot \frac{\mathrm{dSC}}{\mathrm{d}E}, \tag{3.31}$$

The marginal penalty of the Hölttä model potentially meets all the seven criteria because (1) the penalty starts from 0 and increases with E_{leaf}, (2) higher A_{ww} and SC account for the higher penalty at higher C_{a} and lower VPD, (3) higher SC accounts for the higher penalty associated with drought and hydraulic conductance loss (when xylem pressure gets more negative, phloem turgor pressure decreases and more sugar will accumulate in the leaf). The disadvantage of using the Hölttä model for predictive purposes is that it is based on

incompletely understood aspects of phloem function and carbohydrate metabolism, and requires difficult-to-measure physiological traits. Quantifying the assumption of negative feedback between limited phloem export and photosynthetic rate requires knowing where the sugar sinks are and how the sugar concentration impacts photosynthesis. Complicating the calculation is the fact that the root system is not the sole sink for sugar (as assumed by the Hölttä model), because the shoot contains major sinks, whether for storage or new growth. Nevertheless, the penalty concept behind the Hölttä model is promising because it meets all seven criteria for improved modeling of leaf gas exchange.

Similar to the Hölttä model, the model of Huang et al. (2018) assumes the stomata act to coordinate the leaf-xylem-phloem system to maximize sugar transport through the mesophyll cells to the phloem (Huang et al., 2018). The differences between the Huang model and the Hölttä model are that (1) the Huang model does not assume any negative feedback between sugar concentration and photosynthetic rate and thus there is no NSL in the Huang model, and that (2) the Huang model does not model the phloem transport from leaf to root and thus xylem cavitation does not affect the modeling of phloem transport. Therefore, the Huang model, in theory, cannot predict realistic stomatal behavior because there is no penalty function in the model (see Section 3.8.5 for mathematical and biological ambiguities of the Huang model).

3.4.3.2 Dewar model (2018)

Following the format of the Hölttä model, Dewar et al. (2018) presented another two alternative mechanisms of NSL, one through changing leaf photosynthetic capacity (CAP limitation) and the other through changing mesophyll conductance (MES limitation). We present the CAP model here (see Section 3.8.6 for the MES version). The Dewar CAP model assumes leaf photosynthetic metabolism decreases linearly with leaf xylem pressure (namely V_{cmax} and electron transport rate decreased linearly with more negative P). Like the Hölttä model, the Dewar CAP model is written as

$$\max\left(A_{\text{ww}} \cdot \left(1 - \frac{P}{P_{\text{crit}}}\right)\right), \tag{3.32}$$

The NSL penalty to photosynthesis is

$$\Theta' = A_{\text{ww}} \cdot \frac{P}{P_{\text{crit}}}. \tag{3.33}$$

Differentiating equation 3.33, we have

$$\frac{\mathrm{d}\Theta'}{\mathrm{d}E} = \frac{1}{P_{\mathrm{crit}}} \cdot \left(P \cdot \frac{\mathrm{d}A_{\mathrm{ww}}}{\mathrm{d}E} + \frac{A_{\mathrm{ww}}}{K} \right). \tag{3.34}$$

The Dewar CAP model is optimized when $A_{\mathrm{ww}} \cdot (P_{\mathrm{crit}} - P)$ is maximized, namely when $\mathrm{d}(A_{\mathrm{ww}} \cdot [P_{\mathrm{crit}} - P]) = 0$, and thus the marginal penalty of the Dewar CAP model is equivalent to

$$\frac{\mathrm{d}\Theta'}{\mathrm{d}E} = \frac{A}{K \cdot (P_{\mathrm{crit}} - P)}. \tag{3.35}$$

Equation 3.35 mathematically meets all seven criteria for the marginal penalty because the "A_{ww}" term in the numerator makes the marginal penalty start from 0 and increase with higher E_{leaf} and C_{a} and lower VPD (criteria I–V), and the "$P_{\mathrm{crit}} - P$" enables higher marginal penalty with more severe drought and more loss of conductivity (criteria VI and VII). The Dewar CAP model drives the NSL-based penalty function with the hydraulic P/P_{crit} parameter. This hydraulic parameter is easier to measure and model than the phloem-related parameters in the Hölttä model. However, there is little evidence that V_{cmax} and electron transport rate (J, not J_{max}) during water stress are a linear function of P/P_{crit} as assumed by the Dewar CAP model. Furthermore, while V_{cmax} and J can decrease during drought (Zhou et al., 2016), there is no direct evidence for rapid and reversible responses to leaf xylem pressure.

3.4.4 Model performance

Eight of the nine models were evaluated by their ability to fit actual gas exchange data. The Hölttä model was excluded because of the large number of unknown traits required. Three datasets were tested. Wang et al. (2019) dataset were from water birch (*Betula occidentalis* Hook.) exposed to stepped changes in C_{a}, VPD, and soil drought in a growth chamber environment. Venturas et al. (2018) dataset were from plantation grown aspen (*Populus tremuloides* Michx.) subjected to natural variation in VPD combined with drought treatments. Anderegg et al. (2018) dataset were compiled from 36 species plus site combinations (34 species in total) exposed to natural variation in VPD and soil drought. The Wang et al. (2019) and Venturas et al. (2018) datasets had all the traits required for running the optimization models except for a difficult-to-measure rhizosphere conductance (K_{rhiz}) component in the soil-plant-atmosphere continuum. The Anderegg et al. (2018) dataset

lacked K_{rhiz}, $K_{\text{max},0}$, and root and leaf vulnerability curves for all the species, and V_{cmax} for five species.

For the birch and aspen datasets, we fitted the parameters listed in the column "Fitting Parameters" in Table 3.2. Note it here although the Sperry, Eller, and Dewar CAP models do not have fitting parameters in the penalty function, it is important to include the K_{rhiz} as it plays a non-negligible role when soil is dry. Therefore, we fitted K_{rhiz} for all the models that involve plant hydraulics (Table 3.2, column "Fitting Parameters"). For the Anderegg dataset, we used the stem vulnerability curve as a proxy for the root and leaf curves, assumed infinite K_{rhiz}, and fitted the missing $K_{\text{max},0}$ and V_{cmax} as well as the rest of the parameters listed in the column "Fitting Parameters" in Table 3.2.

We used the *scipy.optimize.leastsq* module in Python to minimize the least square error of studentized photosynthetic rate (i.e., A), transpiration rate (i.e., E_{leaf}), and canopy leaf xylem pressure (i.e., P) for each dataset. The code for the models is made publicly available at https://github.com/Yujie-WANG/Published-Codes-Yujie-WANG. This weighted the errors equally across A, E_{leaf}, and P. The mean absolute percentage error (MAPE = mean absolute error / observed mean) for model outputs A, E_{leaf}, and P was calculated (Table 3.3).

The Wolf-Anderegg, Eller, and Sperry models perform better overall, suggesting the penalty of leaf gas exchange can be successfully linked to plant hydraulic function (Fig. 3.3, Table 3.3). Pooling all models and datasets, the Wolf-Anderegg model perform the best, despite not meeting the criteria IV and V, followed by the Sperry and Eller models (Fig. 3.3, Table 3.3). Within the models that have no fitting parameter in the marginal penalty function, the Sperry and Eller models perform equally well and are the best (Fig. 3.3, Table 3.3). Although the Dewar CAP model penalty equation meets all the seven criteria, it does not perform as well as the Sperry and Eller models, and the less satisfactory performance is due to the greater error in predicting photosynthesis (Table 3.3). This suggests it is unrealistic to assume that the penalty reduces the instantaneous photosynthetic rate versus represents a future "shadow cost" that does not influence current A. Indeed, when we treat the Dewar CAP model penalty as a "shadow cost" (i.e., maximizing $(A - \Theta)$ rather than $(A_{\text{ww}} - \Theta')$, its performance increases significantly (Fig. 3.3, Table 3.3).

3.5 Paths Toward Better Optimization Modeling

From the theoretical and experimental comparisons of nine optimization gas exchange models, we summarize four characteristics of a successful penalty function for predictive modeling:

- Basing the penalty function on the hydraulic properties of plant and soil is effective (especially for stomatal response to drought and loss of hydraulic conductance, criteria VI and VII). Most importantly, the underlying physiology is well established, and almost all of the traits related are readily measurable or at least attributable to a specific process (as in the K_{rhiz} case).
- Weighting the penalty by photosynthesis (A or A_{max}) ensures realistic stomatal responses to VPD and C_{a} (criteria IV and V). Though using an arbitrary multiplier in the marginal penalty function (e.g., "constant $\times$ C_{a}/VPD") also satisfies criteria IV and V, such an arbitrary multiplier introduces an unknown parameter that requires curve fitting.
- Framing the penalty as a "shadow cost" of water use and transport appears to produce better A estimation and overall performance than expressing the penalty as an instantaneous reduction in A from NSL. In addition, the NSL concept assumes mathematically specific physiological behavior which can have little empirical support. Moreover, an NSL penalty can require parameters which are difficult to measure.
- Quantifying the penalty based on readily measurable and physiologically established parameters increases model utility and increases predictive power. Physiological parameters can also become variables in cases where their acclimation to long-term environmental change is known, making it possible to model acclimation. Leveraging physiologically measurable parameters will be crucial for using stomatal optimization models in large-scale vegetation models run at regional or global scales.

These observations can drive further improvements in optimization modeling. By way of example, we present a new optimization model based on our seven criteria and these four summary characteristics.

The proposed new model defines the penalty as

$$\Theta = A \cdot \frac{E_{\text{leaf}}}{E_{\text{crit}}}. \tag{3.36}$$

This penalty is based on proximity to hydraulic failure ($E_{\text{leaf}}/E_{\text{crit}}$) as defined by vulnerability curves, is weighted by current photosynthesis, and assumes a shadow cost rather than NSL. Taking the first derivative of equation 3.36, we have

$$\frac{\mathrm{d}\Theta}{\mathrm{d}E} = \frac{1}{E_{\text{crit}}} \cdot \left(E_{\text{leaf}} \cdot \frac{\mathrm{d}A}{\mathrm{d}E} \right). \tag{3.37}$$

By rearranging equation 11b, we find that the new model is optimized when $\mathrm{d}A \times (E_{\text{crit}} - E_{\text{leaf}}) - A \times \mathrm{d}E = 0$, and the marginal penalty (equation 3.37) is equivalent to

$$\frac{\mathrm{d}\Theta}{\mathrm{d}E} = \frac{A}{E_{\text{crit}} - E_{\text{leaf}}}. \tag{3.38}$$

The term "$\frac{A}{E_{\text{crit}} - E_{\text{leaf}}}$" makes the marginal penalty start from 0 and increase monotonically with E_{leaf} (criteria I–III). The term "A" in the numerator enables the margin penalty to increase with higher C_{a} and lower VPD (criteria IV and V). The term $E_{\text{crit}} - E_{\text{leaf}}$ in the denominator enables the marginal penalty to increase with more severe drought and drought history (because drought history reduces E_{crit}, criteria VI and VII). When testing the new model with the same three datasets, it performs equally well in the Wang et al. (2019) and Venturas et al. (2018) datasets and slightly better in the Anderegg et al. (2018) dataset compared to the Sperry and Eller models (red bars in Fig. 3.3, Table 3.3). Furthermore, the new model is computationally more efficient because the model does not need to calculate the soil-plant hydraulic conductance (i.e., $K = \mathrm{d}E/\mathrm{d}P$) as do the Sperry and Eller models. Like these models, the new one also does not rely on curve fitting (except for the K_{rhiz} parameter, which is difficult to measure).

3.6 Conclusion

Stomatal optimization models are based on the premise that stomatal opening comes with a photosynthetic benefit and a physiological penalty that results directly or indirectly from transpiration. Calculating a hypothetically optimal balance between carbon gain and penalty at each time step in a dynamic environment makes it possible to predict stomatal behavior without knowing the underlying stimulus-response physiology and without having to rely on empirical correlations that likely do not apply to novel environmental conditions. As we have shown, the main challenge is in defining the penalty associated with stomatal opening. Models typically make the implicit assumption that one or two key

processes can serve as a proxy for what is probably a much more complex physiological web of colimitation. Ideally, such a penalty must be based on a physiologically defensible process, mathematically sound in providing a unique optimal solution under any environmental conditions, and capable of predicting realistic stomatal responses to environmental cues.

Of the ten optimization models analyzed (including the new model proposed here), the four most promising models have a penalty based on stress-induced failure of vascular water transport. Although the four models differ in mathematical details, they all track observed stomatal responses similarly well. This convergence supports the underlying hypothesis that stomatal behavior evolved in coordination with vascular vulnerability, a concept that goes back to the first measurement of xylem cavitation (Milburn, 1979). The Darcy's Law based physics of xylem transport facilitates modeling, and there are rapidly growing databases of hydraulic traits for parameterization. We also found that successful penalty functions are scaled by current photosynthetic opportunity, a weighting that standardizes the balance between the two sides of stomatal opening and produces realistic stomatal behavior. Future research on the coordination between hydraulic and photosynthetic traits, and their acclimation to the environment, will allow optimization modeling to predict longer-term responses to climate change and further advance the modeling of carbon and water cycles globally.

3.7 References

Anderegg, W. R. L., Wolf, A., Arango-Velez, A., Choat, B., Chmura, D. J., Jansen, S., … Pacala, S. (2018). Woody plants optimise stomatal behaviour relative to hydraulic risk. *Ecology Letters*, *21*(7), 968–977.

Ball, J. T., Woodrow, I. E., & Berry, J. A. (1987). A model predicting stomatal conductance and its contribution to the control of photosynthesis under different environmental conditions. In *Progress in photosynthesis research* (pp. 221–224). Springer.

Buckley, T. N. (2017). Modeling stomatal conductance. *Plant Physiology*, *174*(2), 572–582.

Buckley, T. N., Sack, L., & Farquhar, G. D. (2017). Optimal plant water economy. *Plant, Cell & Environment*, *40*(6), 881–896.

Buckley, T. N., & Schymanski, S. J. (2014). Stomatal optimisation in relation to atmospheric CO_2. *New Phytologist*, *201*(2), 372–377.

Chen, Z.-H., Hills, A., Bätz, U., Amtmann, A., Lew, V. L., & Blatt, M. R. (2012). Systems dynamic modeling of the stomatal guard cell predicts emergent behaviors in transport, signaling, and volume control. *Plant Physiology*, *159*(3), 1235–1251.

Cowan, I. R., & Farquhar, G. D. (1977). Stomatal function in relation to leaf metabolism and environment. *Symposia of the Society for Experimental Biology*, *31*, 471–505.

Dewar, R., Mauranen, A., Mäkelä, A., Hölttä, T., Medlyn, B., & Vesala, T. (2018). New insights into the covariation of stomatal, mesophyll and hydraulic conductances from optimization models incorporating nonstomatal limitations to photosynthesis. *New Phytologist*, *217*(2), 571–585.

Drake, J. E., Power, S. A., Duursma, R. A., Medlyn, B. E., Aspinwall, M. J., Choat, B., … Tissue, D. T. (2017). Stomatal and non-stomatal limitations of photosynthesis for four tree species under drought: A comparison of model formulations. *Agricultural and Forest Meteorology*, *247*, 454–466.

Eller, C. B., Rowland, L., Oliveira, R. S., Bittencourt, P. R. L., Barros, F. V., da Costa, A. C. L., … Cox, P. (2018). Modelling tropical forest responses to drought and El Niño with a stomatal optimization model based on xylem hydraulics. *Philosophical Transactions of the Royal Society B: Biological Sciences*, *373*(1760), 20170315.

Farquhar, G. D., von Caemmerer, S., & Berry, J. A. (1980). A biochemical model of photosynthetic CO_2 assimilation in leaves of C_3 species. *Planta*, *149*(1), 78–90.

Flexas, J., Barbour, M. M., Brendel, O., Cabrera, H. M., Carriquí, M., Díaz-Espejo, A., … Warren, C. R. (2012). Mesophyll diffusion conductance to CO_2: An unappreciated central player in photosynthesis. *Plant Science*, *193*, 70–84.

Flexas, J., Scoffoni, C., Gago, J., & Sack, L. (2013). Leaf mesophyll conductance and leaf hydraulic conductance: An introduction to their measurement and coordination. *Journal of Experimental Botany*, *64*(13), 3965–3981.

Hari, P., Mäkelä, A., Berninger, F., & Pohja, T. (1999). Field evidence for the optimality hypothesis of gas exchange in plants. *Functional Plant Biology*, *26*(3), 239–244.

Hills, A., Chen, Z.-H., Amtmann, A., Blatt, M. R., & Lew, V. L. (2012). OnGuard, a computational platform for quantitative kinetic modeling of guard cell physiology. *Plant Physiology*, *159*(3), 1026–1042.

Huang, C.-W., Domec, J.-C., Palmroth, S., Pockman, W. T., Litvak, M. E., & Katul, G. G. (2018). Transport in a coordinated soil-root-xylem-phloem leaf system. *Advances in Water Resources*, *119*, 1–16.

Hölttä, T., Lintunen, A., Chan, T., Mäkelä, A., & Nikinmaa, E. (2017). A steady-state stomatal model of balanced leaf gas exchange, hydraulics and maximal source–sink flux. *Tree Physiology*, *37*(7), 851–868.

Hölttä, T., Mencuccini, M., & Nikinmaa, E. (2009). Linking phloem function to structure: Analysis with a coupled xylem–phloem transport model. *Journal of Theoretical Biology*, *259*(2), 325–337.

Katul, G. G., Manzoni, S., Palmroth, S., & Oren, R. (2010). A stomatal optimization theory to describe the effects of atmospheric CO_2 on leaf photosynthesis and transpiration. *Annals of Botany*, *105*(3), 431–442.

Katul, G. G., Palmroth, S., & Oren, R. A. M. (2009). Leaf stomatal responses to vapour

pressure deficit under current and CO_2-enriched atmosphere explained by the economics of gas exchange. *Plant, Cell & Environment*, *32*(8), 968–979.

Leuning, R. (1995). A critical appraisal of a combined stomatal-photosynthesis model for C_3 plants. *Plant, Cell & Environment*, *18*(4), 339–355.

Lu, Y., Duursma, R. A., & Medlyn, B. E. (2016). Optimal stomatal behaviour under stochastic rainfall. *Journal of Theoretical Biology*, *394*, 160–171.

Manzoni, S., Vico, G., Palmroth, S., Porporato, A., & Katul, G. (2013). Optimization of stomatal conductance for maximum carbon gain under dynamic soil moisture. *Advances in Water Resources*, *62*, 90–105.

Medlyn, B. E., Duursma, R. A., Eamus, D., Ellsworth, D. S., Prentice, I. C., Barton, C. V. M., … Wingate, L. (2011). Reconciling the optimal and empirical approaches to modelling stomatal conductance. *Global Change Biology*, *17*(6), 2134–2144.

Milburn, J. A. (1979). *Water flow in plants*. Longman Inc.

Novick, K. A., Miniat, C. F., & Vose, J. M. (2016). Drought limitations to leaf-level gas exchange: Results from a model linking stomatal optimization and cohesion–tension theory. *Plant, Cell & Environment*, *39*(3), 583–596.

Prentice, I. C., Dong, N., Gleason, S. M., Maire, V., & Wright, I. J. (2014). Balancing the costs of carbon gain and water transport: Testing a new theoretical framework for plant functional ecology. *Ecology Letters*, *17*(1), 82–91.

Rockwell, F. E., Gersony, J. T., & Holbrook, N. M. (2018). Where does Münch flow begin? Sucrose transport in the pre-phloem path. *Current Opinion in Plant Biology*, *43*, 101–107.

Sperry, J. S., Adler, F. R., Campbell, G. S., & Comstock, J. P. (1998). Limitation of plant water use by rhizosphere and xylem conductance: Results from a model. *Plant, Cell & Environment*, *21*(4), 347–359.

Sperry, J. S., & Love, D. M. (2015). What plant hydraulics can tell us about responses to climate-change droughts. *New Phytologist*, *207*(1), 14–27.

Sperry, J. S., & Tyree, M. T. (1988). Mechanism of water stress-induced xylem embolism. *Plant Physiology*, *88*(3), 581–587.

Sperry, J. S., Venturas, M. D., Anderegg, W. R. L., Mencuccini, M., Mackay, D. S., Wang, Y., & Love, D. M. (2017). Predicting stomatal responses to the environment from the optimization of photosynthetic gain and hydraulic cost. *Plant, Cell & Environment*, *40*(6), 816–830.

Sperry, J. S., Wang, Y., Wolfe, B. T., Mackay, D. S., Anderegg, W. R. L., McDowell, N. G., & Pockman, W. T. (2016). Pragmatic hydraulic theory predicts stomatal responses to climatic water deficits. *New Phytologist*, *212*(3), 577–589.

Venturas, M. D., Sperry, J. S., Love, D. M., Frehner, E. H., Allred, M. G., Wang, Y., & Anderegg, W. R. L. (2018). A stomatal control model based on optimization of carbon gain versus hydraulic risk predicts aspen sapling responses to drought. *New Phytologist*, *220*(3), 836–850.

Vico, G., Manzoni, S., Palmroth, S., Weih, M., & Katul, G. (2013). A perspective on optimal leaf stomatal conductance under CO_2 and light co-limitations. *Agricultural and Forest Meteorology*, *182*, 191–199.

Wang, Y., Sperry, J. S., Venturas, M. D., Trugman, A. T., Love, D. M., & Anderegg, W. R. L. (2019). The stomatal response to rising CO_2 concentration and drought is predicted by a hydraulic trait-based optimization model. *Tree Physiology*, *39*, 1416–1427.

Wolf, A., Anderegg, W. R. L., & Pacala, S. W. (2016). Optimal stomatal behavior with competition for water and risk of hydraulic impairment. *Proceedings of the National Academy of Sciences*, *113*(46), E7222–E7230.

Yin, J., & Bauerle, T. L. (2017). A global analysis of plant recovery performance from water stress. *Oikos*, *126*(10), 1377–1388.

Zhou, S., Medlyn, B. E., & Prentice, I. C. (2016). Long-term water stress leads to acclimation of drought sensitivity of photosynthetic capacity in xeric but not riparian *Eucalyptus* species. *Annals of Botany*, *117*(1), 133–144.

Table 3.1: List of key symbols used in the text.

Symbol	Description	Unit
a	Fitting constant for Wolf-Anderegg model	μmol CO_2 m^{-2} s^{-1} MPa^{-2}
b	Fitting constant for Wolf-Anderegg model	μmol CO_2 m^{-2} s^{-1} MPa^{-1}
A	Net photosynthetic rate; instantaneous carbon gain	μmol CO_2 m^{-2} s^{-1}
A_{max}	Maximal A when E_{leaf} is varied from 0 to its E_{crit}	μmol CO_2 m^{-2} s^{-1}
A_{ww}	A without NSL (photosynthetic inhibition independent of stomatal closure)	μmol CO_2 m^{-2} s^{-1}
c_E	Unit cost of transpiration rate	μmol CO_2 mol^{-1} H_2O
c_V	Unit cost of photosynthetic capacity	unitless
C_a	Atmospheric CO_2 concentration	ppm (μ mol mol^{-1})
D	Leaf-to-air vapor pressure deficit relative to atmospheric pressure	unitless
E, E_{leaf}	Leaf transpiration rate per leaf area	mol H_2O m^{-2} s^{-1}
E_{remain}	Water remained in the soil per leaf area	mol H_2O m^{-2}
E_{total}	A given amount of water per leaf area	mol H_2O m^{-2}
E_{crit}	Maximal E, beyond which the tree desiccates by hydraulic failure	mol H_2O m^{-2} s^{-1}
G_M	Mesophyll conductance to CO_2 per leaf area	mol m^{-2} s^{-1}
J	Electron transport rate	μmol CO_2 m^{-2} s^{-1}
J_{max}	Maximal electron transport at 25 °C	μmol CO_2 m^{-2} s^{-1}
K	Soil-plant hydraulic conductance at canopy xylem pressure per basal area, dE/dP	kg H_2O m^{-2} h^{-1} MPa^{-1}
K_{max}	Maximal K when $E_{leaf} = 0$	kg H_2O m^{-2} h^{-1} MPa^{-1}
$K_{max,0}$	Maximal K when there is no cavitation	kg H_2O m^{-2} h^{-1} MPa^{-1}
K_{rhiz}	Rhizosphere hydraulic conductance per basal area	kg H_2O m^{-2} h^{-1} MPa^{-1}
NSL	Non-stomatal limitation to photosynthesis	
P	Leaf xylem water pressure	−MPa
P_{crit}	Most negative P at E_{crit}, beyond which tree desiccates	−MPa
P_{soil}	Soil water potential	−MPa
SC	Sugar concentration in mesophyll cells	mol m^{-3}
SC_{max}	Maximal SC at which photosynthesis is fully inhibited	mol m^{-3}
t_{total}	A given time period	s
V_{cmax}	Maximal carboxylation rate at 25 °C	μmol CO_2 m^{-2} s^{-1}
VPD	Atmospheric vapor pressure deficit	kPa
Γ	CO_2 compensation point with the presence of respiration	ppm
λ	Lagrangian multiplier, optimal dE/dA	mol H_2O μmol^{-1} CO_2
Λ	Proportionality constant for additional carbon gain	mol H_2O μmol^{-1} CO_2
Θ	Instantaneous carbon penalty	μmol CO_2 m^{-2} s^{-1}
Θ′	Instantaneous carbon penalty, results in decline in A	μmol CO_2 m^{-2} s^{-1}

Table 3.2: Ten optimization models (nine published and one new model). The carbon penalty is defined as a future "shadow cost" that does not reduce current photosynthesis (Θ) or as an instantaneous reduction in photosynthesis resulting from a non-stomatal limitation (Θ'). Symbols are defined in Table 3.1. The criteria I–III column indicates whether the model complies (Y) or does not comply (N) with the first three criteria for a unique solution to the optimization. The response criteria IV–VII column indicates whether the model always produces qualitatively realistic responses (Y/N) to VPD (D), C_a (C), soil drought (P), and loss of hydraulic conductance (K). Fitting parameters refer to key model inputs which are difficult to assess a priori and are generally determined by posthoc analysis.

Model	Reference	Carbon Penalty (Θ or Θ')	Marginal Penalty ($\mathrm{d}\Theta/\mathrm{d}E$ or $\mathrm{d}\Theta'/\mathrm{d}E$)	Criteria I–III	Response Criteria IV–VII	Fitting parameters
					DCPK	
Cowan-Farquhar	(Cowan & Farquhar, 1977)	$\Theta = \frac{E_{\mathrm{leaf}}}{\lambda}$	$\frac{\mathrm{d}\Theta}{\mathrm{d}E} = \frac{1}{\lambda}$	YNN	NNNN	λ
Manzoni	(Manzoni et al., 2013)	$\Theta = \frac{E_{\mathrm{leaf}}}{\Lambda}$	$\frac{\mathrm{d}\Theta}{\mathrm{d}E} = \frac{1}{\Lambda}$	YNN	NNNN	Λ
Prentice	(Prentice et al., 2014)	$\Theta = A \cdot \left(1 - \frac{1}{c_{\mathrm{E}} E_{\mathrm{leaf}} + c_{\mathrm{V}} V_{\mathrm{cmax}}}\right)$	$\frac{\mathrm{d}\Theta}{\mathrm{d}E} = \frac{A}{E_{\mathrm{leaf}} + \frac{c_{\mathrm{V}}}{c_{\mathrm{E}}} V_{\mathrm{cmax}}}$	YNY	YYNN	c_{E}, c_{V}
Lu	(Lu et al., 2016)	$\Theta = \frac{E_{\mathrm{leaf}}}{\lambda}$	$\frac{\mathrm{d}\Theta}{\mathrm{d}E} = \frac{1}{\lambda}$	YNN	NNNN	λ
Wolf-Anderegg	(Wolf et al., 2016) (Anderegg et al., 2018)	$\Theta = aP^2 + bP + c$	$\frac{\mathrm{d}\Theta}{\mathrm{d}E} = \frac{2aP + b}{K}$	YYN	NNYY	a, b, K_{rhiz}
Sperry	(Sperry et al., 2017)	$\Theta = A_{\mathrm{max}} \cdot \left(1 - \frac{K}{K_{\mathrm{max}}}\right)$	$\frac{\mathrm{d}\Theta}{\mathrm{d}E} = -\frac{\mathrm{d}K}{\mathrm{d}E} \cdot \frac{A_{\mathrm{max}}}{K_{\mathrm{max}}}$	YYY	YYYY	K_{rhiz}
Eller	(Eller et al., 2018)	$\Theta = A \cdot \left(1 - \frac{K}{K_{\mathrm{max},0}}\right)$	$\frac{\mathrm{d}\Theta}{\mathrm{d}E} = -\frac{\mathrm{d}K}{\mathrm{d}E} \cdot \frac{A}{K}$	YYY	YYYN	K_{rhiz}
Hölttä	(Hölttä et al., 2017)	$\Theta' = A_{\mathrm{ww}} \cdot \frac{\mathrm{SC}}{\mathrm{SC}_{\mathrm{max}}}$	$\frac{\mathrm{d}\Theta'}{\mathrm{d}E} = \frac{A}{\mathrm{SC}_{\mathrm{max}} - \mathrm{SC}} \cdot \frac{\mathrm{dSC}}{\mathrm{d}E}$	YYY	YYYY	$\mathrm{SC}_{\mathrm{max}}$, K_{rhiz}, anatomy
Dewar CAP	(Dewar et al., 2018)	$\Theta' = A_{\mathrm{ww}} \cdot \frac{P}{P_{\mathrm{crit}}}$	$\frac{\mathrm{d}\Theta'}{\mathrm{d}E} = \frac{A}{K \cdot (P_{\mathrm{crit}} - P)}$	YYY	YYYY	K_{rhiz}
New Model		$\Theta = A \cdot \frac{E_{\mathrm{leaf}}}{E_{\mathrm{crit}}}$	$\frac{\mathrm{d}\Theta}{\mathrm{d}E} = \frac{A}{E_{\mathrm{crit}} - E_{\mathrm{leaf}}}$	YYY	YYYY	K_{rhiz}

Table 3.3: Optimization model performance on three datasets. The MAPE stands for mean absolute percentage error (i.e., absolute error relative to the observed mean) for leaf photosynthetic rate (A), tree transpiration (E_{leaf}), and leaf xylem pressure (P). The Dewar CAP* model assumes the penalty is a "shadow cost" rather than a real decline in the instantaneous photosynthetic rate as in the original Dewar CAP version (Dewar et al., 2018).

Model	MAPE for birch				MAPE for aspen				MAPE for 36
	A	E	P	mean	A	E	P	mean	species + sites
Cowan-Farquhar	44.3	52.7	26.3	41.1	42.0	56.5	33.2	43.9	111.2 ± 51.9
Manzoni	44.3	52.7	26.3	41.1	42.0	56.5	33.2	43.9	111.2 ± 51.9
Prentice	44.6	49.1	21.5	38.4	36.3	57.5	35.8	43.2	114.1 ± 62.5
Lu	44.3	52.7	26.3	41.1	42.0	56.5	33.2	43.9	111.2 ± 51.9
Wolf-Anderegg	38.2	34.1	16.7	29.7	34.9	24.9	11.7	23.8	47.3 ± 14.0
Sperry	38.1	27.8	14.5	26.8	29.5	39.5	23.9	29.7	61.4 ± 38.8
Eller	38.3	31.4	16.8	28.8	25.7	36.8	24.5	29.0	60.9 ± 39.8
Dewar CAP	63.2	50.0	38.6	50.6	66.3	37.2	38.4	47.3	89.9 ± 39.6
Dewar CAP*	38.1	31.7	42.1	37.3	52.5	25.3	40.2	39.4	70.0 ± 37.5
New Model	37.4	34.2	12.7	28.1	25.1	37.7	24.8	29.2	52.9 ± 21.3

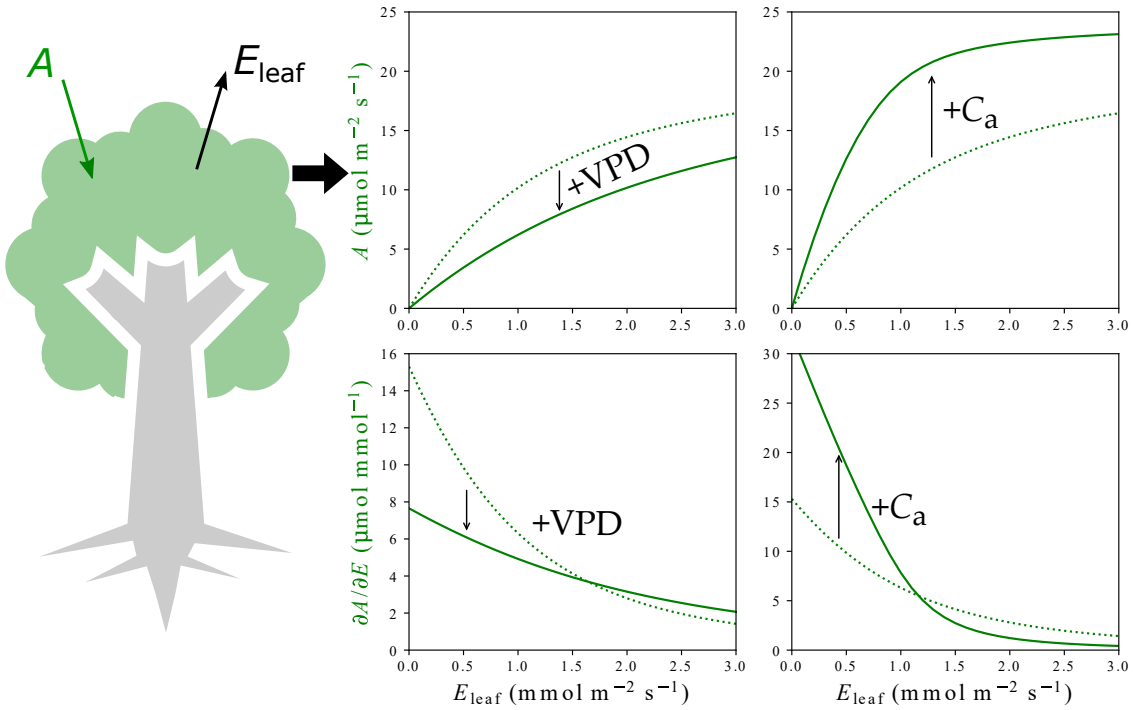

Figure 3.1: Leaf carbon gain (A) and marginal carbon gain as a function of leaf transpiration rate (E_{leaf}, all else constant). The instantaneous A(E_{leaf}) function and corresponding marginal leaf carbon gain (dA/dE) varies with atmospheric vapor pressure deficit (VPD) and atmospheric [CO_2] (C_a) (arrows show increasing VPD (+VPD) and C_a(+C_a)).

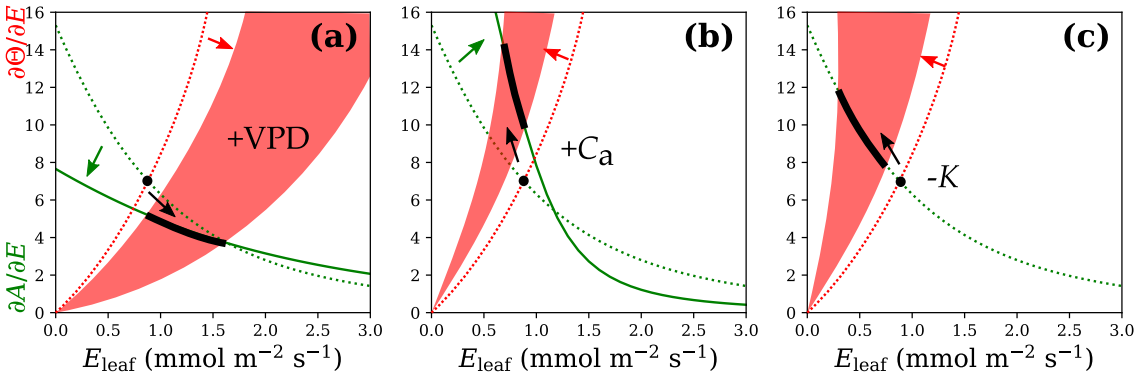

Figure 3.2: Required behavior of a penalty function that produces realistic responses to specific environmental cues (all else constant). The dotted curves are default marginal gain (green) and marginal penalty (red) as a function of E_{leaf} for a given moment in time. The solid circle at their intersection is the original optimal solution for that moment. The solid curves or shaded regions indicate changes in the marginal gain (green line) or marginal penalty (red shaded region) induced by a change in the indicated environmental cue. The thickened black band at the new intersection between the updated marginal gain curve (solid green) and range of penalty curves (red shading) indicates a range of qualitatively realistic optimal solutions. Arrows indicate the direction of the stomatal response to the environmental cue. (a) Response to an increase in vapor pressure deficit (+VPD). The optimal solution must typically predict either no change or an increase in transpiration rate (E_{leaf}). (b) Response to an increase in atmospheric CO_2 concentration (+C_a). The optimal solution must predict either no change in E_{leaf} or (more typically) a decrease in E_{leaf}. (c) Response to a decrease in plant hydraulic conductance caused by ongoing drought or prior drought ($-K$). The marginal gain curve (dotted line) does not change. The optimal solution must predict a reduction in E_{leaf}.

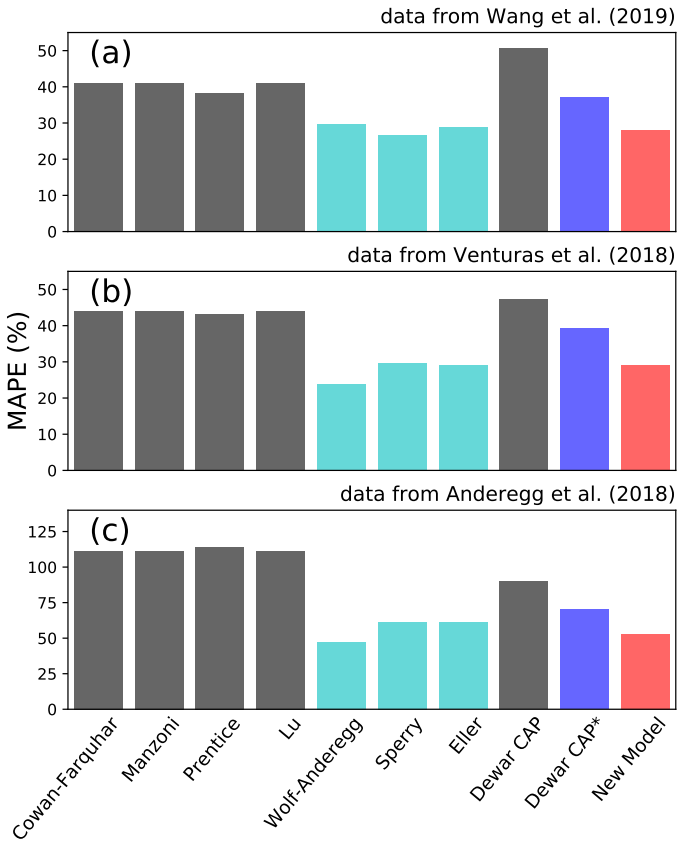

Figure 3.3: Model performance in fitting three datasets. Performance is measured in terms of the mean absolute percentage errors (MAPEs) of the model fitting for photosynthetic rate, transpiration rate, and leaf xylem pressure (bars above each indicated model). The cyan bars highlight the best-fitting previously published models. The blue bar is for the Dewar CAP* model where we assume the penalty is a "shadow cost" rather than a reduction in photosynthesis caused by a non-stomatal limitation as originally intended. The red bar refers to the model developed in this review. (a) Data from water birch saplings exposed to change in CO_2, atmospheric vapor pressure deficit (VPD), and soil moisture in a growth chamber (Wang et al., 2019). (b) Data from aspen saplings exposed to natural changes in VPD and various levels of drought (Venturas et al., 2018). (c) Data from 36 species + site combinations exposed to natural variation in VPD and soil drought (Anderegg et al., 2018).

3.8 Supporting Information

3.8.1 Marginal water use efficiency when $E_{\text{leaf}} = 0$

Marginal water use efficiency must be higher than the marginal risk when $E_{\text{leaf}} = 0$ for the two functions intersect. When $E_{\text{leaf}} = 0$, net assimilation rate is 0 during the day. With an incremental increase in E_{leaf} to $\mathrm{d}E$, the leaf diffusive conductance for CO_2 increases by $\mathrm{d}G = \dfrac{\mathrm{d}E}{1.6 \cdot D}$ (in mol m^{-2} s^{-1}), where D is the leaf-to-air vapor pressure deficit relative to atmospheric pressure. The net photosynthesis increases by $\mathrm{d}A$:

$$\mathrm{d}A = \mathrm{d}G \cdot (C_{\mathrm{a}} - C_{\mathrm{i}}) = \frac{\mathrm{d}E}{1.6 \cdot D} \cdot (C_{\mathrm{a}} - C_{\mathrm{i}}), \tag{3.39}$$

where C_{a} is the atmospheric CO_2 concentration in μmol mol^{-1}, and C_{i} is the intercellular CO_2 concentration. As $\mathrm{d}E$ is infinitesimal, $C_{\mathrm{a}} - C_{\mathrm{i}} = C_{\mathrm{a}} - \Gamma$, where Γ is the CO_2 compensation point with the presence of dark respiration. Thus, the marginal water use efficiency when $E_{\text{leaf}} = 0$ is given as

$$\left.\frac{\mathrm{d}A}{\mathrm{d}E}\right|_{E_{\text{leaf}}=0} = \frac{C_{\mathrm{a}} - \Gamma}{1.6 \cdot D}. \tag{3.40}$$

The unit for $\mathrm{d}A/\mathrm{d}E$ is μmol H_2O μmol^{-1} CO_2.

3.8.2 Derivation of the Manzoni model

The Manzoni model posits a plant maximizes the cumulative photosynthesis in a given amount of time plus an additional carbon gain by using the water remaining in the soil (Manzoni et al., 2013):

$$\max\left(\int_0^{t_{\text{total}}} A \cdot \mathrm{d}t + \frac{1}{\lambda} \cdot E_{\text{remain}}\right) \text{ while } \int_0^{t_{\text{total}}} E_{\text{leaf}} \cdot \mathrm{d}t = E_{\text{total}}. \tag{3.41}$$

The more the plant uses water during the time, the less water remains in the soil, and thus we have

$$\mathrm{d}E_{\text{total}} = -\mathrm{d}E_{\text{remain}}. \tag{3.42}$$

Further, according to the Cowan-Farquhar model, during the time, the marginal water use efficiency, that is, $\dfrac{\mathrm{d}A}{\mathrm{d}E} = \dfrac{1}{\lambda}$; and for an infinitesimal increase of $\mathrm{d}E_{\text{total}}$, the change of marginal water use efficiency is negligible. Therefore, at the optima of the Manzoni model, that is,

$$\frac{\mathrm{d}(\int A \cdot \mathrm{d}t)}{\mathrm{d}E_{\text{total}}} + \frac{d(E_{\text{remain}}/\Lambda)}{\mathrm{d}E_{\text{total}}} = 0, \tag{3.43}$$

we have

$$\frac{\mathrm{d}(\int A \cdot \mathrm{d}t)}{\mathrm{d}E_{\text{total}}} = \frac{1}{\lambda}, \tag{3.44}$$

$$\frac{\mathrm{d}(E_{\text{remain}}/\Lambda)}{\mathrm{d}E_{\text{total}}} = -\frac{1}{\Lambda}, \tag{3.45}$$

meaning the Manzoni model is optimized when $\lambda = \Lambda$.

The penalty and marginal penalty of the Manzoni model are defined as

$$\Theta = \frac{E_{\text{leaf}}}{\Lambda}, \tag{3.46}$$

$$\frac{\mathrm{d}\Theta}{\mathrm{d}E} = \frac{1}{\Lambda}. \tag{3.47}$$

3.8.3 Derivation of the Prentice model

Prentice et al. (2014) made two contradicting assumptions (see equations 3.13 and 3.14). In the main text, we assumed that equation 3.13 was correct. Alternatively, if equation 3.14 in the main text (their equation 1) is correct, the solution for the Prentice model is $\max\left(\frac{A}{\text{constant} + c_{\text{V}} V_{\text{cmax}}}\right)$. Given that c_{V} is independent of E_{leaf} and that V_{cmax} is constant in a short time (e.g., days), the penalty defined in equation 3.14 in the main text is proportional to A. The solution for the Prentice model is equivalent to $\max(A)$ and $\mathrm{d}A/\mathrm{d}E = 0$. In this case, the optimal marginal penalty of the Prentice model is equivalent to $\mathrm{d}\Theta/\mathrm{d}E = 0$, which is a special case of the Cowan-Farquhar model and violates the criteria IV–VII. This version of the Prentice model also violates criteria I–III for a solution to equation 3.1 in the main text, because it defines $\Theta = \text{constant} \cdot A$ (equations 3.12 and 3.14), and the $\mathrm{d}\Theta/\mathrm{d}E = \text{constant} \cdot \mathrm{d}A/\mathrm{d}E$.

The Prentice model also fits the general gain-penalty framework as the model can be written as

$$\min\left(\frac{c_{\text{E}} E_{\text{leaf}} + c_{\text{V}} V_{\text{cmax}}}{A}\right) \equiv \max\left(\frac{A}{c_{\text{E}} E_{\text{leaf}} + c_{\text{V}} V_{\text{cmax}}}\right). \tag{3.48}$$

Therefore, the penalty of the Prentice model is

$$\Theta = A \cdot \left(1 - \frac{1}{c_{\text{E}} E_{\text{leaf}} + c_{\text{V}} V_{\text{cmax}}}\right). \tag{3.49}$$

Differentiating equation 3.49 gives

$$\frac{\mathrm{d}\Theta}{\mathrm{d}E} = \frac{\mathrm{d}A}{\mathrm{d}E} \cdot \left(1 - \frac{1}{c_\mathrm{E} E_\mathrm{leaf} + c_\mathrm{V} V_\mathrm{cmax}}\right) + \frac{c_\mathrm{E} A}{\left(c_\mathrm{E} E_\mathrm{leaf} + c_\mathrm{V} V_\mathrm{cmax}\right)^2}. \tag{3.50}$$

However, there is a $\mathrm{d}A/\mathrm{d}E$ term in the marginal penalty function. As the gain-penalty model is optimized when $\mathrm{d}A/\mathrm{d}E = \mathrm{d}\Theta/\mathrm{d}E$, the Prentice model is optimized when

$$\frac{\mathrm{d}A}{\mathrm{d}E} = \frac{\mathrm{d}A}{\mathrm{d}E} \cdot \left(1 - \frac{1}{c_\mathrm{E} E_\mathrm{leaf} + c_\mathrm{V} V_\mathrm{cmax}}\right) + \frac{c_\mathrm{E} A}{\left(c_\mathrm{E} E_\mathrm{leaf} + c_\mathrm{V} V_\mathrm{cmax}\right)^2}. \tag{3.51}$$

Rearranging equation 3.51 gives

$$\frac{\mathrm{d}A}{\mathrm{d}E} = \frac{c_\mathrm{E} A}{c_\mathrm{E} E_\mathrm{leaf} + c_\mathrm{V} V_\mathrm{cmax}} = \frac{A}{E_\mathrm{leaf} + \frac{c_\mathrm{V}}{c_\mathrm{E}} V_\mathrm{cmax}}. \tag{3.52}$$

Therefore, the marginal risk function of the Prentice model is equivalent to

$$\frac{\mathrm{d}\Theta}{\mathrm{d}E} = \frac{A}{E_\mathrm{leaf} + \frac{c_\mathrm{V}}{c_\mathrm{E}} V_\mathrm{cmax}}. \tag{3.53}$$

3.8.4 Mathematical errors in the Lu model

The Lu model assumes a plant maximizes the mean photosynthetic rate weighted by the soil moisture distribution in a given amount of time. This assumption is equivalent to maximizing the total amount of the cumulative photosynthesis (Lu et al., 2016). Thus, the Lu model is identical to the Cowan-Farquhar model.

The reason why the Lu model solution differed from the Cowan-Farquhar model is that mathematical errors were apparently made. For example, in their equation 12, the authors assumed

$$\frac{\mathrm{d}(\int z \cdot \mathrm{d}x)}{\mathrm{d}y} = \int \frac{\mathrm{d}z}{\mathrm{d}y} \cdot \mathrm{d}x, \tag{3.54}$$

which can be proven wrong by setting $z = 1$ and $x = y$ (then $\frac{\mathrm{d}(\int z \cdot \mathrm{d}x)}{\mathrm{d}y}$ equals 1 but $\int \frac{\mathrm{d}z}{\mathrm{d}y} \cdot \mathrm{d}x$ equals 0). The correct equation should be

$$\frac{\mathrm{d}(\int z \cdot \mathrm{d}x)}{\mathrm{d}y} = \frac{\mathrm{d}\left(\int z \cdot \frac{\mathrm{d}x}{\mathrm{d}y} \cdot \mathrm{d}y\right)}{\mathrm{d}y} = z \cdot \frac{\mathrm{d}x}{\mathrm{d}y}. \tag{3.55}$$

3.8.5 Mathematical and biological ambiguities in the Huang model

The Huang model assumes the stomata act to coordinate the leaf-xylem-phloem system to maximize the sugar transport through the mesophyll cells to the phloem (Huang et al., 2018). The difference between the Huang model and the Hölttä model is that the Huang model does not assume any negative feedback between sugar concentration and photosynthetic rate. From the physiological perspective, the Huang model can be written as

$$\max(K_{\mathrm{xp}} \cdot S_{\mathrm{xp}} \cdot (P_{\mathrm{xy}} - P_{\mathrm{ph}}) \cdot \mathrm{SC}_{\mathrm{ph}}), \tag{3.56}$$

where K_{xp} is the water permeability from xylem conduit to phloem, S_{xp} is the contact area between xylem conduit and phloem, P_{xy} is the water potential of the leaf xylem, P_{ph} is the water potential of the phloem cell, and $\mathrm{SC}_{\mathrm{ph}}$ is the sugar concentration in the phloem cell. Note here that leaf xylem water potential, P_{xy}, is different from leaf xylem pressure, P. In the xylem conduit, P_{xy} is the sum of water pressure (here it is P), osmotic water potential, and gravitational potential:

$$P_{\mathrm{xy}} = P - \mathrm{SC}_{\mathrm{xy}} RT + \rho g h, \tag{3.57}$$

where $\mathrm{SC}_{\mathrm{xy}}$ is the solute concentration of xylem sap that is neglectable, RT is the gas constant times the Kelvin temperature, and h is the height of the xylem conduit. In the phloem conduit, P_{ph} is the sum of water pressure (here it is the turgor pressure of the phloem cell, $\mathrm{TP}_{\mathrm{ph}}$), osmotic water potential, and gravitational potential:

$$P_{\mathrm{ph}} = \mathrm{TP}_{\mathrm{ph}} - \mathrm{SC}_{\mathrm{ph}} RT + \rho g h, \tag{3.58}$$

Combining equations 3.56–3.58, the Huang model can be written as

$$\max(K_{\mathrm{xp}} \cdot S_{\mathrm{xp}} \cdot (P - \mathrm{TP}_{\mathrm{ph}} + \mathrm{SC}_{\mathrm{ph}} RT) \cdot \mathrm{SC}_{\mathrm{ph}}). \tag{3.59}$$

Equation 3.59 differs from their equations 10 and A.1 of Huang et al. (2018) because the authors made the following assumptions:

- phloem turgor pressure can be neglected;
- xylem water is the sole source of water into the phloem;
- xylem water pressure equals xylem water potential;
- all photosynthetic products are transported via the phloem.

The first assumption can only stand if the phloem sugar transport relies only on diffusion, which is not possible as more and more evidence suggests the transport is driven by Munch flow (e.g., Hölttä et al., 2009; Rockwell et al., 2018). The second assumption cannot stand because of the symplastic flow between phloem cell and its companion cell. The third assumption results in great error when h is unneglectable. The last assumption is not true because the sugars are also metabolized within the mesophyll cells.

Solving equation 3.59 requires modeling the carbon sink strength and computing the turgor pressure in the loading phloem cell, as the Hölttä model does. However, Huang et al. (2018) neglect the turgor pressure and further erroneously compute SC_{ph}. The unrealistic assumptions made by Huang et al. (2018) result in incorrect interpretation of their model. The Huang model, if TP solved numerically, is the case of the Hölttä model that has no negative feedback from sugar concentration. The optimal solution of the Huang model, therefore, is max(A), and penalty and marginal penalty of Huang model are

$$\Theta = 0, \tag{3.60}$$

$$\frac{\mathrm{d}\Theta}{\mathrm{d}E} = 0. \tag{3.61}$$

Therefore, the Huang model is a special case of the Cowan-Farquhar model ($\lambda = 0$) and violates criteria I and III–VII.

3.8.6 The Dewar MES model

The Dewar MES model assumes that G_M decreases as P gets more negative. This assumption holds correct if the more negative P results from drier soil because stomata also close more (Dewar et al., 2018). However, if the more negative P results from more stomatal opening (i.e., when G_H increases), the assumption is not supported as G_M is reported to increase with G_H (Flexas et al., 2013). Further, there is no experimental evidence for how the liquid-phase G_M varies with the environment. Both the CAP and MES hypotheses that leaf photosynthetic capacity and G_M (liquid-phase part), like the sugar inhibition hypothesis made by the Hölttä model, hold promise for improving the modeling of photosynthesis, especially for long-term simulations. However, more investigations of whether and how the photosynthetic capacity and liquid-phase G_M change with the environment are required.

CHAPTER 4

THE STOMATAL RESPONSE TO RISING CO_2 CONCENTRATION AND DROUGHT IS PREDICTED BY A HYDRAULIC TRAIT-BASED OPTIMIZATION MODEL

Reprinted with permission from Yujie Wang, John S. Sperry, Martin D. Venturas, Anna T. Trugman, David D. Love, and William R.L. Anderegg. (2019). The stomatal response to rising CO_2 concentration and drought is predicted by a hydraulic trait-based optimization model. Tree Physiology, 39:1416–1427.

Tree Physiology 39, 1416–1427
doi:10.1093/treephys/tpz038

Research paper

The stomatal response to rising CO_2 concentration and drought is predicted by a hydraulic trait-based optimization model

Yujie Wang[1,3], John S. Sperry[1], Martin D. Venturas[1], Anna T. Trugman[1], David M. Love[1,2] and William R. L. Anderegg[1]

[1]School of Biological Sciences, University of Utah, Salt Lake City, 257S 1400E, UT 84112, USA; [2]Warnell School of Forestry and Natural Resources, University of Georgia, 180 E Green Street, Athens, GA 30602-2152, USA; [3]Corresponding author yujie.wang@utah.edu orcid.org/0000-0002-3729-2743

Received December 6, 2018; accepted March 22, 2019; handling Editor Annikki Mäkelä

Modeling stomatal control is critical for predicting forest responses to the changing environment and hence the global water and carbon cycles. A trait-based stomatal control model that optimizes carbon gain while avoiding hydraulic risk has been shown to perform well in response to drought. However, the model's performance against changes in atmospheric CO_2, which is rising rapidly due to human emissions, has yet to be evaluated. The present study tested the gain–risk model's ability to predict the stomatal response to CO_2 concentration with potted water birch (*Betula occidentalis* Hook.) saplings in a growth chamber. The model's performance in predicting stomatal response to changes in atmospheric relative humidity and soil moisture was also assessed. The gain–risk model predicted the photosynthetic assimilation, transpiration rate and leaf xylem pressure under different CO_2 concentrations, having a mean absolute percentage error (MAPE) of 25%. The model also predicted the responses to relative humidity and soil drought with a MAPE of 21.9% and 41.9%, respectively. Overall, the gain–risk model had an MAPE of 26.8% compared with the 37.5% MAPE obtained by a standard empirical model of stomatal conductance. Importantly, unlike empirical models, the optimization model relies on measurable physiological traits as inputs and performs well in predicting responses to novel environmental conditions without empirical corrections. Incorporating the optimization model in larger scale models has the potential for improving the simulation of water and carbon cycles.

Keywords: CO_2 concentration, drought, gain–risk optimization model, gas exchange, hydraulic risk, stomatal control.

Introduction

During the past 60 years, atmospheric CO_2 concentration has increased from 314 to 410 ppm. This accumulation of greenhouse gas has led to a 0.85 °C increase in the global mean annual temperature (IPCC 2014). The rapid temperature increase has likely exacerbated drought stress on forests in many regions, leading to episodes of drought-induced tree mortality across the globe (Adams et al. 2009, Allen et al. 2010). However, concurrent atmospheric CO_2 fertilization may mitigate the negative temperature effects on drought (Zinta et al. 2014, AbdElgawad et al. 2015, Gonzalez-Benecke et al. 2017). Fully understanding and predicting the outcomes of climate change and CO_2 fertilization on terrestrial ecosystems are contingent on models that can be used to predict responses to novel future environments (Katul et al. 2009, 2010, Medlyn et al. 2011, Chen et al. 2012, Mcdowell et al. 2013, Mackay et al. 2015, Anderegg et al. 2017, Tai et al. 2017).

A critical modeling challenge is how to represent the complexity of stomatal behavior that influences plant water loss and CO_2 uptake. To date, most land surface models rely on empirical representations of stomatal responses to environmental cues based on curve fitting to existing data sets (Ball et al. 1987, Leuning 1995, Tuzet et al. 2003, De Kauwe et al. 2013, Walker et al. 2014, Drake et al. 2017). The empirical models are computationally efficient and do not require an understanding of

[†]The present study is a revision for TP-2018-481.

the complex mechanisms underlying stomatal regulation (Chen et al. 2012, Hills et al. 2012). However, the fitted parameters of these models lack physiological or physical identities and cannot be derived explicitly from measurable plant traits (Anderegg et al. 2016, Sperry et al. 2017). Consequently, the empirical approach has a strong risk of being inadequate for accurately predicting plant responses to novel conditions (Powell et al. 2013, Anderegg et al. 2015, Drake et al. 2017, Trugman et al. 2018*b*). These models also do not directly predict the impact of drought stress on the plant's vascular transport system, the damage of which is strongly linked to the plants' drought responses and mortality risk (Sperry and Love 2015, Sperry et al. 2016, Adams et al. 2017, Trugman et al. 2018*a*).

As an alternative to the strictly empirical approach, a goal-oriented solution for stomatal behavior is potentially powerful, i.e., assuming that plants optimize water use relative to photosynthetic gain. A commonly used approach is the Water Use Efficiency Hypothesis (WUEH), which maximizes the photosynthetic gain for a given amount of water during a given time period (Cowan and Farquhar 1977). This WUEH model is a 'constrained-optimization' problem without an exact solution (Katul et al. 2009, 2010, Wolf et al. 2016, Buckley et al. 2017) and often struggles to predict accurate response to [CO_2] and soil moisture (Buckley and Schymanski 2014, Buckley 2017). The WUEH holds that stomata regulate to maintain a constant marginal water-use efficiency, λ. Katul et al. (2009, 2010) solved the optimal stomatal conductance as a function of atmospheric humidity, atmospheric [CO_2] and λ, recovering the stomatal response to atmospheric humidity used by a standard empirical approach (Medlyn et al. 2011). However, the stomatal responses to atmospheric [CO_2] and soil moisture were unrealistic unless λ is a function of both. Manzoni et al. (2013) further advanced the theory by incorporating the soil–plant limitation to leaf water supply and managed to predict realistic stomatal response to soil moisture, but did not consider the response to atmospheric [CO_2]. Thus, a perpetual challenge for the WUEH has been the need to predict λ and its dynamics in response to the full suite of fluctuating environmental stimuli, including [CO_2].

A recently proposed model assumes that the stomata regulate gas exchange so as to maximize the instantaneous carbon gain minus the risk of hydraulic failure by embolism formation (Sperry et al. 2017). The gain and risk of the stomatal opening are given equal weight, each being normalized to start from 0 at stomatal closure (no hydraulic risk but no carbon gain) and rise to 1 as stomata open (maximum photosynthesis but desiccation due to hydraulic failure). This optimization concept predicts realistic theoretic gas exchange response to environmental cues including the response to [CO_2] and soil moisture stress (Sperry et al. 2017). The gain–risk model has been shown to predict stomatal behavior and plant water status in natural droughts and research garden experiments (Anderegg et al. 2018, Venturas et al. 2018). Importantly, the gain–risk model is based on measurable plant physiological traits and hence directly calculates plant physiological status for any combination of environmental conditions, past or future.

The gain versus risk trade-off algorithm has not been fully tested under elevated [CO_2] (Venturas et al. 2018). The atmospheric [CO_2], however, is predicted to at least double to 800 ppm by the end of 21st century (RCP8.5, IPCC 2014). Thus, rigorous testing of the algorithm at elevated [CO_2] is needed to validate the model predictions of plant responses under novel future environmental conditions.

The goal of the present paper is to evaluate the gain–risk algorithm with particular emphasis on its ability to predict the response to short-term changes in [CO_2]. Experiments were conducted in a growth chamber to provide maximal control of environmental conditions. Water birch (*Betula occidentalis* Hook.) was chosen as the study species as it is relatively vulnerable to drought (Sperry and Saliendra 1994). The plants were potted to simplify the modeling of rooting depth and soil water balance. The growth chamber setting also allowed testing the modeled responses to individual stimuli in isolation ([CO_2], relative humidity (RH) and soil drought), which was not possible to do in the research garden experiment (Venturas et al. 2018). The ability of the gain–risk model to predict the experimental results was compared with a standard empirical stomatal model (Medlyn et al. 2011) parameterized to the best fit the same experimental data.

Materials and methods

Plant materials

Water birch (*B. occidentalis* Hook.) trees were grown from seedlings in the greenhouse of the School of Biological Sciences, University of Utah (40° 45′ 48.75″ N, 11° 50′ 57.66″ W, 1425 m above sea level) starting in October 2016. Each tree was grown in a 5-gallon pot with local sandy clay loam soil. Plants were well watered and day length was regulated to 10 h from 8:00 a.m. to 6:00 p.m. with supplemental light (Lucalox LU1000, GE Lighting, East Cleveland, Ohio, USA). In February 2017, 2 weeks prior to the experiments, 10 trees (1–1.5 m tall, 2 years old) were moved into a growth chamber (Model PR-915, Percival Scientific, Perry, Iowa, USA) in order to acclimate the trees to the growth chamber environment. The growth chamber was set at the default settings of ambient CO_2 concentration at 400 ppm, air temperature at 25 °C, RH at 55%, light intensity (photosynthetic active radiation, PAR) at 1000 μmol m^{-2} s^{-1} and day length at 10 h (from 8:00 a.m. to 6:00 p.m. local time). Trees were watered with 1 l water at the end of each day until the drought experiment was initiated.

Experimental design

Growth chamber trees were subjected to three sequential treatments: ambient CO_2 concentration, RH and soil drought. The responses of leaf xylem pressure and leaf gas exchange were measured during each treatment. The CO_2 treatment was conducted on six trees (trees no. 1–6) at a series of ambient CO_2 concentrations starting at 800 ppm, and stepping down to 600, 400, 300 and 200 ppm. All other environmental conditions were kept at default settings. Trees were held at each concentration for at least 90 min prior to measurements. The CO_2 response was measured from high to low [CO_2] in order to avoid any legacy impact of cavitation due to more negative leaf xylem pressures at lower [CO_2]. At the end of the experiment, the chamber [CO_2] was returned to the default at 400 ppm.

Next, the RH treatment was conducted on six trees (trees no. 1, 2 and 7–10) at a series of RH settings of 75%, 65%, 55%, 45% and 35% while keeping other environmental conditions at default settings. The actual chamber vapor pressure deficit (air VPD) was estimated for each gas exchange measurement based on spot measurements of RH and air temperature. The humidity response was measured going from high to low RH in order to avoid the potential legacy of cavitation due to lower leaf xylem pressure in drier air. A different set of trees were chosen for the RH (and soil drought, below) treatments to decrease the reduction in leaf area caused by sampling for pressure chamber measurements of xylem pressure. After the RH experiment, the chamber RH was set back to the default 55%.

The final drought response experiment was also performed on six trees (trees no. 2, 4, 6 and 8–10). Trees were watered only on the first day and dried for four successive days, with measurements conducted at the end of the day. After the measurements, trees were bagged and placed in the dark for at least 3 h to suppress transpiration and equilibrate leaf xylem pressure with soil water potential. Leaf xylem pressure was measured on two to three leaves for each bagged tree and served as a proxy for the soil water potential at the end of the day. Trees were then moved back into the growth chamber for further drought. The growth chamber conditions and timing for leaf xylem pressure measurements of the CO_2, RH and drought treatments are listed in supplementary data Table S1 (available as Supplementary Data at *Tree Physiology* Online).

The tree response to each treatment (CO_2, RH, soil drought) was assessed from measurements of gas exchange and xylem pressure. Gas exchange measurements were performed only when the light had been turned on for at least 120 min and when the growth chamber environment had stabilized for 90 minutes. The whole-tree transpiration rate (E_{tree}) was measured with a 0.5 g precision 34 kg range balance (Sartorius LP34000P, Sartorius Corporation, Goettingen, Germany). The total weight was recorded to the computer every 10 s for 6–10 min. Whole-tree transpiration rate was estimated from the slope of the linear regression of weight loss versus time. Leaf level gas exchange (including photosynthetic rate, stomatal conductance and leaf temperature, T_{leaf}) was measured on two to four leaves on each tree at each treatment stage with a portable photosynthesis system (Li-6800, LICOR Inc., Lincoln NE, USA) by setting the Li-6800 chamber temperature at the growth chamber temperature. One of the leaves used in the photosynthesis measurement was then used in the leaf xylem pressure measurement with a pressure chamber (PMS Instruments, Corvallis, OR, USA; precision ±0.05 MPa) for each tree at different stages of three treatments. Transpiring leaf xylem pressures were measured only for three stages in each treatment in order to minimize the disturbance of decreased leaf area.

Model description

The gain–risk model (Sperry et al. 2017) was modified for the input/output of this study (Table 1). The model was coded with Julia (Julia 0.4.7, NumFocus) and is publicly available (https://github.com/Yujie-WANG/Published-Codes-Yujie-WANG). The plant was represented by one canopy sunlit layer, one stem element, one root layer and one rhizosphere and soil layer in series. No shaded canopy layer was modeled because there was no significant leaf shading for the small saplings (1.0–1.5 m tall) in the growth chamber, and only one root layer was used due to the homogeneous soil moisture in a small pot. Leaf temperature was not modeled in this version because the main purpose of the study was to test the accuracy of the optimization algorithm itself rather than the additional energy balance routine that predicts T_{leaf} in the full version (Sperry et al. 2017, Venturas et al. 2018). Instead, the T_{leaf} required by the model was an input and was averaged from the T_{leaf} measurements for each tree. The model simulations assumed that cavitation of xylem conduits was irreversible (no xylem refilling). Examples of how xylem water pressure and hydraulic conductivity loss respond to the environmental cues can be found in Figure S1 (available as Supplementary Data at *Tree Physiology* Online).

The gain–risk model calculates the relative photosynthetic gain and hydraulic risk of stomatal opening at each time step. The gain is the photosynthetic rate relative to the maximum possible achieved by stomata opening at that time step. Maximal carboxylation rate at 25 °C (V_{cmax}), maximal electron transport at 25 °C (J_{max}), air temperature, T_{leaf}, PAR and ambient [CO_2] are the necessary inputs for computing the photosynthetic gain (Table 1). The risk function measures the relative loss of hydraulic conductance at the end of the transpiration stream, which rises from 0 at stomatal closure to 1 for complete failure at the runaway cavitation. Necessary inputs include the soil moisture, rhizosphere resistance, vulnerability curves (VCs) and maximal conductances of the root, stem and leaf elements of the flow path, as well as the leaf area per basal area (Table 1). Once the gain and risk functions are calculated as a function

Table 1. List of symbols, definitions and status as model input or output. Note that leaf temperature and soil water potential are used as input in this model to test the gain–risk algorithm while they are used as outputs in other versions of the model (Venturas et al. 2018).

Symbol	Definition	Unit	Input/output
A	Photosynthetic assimilation, photosynthetic rate	μmol CO_2 m^{-2} s^{-1}	Output
C_a	Atmospheric CO_2 concentration	ppm	Input
C_i	Intercellular CO_2 concentration	ppm	Output
D	Leaf-to-air vapor pressure deficit	kPa	–
E_{tree}	Transpiration rate of the tree per basal area	kg h^{-1} m^{-2}	Output
J_{max}	Maximal electron transport at 25 °C	μmol CO_2 m^{-2} s^{-1}	Input
K_{max}	Maximal tree hydraulic conductance	kg h^{-1} MPa^{-1} m^{-2}	Input
K_{rhizo}	Maximal tree rhizosphere conductance	kg h^{-1} MPa^{-1} m^{-2}	Input
La:Ba	Leaf area to basal area ratio	m^2 m^{-2}	Input
MAPE	Mean absolute percent error	%	–
PAR	Photosynthetic active radiation	μmol m^{-2} s^{-1}	Input
P_{leaf}	Leaf xylem pressure under light condition	MPa	Output
P_{pd}	Predawn leaf xylem pressure, a proxy for soil water potential	MPa	–
P_{soil}	Soil water potential	MPa	Input
RH	Relative humidity	%	–
T_{leaf}	Leaf temperature	°C	Input
VC	Xylem vulnerability curve to cavitation	–	Input
V_{cmax}	Maximal carboxylation rate at 25 °C	μmol CO_2 m^{-2} s^{-1}	Input
VPD	Vapor pressure deficit in the air	kPa	Input
Weibull B	Fitting parameter of the VC Weibull function	−MPa	Input
Weibull C	Fitting parameter of the VC Weibull function	–	Input

of stomatal opening, the optimization algorithm finds the point at which the gain minus risk difference is maximized. This predicts the gas exchange and water status parameters (e.g., photosynthetic rate, transpiration rate, leaf xylem pressure) at the time step. Model details can be found in Sperry et al. (2017) and Venturas et al. (2018).

Measuring model input parameters

Photosynthesis parameters V_{cmax} and J_{max} at 25 °C were obtained from the measured relationship between the photosynthetic rate (A) and intercellular CO_2 concentration (C_i), A–C_i curves. These curves were obtained for each tree in the growth chamber prior to each experimental treatment. For each curve, the net photosynthetic rates were measured at the leaf temperature of 25 °C and light intensity of 1000 μmol m^{-2} s^{-1} under a series of CO_2 concentrations: 50, 100, 150, 200, 300, 400, 500, 600, 800, 1000, 1200, 1400, 1600, 1800 and 2000 ppm. The dark respiration rate was then measured at the leaf temperature of 25 °C and PAR = 0. The gas exchange measurements were done with a portable photosynthesis system (Li-6800). A–C_i curves were fitted to obtain the V_{cmax} and J_{max} with the *scipy.optimize.leastsq* module in Python 3.6.5 (code provided with the gain–risk model). A total of 43 A–C_i curves were constructed for the 10 trees and the average V_{cmax} and J_{max} for each tree were calculated and used as model input. Ambient [CO_2] and light were recorded from the growth chamber. Leaf temperatures were recorded from the Li-6800 where the inlet air temperature was set to the chamber air temperature.

Vulnerability curves for the root and stem Vulnerability curves of root, stem and leaf were constructed from well-watered, greenhouse-grown trees of the same cohort for the growth chamber experiments. Branches ~80 cm long and roots were harvested, wrapped with black plastic bags and transported to the lab within 5 min of the collection. Stem and root segments 16–20 cm long were cut under water. The segments were vacuum infiltrated in 10 mM KCl for 30 min to remove the emboli in vessels. The segments were trimmed to 13.8 cm and maximal hydraulic conductivity was measured with a conductivity apparatus (Sperry et al. 1988). Stem and root segments were then spun in a custom built rotor in a centrifuge for 10 min to introduce embolism under different pressures (Alder et al. 1997). Hydraulic conductivity was measured immediately after taking the segment out of the centrifuge by correcting the background flow (Hacke et al. 2000, Torres-Ruiz et al. 2012). Each segment was only used to measure the maximal conductivity and conductivity after spinning in the centrifuge (single spin method, Hacke et al. 2015). A total of 39 stem segments and 24 root segments were used to construct the VCs for stem and root, respectively. Root and stem VCs were fitted to the Weibull function, $k = k_{max} \times \exp[-(P/B)\hat{}C]$, where k_{max} is the maximal hydraulic conductance of the element, B and C are the fitted Weibull parameters and P is the xylem pressure in MPa.

Vulnerability curve for the leaf Potted trees in the greenhouse were dried to different leaf xylem pressures and then transported to the lab. Leaf xylem pressure was measured

on two to three bagged leaves for each stressed tree and then a leafy branch (basal diameter >5 mm) was harvested from the tree. Leaf edges were trimmed to expose the minor veins. The hydraulic conductance of the branch (k_{br}) was measured using the vacuum chamber method (Kolb et al. 1996). Then leaves were cut from the branches at the proximal base of the petiole and hydraulic conductance of the stem (k_{st}) was measured under a series of vacuum pressures. The hydraulic conductance of the leaf xylem was computed as $k_{lf} = 1/(1/k_{br} - 1/k_{st})$. The leaf VC was constructed with 31 branches by plotting the k_{lf} versus leaf xylem pressure and fitting the Weibull function.

Maximal tree hydraulic conductance and its partitioning

The whole-tree K_{max} per basal area represents the hydraulic conductance in the absence of any embolism. It was back-calculated from measured tree conductance under well-watered conditions, based on the VCs (Sperry and Love 2015, Venturas et al. 2018). Tree conductance (per growth chamber tree) was the quotient of measured midday transpiration rate and the difference between midday leaf xylem pressure and predawn leaf xylem pressure. The Python script to solve for K_{max} from measured tree conductance can be found along with the model code.

The K_{max} had to be partitioned into root, stem and leaf components (the rhizosphere resistance under wet soil conditions is negligible). The fraction of tree hydraulic resistance (reverse of conductance) in the roots was computed as $(P_{md,b} - P_{pd})/(P_{md} - P_{pd})$, where P_{pd} is the predawn leaf xylem pressure, $P_{md,b}$ is midday bagged leaf xylem pressures of leaves inserted near the root crown and P_{md} is midday xylem pressure of transpiring leaves in the canopy. The stem versus leaf resistance ratio was obtained from the vacuum method, i.e., k_{lf}/k_{st}. The resistance ratios of the stem and leaf to the whole tree were calculated as $(P_{md} - P_{md,b})/(P_{md} - P_{pd}) \times k_{lf}/(k_{lf} + k_{st})$ and $(P_{md} - P_{md,b})/(P_{md} - P_{pd}) \times k_{st}/(k_{lf} + k_{st})$, respectively.

Leaf area and stem area After the experimental treatments were concluded in the growth chamber, the 10 experimental trees were cut to measure the leaf area and stem area. All the shoots were cut from the trees; leaf area and stem area were measured to obtain the leaf area to stem area ratio (La:Ba). Leaf areas were measured with a leaf area meter (Li-3100, LICOR Inc. Lincoln NE, USA). Three out of 10 trees (trees no. 3, 5 and 7) had a smaller La:Ba while 7 out of 10 trees (trees no. 1, 2, 4, 6 and 8–10) had a bigger La:Ba, so two different average ratios were computed for these two subsets and used as model input. Stem basal area was summed from the shoots in the pot. The average leaf area per basal area and stem basal area per tree were used to convert between leaf area-specific versus whole-tree transpiration rate.

Rhizosphere resistance The hydraulic conductance in the rhizosphere (K_{rhizo}) cannot be measured directly. The rhizosphere conductance was obtained from the value that minimized the sum of standardized square error (i.e., the sum of [measured − modeled/mean measured]^2) of leaf xylem pressure, transpiration rate and photosynthetic rate across all comparisons in the CO_2, RH and drought treatments (90 observations in total).

Soil moisture For the CO_2 and RH treatments, 'predawn' leaf xylem pressure (a proxy for soil water potential) was measured with a pressure chamber in the early morning before the lights were turned on. Trees were bagged during the night to ensure the suppression of nocturnal transpiration. The P_{pd} was measured for each tree in the CO_2 and RH treatments and was assumed to be constant throughout the treatment day. For the drought treatment, the soil water potential was assessed from 'predawn' xylem pressures measured at the end of each drought day as already described.

Testing the gain–risk model

The gain–risk model was run for each tree for the same set of environmental conditions corresponding to the measurement of the tree's response to CO_2, RH or drought. The predicted transpiration rate (E_{tree}), photosynthetic rate (A) and leaf xylem pressure (P_{leaf}) were compared with experimental observations to evaluate the model performance in predicting the stomatal responses to environmental cues. The comparison was quantified by calculating the mean absolute error (MAE) and mean absolute percentage error (MAPE; mean absolute difference as a percentage of the observed mean) for each comparison of A, E_{tree} and P_{leaf} for each treatment. Errors were equally weighted across the three variables by studentizing each value (subtracting the observed mean and dividing by the observed standard deviation). Model performance per treatment (CO_2, RH, soil drought) was averaged from the MAPE for the A, E_{tree} and P_{leaf} response obtained for each treatment. Model performance per variable was the variable's MAPE averaged over all treatments. The overall model performance was evaluated by the MAPE averaged across all three variables and treatments.

Comparison with an empirical model

For comparison with the widely used empirical approach for modeling plant water status and gas exchange, a standard version of Ball–Berry–Leuning–Medlyn-type model was used (Ball et al. 1987, Leuning 1995, Medlyn et al. 2011). For the empirical model, stomatal conductance, g_s, was predicted as

$$g_s = g_0 + \frac{1.6A}{C_a} \bullet \left(1 + \frac{g_1}{\sqrt{D}}\right) \bullet \left(\frac{P_{soil} - P_{min}}{P_{max} - P_{min}}\right), \quad (1)$$

where C_a is atmospheric [CO_2], D is the leaf-to-air vapor pressure deficit, g_0, g_1, P_{min} and P_{max} are four parameters

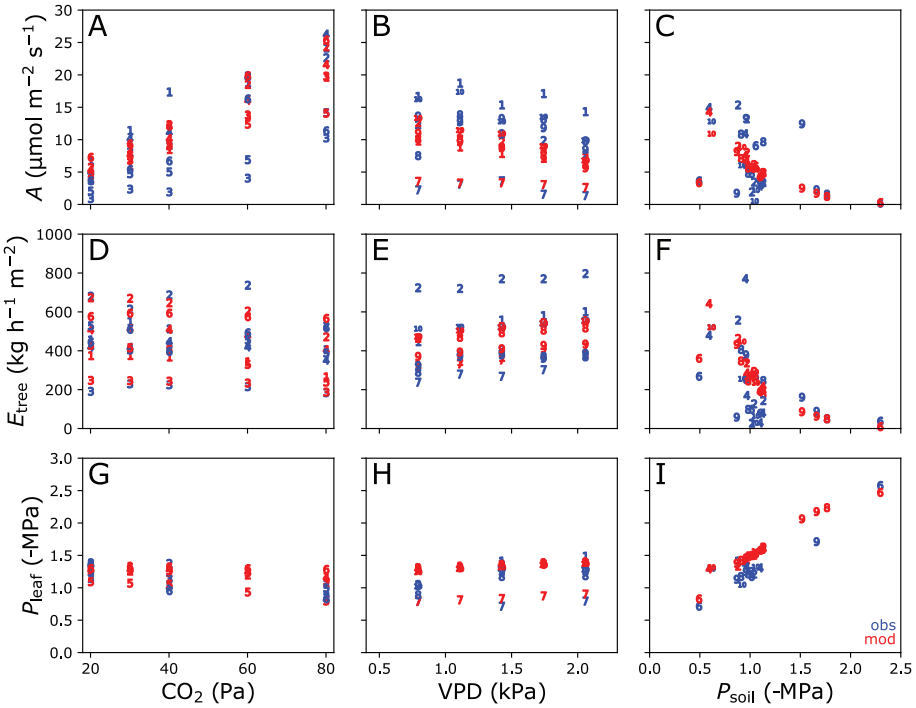

Figure 1. Observations and gain–risk model predictions in the CO_2, humidity and drought treatments. The blue numbers show the observations while the red numbers show the model prediction of each tree (identification number from 1 to 10). Panels (A)–(C) show the observed and modeled photosynthetic rate (A). Panels (D)–(F) show the observed and modeled tree transpiration (E_{tree}). Panels (G)–(I) show the observed and modeled leaf xylem pressure (P_{leaf}). The VPD is the vapor pressure deficit in the air.

fitted to the data and P_{soil} is the soil water potential (predawn leaf xylem pressure was the proxy for P_{soil}). Standard empirical stomatal conductance models lack a soil moisture term (e.g., the right-hand bracketed term; Ball et al. 1987, Leuning 1995, Medlyn et al. 2011), which is added to account for drought stress in large-scale ecosystem models (Trugman et al. 2018b). Equation 1 without the soil moisture term is consistent with the WUEH (Cowan and Farquhar 1977) assuming that RuBP regeneration governs the photosynthesis and marginal water use efficiency is independent of C_a and P_{soil}. The solution of Eq. 1 must also satisfy the physiological relationship between g_s and A, which was assumed to be identical to the gain function for consistency with the gain–risk model (g_s and A were calculated from the intersection of the A–C_i curve and Eq. 1). Similarly, g_s was linked to E_{tree} and P_{leaf} as dictated by the risk function. The fitting parameters were optimized to minimize the sum of studentized MAE (measured versus modeled A, E_{tree} and P_{leaf}; values were studentized by subtracting the observed mean and dividing by the observed standard deviation) for combined [CO_2], RH and drought treatments. Once parameterized, Eq. 1 was numerically solved for the g_s and associated A, E_{tree} and P_{leaf} that satisfied the gain and risk function specific to each tree and measurement period. The code for the empirical model is available at https://github.com/Yujie-WANG/Published-Codes-Yujie-WANG.

Results

Plant traits and model inputs

Mean V_{cmax} for each tree ranged from 12.8 to 96.6 μmol m^{-2} s^{-1} and mean J_{max} ranged from 24.0 to 203.0 μmol m^{-2} s^{-1}. J_{max} was linearly correlated with V_{cmax} (R^2 = 0.992, N = 43) with a ratio of 1.86 (see Figure S2 available as Supplementary Data at *Tree Physiology* Online). Trees no. 3, 5 and 7 had significantly lower leaf area to basal area ratio averaging 2648 m^2 m^{-2} compared with the rest of the trees, which averaged 5663

m^2 m^{-2}, and the model was parameterized accordingly. The average percentage of tree hydraulic resistance in root, stem and leaf pathways was 53.7%, 24.3% and 22.0%, respectively. Estimated rhizosphere conductance was 6×10^8 times the K_{max} of each tree (yielding an average rhizosphere resistance of 36.2% over the full range of soil water potential from zero to the value at which gas exchange would cease). The K_{max} of each tree ranged from 560 to 1970 kg h^{-1} MPa^{-1} m^{-2}. Roots and leaves were more vulnerable to cavitation than the stems with the P_{50} (xylem pressure at 50% loss of conductance) of −1.14 MPa and −1.10 MPa, respectively, compared with the −1.97 MPa in stems. The traits used for modeling each tree can be found in the supplementary data (see Table S2 available as Supplementary Data at *Tree Physiology* Online).

Performance of the gain–risk model

In the CO_2 experiment, as CO_2 concentration was decreased from high (800 ppm) to low (200 ppm), the observed photosynthetic rate decreased ($P < 0.001$, linear regression, Figure 1A, blue data), whole tree transpiration increased non-significantly ($P = 0.13$, linear regression, Figure 1D, blue data) and leaf xylem pressure became more negative ($P = 0.03$, linear regression, Figure 1G, blue data). The gain–risk model tracked these measured trends well (Figure 1A,D, and G, red data). The standardized MAPE was 25.0%, averaged across all photosynthesis, transpiration and leaf xylem pressure comparisons (Figure 2A, Table 2). The error was lower for the predictions of transpiration and xylem pressure than for photosynthesis (Table 2). The linear regression slope for modeled versus measured transpiration was not significantly different from 1 ($P = 0.14$, Table 2), and the rest of the variable sets had slopes significantly shallower than 1 ($P < 0.001$, Table 2).

In the RH treatment, as RH was decreased from high to low (from 75% to 35%, corresponding to an atmospheric VPD ranging from 0.79–2.06 kPa), the observed photosynthetic rate decreased ($P < 0.001$, linear regression, Figure 1B, blue data) while tree transpiration rate increased ($P = 0.05$, linear regression, Figure 1E, blue data) and leaf xylem pressure became more negative ($P = 0.84$, Figure 1H, blue data). The gain–risk model tracked these trends (Figure 1B, E and H red data) with an overall MAPE of 21.9% (Figure 2B). The error was greatest for photosynthesis and least for xylem pressure (Table 2). The linear regression slope for each modeled versus measured variable set (i.e., A, E_{tree}, P_{leaf} and All) was significantly lower than 1 ($P < 0.001$, Table 2).

In the soil drought treatment, as predawn xylem pressure fell from −0.5 MPa to −2.3 MPa during the drought, the observed photosynthesis, transpiration and leaf xylem pressure fell ($P < 0.001$, linear regression, Figure 1C, F and I, blue data). These trends were predicted by the gain–risk model (Figure 1C, F and I, red data), but the percentage error was greater at 41.9% (Figure 2C). The percentage error was larger for photosynthesis and transpiration than xylem pressure (Table 2). The larger percentage error in the drought treatment compared with the CO_2 and RH treatments resulted from the lower mean photosynthesis and transpiration rates measured under drought stress. In terms of average absolute value of the error, the drought treatment was comparable to the [CO_2] and RH treatments. The linear regression slopes for the modeled versus measured transpiration and leaf xylem pressure were not significantly different from 1 ($P = 0.58$ and 0.13, respectively, Table 2), but the slopes for photosynthesis and combined variable set were significantly lower than 1 ($P < 0.001$, Table 2).

Pooling the CO_2, RH and soil drought treatments, the overall MAPE for the gain–risk model was 26.8% (Figure 2D), with more error in the photosynthesis prediction (38.1%) than the xylem pressure prediction (14.5%). Transpiration MAPE was intermediate (27.8%, Table 2). The model predictions fell close to the 1:1 line that was also within the 95% confidence limits of the regression. A linear regression of the studentized model prediction versus observations had slope lower than 1 for each treatment, each variable and combined treatments ($P < 0.01$, Figure 2A–D, Table 2).

Comparison with the empirical model

Pooling across all treatments and variables, the gain–risk model predicted observed tree responses more skillfully (MAPE = 26.8%) than the Ball–Berry–Leuning–Medlyn empirical model (MAPE = 37.5%; Figure 2D and H). On a per treatment basis, the gain–risk model gave lower errors for all the [CO_2], RH and drought responses (Figure 2A–C, E–G). Per variable, the gain–risk model better predicted the photosynthesis, whole-tree transpiration and leaf xylem pressure for combined treatments. The empirical model only performed slightly better for photosynthesis in the [CO_2] treatment and whole-tree transpiration in the drought treatment (Table 2). A linear regression of the studentized empirical fitting had slope lower than 1 for each treatment and combined treatments ($P < 0.001$, Figure 2E–H, Table 2). Per variable, only the linear regression for leaf xylem pressure in the RH, drought and all treatments combined showed slopes not significantly different from 1 ($P = 0.34$, 0.91 and 0.76, respectively, Table 2). In the RH treatment, the empirical model underestimated A, E_{tree} and P_{leaf} as the modeled values were below the 1:1 line (Figure 2F).

Discussion

The gain–risk optimization model was able to capture the [CO_2], air humidity and soil drought responses in novel conditions, suggesting that patterns of tree-level gas exchange are consistent with an optimization of carbon gain and hydraulic risk. The gain–risk model showed better overall predicting power than

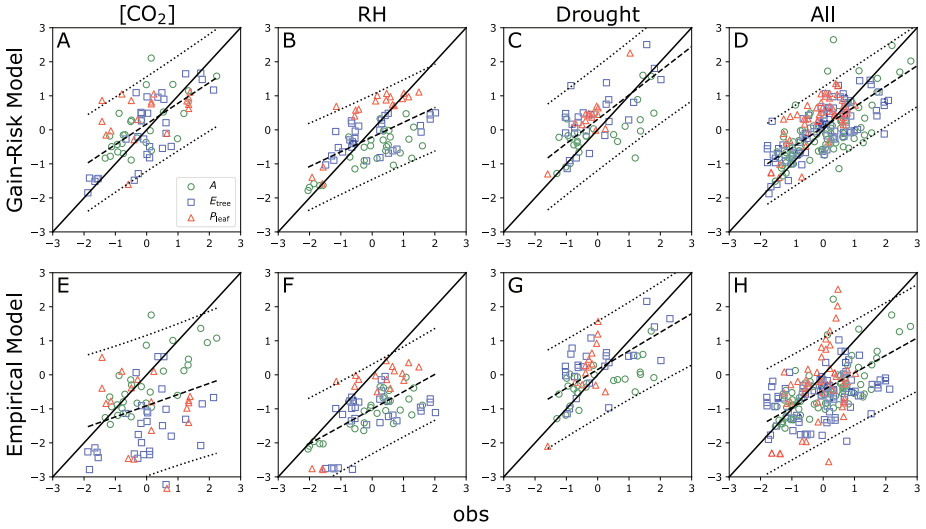

Figure 2. Comparison of model predictions of studentized photosynthesis (A, green circle), transpiration (E_{tree}, blue square) and leaf xylem pressure (P_{leaf}, red triangle) versus experimental observations. Panels (A)–(D) show the gain–risk model predictions for CO_2, RH, drought and all treatments, respectively. Panels (E)–(H) show the empirical model fittings for CO_2, RH, drought and all treatments, respectively. Solid black lines are the 1:1 relationship. Dashed lines are the regression lines. Dotted lines are the 95% confidence intervals for the linear regression. The mean absolute percentage error and the regression statistics are listed in Table 2.

the empirical model, which had the advantage of freely tuning four parameters to best fit the data. The only parameter adjusted post-hoc in the gain–risk approach was the rhizosphere conductance, which is a difficult trait to measure. This trait selectively influences the model under drought conditions because only in drying soil does rhizosphere hydraulic conductance become limiting (Sperry et al. 1998, Sperry and Love 2015, Wolfe et al. 2016). Thus, the post-hoc adjustment of the rhizosphere conductance had a minimal influence on the good fits observed in the well-watered CO_2 and RH treatments. The advantage of having all model parameters associated with identifiable traits is that this makes it easier to assign a value and uncertainty to them a priori when true predictions are required (as opposed to the hind-casting that is possible during model validation). One can also better understand the physiological basis for uncertainties in model projections when all inputs are linked to trait and process. At the same time, it is important to restrict the model to well-understood trait and process, or risk regression to post-hoc fitting that becomes equivalent to the empirical approach. For example, it can be conceptually useful to incorporate phloem transport in an optimization model, but this approach has the downside of adding a suite of currently poorly known parameters (Nikinmaa et al. 2013, Huang et al. 2018).

The present results add to the prior validations of the gain–risk algorithm in controlled plantation experiment with aspen (*Populus tremuloides*; Venturas et al. 2018), and meta-analysis of gas exchange data from a variety of species (Anderegg et al. 2018). The work adds to this body of literature and is the first testing of the model's CO_2 response to both elevated and decreased CO_2 concentrations. The overall error (26.8% for all treatments) was comparable to that for the Venturas et al. (2018) study (27.9% for control and drought treatments). Although the percentage error was higher for the drought treatment (41.9%), this was owing to lower mean values rather than to a greater absolute error. The MAEs for water birch (A: 2.83, E_{tree}: 135.52 and P_{leaf}: 0.23 for drought treatment, units in Table 1) were comparable to the MAEs for aspen in the Venturas study (A: 2.3, E_{tree}: 151.2 and P_{leaf}: 0.4, units in Table 1). An advantage of the growth chamber experiments was the ability to isolate the model error for each individual driver ($[CO_2]$, RH and soil drought). Similar absolute error values indicated that the gain–risk model represented all responses with equal fidelity (Table 2).

The slope of the model predictions and observations in Figure 2D was significantly lower than 1, suggesting that the model either underestimated gas exchange rates under

Table 2. The comparison of gain–risk model and empirical model predictions. MAE (units for A, E_{tree} and P_{leaf} reported in Table 1) and MAPE stand for mean absolute error and mean absolute percentage error, respectively. The row 'slope' denotes the slope of the regression between observed values (x) and modeled values (y). The row 'slope = 1' denotes the P-value for the linear regression slope being different from 1. Units as in Table 1.

Treatment/Model		Predicted			
		A	E_{tree}	P_{leaf}	All
CO_2/Gain–risk	MAPE	41.1%	17.8%	16.2%	25.0%
	MAE	4.25	78.83	0.18	
	Slope	0.62 ± 0.11	0.81 ± 0.12	0.25 ± 0.15	0.61 ± 0.08
	Slope = 1	0.00	0.14	0.00	0.00
	R^2	0.527	0.606	0.140	0.441
CO_2/Empirical	MAPE	40.7%	49.1%	26.7%	38.8%
	MAE	4.21	217.29	0.30	
	Slope	0.63 ± 0.11	0.36 ± 0.16	−0.23 ± 0.24	0.33 ± 0.12
	Slope = 1	0.00	0.00	0.00	0.00
	R^2	0.539	0.155	0.059	0.094
RH/Gain–risk	MAPE	31.5%	23.5%	10.7%	21.9%
	MAE	3.50	111.66	0.12	
	Slope	0.45 ± 0.08	0.25 ± 0.07	0.71 ± 0.11	0.43 ± 0.07
	Slope = 1	0.00	0.00	0.02	0.00
	R^2	0.563	0.287	0.708	0.332
RH/Empirical	MAPE	46.9%	41.7%	14.0%	34.2%
	MAE	5.20	198.18	0.16	
	Slope	0.45 ± 0.07	0.37 ± 0.12	0.85 ± 0.16	0.51 ± 0.07
	Slope = 1	0.00	0.00	0.34	0.00
	R^2	0.632	0.237	0.651	0.382
Drought/Gain–risk	MAPE	43.0%	65.4%	17.3%	41.9%
	MAE	2.83	135.52	0.23	
	Slope	0.44 ± 0.10	0.91 ± 0.17	0.85 ± 0.10	0.71 ± 0.09
	Slope = 1	0.00	0.58	0.13	0.00
	R^2	0.421	0.544	0.849	0.483
Drought/Empirical	MAPE	45.5%	59.2%	21.7%	42.1%
	MAE	2.99	122.56	0.29	
	Slope	0.36 ± 0.08	0.45 ± 0.12	1.02 ± 0.20	0.55 ± 0.09
	Slope = 1	0.00	0.00	0.91	0.00
	R^2	0.446	0.373	0.658	0.381
All/Gain–risk	MAPE	38.1%	27.8%	14.5%	26.8%
	MAE	3.58	106.58	0.17	
	Slope	0.56 ± 0.07	0.54 ± 0.05	0.79 ± 0.07	0.60 ± 0.04
	Slope = 1	0.00	0.00	0.01	0.00
	R^2	0.463	0.541	0.690	0.506
All/Empirical	MAPE	44.2%	47.6%	20.7%	37.5%
	MAE	4.17	181.80	0.25	
	Slope	0.51 ± 0.06	0.25 ± 0.07	0.95 ± 0.15	0.51 ± 0.05
	Slope = 1	0.00	0.00	0.76	0.00
	R^2	0.479	0.153	0.455	0.304

favorable conditions or overestimated them under stressful conditions. The results suggest that the latter case applies to the water birch because the model predicted leaf xylem pressure became overly negative under stressed conditions (Figures 1F and I, and 2C). This behavior would occur if the measured leaf VC was more resistant than the actual leaf VC. An overly resistant leaf VC would lead to more negative predicted P_{leaf} and higher predicted transpiration at any soil moisture condition (Figures 1F and I, and 2C). The measured leaf VC was for leaf xylem only, and so excluded potential declines in leaf hydraulic conductance in the extra-xylary flow path. The response of extra-xylary hydraulic conductance to water stress requires more quantitative investigation (Bartlett et al. 2014, Meinzer et al. 2016, Scoffoni et al. 2017) and may improve model performance. Incorporating the mesophyll conductance in the model may also improve the predictions (Dewar et al. 2018, Flexas et al. 2008), but there are still knowledge gaps that prevent incorporating it in the gain–risk model such as how

to quantifiy the change of mesophyll conductance in response to the environment.

The empirical approach performed less satisfactorily compared with the trait-based gain–risk model, especially in predicting E_{tree} and P_{leaf} in the CO_2 and RH treatments (Table 2). The underperformance of the empirical model was despite the advantage of fitting model parameters to the observed data set and using the same linkage between g_s, A, E_{tree} and P_{leaf} employed in the gain–risk model (i.e., the gain and risk functions). Either the model 'parameters' are not constants as intended or the empirical equation itself does not fully capture the complexity of the stomatal response to CO_2, RH and soil drought. Even if an empirical approach had been as successful as the gain–risk model, as was the case in the aspen study of Venturas et al. (2018), the gain–risk model has the advantage of being parameterized by measurable traits with known uncertainties. The gain–risk approach also capitalizes on the known linkage between stomatal behavior and physiological traits (Pataki et al. 1998, Sperry 2000, Hubbard et al. 2001, Santiago et al. 2004).

While the gain–risk model can predict well the stomatal behavior based on measured traits, the predictions may only be relevant for short timeframes when these measured traits stay unchanged. Acclimation such as changes in leaf respiration, leaf area per basal area, photosynthetic capability and rooting depth has the potential to change plant response over time to the long-term changes in [CO_2], temperature and other factors (Eissenstat et al. 2000, Ainsworth and Long 2005, Guswa 2008). The fact that the gain–risk model is trait-based allows for modeling these acclimation processes as they become better understood. In conclusion, the gain–risk model appears to hold promise for improving predictions of forest health in response to a changing climate.

Conflict of interest

None declared.

Funding

This study was funded by NSF 1450650 granted to J.S.S. W.R.L.A. acknowledges funding from the David and Lucille Packard Foundation, the University of Utah Global Change and Sustainability Center, NSF Grants 1714972 and 1802880, and the USDA National Institute of Food and Agriculture, Agricultural and Food Research Initiative Competitive Programme, Ecosystem Services and Agro-ecosystem Management, Grant No. 2018-67019-27850. A.T.T. acknowledges support from the USDA National Institute of Food and Agriculture Postdoctoral Research Fellowship Grant No. 2018-67012-28020.

References

AbdElgawad H, Farfan-Vignolo ER, de Vos D, Asard H (2015) Elevated CO_2 mitigates drought and temperature-induced oxidative stress differently in grasses and legumes. Plant Sci 231:1–10.

Adams HD, Guardiola-Claramonte M, Barron-Gafford GA, Villegas JC, Breshears DD, Zou CB, Troch PA, Huxman TE (2009) Temperature sensitivity of drought-induced tree mortality portends increased regional die-off under global-change-type drought. Proc Natl Acad Sci USA 106:7063–7066.

Adams HD, Zeppel MJB, Anderegg WRL et al. (2017) A multi-species synthesis of physiological mechanisms in drought-induced tree mortality. Nat Ecol Evol 1:1285–1291.

Ainsworth EA, Long SP (2005) What have we learned from 15 years of free-air CO_2 enrichment (FACE)? A meta-analytic review of the responses of photosynthesis, canopy properties and plant production to rising CO_2. New Phytol 165:351–372.

Alder NN, Pockman WT, Sperry JS, Nuismer S (1997) Use of centrifugal force in the study of xylem cavitation. J Exp Bot 48:665–674.

Allen CD, Macalady AK, Chenchouni H et al. (2010) A global overview of drought and heat-induced tree mortality reveals emerging climate change risks for forests. For Ecol Manage 259:660–684.

Anderegg WRL, Schwalm C, Biondi F et al. (2015) Pervasive drought legacies in forest ecosystems and their implications for carbon cycle models. Science 349:528–532.

Anderegg WRL, Klein T, Bartlett M, Sack L, Pellegrini AFA, Choat B (2016) Meta-analysis reveals that hydraulic traits explain cross-species patterns of drought-induced tree mortality across the globe. Proc Natl Acad Sci USA 113:2–7.

Anderegg WRL, Wolf A, Arango-Velez A et al. (2017) Plant water potential improves prediction of empirical stomatal models. PLoS One 12:e0185481.

Anderegg WRL, Wolf A, Arango-Velez A et al. (2018) Woody plants optimise stomatal behaviour relative to hydraulic risk. Ecol Lett 21:968–977.

Ball JT, Woodrow IE, Berry JA (1987) A model predicting stomatal conductance and its contribution to control of phosynthesis under different environmental conditions. In: Biggins J. (eds) Progress in photosynthesis research. Springer, Dordrecht, pp 221–224.

Bartlett MK, Zhang Y, Kreidler N, Sun S, Ardy R, Cao K, Sack L (2014) Global analysis of plasticity in turgor loss point, a key drought tolerance trait. Ecol Lett 17:1580–1590.

Buckley TN (2017) Modeling stomatal conductance. Plant Physiol 174:572–582.

Buckley TN, Schymanski SJ (2014) Stomatal optimisation in relation to atmospheric CO_2. New Phytol 201:372–377.

Buckley TN, Sack L, Farquhar GD (2017) Optimal plant water economy. Plant Cell Environ 40:881–896.

Chen Z, Hills A, Batz U, Amtmann A, Lew VL, Blatt MR (2012) Systems dynamic modelling of the stomatal guard cell predicts emergent behaviours in transport, signalling and volume control. Plant Physiol 159:1235–1251.

Cowan IR, Farquhar GD (1977) Stomatal function in relation to leaf metabolism and environment. Symp Soc Exp Biol 31:471–505.

De Kauwe MG, Medlyn BE, Zaehle S et al. (2013) Forest water use and water use efficiency at elevated CO_2: a model-data intercomparison at two contrasting temperate forest FACE sites. Glob Chang Biol 19:1759–1779.

Dewar R, Mauranen A, Mäkelä A, Hölttä T, Medlyn B, Vesala T (2018) New insights into the covariation of stomatal, mesophyll and hydraulic conductances from optimization models incorporating nonstomatal limitations to photosynthesis. New Phytol 217:571–585.

Drake JE, Power SA, Duursma RA et al. (2017) Stomatal and non-stomatal limitations of photosynthesis for four tree species under

drought: a comparison of model formulations. Agric For Meteorol 247:454–466.
Eissenstat DM, Wells CE, Yanai RD, Whitbeck JL (2000) Building roots in a changing environment: implications for root longevity. New Phytol 147:33–42.
Flexas J, Ribas-Carbó M, Diaz-Espejo A, Galmés J, Medrano H (2008) Mesophyll conductance to CO_2: current knowledge and future prospects. Plant Cell Environ 31:602–621.
Gonzalez-Benecke CA, Teskey RO, Dinon-Aldridge H, Martin TA (2017) *Pinus taeda* forest growth predictions in the 21st century vary with site mean annual temperature and site quality. Glob Chang Biol 23:4689–4705.
Guswa AJ (2008) The influence of climate on root depth: a carbon cost-benefit analysis. Water Resour Res 44:W02427.
Hacke UG, Sperry JS, Pittermann J (2000) Drought experience and cavitation resistance in six shrubs from the Great Basin, Utah. Basic Appl Ecol 1:31–41.
Hacke UG, Venturas MD, Mackinnon ED, Jacobsen AL, Sperry JS, Pratt RB (2015) The standard centrifuge method accurately measures vulnerability curves of long-vesselled olive stems. New Phytol 205: 116–127.
Hills A, Chen Z, Amtmann A, Blatt MR, Lew VL (2012) OnGuard, a computational platform for quantitative kinetic modelling of guard cell physiology. Plant Physiol 159:1026–1042.
Huang C-W, Domec J-C, Palmroth S, Pockman WT, Litvak ME, Katul GG (2018) Transport in a coordinated soil-root-xylem-phloem leaf system. Adv Water Resour 119:1–16.
Hubbard RM, Ryan MG, Stiller V, Sperry JS (2001) Stomatal conductance and photosynthesis vary linearly with plant hydraulic conductance in ponderosa pine. Plant Cell Environ 24:113–121.
IPCC (2014) Climate change 2014: synthesis report. Core Writing Team, RK Pachauri and LA Meyer (eds) Contribution of Working Groups I, II and III to the Fifth Assessment Report of the Intergovernmental Panel on Climate Change. IPCC, Geneva, Switzerland.
Katul G, Manzoni S, Palmroth S, Oren R (2010) A stomatal optimization theory to describe the effects of atmospheric CO_2 on leaf photosynthesis and transpiration. Ann Bot 105:431–442.
Katul GG, Palmroth S, Oren R (2009) Leaf stomatal responses to vapour pressure deficit under current and CO_2-enriched atmosphere explained by the economics of gas exchange. Plant Cell Environ 32:968–979.
Kolb KJ, Sperry JS, Lamont BB (1996) A method for measuring xylem hydraulic conductance and embolism in entire root and shoot systems. J Exp Bot 47:1805–1810.
Leuning R (1995) A critical appraisal of a combined stomatal-photosynthesis model for C_3 plants. Plant Cell Environ 18: 339–355.
Mackay DS, Roberts DE, Ewers BE, Sperry JS, McDowell NG, Pockman WT (2015) Interdependence of chronic hydraulic dysfunction and canopy processes can improve integrated models of tree response to drought. Water Resour Res 51:6156–6176.
Manzoni S, Vico G, Palmroth S, Porporato A, Katul G (2013) Optimization of stomatal conductance for maximum carbon gain under dynamic soil moisture. Adv Water Resour 62:90–105.
McDowell NG, Fisher RA, Xu C et al. (2013) Evaluating theories of drought-induced vegetation mortality using a multimodel-experiment framework. New Phytol 200:304–321.
Medlyn BE, Duursma RA, Eamus D, et al. (2011) Reconciling the optimal and empirical approaches to modelling stomatal conductance. Glob Chang Biol 17:2134–2144.
Meinzer FC, Woodruff DR, Marias DE, Smith DD, McCulloh KA, Howard AR, Magedman AL (2016) Mapping 'hydroscapes' along the iso- to anisohydric continuum of stomatal regulation of plant water status. Ecol Lett 19:1343–1352.
Nikinmaa E, Hölttä T, Hari P, Kolari P, Mäkelä A, Sevanto S, Vesala T (2013) Assimilate transport in phloem sets conditions for leaf gas exchange. Plant Cell Environ 36:655–669.
Pataki DE, Oren R, Phillips N (1998) Responses of sap flux and stomatal conductance of *Pinus taeda* L. trees to stepwise reductions in leaf area. J Exp Bot 49:871–878.
Powell TL, Galbraith DR, Christoffersen BO et al. (2013) Confronting model predictions of carbon fluxes with measurements of Amazon forests subjected to experimental drought. New Phytol 200:350–365.
Santiago LS, Goldstein G, Meinzer FC, Fisher JB, Machado K, Woodruff D, Jones T (2004) Leaf photosynthetic traits scale with hydraulic conductivity and wood density in Panamanian forest canopy trees. Oecologia 140:543–550.
Scoffoni C, Albuquerque C, Brodersen CR, Townes SV, John GP, Bartlett MK, Buckley TN, McElrone AJ, Sack L (2017) Outside-xylem vulnerability, not xylem embolism, controls leaf hydraulic decline during dehydration. Plant Physiol 173:1197–1210.
Sperry JS (2000) Hydraulic constraints on plant gas exchange. Agric For Meteorol 104:13–23.
Sperry JS, Love DM (2015) What plant hydraulics can tell us about responses to climate-change droughts. New Phytol 207:14–27.
Sperry JS, Saliendra NZ (1994) Intra- and inter-plant variation in xylem cavitation in *Betula occidentalis*. Plant Cell Environ 17: 1233–1241.
Sperry JS, Donnelly JR, Tyree MT (1988) A method for measuring hydraulic conductivity and embolism in xylem. Plant Cell Environ 11:35–40.
Sperry JS, Adler FR, Campbell GS, Comstock JP (1998) Limitation of plant water use by rhizosphere and xylem conductance: results from a model. Plant Cell Environ 21:347–359.
Sperry JS, Wang Y, Wolfe BT, Mackay DS, Anderegg WRL, McDowell NG, Pockman WT (2016) Pragmatic hydraulic theory predicts stomatal responses to climatic water deficits. New Phytol 212:577–589.
Sperry JS, Venturas MD, Anderegg WRL, Mencuccini M, Mackay DS, Wang Y, Love DM (2017) Predicting stomatal responses to the environment from the optimization of photosynthetic gain and hydraulic cost. Plant Cell Environ 40:816–830.
Tai X, Mackay DS, Anderegg WRL, Sperry JS, Brooks PD (2017) Plant hydraulics improves and topography mediates prediction of aspen mortality in southwestern USA. New Phytol 213:113–127.
Torres-Ruiz JM, Sperry JS, Fernández JE (2012) Improving xylem hydraulic conductivity measurements by correcting the error caused by passive water uptake. Physiol Plant 146:129–135.
Trugman AT, Detto M, Bartlett MK, Medvigy D, Anderegg WRL, Schwalm C, Schaffer B, Pacala SW (2018*a*) Tree carbon allocation explains forest drought-kill and recovery patterns. Ecol Lett 21: 1552–1560.
Trugman AT, Medvigy D, Mankin JS, Anderegg WRL (2018*b*) Soil moisture stress as a major driver of carbon cycle uncertainty. Geophys Res Lett 45:6495–6503.
Tuzet A, Perrier A, Leuning R (2003) A coupled model of stomatal conductance, photosynthesis and transpiration. Plant Cell Environ 26:1097–1116.
Venturas MD, Sperry JS, Love DM, Frehner EH, Allred MG, Wang Y, Anderegg WRL (2018) A stomatal control model based on optimization of carbon gain versus hydraulic risk predicts aspen sapling responses to drought. New Phytol 220:836–850.
Walker A, Hanson P, De Kauwe MG et al. (2014) Comprehensive ecosystem model-data synthesis using multiple data sets at two temperate forest free-air CO_2 enrichment experiments: model performance at ambient CO_2 concentration. J Geophys Res Biogeo sci 119:937–964.

Wolf A, Anderegg WRL, Pacala SW (2016) Optimal stomatal behavior with competition for water and risk of hydraulic impairment. Proc Natl Acad Sci USA 113:E7222–E7230.

Wolfe BT, Sperry JS, Kursar TA (2016) Does leaf shedding protect stems from cavitation during seasonal droughts? A test of the hydraulic fuse hypothesis. New Phytol 212:1007–1018.

Zinta G, Abdelgawad H, Domagalska MA, Vergauwen L, Knapen D, Nijs I, Janssens IA, Beemster GTS, Asard H (2014) Physiological, biochemical, and genome-wide transcriptional analysis reveals that elevated CO_2 mitigates the impact of combined heat wave and drought stress in *Arabidopsis thaliana* at multiple organizational levels. Glob Chang Biol 20:3670–3685.

4.8 Supporting Information

4.8.1 Table of experimental design

Table 4.S1: Default setting of the growth chamber and the settings for the treatments. Row [CO_2] was the chamber CO_2 concentration; row RH was the relative humidity; row Soil indicated whether the trees were watered (W for watered, NW for not watered); row PAR was the light intensity; row T_{air} was the chamber air temperature; row Day time was the time frame for light in the chamber. Column Default and Treatment stages showed the default settings of the chamber. The P_{pd} and P_{leaf} indicated that predawn water potential and leaf xylem pressure were measured for that treatment. The P_{pd} was measured once for the [CO_2] and RH treatment. The P_{pd} was measured after each stage in the drought treatment. PAR was set at a constant 1000 μmol m^{-2} s^{-1} during the day and air temperature was set at 25 °C throughout the experiment.

Treatment	Default	Stage 1	Stage 2	Stage 3	Stage 4	Stage 5	Note
[CO_2] (ppm)	400	800 P_{leaf}	600	400 P_{leaf}	300	200 P_{leaf}	Same day P_{pd} for all stages
RH (%)	55	75 P_{leaf}	65	55 P_{leaf}	45	35 P_{leaf}	Same day P_{pd} for all stages
Soil	W	W P_{pd}, P_{leaf}	NW P_{pd}	NW P_{pd}, P_{leaf}	NW P_{pd}	NW P_{pd}, P_{leaf}	Different P_{pd} for all stages
PAR (μmol m^{-2} s^{-1})	1000						Constant
T_{air} (°C)	25						Constant
Day time	8 am to 6pm						Constant

4.8.2 Table of traits for each tree

Table 4.S2: Traits for each tree. Top: vulnerability curves for root, stem, and leaf elements. The "B" and "C" are parameters of the Weibull function used to fit vulnerability curve data. Resistance partition is the resistance of each segment as a percentage of the whole plant resistance. The VCs were same for each tree. Below: tree-specific traits. In the column "Note", C, D, and P denoted if the tree was used in the CO_2, RH, and drought treatment, respectively.

Vulnerability Curves:

	B	C	Resistance Partition
Root	1.879	2.396	53.7%
Stem	2.238	9.380	24.3%
Leaf	1.897	2.203	22.0%

Traits for each individual:

Tree	Note	Root K_{max}	Stem K_{max}	Leaf K_{max}	K_{max}	V_{cmax}	J_{max}	LaBa
		kg h^{-1} MPa^{-1} m^{-2}				μmol m^{-2} s^{-1}		
1	CD	2589.516	5725.834	6304.174	1389.961	54.947	107.505	5663
2	CDP	3478.758	7692.092	8469.033	1867.275	69.840	128.280	5663
3	C	1043.779	2307.963	2541.080	560.264	59.719	104.973	2648
4	CP	2893.333	6397.621	7043.815	1553.039	64.618	118.730	5663
5	C	1451.979	3210.557	3534.840	779.371	50.968	68.376	2648
6	CP	2241.282	4955.832	5456.397	1203.041	96.578	202.987	5663
7	D	2161.774	4780.028	5262.836	1160.364	12.794	24.004	2648
8	DP	2494.907	5516.638	6073.847	1339.178	67.316	126.116	5663
9	DP	2055.616	4545.295	5004.394	1103.382	65.145	122.198	5663
10	DP	1869.949	4134.758	4552.390	1003.723	75.456	141.540	5663

4.8.3 Example of tree response to the environment

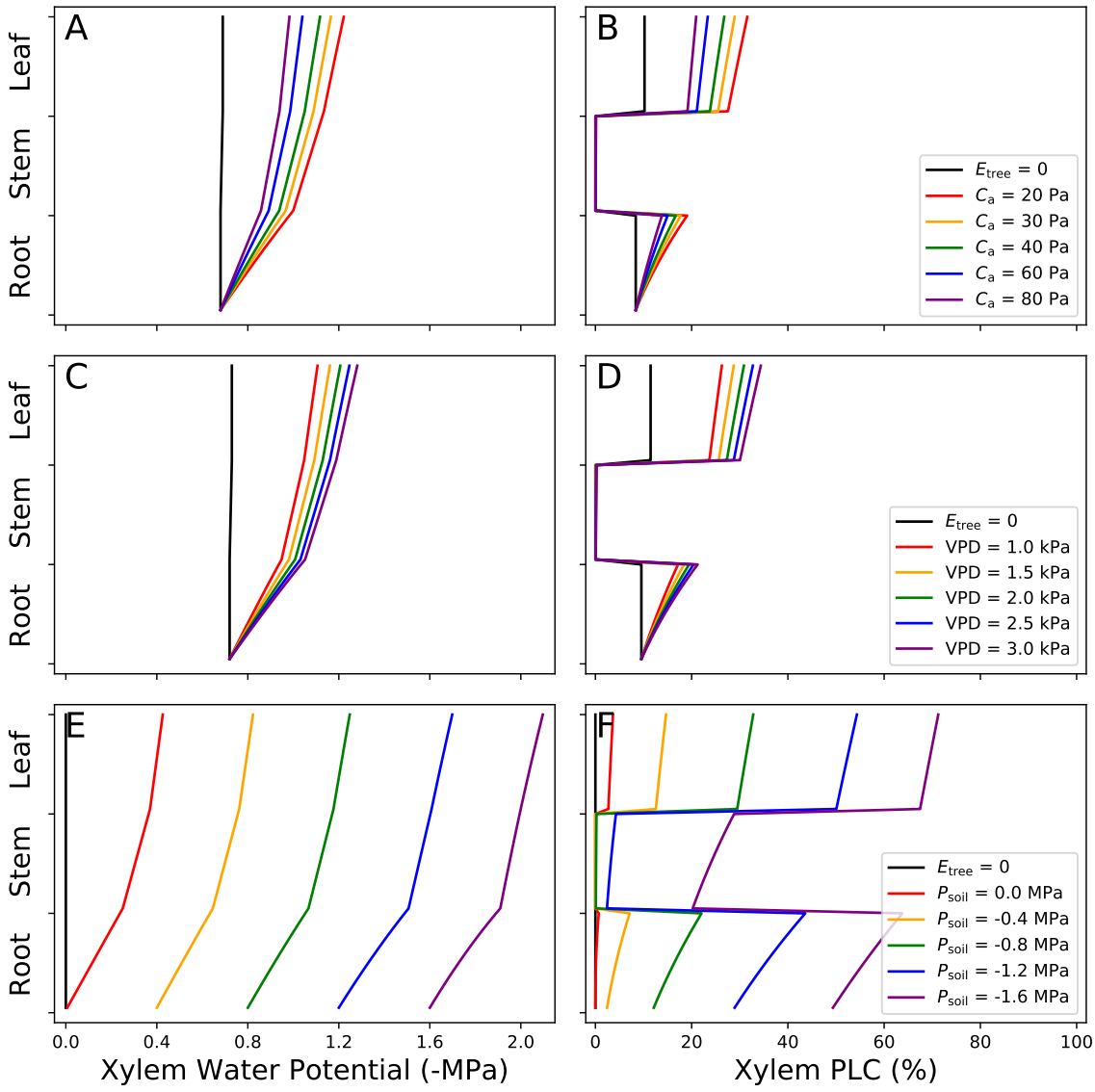

Figure 4.S1: Xylem water potential (P_x) and percentage loss of conductance (PLC) in root, stem, and leaf at different environmental conditions. Panel A and B: responses of P_x and PLC to atmospheric [CO_2] at a soil water potential of -0.68 MPa (mean value for six trees). Panel C and D: responses to atmosphere vapor pressure deficit (VPD) for a soil water potential of -0.72 MPa (mean value for six trees). Panel E and F: responses to soil water potential. The black line in each panel represents when whole tree transpiration is 0 meaning only gravity governs the xylem water potential drop. Vulnerability curve parameters of root, stem, and leaf are from Table 4.S1. The K_{max}, V_{cmax}, J_{max}, and LaBa are the average values of the ten trees from Table 4.S1. Stem height is set to 1 m.

4.8.4 Correlation of V_{cmax} and J_{max}

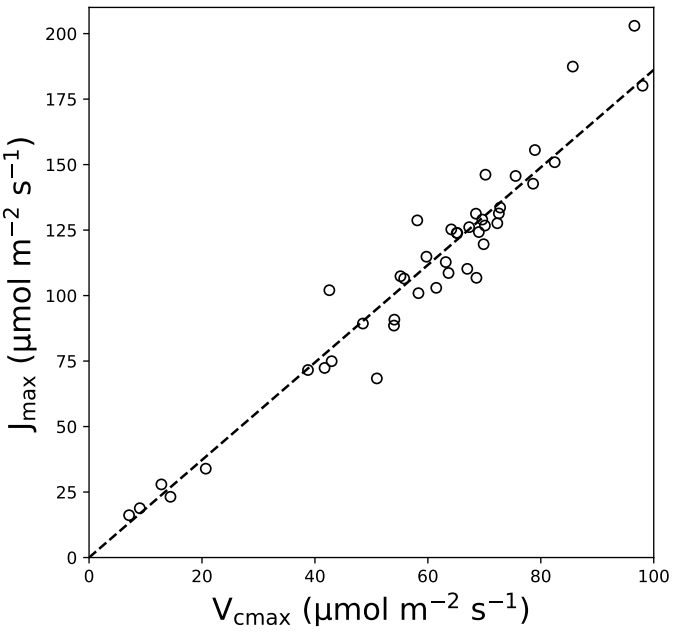

Figure 4.S2: Correlation between maximal carboxylation rate at 25 °C (V_{cmax}) and maximal electron transport at 25 °C (J_{max}). The dashed line plots the linear regression ($y = 1.86x$, R^2 = 0.992).

CHAPTER 5

A CANOPY PROFIT MAXIMIZATION MODEL IDENTIFIES MAJOR DRIVERS FOR OPTIMAL LEAF INVESTMENT AND PREDICTS CONSERVED C_I/C_A RATIO AND REALISTIC SPATIAL PATTERNS OF GREENNESS IN UNITED STATES

5.1 Summary

Leaf area and photosynthetic capacity are very plastic traits and presumably coordinate with other less plastic physiological traits to maximize the fitness of trees in a highly variable environment. However, quantifying the trade-offs involved in optimal leaf investment is challenging. Based on recent advances in trait-based optimal stomatal control models, we proposed a canopy profit maximization model that optimizes leaf area and photosynthetic capacity simultaneously. We evaluated how the less plastic plant traits, including hydraulic safety and efficiency, leaf traits, root zone water supply, and environmental conditions, impact optimal leaf investment. Our model predicted that, besides the environment, leaf construction costs and root depth are key traits that drive optimal leaf investment. However, out of these important environmental and physiological variables, only leaf construction costs impacted optimal leaf photosynthetic capacity. Our model also predicted conserved C_i/C_a ratio (C_i: leaf internal [CO_2], C_a: atmospheric [CO_2]) within each different tested site, agreeing with typically observed C_i/C_a homeostasis. The C_i/C_a conservation disappeared across habitats, probably due to unrealistically constant traits used for every site. The optimal leaf investment model further showed great potential in predicting spatial greenness patterns in the United States. Last, we highlighted the knowledge gaps that need to be filled to better understand and model how trees optimize leaf investment mechanistically.

- **Keywords**: gas exchange, leaf area, construction cost, optimization model,

photosynthetic capacity, root depth, traits

5.2 Introduction

Current earth system models struggle to predict similar and reliable magnitudes of climate change and its impact (Anav et al., 2013; Arora et al., 2013; Jones et al., 2013). The divergent model predictions are mainly due to the highly uncertain land surface component, which is also the biggest carbon sink for the last two decades (Beer et al., 2010; Quéré et al., 2018). The uncertainty arises partly from highly variable environmental factors that are boundary conditions for land surface models (LSMs), for example, soil moisture (Powell et al., 2013; Trugman, Medvigy, et al., 2018). Another problem with current LSMs is that they use a statistical regression-based approach to model terrestrial carbon and water fluxes (Walker, Hanson, et al., 2014). There is no guarantee that regression parameters from the past will apply to a climatically different future. One way to improve the LSMs is to incorporate a physiology-based model of plant gas exchange which can account for the acclimation of plant traits spatially and temporally (e.g., Sperry et al., 2019).

Leaf area (LA) and leaf photosynthetic capacity are two highly plastic traits that exhibit intraspecific acclimation and have a great impact on CO_2 and H_2O fluxes (Pettorelli et al., 2005). Leaf photosynthetic capacity is often represented by maximal carboxylation rate and maximal electron transport at 25 °C (V_{cmax} and J_{max}, respectively). The V_{cmax} and J_{max} are coupled (Medlyn et al., 2002; Wang et al., 2019), and thus we use V_{cmax} as the proxy for leaf photosynthetic capacity in this study. In theory, plants ought to optimize LA and V_{cmax} depending on both other less plastic (more species-specific) plant traits (Santiago et al., 2004) and the local environment (Trugman, Anderegg, Wolfe, et al., 2019). However, due to the elusive understanding of how trees optimize leaf allocation, leaf investment is often modeled by empirical scaling relationships and sometimes arbitrary optimization assumptions (Trugman, Anderegg, Sperry, et al., 2019). The empirical or arbitrary parameterizations for modeling leaf investment are challenged by global climate change due to potential changes of both species-specific plant traits (Guswa, 2008; Zhou et al., 2016) and the environment (IPCC, 2014). Moreover, the predicted increasing drought frequency and severity impose threaten trees with greater mortality risk (Allen et al., 2010; Hartmann et al., 2015, 2013), potentially resulting in changes of forest composition and

stand density and further necessitating a mechanistic understanding and modeling of optimal leaf investment.

Mechanistic trait-based gas exchange models do not require empirical parameterizations and can realistically capture feedbacks between traits and responses (Mencuccini, Manzoni, & Christoffersen, 2019; Sperry et al., 2017; Wolf et al., 2016). Such models are an ideal platform for exploring the acclimation of leaf investment. These trait-based models perform well in predicting stomatal behavior, especially under drought and elevated CO_2 (Anderegg et al., 2018; Venturas et al., 2018; Wang et al., 2019). They also enable modeling shift of optimal leaf investment because changes in species-specific traits feed back to water use strategy in these models, which is not possible in a strictly regression-based model. For instance, if water availability becomes more limiting, the species will reduce its LA to save water (Trugman, Anderegg, Sperry, et al., 2019), and the lower LA impacts the stomatal behavior because the water supply to each leaf increases. In contrast, regression-based models cannot capture this change in water use strategy because the plasticity of plant traits like LA does not play a role in these regression parameters (Ball et al., 1987; Leuning, 1995; Medlyn et al., 2011).

Models usually optimize LA and V_{cmax} separately due to a gap in understanding how the two traits coordinate. As a result, optimal LA or V_{cmax} obtained is a local optimum other than a global optimization of the two. The main reason for optimizing LA and V_{cmax} separately is that the optimizations operate at different scales, typically with LA at tree level (Trugman, Detto, et al., 2018) and V_{cmax} at leaf level (Quebbeman & Ramirez, 2016; Smith et al., 2019). To force coordination between the two, Sperry et al. (2019) assumed that leaves maintain an average C_i/C_a ratio of 0.7 under favorable conditions (C_i is the [CO_2] in the leaf and C_a is the atmospheric [CO_2]), an assumption that constrains the set of LA + V_{cmax} combinations. From this set, the authors selected a single optimal combination that maximized the return on leaf investment. The Sperry et al. (2019) model predicted realistic LA + V_{cmax} combination but also highlighted a question that has puzzled gas exchange researchers for years: why is C_i/C_a ratio conserved? Moreover, species-specific traits such as xylem vulnerability to drought and root depth (Trugman, Anderegg, Wolfe, et al., 2019; Venturas et al., 2017) may also have a great impact on leaf investment and are subject to change with the environment. Yet, how plant traits coordinate to optimize leaf investment

has not been well understood and requires a more in-depth investigation.

Here, we advance the trait-based tree model to optimize LA and V_{cmax} simultaneously by maximizing the return on leaf investment without additional constraints such as a conservative C_i/C_a ratio. We use our model to answer the following questions: (1) How does leaf investment depend on species-specific traits which may be assumed to be less plastic? (2) How does leaf investment within a given species depend on the environment? (3) Is the C_i/C_a ratio conserved across species and the environment? If yes, why? (4) How well does the optimization theory perform in predicting leaf investment? (5) What knowledge gaps need to be filled to gain a better understanding of leaf investment?

5.3 Materials and Methods

5.3.1 Canopy profit maximization hypothesis

We hypothesized that a tree maximizes its growing season canopy profit (GCP, normalized per basal area, BA; see Table 5.1 for symbols' descriptions). The GCP is the difference between canopy net primary productivity per BA (CNPP) and leaf construction costs per BA (LCC):

$$\max(\text{GCP}) = \max(\text{CNPP} - \text{LCC}). \tag{5.1}$$

We did not account for stem and root respiration rates because root and stem biomass were held constant in our simulations, and their respiration rates neither influence nor are influenced by leaf investment. We maximized GCP rather than CNPP because investment into leaves (i.e., LCC) represents the one-time investment for building leaves and is irreversible. The CNPP throughout a growing season was computed using

$$\text{CNPP} = \frac{\text{LA}}{\text{BA}} \cdot \int (A(t) - R(t)) \cdot \mathrm{d}t, \tag{5.2}$$

where $A(t)$ and $R(t)$ are average gross photosynthetic rate and leaf respiration rate per LA at time t, respectively. The one-time investment LCC consists of costs for leaf carbon biomass (LCBM, Poorter et al., 2006) and nutrient supply (NS, Evans & Clarke, 2019):

$$\text{LCC} = \text{LCBM} + \text{NS}. \tag{5.3}$$

Note that both LCBM and NS are one-time costs but are amortized over the leaf life span (T_{LL}), and the continued respiration costs after building the leaves are part of CNPP

as described in equation 5.1. For simplicity, we assumed that (1) trees grow leaves to maintain LA at the beginning of a growing season and all the leaves have the same V_{cmax}, (2) throughout the growing season, LA and V_{cmax} stay constant, and (3) when aged leaves drop, new leaves grow immediately to maintain the constant LA.

The LCBM compromises only the carbon part of organic matter in leaves (i.e., the carbohydrates such as fibers and noncarbohydrates such as proteins). The inorganic matter such as minerals and other nutrients in the noncarbohydrates such as N and P are not part of LCBM, and the energy paid for these nutrients belongs to NS. The LCBM is proportional to LA per BA:

$$\mathrm{LCBM} = \mathrm{invest_C} \cdot \frac{\mathrm{LA}}{\mathrm{BA}}, \tag{5.4}$$

where $\mathrm{invest_C}$ is a constant biomass cost factor. It should be noted that there is an exchange rate between leaf dry mass and fixed CO_2 by the leaves (e.g., 1 gram of carbohydrate translates to $1/30$ mole of CO_2). Further, the LCBM accounts for all the leaf carbon biomass costs in the growing season with length T_{GS}, and hence is proportional to $T_{\mathrm{GS}}/T_{\mathrm{LL}}$. Thus, the $\mathrm{invest_C}$ is related to leaf dry mass per area (LMA), T_{LL}, and T_{GS}:

$$\mathrm{invest_C} = f_{\mathrm{MC}} \cdot \mathrm{LMA} \cdot \frac{T_{\mathrm{GS}}}{T_{\mathrm{LL}}}, \tag{5.5}$$

where f_{MC} converts leaf mass to equivalent moles of fixed CO_2. The f_{MC} depends on organic matter contents of leaves. To simplify the modeling, we used the final term "$\mathrm{invest_C}$" in the present study rather than f_{MC}, LMA, T_{LL}, and T_{GS} as in equation 5.5.

The NS includes energy paid for taking up nutrients from the soil and transporting them to the leaves, and metabolic costs for assembling the organic matter. The difference between LCBM and NS in our model is that fixed CO_2 is used as material for LCBM but as consumable (energy) for NS. Similar to LCBM, NS is proportional to LA:BA and nutrient content per LA (N_{N}):

$$\mathrm{NS} = \mathrm{invest_N} \cdot N_{\mathrm{N}} \cdot \frac{\mathrm{LA}}{\mathrm{BA}}, \tag{5.6}$$

where $\mathrm{invest_N}$ is the carbon cost factor per N_{N}. Though the nutrients include all chemical elements except for H, C, and O, we used the nitrogen content as a proxy for N_{N} in the present study. Concerning leaf life span, $\mathrm{invest_N}$ is also proportional to $T_{\mathrm{GS}}/T_{\mathrm{LL}}$:

$$\text{invest}_{\text{N}} = f_{\text{NC}} \cdot \frac{T_{\text{GS}}}{T_{\text{LL}}}, \tag{5.7}$$

where f_{NC} converts N_{N} to equivalent moles of fixed CO_2. Due to the difficulty to quantify NS, models often neglect it (e.g., Sperry et al., 2019; Trugman, Detto, et al., 2018). However, a separate NS term from LCBM is necessary to produce realistic leaf investment patterns at varying soil nutrient availability. To simplify the modeling, we used the final term "invest_{N}" in the present study rather than f_{NC}, T_{LL}, and T_{GS} as in equation 5.7.

We estimated N_{N} from V_{cmax}, assuming the total nutrients are related to the nitrogen content of photosynthetic machinery. We modeled J_{max} using $J_{\text{max}} = 1.67 \cdot V_{\text{cmax}}$ Medlyn et al. (2002), and thus J_{max} did not impact N_{N} V_{cmax} correlation in our model. An advantage of linking N_{N} and V_{cmax} is that all costs related to nutrients (NS and $R(t)$) can be directly computed from V_{cmax}. Importantly, we assumed a nonlinear correlation between N_{N} and V_{cmax}, which tends to saturate at an upper limit (V_{limit}; Grassi & Bagnaresi, 2001; Manter et al., 2005; Simioni et al., 2004). This saturation results from ever-greater self-shading and resistance to intracellular liquid-phase CO_2 diffusion as more chloroplasts are added to leaf cells (more N_{N}). In reality, plants seldom achieve a V_{cmax} higher than 120 μmol CO_2 m^{-2} s^{-1} (Smith et al., 2019). Thus, we incorporated an arbitrarily nonlinear correlation between V_{cmax} and N_{N}:

$$N_{\text{N}} = \frac{V_{\text{cmax}} + V_{\text{limit}} \cdot \log\left(\frac{V_{\text{limit}}}{V_{\text{limit}} - V_{\text{cmax}}}\right)}{2}, \tag{5.8}$$

and N_{N} increased exponentially with V_{cmax} when approaching V_{limit}. The V_{limit} ought to vary with species (depending on leaf thickness, light exposure, leaf orientation, etc.). We used a default V_{limit} = 100 μmol CO_2 m^{-2} s^{-1} in our model.

Like Sperry et al. (2019), we modeled mature trees where trunk diameters and canopy heights were constant along with the constant biomass of root and stem systems. The optimal leaf investment was calculated by varying LA and V_{cmax} independently and finding the optimal combination that maximized GCP. The computation of CNPP is detailed in the next Section. A full version of the model written in Julia (1.2.0, NumFocus) is available at https://github.com/Yujie-WANG/Published-Codes-Yujie-WANG.

5.3.2 Tree model

We used a trait-based tree model to calculate CNPP. All model variables had environmental or physiological identities (see Table 5.1), so we could optimize (acclimate) LA:BA and V_{cmax} within a given set of less plastic species-specific traits for a given environment. We did not allow the species-specific traits to vary within a growing season, and the impacts from varying these traits were tested below. The tree model resembles the Sperry model (Sperry et al., 2017; Venturas et al., 2018) in most details, so here we only highlight the differences.

Briefly, starting from 1:00 AM on the first day of a growing season, we computed hourly net CO_2 assimilation rate, $A(t) - R(t)$, assuming gas exchange was at steady state. If the zenith angle was higher than 85 ° (before sunrise and after sunset) or the photosynthetically active radiation was below 10 μmol m^{-2} s^{-1}, we treated the period as "night" time, but "day" time otherwise. During the "night," we did not partition tree canopy to different layer and computed leaf temperature for the whole canopy, assuming no nighttime transpiration due to a lack of mechanistic understanding (Yu et al., 2019). Leaf respiration at night (R_{night}) was computed as a function of leaf temperature and V_{cmax} (Sperry et al., 2017) and scaled to give the canopy respiration.

During the "day," we partitioned the hemispherical tree canopy to a sunlit layer and a shade layer based on the zenith angle and leaf area index (LAI = LA:GA (ground area) in our model, Campbell & Norman, 1998). The LA was portioned to LA_{sl} and LA_{sh}, where subscripts "sl" and "sh" represent sunlit and shade layer, respectively. Leaf temperatures and net assimilation rates (A_{sl} and A_{sh}) were computed from the transpiration rate for each layer with the classic photosynthesis model (Farquhar et al., 1980).

To better estimate the photosynthetic rate at low leaf diffusive conductance (G_H for H_2O and G_C for CO_2), we incorporated a dynamic intercellular airspace limitation to photosynthesis (IAL). Usually, G_C is computed using $G_H/1.6$, where the constant 1.6 converts diffusion coefficients of CO_2 and H_2O in air. This conversion ($G_C = G_H/1.6$) accounts for CO_2 diffusion from air to substomatal cavity, but neglects the extra CO_2 diffusion in gas-phase through the intercellular airspace and in liquid-phase to the chloroplasts. Due to limited quantitative knowledge of liquid-phase diffusion, we only mechanistically modeled the gas-phase component (i.e., IAL). The IAL varies with leaf

anatomical traits (such as intercellular air fraction, stomatal frequency, lower epidermis thickness, and spongy mesophyll thickness) and scales with G_H (Chapter 2; Wang et al., in review). With minor modification to the classic photosynthesis model, we modeled IAL as a correction factor between G_C versus G_H correlation via two species-specific parameters depending on leaf anatomy—con (default at 0.65) and pow (default at 0.37). The IAL-corrected correlation takes the following form:

$$G_C = \frac{G_H}{1.6 \cdot (\text{con} \cdot G_H^{\text{pow}})}, \tag{5.9}$$

where the constant 1 represents stomatal limitation to CO_2 diffusion form air to substomatal cavity, and $\text{con} \cdot G_H^{\text{pow}}$ represents IAL relative to stomatal limitation. Note that as we accounted for the IAL, the V_{cmax} used in our model represents the apparent value at palisade cell walls rather than at substomatal cavity as is typically done (Niinemets et al., 2009). Though an apparent V_{cmax} at palisade cell walls is still not the true photosynthetic capacity in the chloroplasts (Knauer et al., 2020), it allows us to mechanistically account for the intercellular limitation, whereas the apparent V_{cmax} at substomatal cavity cannot.

Further, we did not allow G_H being higher than its physiological limit (Sperry & Love, 2015; Sperry et al., 2016):

$$G_H \leq G_{max} \cdot \left(\frac{273.15 + \frac{T_{air} + T_{leaf}}{2}}{298.15} \right)^{1.8}, \tag{5.10}$$

where G_{max} is the maximal G_H when stomata are fully open at 25 °C (default at 0.8mol m^{-2} s^{-1}), T_{air} and T_{leaf} are air and leaf temperature in °C, and the power term after G_{max} corrects for the temperature effect on the diffusive coefficient of H_2O vapor in air (Nobel, 2009). The G_{max} results from leaf anatomical traits and is mainly driven by guard cell dimensions, stomatal frequency, and lower epidermis thickness (Franks & Beerling, 2009). We highlighted IAL and G_{max} because they may significantly influence leaf gas exchange efficiency.

We used a recently developed stomatal control model (Chapter 3; Wang et al., in review) to model optimal stomatal behavior. The Wang model posits that a plant maximizes the difference between instantaneous photosynthesis (i.e., A) and the penalty (Θ) associated with the stomatal opening ($\Theta = A \cdot \frac{E}{E_{crit}}$):

$$\max\left(A \cdot \left(1 - \frac{E}{E_{\text{crit}}}\right)\right), \tag{5.11}$$

where E is tree transpiration rate, and E_{crit} is the maximal E allowed by hydraulic transport capacity. The Wang model differs with the Sperry model (Sperry et al., 2017) in that the Sperry model defines the penalty as $\Theta = A_{\max} \cdot \left(1 - \frac{K}{K_{\max}}\right)$, where $A_{\max}$ is the maximal A while ranging E from 0 to E_{crit}, K is the soil-plant hydraulic conductance, and $K_{\max}$ is the maximal K when E = 0. The Wang model has been tested with three datasets (Anderegg et al., 2018; Venturas et al., 2018; Wang et al., 2019) and performs equally well as the Sperry model while being computationally more efficient (Chapter 3; Wang et al., in review). Furthermore, we expanded equation 5.11 to optimize transpiration partition between sunlit and shade layers:

$$\max\left((\text{LA}_{\text{sl}} \cdot A_{\text{sl}} + \text{LA}_{\text{sh}} \cdot A_{\text{sh}}) \cdot \left(1 - \frac{E_{\text{sl}} + E_{\text{sh}}}{E_{\text{crit}}}\right)\right), \tag{5.12}$$

where E_{sl} and E_{sh} are transpiration rates of sunlit and shade layers, respectively. For each realistic combination of E_{sl} and E_{sh} (not violating equation 5.10), we computed G_{H} for each layer with $G_{\text{H,sl}} = \frac{E_{\text{sl}}}{\text{LA}_{\text{sl}} \cdot D_{\text{sl}}}$ and $G_{\text{H,sh}} = \frac{E_{\text{sh}}}{\text{LA}_{\text{sh}} \cdot D_{\text{sh}}}$ (D is leaf-to-air vapor pressure deficit relative to atmospheric pressure for each layer depending on leaf temperature), G_{C} with equation 5.9, and A_{sl} and A_{sh} from the Farquhar et al. (1980) photosynthesis model. By varying E_{sl} and E_{sh} independently, we found optimal E_{sl} and E_{sh} combination that maximized equation 5.12. An example of this optimal partition can be found in Supporting Information. The canopy net CO_2 assimilation rate was given as $\text{LA}_{\text{sl}} \cdot A_{\text{sl}} + \text{LA}_{\text{sh}} \cdot A_{\text{sh}}$.

To simplify the root zone water budget, we assumed a one-layer root system with a depth of H_{root}, and the soil within the rooting depth was at its field capacity at the beginning of a growing season. We also assumed that the xylem was fully functional at the beginning of a growing season. Each of root, stem, and leaf was divided into 20 elements, and each element had its "memory" of previous drought history as a result of xylem cavitation (Anderegg et al., 2015; Sperry & Tyree, 1988). At each hourly time step, we calculated the optimal transpiration rate and xylem pressure profile in the tree (including the impact from gravity). If xylem pressure got more negative than the "memory" of each element, the "memory" was updated. The drought "memory" influenced future gas exchange via altering E_{crit} of the tree (equation 5.12). After each time step, we updated the soil water

storage based on tree transpiration, soil evaporation, and precipitation during that hour. Throughout the growing season, we did not allow xylem refilling or growth, so the drought legacy persisted till the end of the growing season (24:00 PM of the last day). We calculated CNPP using

$$\mathrm{CNPP} = \frac{1}{\mathrm{BA}} \cdot \left(\int_{\mathrm{day}} \left(\mathrm{LA_{sl}} \cdot A_{\mathrm{sl}} + \mathrm{LA_{sh}} \cdot A_{\mathrm{sh}} \right) - \int_{\mathrm{night}} \left(\mathrm{LA} \cdot R_{\mathrm{night}} \right) \right). \tag{5.13}$$

For each simulation of a growing season, at optimal LA and V_{cmax} we also calculated GCP (equation 5.1) and photosynthetically weighted growing season $C_{\mathrm{i}}/C_{\mathrm{a}}$ ratio:

$$\frac{C_{\mathrm{i}}}{C_{\mathrm{a}}} = \frac{\int_{\mathrm{day}} \left(\mathrm{LA_{sl}} \cdot A_{\mathrm{sl}} \cdot \frac{C_{\mathrm{i,sl}}}{C_{\mathrm{a}}} + \mathrm{LA_{sh}} \cdot A_{\mathrm{sh}} \cdot \frac{C_{\mathrm{i,sh}}}{c_{\mathrm{a}}} \right)}{\int_{\mathrm{day}} \left(\mathrm{LA_{sl}} \cdot A_{\mathrm{sl}} + \mathrm{LA_{sh}} \cdot A_{\mathrm{sh}} \right)} \tag{5.14}$$

where $C_{\mathrm{i,sl}}$ and $C_{\mathrm{i,sl}}$ are C_{i} for sunlit and shade layers, respectively. This weighted $C_{\mathrm{i}}/C_{\mathrm{a}}$ ratio ought to be more representative of carbon discrimination recorded in stem or leaf than a nonweighted average.

5.3.3 Weather and soil data

Default weather conditions were hourly weather data for 35 consecutive years (1971 to 2005) at Flagstaff, Arizona, USA (data from Sperry et al., 2019). The mean annual precipitation at this site averaged 575 mm and supported an extensive forest of *Pinus ponderosa* and *Populus tremuloides*. The mean annual temperature was 7.7 °C. The default CO_2 concentration was set to 400 ppm. The 35-year weather data were intended to represent realistic interannual variations, to which trees would acclimate over the long term. To obtain the long-term optimal investment, we used the 35-year average of optimal investment determined for each individual year. The default weather data were altered as described below to determine the influence of climate parameters on long-term optimal leaf investment.

We used a soil texture of clay loam for this site and held it constant during the simulations. As we assumed soil was at its field capacity at the beginning of each growing season, the total amount of water available was the sum of soil water and growing season precipitation. The H_{root} and GA:BA in our model determined water availability from nongrowing season precipitation via root zone soil volume, and GA:BA determined that

from growing season precipitation. For each simulation of optimal leaf investment, H_{root} and GA:BA were held constant, and hence the soil water plus precipitation was constant for each simulation.

5.3.4 Influence of species-specific traits and environment on optimal leaf investment

We conducted a sensitivity analysis to determine how long-term acclimation of optimal leaf investment (the 35-year mean) depended on settings for what we assumed to be less plastic and more species-specific traits, including plant hydraulic traits and leaf traits besides photosynthetic capacity and LA:BA. For a given set of species-specific traits, we also determined how the acclimation to optimal leaf investment depended on environmental factors, including water availability and atmospheric conditions. For this sensitivity analysis, we varied only one species-specific or environmental parameter (other than LA and V_{cmax}) while holding all other parameters at defaults. We solved for the optimal LA + V_{cmax} combination and computed GCP and growing season C_i/C_a ratio assuming optimal LA + V_{cmax} for the given weather record. To evaluate any dependency of the sensitivity analysis on the default Flagstaff weather data, we repeated the analysis for weather data from three other sites of contrasting climate, and the sites were Durango (wetter and cooler, Colorado), Hattiesburg (wetter and warmer, Mississippi), and Trinity (drier and warmer, California). See Sperry et al. (2019) and supporting information about these sites.

5.3.4.1 Plant hydraulic traits

The safety and efficiency of trees are typically described by a Weibull function $k = k_{max} \cdot \exp\left(-\left(-\frac{P}{B}\right)^C\right)$, where k is the hydraulic conductance for an element at xylem pressure of P, k_{max} is the maximal hydraulic conductance when there is no cavitation in the xylem (efficiency), and B and C are Weibull parameters that describe xylem resistance to cavitation (safety). The soil-plant hydraulic conductance per BA (i.e., K) was affected by k (note that K included a rhizosphere component besides the plant vascular system, Sperry et al., 1998, 2016). Higher B, C, and k each meant more resistant (safer) to drought, more sensitive to drought, and more hydraulically conductive, respectively. We used uniform B and C for root, stem, and leaf without segmenting them (Sperry et al., 2016). We used different maximal hydraulic conductance of root (k_{root} per BA), stem (k_{stem} per

BA), and leaf (k_{sla} per LA), and kept the ratio of the three fixed (meaning the three changed simultaneously by the same magnitude). We varied each of B, C, and K (including k_{root}, k_{stem}, and k_{sla}) to 20%, 60%, 150%, and 200% of its default value, and determined how these settings influenced the long-term optimal LA and V_{cmax}. To test whether Weibull B and C impacted the optimal leaf investment, we tested the sensitivity to Weibull B at different Cs of 1 and 3 (default at 5). To examine whether wood and leaf had different impacts on optimal leaf investment, we also tested the scenario where only the wood (k_{root} and k_{stem}) or leaf partition (k_{sla}) was varied to 20%, 60%, 150%, and 200% of its default value.

5.3.4.2 Leaf traits

The evaluated leaf traits included leaf construction costs measured by $invest_C$ and $invest_N$, intercellular airspace limitation measured by IAL con (assuming pow constant at its default), and leaf maximal diffusive conductance G_{max}. A higher $invest_C$, $invest_N$, con, and G_{max} each meant more costs in leaf carbon, more costs in leaf nutrient supply, more limited intercellular resistance, and less limited leaf-level gas exchange. We varied each of $invest_C$, $invest_N$, con, and G_{max} to 20%, 60%, 150%, and 200% of its default value.

5.3.4.3 Water supply

Water supply to the plant in our model was represented by GA:BA and H_{root}. We varied GA:BA and H_{root} independently to 20%, 60%, 150%, and 200% of their default values (less to more water availability). Note that increasing GA:BA also resulted in better light availability for the trees and that increasing H_{root} also resulted in slightly more gravitational pressure drop in roots.

5.3.4.4 Environmental conditions

Climate change causes changes in all environmental conditions for trees, typically with drier air, higher air temperature, and elevated CO_2. However, changing any environmental condition inevitably results in a shift of the others, making it difficult to tease apart the impact of each environmental cue. Therefore, we arbitrarily modified the 35-year weather data by changing only one environmental condition at a time, and inspected how atmospheric vapor pressure deficit (VPD), air temperature, and atmospheric [CO_2] drive optimal leaf investment. Though the modified weather data were not realistic, they allowed

us to isolate the impact of each environmental cue. The VPD was varied to 60%, 80%, 120%, and 140% (wetter to drier air) of its hourly value while holding the air temperature (T_{air}) constant. The T_{air} was varied to -2, +2, +4, and +6 °C for each hourly value while holding the air relative humidity constant. The atmospheric [CO_2] was varied to 200, 300, 600, and 800 ppm.

5.3.5 Predicting continental-level optimal leaf investment

To better examine whether the model predicts realistic leaf investment patterns at the continental level, we further tested our model with more realistic climatic data from different sites in the lower 48 states of the United States. We evenly gridded the lower 48 states per 1 ° both latitudinally and longitudinally. The mean growing season temperature (MGST) ranged from 8 to 32 °C, and the mean growing season precipitation (MGSP) ranged from 10 to 1200 mm. For all grid locations, we extracted the 3-hour weather data from year 1978 to 2016 from 0.25 × 0.25 gridded weather (http://hydrology.princeton.edu/data/pgf/v3/0.25deg/3hourly/; Sheffield et al., 2006) and interpolated it to hourly data. Precipitation was obtained from the daily record and added at midnight (0:00 AM of the next day). We optimized LA:BA and V_{cmax} for each year of each site for our default setting (i.e., plant the same tree with the same density across the United States), and at the optimum we calculated GCP and growing season C_i/C_a.

5.4 Result

A unique global optimal LA + V_{cmax} combination that maximized GCP existed for each simulated growing season (an example of the optimum at the year 2005 shown in Fig. 5.1, white "+"). The trade-offs underlying this optimal pairing are best seen from the influence of one variable at a time. At a fixed photosynthetic capacity (represented by V_{cmax} and J_{max}), for example, V_{cmax} = 50 μmol CO_2 m^{-2} s^{-1}, increasing LA from zero initially caused GCP to increase because there was plenty of light and water available. However, if LA was increased too much, the GCP started to decrease because photosynthetic gains were compromised by self-shading and increasing leaf respiratory and construction costs. Alternatively, at a fixed LA:BA (e.g., 2000 m^2 m^{-2}), increasing V_{cmax} from zero caused GCP to increase because of the stimulation of photosynthesis. However, if V_{cmax} was increased

too much the GCP started to decline because respiration costs and nutrient supply costs began to increase faster than the gain in photosynthesis.

We would like to highlight that there was a very broad region where GCP was only slightly lower than the maximum (GCP $>$ 85% of the maximum), for example, the dark green region in Fig. 5.1, where LA:BA ranged from about 800 to 2100 $m^2\ m^{-2}$ and V_{cmax} ranged from 43 to 95 $\mu mol\ CO_2\ m^{-2}\ s^{-1}$. The weighted C_i/C_a in the region was also conserved from 0.70 to 0.77. When we plotted the rest 34 optima for different growing seasons at Flagstaff (the year 1971 to 2004), they all fell in this flat region (gray circles in Fig. 5.1). This suggested the average optimal leaf investment (mean of the scatters in Fig. 5.1) was able to capture the long-term acclimation to the environment.

5.4.1 Hydraulic traits

Plant hydraulic safety and efficiency traits had a minor impact on the optimal LA + V_{cmax} combination, C_i/C_a, and GCP (Fig. 5.2). When Weibull B varied from 60% to 200% of its default value, no significant change with optimal LA + V_{cmax} combination, C_i/C_a, or GCP was found (Fig. 5.2a,b). However, when Weibull B decreased to 20% of the default, 5.2 decreased by 6–7% whereas optimal LA did not change (red region in Fig. 5.2a), C_i/C_a decreased from 0.70 to 0.55, and GCP decreased by 26% (red symbols in Fig. 5.2b). When we varied Weibull B at a Weibull C of 1 and 3, we found similar patterns as Fig. 5.2a and 5.2b. When the Weibull C varied from 20% to 200% of the default value, no significant change for any of LA + V_{cmax} combination,C_i/C_a, or GCP was found (Fig. 5.2c,d). When k_{root}, k_{stem}, and k_{sla} all varied from 60% to 200% of their default values, no significant change in LA + V_{cmax} combination, C_i/C_a, or GCP was found (Fig. 5.2e,f). However, when k_{root}, k_{stem}, and k_{sla} all decreased to 20% of the default, optimal LA increased by about 10%, V_{cmax} decreased by about 6% (red region in Fig. 5.2e), C_i/C_a decreased from 0.70 to 0.61, and GCP decreased by about 17% (red symbols in Fig. 5.2f). When we varied only k_{root} and k_{stem}, optimal LA + V_{cmax} combination, C_i/C_a, and GCP were still insensitive to hydraulic conductance. When we varied only k_{sla}, optimal LA increased and V_{cmax} decreased when k_{sla} decreased to its 20%, suggesting the shift of LA + V_{cmax} at low hydraulic conductance in Fig. 5.2e was due to the leaf component. We found similar patterns at the other three sites (Durango, Hattiesburg, and Trinity, see Section 5.7.2).

5.4.2 Leaf traits

Optimal LA + V_{cmax} combination, C_i/C_a, and GCP were sensitive to the leaf traits tested (Fig. 5.3). When $invest_C$ increased from 20% to 200% of the default value, LA and V_{cmax} decreased significantly (Fig. 5.3a), C_i/C_a increased from 0.62 to 0.80 (Fig. 5.3b), and GCP decreased by more than 90% (Fig. 5.3b). When $invest_N$ increased from 20% to 200% of its default value, LA and V_{cmax} decreased significantly (Fig. 5.3c), C_i/C_a increased from 0.66 to 0.72 (Fig. 5.3d), and GCP decreased by about 32% (Fig. 5.3d). When IAL became more limiting (as con increased in equation 5.9), optimal LA did not change and V_{cmax} decreased slightly (Fig. 5.3e), whereas both C_i/C_a and GCP slightly decreased (Fig. 5.3f). A change in G_{max} had a minor impact on LA + V_{cmax} combination, C_i/C_a, or GCP, except for when G_{max} was low (0.16 mol m^{-2} s^{-1}, Fig. 5.3g,h). At the low G_{max}, LA increased (Fig. 5.3g), whereas V_{cmax}, C_i/C_a, and GCP decreased (Fig. 5.3h). We found similar patterns at the other three sites (Section 5.7.2).

5.4.3 Water supply

Plant water supply influenced optimal LA:BA, C_i/C_a, and GCP but had a minor impact on optimal V_{cmax} (Fig. 5.4). When GA:BA increased, optimal LA:BA increased (Fig. 5.4a), and GCP increased linearly (Fig. 5.4b) because higher GA:BA resulted in higher precipitation and light availability to the plant. However, optimal V_{cmax} and C_i/C_a were not sensitive to changes in GA:BA (Fig. 5.4a,b). When H_{root} was increased (giving the plant more access to stored soil water), the optimal LA:BA, C_i/C_a, and GCP increased (Fig. 5.4c,d), whereas optimal V_{cmax} was not sensitive (Fig. 5.4c). We found similar patterns at the other three sites (Section 5.7.2).

5.4.4 Environmental conditions

Environmental conditions, including atmospheric VPD, T_{air}, and [CO_2], had a great impact on optimal leaf investment. Drier air resulted in slightly lower LA and V_{cmax} (Fig. 5.5a), and lower GCP and growing season C_i/C_a (Fig. 5.5b). Higher T_{air} resulted in lower LA but no change in V_{cmax} (Fig. 5.5c), and slight lower GCP and C_i/C_a (Fig. 5.5d). A higher C_a increased optimal LA significantly and V_{cmax} less significantly compared to LA (Fig. 5.5e). The GCP increased at higher C_a, but C_i/C_a decreased (Fig. 5.5f). We found similar patterns at the other three sites (Section 5.7.2).

5.4.5 Conserved C_i/C_a ratio

The photosynthesis-weighted growing season C_i/C_a at optimal leaf investment was conserved for species at a given site. Take Flagstaff as an example, though with variations among growing seasons, the C_i/C_a ratio ranged from 0.62 to 0.75 and averaged 0.70 for the default 35-year weather data. Further, varying GA:BA (Fig. 5.4b), T_{air} (keeping RH unchanged, Fig. 5.5d), and C_a (Fig. 5.5f) did not influence much the C_i/C_a ratio. However, increasing VPD alone (keeping T_{air} unchanged) resulted decreased C_i/C_a, but C_i/C_a was still in the conserved range (Fig. 5.5b). Overall, for a given set of less plastic species-specific traits, optimal leaf investment of the more plastic LA:BA and V_{cmax} resulted in a conserved C_i/C_a for a given site. In comparison, optimal LA:BA and V_{cmax} showed much higher variation, with LA:BA ranged from 200 to 3000 $m^2\ m^{-2}$, and V_{cmax} from 60 to 100 $\mu mol\ CO_2\ m^{-2}\ s^{-1}$ (Fig. 5.2–5.5). Similar patterns were found in the other three sites (Section 5.7.2).

The C_i/C_a was sensitive to leaf construction costs and root depth (soil water supply), which impacted optimal leaf investment. In general, when soil water supply remained constant, C_i/C_a increased with lower LA:BA and lower V_{cmax} (Fig. 5.3b,d) because of better water supply and lower CO_2 demand. When soil water supply increased, C_i/C_a decreased with lower LA:BA as a result of water limitation (Fig. 5.4d). Further, more limited leaf intercellular airspace also decreased C_i/C_a even though LA:BA and V_{cmax} were not impacted (Fig. 5.3f).

The C_i/C_a conservation varied among different tested sites. Comparing to the conservative 0.60–0.80 range for Flagstaff, the C_i/C_a ratio was conserved at 0.63–0.82 for weather from Durango, 0.60–0.82 for Hattiesburg, and 0.50–0.70 for Trinity (Section 5.7.2). However, the nonconserved C_i/C_a ratio among sites did not bias the commonly assumed C_i/C_a homeostasis because we used identical traits for every site, and the more realistic species-specific traits ought to reduce the variation of C_i/C_a across habitats (see Discussion).

5.4.6 Prediction of continental-level leaf investment

Our model predicted realistic spatial patterns of leaf investment across the lower 48 states of the United States (Fig. 5.6). Our model predicted lower LA:BA for the climate in

Mountain west regions and highest LA:BA in the east (Fig. 5.6c), agreeing with the MGSP patterns (Fig. 5.6a). The optimal LA:BA increased with higher MGSP and decreased with higher MGST. The LA:BA patterns agreed with the spatial NDVI (normalized difference vegetation index) and EVI (enhanced vegetation index) patterns (MODIS, MOD13Q1 series data; Didan, 2015). As to optimal V_{cmax}, our model predicted lower V_{cmax} in Southeast and Mountain west (Fig. 5.6d), which was likely due to the higher temperature in these regions that caused higher respiratory costs (Fig. 5.6b). Optimal V_{cmax} decoupled with MGSP or MGST, and was highest in the region where MGSP ranged from 200 to 500 mm and MGST ranged from 15 to 20 °C. Our model also predicted a lower C_i/C_a ratio from 0.55 to 0.70 in the Mountain West region but a higher ratio from 0.70 to 0.86 in East United States (Fig. 5.6e). The C_i/C_a at optimal leaf investment increased with lower MGST and higher MGSP, a pattern found in carbon discrimination record (Cernusak et al., 2013; Prentice et al., 2014). Our model predicts a higher GCP in East United States and Pacific coastal but a lower GCP in Mountain West (Fig. 5.6f). The GCP at optimal leaf investment increased with MGSP but showed no obvious trend with MGST.

5.5 Discussion

For each growing season at a given site, there is a unique optimal LA:BA and V_{cmax} combination that maximizes return on leaf investment. Though optimal leaf investments vary for each growing season, they tend to fall into a conserved region where the return on investment does not differ much from the optima for that particular growing season (Fig. 5.1). To simplify the modeling of leaf investment, we assumed all other traits constant are species-specific and do not change in a growing season. According to our model, optimal leaf investment is influenced by both the species-specific traits, but is only sensitive leaf construction costs related traits (both invest_C and invest_N) and root depth among those tested. Leaf investment is also sensitive to environmental conditions. While optimal LA:BA is significantly impacted by all the listed important traits and environmental cues, optimal V_{cmax} is only sensitive to invest_C and invest_N, and slightly sensitive to atmospheric [CO_2]. The rest of the plant traits (including Weibull B and C, hydraulic conductance, IAL con, and G_{max}) have a minor impact on optimal LA:BA and V_{cmax}.

Species-specific traits and environmental conditions impact photosynthesis-weighted

growing season C_i/C_a ratio at optimal LA + V_{cmax}. Despite the impacts, the C_i/C_a ratio at a given site is often conserved (Fig. 5.2–5.5, Section 5.7.2), agreeing with typically observed homeostasis in C_i/C_a ratio across species and habitats (Voelker et al., 2016). Our results suggest that a conserved C_i/C_a ratio may be an evolutionary target for plants. However, it should be aware that nonoptimal LA + V_{cmax} combinations may also result in C_i/C_a in the conservative range, and thus research needs to constrain optimal LA + V_{cmax} combination with plant productivity rather than simply a conserved C_i/C_a ratio (as did by Trugman, Detto, et al. (2018), Sperry et al. (2019), and the present study).

Potential deficits with our analysis were that our default plant settings were not realistic for the changing environment and the sensitivity analysis was done by varying one particular trait at a time. However, it was necessary to do the sensitivity analysis in this unrealistic way to tease apart the major drivers for optimal leaf investment. Further, our results that optimal leaf investment is only sensitive to leaf construction costs and root depth narrows the problem to these particular traits. Despite using constant default plant traits for different regions in the lower 48 states of the United States, our model still predicted broadly realistic spatial patterns for leaf investment and C_i/C_a ratio, showing great potential of improving future projections of leaf investment. Below we discuss what needs to be done to better project leaf area both spatially and temporally.

5.5.1 Why leaf investment is not sensitive to plant hydraulics

Though plant hydraulic safety and efficiency traits are essential to many stomatal control models (Chapter 3; Anderegg et al., 2018; Sperry et al., 2017) and are important indicators of plant water stress (Venturas et al., 2018), these hydraulic traits were not found to materially influence optimal leaf investment unless the plant was very vulnerable to cavitation or inefficient in conducting water. It may be presumed that if a tree is more resistant to drought or conductive, it should put on more leaves. However, when the tree becomes more resistant while holding everything else constant including LA, the optimal water use will increase, for example, the risk in hydraulic integrity decreases as in the Sperry model (Sperry et al., 2017) and the E_{crit} increases as in equation 5.11 (Chapter 3; Wang et al., in review). Thus, for the same sized trees, a more resistant tree will drain the soil faster and obtain more photosynthesis at the beginning of the growing season, but photosynthesis will be lower

later in the season as soil is drier (examples of soil water content for different Bs at optimal LA + V_{cmax} in Supporting Information). Similarly, a more hydraulically efficient tree also drains the soil faster, and putting more leaves ought to make it worse (examples of soil water content for different Ks at optimal LA + V_{cmax} in Supporting Information). These tradeoffs may explain why optimal leaf investment is not sensitive to plant hydraulic traits in a given environment when other traits are constant.

This finding simplifies the modeling of optimal leaf investment projection because a -40% to $+100\%$ change in hydraulic traits has almost no impact on the optimal leaf investment. Though a recent meta-analysis suggests plant hydraulics as well as leaf economics drive leaf : wood area ratio (Mencuccini, Rosas, et al., 2019), it is likely due to the correlation between plant hydraulic conductance and leaf costs, which according to our model is the actual driver (Fig. 5.3). However, knowledge of how hydraulic safety and efficiency traits acclimate in the future is still crucial because these traits influence susceptibility to water stress and drought-induced mortality (Hammond et al., 2019; Venturas et al., 2018).

5.5.2 Difficult-to-measure key plant traits

Though our model highlights that the key plant trait drivers for optimal leaf investment are leaf construction costs and rooting depth, these are extremely difficult to measure. Therefore, mechanistically incorporating optimal leaf investment into gas exchange models and hence quantitatively predicting optimal leaf investment for novel environmental conditions are challenging. Here we analyze what can be done to fill the gaps in understanding optimal leaf investment.

The invest_C is relatively easier as most of the parameters involved have been widely reported, such as LMA, T_{GS}, and T_{LL}. However, it should be aware that LMA needs to be partitioned to organic and inorganic matter, the former of which needs to be further partitioned to carbohydrate and noncarbohydrates (equation 5.5). For simplicity, it can be assumed that all the noncarbohydrates are proteins, and then a unit mass of noncarbohydrates converts to n/M moles of equivalent CO_2, where n is the number of C elements and M is the molar weight of the average amino acid (Young & Pellett, 1994). Further, carbohydrate and noncarbohydrate contents will help resolve intra- and

interspecies variation.

The invest_N is harder to quantify due to the difficulty of isolating costs related to nutrient uptake, transport, and metabolism and correlating the nutrients with V_{cmax}. There are two potential sources of nitrogen supply to leaves: stored nitrogen in the tree and free nitrogen in the soil (including the N-fixers), and nutrient uptake costs are different for the two sources as the former is cheaper. Therefore, for a multiyear plant, nitrogen in the plant may be the greatest nitrogen source for leaves. In this scenario, the challenge is to partition the stored nitrogen to leaves, and invest_N will not be constant but dependent on LA unless there is sufficient nutrient supply. For smaller plants such as annuals, it is wise to assume little nitrogen storage and attribute all the nitrogen supply to the soil. As to the transport and metabolism, more research needs to be done to tease apart nutrient uptake related respiration from basic respiration. A great amount of work has been done to correlate leaf nitrogen content with V_{cmax}. Though most of these studies have tended to assume linear correlation between the two, a nonlinear correlation is often found as the intercept of linear regression is above zero (Clearwater & Meinzer, 2001; Crous et al., 2008; Han & Chiba, 2009; Ripullone et al., 2003; Walker, Beckerman, et al., 2014). Further, the upper limit (V_{limit}) ought to vary within and among species due to leaf anatomy, and we should not vary V_{cmax} or J_{max} freely from 0 to infinity for any species (e.g., equation 5.8).

Root depth and distribution are not often measured, despite its importance for plant water supply (Love et al., 2019; Sperry et al., 1998). In our model, we vary H_{root} solely while keeping other traits unchanged. However, in reality, more investment into H_{root} also means less to stem, and thus hydraulic conductance in the stem ought to decrease. This opens another optimization question, namely what is the optimal root and stem investment partition, which is beyond the scope of this study. However, as our model suggests that changes in root and stem hydraulic conductance have a minor impact on optimal leaf investment (Fig. 5.2), varying H_{root} alone would not result in much error. Better resolution of root profile (soil water supply) and its incorporation to large-scale modeling will advance the modeling of gas exchange (Fan, 2015; Fan et al., 2017, 2019).

Though optimal leaf investment is less sensitive to other traits like plant hydraulic traits, IAL con, and G_{max}, these traits do influence GCP and C_i/C_a ratio. Moreover, as all these traits are related to anatomy, it is very unlikely that these traits are independent of other

anatomy-related traits such as invest_C. For example, when leaf intercellular air fraction increases while other anatomical traits are held constant, leaf LMA and hence invest_C ought to decrease; and meanwhile, IAL con will be lower (Chapter 2; Wang et al., in review). Also, lower plant hydraulic efficiency is often coupled with higher costs in leaves (Mencuccini, Rosas, et al., 2019), because it is not necessary to build very efficient xylem when leaf water demand is low. Therefore, it is also essential to learn how plant traits coordinate with each other, especially those traits related to construction costs. Further, more complicating is how all these impacting traits change at different environmental conditions. Though research has to neglect or assume no change in these traits due to our current elusive understanding (Sperry et al., 2019; Trugman, Anderegg, Sperry, et al., 2019), more investigations to resolve these mysteries will advance the land surface models.

5.5.3 Model predictions and experimental observations

5.5.3.1 Drought

Our model predicts lower LA:BA but only a minor change in V_{cmax} with drier air (Fig. 5.5) or lower soil water supply (Fig. 5.4) while holding all other traits constant. The predicted lower LA:BA agrees with typical observations of lower LA (Trugman, Anderegg, Wolfe, et al., 2019; Yang et al., 2018). However, the predicted almost constant V_{cmax} confronts the often observed declining V_{cmax} for drought-stressed plants (Smith et al., 2019; Zhou et al., 2014, 2016). The possible reasons are (1) our model optimizes V_{cmax} for a whole growing season and does not allow it to vary in the growing season, and thus cannot predict a variable V_{cmax}, decreasing or increasing. (2) The V_{cmax} in our model represents the apparent value at palisade cell walls, whereas V_{cmax} reported is the apparent value at the substomatal cavity, which does not account for intercellular airspace limitation. In theory, when stomata close more, intercellular resistance increases (Chapter 2; Wang et al., in review), and the apparent V_{cmax} at the substomatal cavity would decrease (Knauer et al., 2020; Niinemets et al., 2009). Thus, it is possible that the V_{cmax} decline in these studies is due to IAL rather than a decline in real photosynthetic capacity (Zhou et al., 2014). (3) Increase in leaf construction costs will result in lower V_{cmax} (Fig. 5.3), and leaves tend to be more expensive during drought as LMA increases (Fernández & Reynolds, 2000; Poorter et al., 2009).

5.5.3.2 Elevated CO_2

Our model predicts higher LA:BA and V_{cmax} at elevated CO_2 (Fig. 5.5c). The predicted higher LA:BA corresponds with typically observed higher LA in the free-air CO_2 enrichment (FACE) experiments (Ainsworth & Long, 2005; Trugman, Anderegg, Wolfe, et al., 2019; Tyree & Alexander, 1993). The predicted slightly higher V_{cmax}, however, contrasts with the reported slightly lower V_{cmax} in these FACE experiments (Ainsworth et al., 2002; Ainsworth & Long, 2005). The disagreement in V_{cmax} suggests there must be increasing costs related to leaf construction (Fig. 5.3). Unfortunately, not all FACE experiments measured or reported the construction costs related parameters (e.g., LMA, T_{LL}, and nutrient availability). However, studies that did report these parameters support our hypothesis as higher LMA has been found in these FACE experiments (Ainsworth et al., 2002; Ainsworth & Long, 2005). Our model prediction of slightly higher V_{cmax} differs from the Sperry et al. (2019) model, which predicted slightly lower V_{cmax}. The reason is that our model constrains the optimum only by maximizing GCP, whereas the Sperry et al. (2019) model constrains the optimum by maximizing GCP at a constant C_i/C_a ratio for favorable reference conditions. As the C_i/C_a contours are hyperbolic shaped (dashed lines in Fig. 5.1), the Sperry et al. (2019) model tends to predict higher LA:BA but lower V_{cmax}, while our model allows V_{cmax} to vary independently. Though our model and the Sperry et al. (2019) model also differs in that we have a nutrient supply costs, the ever-greater NS at higher V_{cmax} tends to limit the increase of V_{cmax} in our model, and thus the different V_{cmax} trends between the models may result from different model constraints.

5.5.3.3 PAR

The light availability also has a great impact on optimal leaf investment as shaded leaves tend to have lower V_{cmax} (Anteb et al., 1996; Seemann et al., 1987; Yamori et al., 2010). Thus, our assumption that all leaves have the same V_{cmax}, though a shortcut for modeling leaf investment, neglects finer scale optimization within a tree among sunlit and shade leaves. A more detailed model concerning the light environment of individual leaves is required for this finer scale optimization. However, such a model would be computationally expensive and hence may not be practical for the forest level or beyond.

5.5.4 Is C_i/C_a ratio conserved?

Our model predicted conserved C_i/C_a ratio for a given site, and varying environmental conditions did not influence much the conservation (Fig. 5.4, 5.5, Section 5.7.2). The homeostasis in C_i/C_a, however, disappeared in the simulations across the lower 48 states of the United States (Fig. 5.6). This was because we used the same default traits combinations for all the grids. As the leaf construction costs are higher for drier environment (Fernández & Reynolds, 2000; Poorter et al., 2009), our model prediction tends to underestimate the C_i/C_a for drier areas but overestimate it for wetter areas. Thus, the C_i/C_a ratio ought to be more conserved than predicted in Fig. 5.6e. Knowledge of how the plant traits vary spatially will help address the C_i/C_a conservation more reliably.

5.5.5 Conclusion

Optimal leaf investment can be modeled with our canopy profit maximization model, and optimal LA:BA and V_{cmax} are coordinated in a conserved region for a given long-term climate. With the model, we conclude the following: (1) Optimal leaf investment is sensitive to leaf construction costs and root depth. (2) Optimal leaf investment is environmental conditions. (3) A conservative C_i/C_a ratio corresponds with the optimal LA:BA and V_{cmax} for a given site though the conservation varies among sites. (4) Optimal leaf investment model shows great potential predicting spatial patterns of leaf investment and is promising to predict optimal leaf investment temporally. (5) More research needs to be done to fill the gaps in how to quantify the key traits, how the traits coordinate, and how the traits acclimate to the environment.

5.6 References

Ainsworth, E. A., Davey, P. A., Bernacchi, C. J., Dermody, O. C., Heaton, E. A., Moore, D. J., … Long, S. P. (2002). A meta-analysis of elevated [CO_2] effects on soybean (*Glycine max*) physiology, growth and yield. *Global Change Biology*, *8*(8), 695–709.

Ainsworth, E. A., & Long, S. P. (2005). What have we learned from 15 years of free-air CO_2 enrichment (FACE)? A meta-analytic review of the responses of photosynthesis, canopy properties and plant production to rising CO_2. *New Phytologist*, *165*(2), 351–372.

Allen, C. D., Macalady, A. K., Chenchouni, H., Bachelet, D., McDowell, N., Vennetier, M., … Cobb, N. (2010). A global overview of drought and heat-induced tree mortality reveals emerging climate change risks for forests. *Forest Ecology and Management*, *259*(4), 660–684.

Anav, A., Friedlingstein, P., Kidston, M., Bopp, L., Ciais, P., Cox, P., ... Zhu, Z. (2013). Evaluating the land and ocean components of the global carbon cycle in the CMIP5 earth system models. *Journal of Climate*, *26*(18), 6801–6843.

Anderegg, W. R. L., Schwalm, C., Biondi, F., Camarero, J. J., Koch, G., Litvak, M., ... Pacala, S. (2015). Pervasive drought legacies in forest ecosystems and their implications for carbon cycle models. *Science*, *349*(6247), 528–532.

Anderegg, W. R. L., Wolf, A., Arango-Velez, A., Choat, B., Chmura, D. J., Jansen, S., ... Pacala, S. (2018). Woody plants optimise stomatal behaviour relative to hydraulic risk. *Ecology Letters*, *21*(7), 968–977.

Anteb, N. P. R., Hernandez, R., & Medina, E. M. (1996). The photosynthetic capacity and leaf Nitrogen concentration as related to light regime in shade leaves of a montane tropical forest tree, *Tetrochidium rubrivenium*. *Functional Ecology*, *10*, 491–500.

Arora, V. K., Boer, G. J., Friedlingstein, P., Eby, M., Jones, C. D., Christian, J. R., ... Wu, T. (2013). Carbon–concentration and carbon–climate feedbacks in CMIP5 earth system models. *Journal of Climate*, *26*(15), 5289–5314.

Ball, J. T., Woodrow, I. E., & Berry, J. A. (1987). A model predicting stomatal conductance and its contribution to the control of photosynthesis under different environmental conditions. In *Progress in photosynthesis research* (pp. 221–224). Springer.

Beer, C., Reichstein, M., Tomelleri, E., Ciais, P., Jung, M., Carvalhais, N., ... Papale, D. (2010). Terrestrial gross carbon dioxide uptake: Global distribution and covariation with climate. *Science*, *329*(5993), 834–838.

Campbell, G. S., & Norman, J. M. (1998). *An introduction to environmental biophysics*. Springer Science & Business Media.

Cernusak, L. A., Ubierna, N., Winter, K., Holtum, J. A. M., Marshall, J. D., & Farquhar, G. D. (2013). Environmental and physiological determinants of carbon isotope discrimination in terrestrial plants. *New Phytologist*, *200*(4), 950–965.

Clearwater, M. J., & Meinzer, F. C. (2001). Relationships between hydraulic architecture and leaf photosynthetic capacity in nitrogen-fertilized *Eucalyptus grandis* trees. *Tree Physiology*, *21*(10), 683–690.

Crous, K. Y., Walters, M. B., & Ellsworth, D. S. (2008). Elevated CO_2 concentration affects leaf photosynthesis–nitrogen relationships in *Pinus taeda* over nine years in FACE. *Tree Physiology*, *28*(4), 607–614.

Didan, K. (2015). MOD13Q1 MODIS/Terra vegetation indices 16-day L3 global 250m SIN grid V006. *NASA EOSDIS Land Processes DAAC*.

Evans, J. R., & Clarke, V. C. (2019). The nitrogen cost of photosynthesis. *Journal of Experimental Botany*, *70*(1), 7–15.

Fan, Y. (2015). Groundwater in the Earth's critical zone: Relevance to large-scale patterns and processes. *Water Resources Research*, *51*(5), 3052–3069.

Fan, Y., Clark, M., Lawrence, D. M., Swenson, S., Band, L. E., Brantley, S. L., ... Yamazaki, D.

(2019). Hillslope hydrology in global change research and earth system modeling. *Water Resources Research*, *55*(2), 1737–1772.

Fan, Y., Miguez-Macho, G., Jobbágy, E. G., Jackson, R. B., & Otero-Casal, C. (2017). Hydrologic regulation of plant rooting depth. *Proceedings of the National Academy of Sciences*, *114*(40), 10572–10577.

Farquhar, G. D., von Caemmerer, S., & Berry, J. A. (1980). A biochemical model of photosynthetic CO_2 assimilation in leaves of C_3 species. *Planta*, *149*(1), 78–90.

Fernández, R. J., & Reynolds, J. F. (2000). Potential growth and drought tolerance of eight desert grasses: Lack of a trade-off? *Oecologia*, *123*(1), 90–98.

Franks, P. J., & Beerling, D. J. (2009). Maximum leaf conductance driven by CO_2 effects on stomatal size and density over geologic time. *Proceedings of the National Academy of Sciences*, *106*(25), 10343–10347.

Grassi, G., & Bagnaresi, U. (2001). Foliar morphological and physiological plasticity in *Picea abies* and *Abies alba* saplings along a natural light gradient. *Tree Physiology*, *21*(12-13), 959–967.

Guswa, A. J. (2008). The influence of climate on root depth: A carbon cost-benefit analysis. *Water Resources Research*, *44*(2), W02427.

Hammond, W. M., Yu, K., Wilson, L. A., Will, R. E., Anderegg, W. R. L., & Adams, H. D. (2019). Dead or dying? Quantifying the point of no return from hydraulic failure in drought-induced tree mortality. *New Phytologist*, *223*, 1834–1843.

Han, Q., & Chiba, Y. (2009). Leaf photosynthetic responses and related nitrogen changes associated with crown reclosure after thinning in a young *Chamaecyparis obtusa* stand. *Journal of Forest Research*, *14*(6), 349–357.

Hartmann, H., Adams, H. D., Anderegg, W. R. L., Jansen, S., & Zeppel, M. J. B. (2015). Research frontiers in drought-induced tree mortality: Crossing scales and disciplines. *New Phytologist*, *205*(3), 965–969.

Hartmann, H., Ziegler, W., Kolle, O., & Trumbore, S. (2013). Thirst beats hunger–declining hydration during drought prevents carbon starvation in Norway spruce saplings. *New Phytologist*, *200*(2), 340–349.

IPCC. (2014). *Climate change 2014: Synthesis report. Contribution of working groups I, II and III to the fifth assessment report of the Intergovernmental Panel on Climate Change* (Core Writing Team, R. K. Pachauri, & L. A. Meyer, Eds.). IPCC, Geneva, Switzerland.

Jones, C., Robertson, E., Arora, V., Friedlingstein, P., Shevliakova, E., Bopp, L., … Tjiputra, J. (2013). Twenty-first-century compatible CO_2 emissions and airborne fraction simulated by CMIP5 earth system models under four representative concentration pathways. *Journal of Climate*, *26*(13), 4398–4413.

Knauer, J., Zaehle, S., De Kauwe, M. G., Haverd, V., Reichstein, M., & Sun, Y. (2020). Mesophyll conductance in land surface models: Effects on photosynthesis and transpiration. *The Plant Journal*, *101*(4), 858–873.

Leuning, R. (1995). A critical appraisal of a combined stomatal-photosynthesis model for C_3 plants. *Plant, Cell & Environment*, *18*(4), 339–355.

Love, D. M., Venturas, M. D., Sperry, J. S., Brooks, P. D., Pettit, J. L., Wang, Y., … Mackay, D. S. (2019). Dependence of aspen stands on a subsurface water subsidy: Implications for climate change impacts. *Water Resources Research*, *55*(3), 1833–1848.

Manter, D. K., Kavanagh, K. L., & Rose, C. L. (2005). Growth response of Douglas-fir seedlings to nitrogen fertilization: Importance of Rubisco activation state and respiration rates. *Tree Physiology*, *25*(8), 1015–1021.

Medlyn, B. E., Dreyer, E., Ellsworth, D., Forstreuter, M., Harley, P. C., Kirschbaum, M. U. F., … Loustau, D. (2002). Temperature response of parameters of a biochemically based model of photosynthesis. II. A review of experimental data. *Plant, Cell & Environment*, *25*(9), 1167–1179.

Medlyn, B. E., Duursma, R. A., Eamus, D., Ellsworth, D. S., Prentice, I. C., Barton, C. V. M., … Wingate, L. (2011). Reconciling the optimal and empirical approaches to modelling stomatal conductance. *Global Change Biology*, *17*(6), 2134–2144.

Mencuccini, M., Manzoni, S., & Christoffersen, B. (2019). Modelling water fluxes in plants: From tissues to biosphere. *New Phytologist*, *222*(3), 1207–1222.

Mencuccini, M., Rosas, T., Rowland, L., Choat, B., Cornelissen, H., Jansen, S., … Martinez-Vilalta, J. (2019). Leaf economics and plant hydraulics drive leaf : wood area ratios. *New Phytologist*, *224*(4), 1544–1556.

Niinemets, U., Díaz-Espejo, A., Flexas, J., Galmés, J., & Warren, C. R. (2009). Importance of mesophyll diffusion conductance in estimation of plant photosynthesis in the field. *Journal of Experimental Botany*, *60*(8), 2271–2282.

Nobel, P. S. (2009). *Physicochemical and environmental plant physiology*. Academic Press.

Pettorelli, N., Vik, J. O., Mysterud, A., Gaillard, J.-M., Tucker, C. J., & Stenseth, N. C. (2005). Using the satellite-derived NDVI to assess ecological responses to environmental change. *Trends in Ecology & Evolution*, *20*(9), 503–510.

Poorter, H., Niinemets, U., Poorter, L., Wright, I. J., & Villar, R. (2009). Causes and consequences of variation in leaf mass per area (LMA): A meta-analysis. *New Phytologist*, *182*(3), 565–588.

Poorter, H., Pepin, S., Rijkers, T., De Jong, Y., Evans, J. R., & Körner, C. (2006). Construction costs, chemical composition and payback time of high-and low-irradiance leaves. *Journal of Experimental Botany*, *57*(2), 355–371.

Powell, T. L., Galbraith, D. R., Christoffersen, B. O., Harper, A., Imbuzeiro, H., Rowland, L., … Moorcroft, P. R. (2013). Confronting model predictions of carbon fluxes with measurements of Amazon forests subjected to experimental drought. *New Phytologist*, *200*(2), 350–365.

Prentice, I. C., Dong, N., Gleason, S. M., Maire, V., & Wright, I. J. (2014). Balancing the costs of carbon gain and water transport: Testing a new theoretical framework for plant functional ecology. *Ecology Letters*, *17*(1), 82–91.

Quebbeman, J. A., & Ramirez, J. A. (2016). Optimal allocation of leaf-level nitrogen: Implications for covariation of V_{cmax} and J_{max} and photosynthetic downregulation. *Journal of Geophysical Research: Biogeosciences*, *121*(9), 2464–2475.

Quéré, C., Andrew, R. M., Friedlingstein, P., Sitch, S., Pongratz, J., Manning, A. C., … Zhu, D. (2018). Global carbon budget 2017. *Earth System Science Data*, *10*, 405–448.

Ripullone, F., Grassi, G., Lauteri, M., & Borghetti, M. (2003). Photosynthesis–nitrogen relationships: Interpretation of different patterns between *Pseudotsuga menziesii* and *Populus* × *euroamericana* in a mini-stand experiment. *Tree Physiology*, *23*(2), 137–144.

Santiago, L. S., Goldstein, G., Meinzer, F. C., Fisher, J. B., Machado, K., Woodruff, D., & Jones, T. (2004). Leaf photosynthetic traits scale with hydraulic conductivity and wood density in Panamanian forest canopy trees. *Oecologia*, *140*(4), 543–550.

Seemann, J. R., Sharkey, T. D., Wang, J., & Osmond, C. B. (1987). Environmental effects on photosynthesis, nitrogen-use efficiency, and metabolite pools in leaves of sun and shade plants. *Plant Physiology*, *84*(3), 796–802.

Sheffield, J., Goteti, G., & Wood, E. F. (2006). Development of a 50-year high-resolution global dataset of meteorological forcings for land surface modeling. *Journal of Climate*, *19*(13), 3088–3111.

Simioni, G., Le Roux, X., Gignoux, J., & Walcroft, A. S. (2004). Leaf gas exchange characteristics and water-and nitrogen-use efficiencies of dominant grass and tree species in a West African savanna. *Plant Ecology*, *173*(2), 233–246.

Smith, N. G., Keenan, T. F., Prentice, I. C., Wang, H., Wright, I. J., Niinemets, U., … Zhou, S. (2019). Global photosynthetic capacity is optimized to the environment. *Ecology Letters*, *22*(3), 506–517.

Sperry, J. S., Adler, F. R., Campbell, G. S., & Comstock, J. P. (1998). Limitation of plant water use by rhizosphere and xylem conductance: Results from a model. *Plant, Cell & Environment*, *21*(4), 347–359.

Sperry, J. S., & Love, D. M. (2015). What plant hydraulics can tell us about responses to climate-change droughts. *New Phytologist*, *207*(1), 14–27.

Sperry, J. S., & Tyree, M. T. (1988). Mechanism of water stress-induced xylem embolism. *Plant Physiology*, *88*(3), 581–587.

Sperry, J. S., Venturas, M. D., Anderegg, W. R. L., Mencuccini, M., Mackay, D. S., Wang, Y., & Love, D. M. (2017). Predicting stomatal responses to the environment from the optimization of photosynthetic gain and hydraulic cost. *Plant, Cell & Environment*, *40*(6), 816–830.

Sperry, J. S., Venturas, M. D., Todd, H. N., Trugman, A. T., Anderegg, W. R. L., Wang, Y., & Tai, X. (2019). The impact of rising CO_2 and acclimation on the response of US forests to global warming. *Proceedings of the National Academy of Sciences*, *116*(51), 25734–25744.

Sperry, J. S., Wang, Y., Wolfe, B. T., Mackay, D. S., Anderegg, W. R. L., McDowell, N. G., & Pockman, W. T. (2016). Pragmatic hydraulic theory predicts stomatal responses to climatic water deficits. *New Phytologist*, *212*(3), 577–589.

Trugman, A. T., Anderegg, L. D. L., Sperry, J. S., Wang, Y., Venturas, M., & Anderegg, W. R. L. (2019). Leveraging plant hydraulics to yield predictive and dynamic plant leaf allocation in vegetation models with climate change. *Global Change Biology*, *25*, 4008–4021.

Trugman, A. T., Anderegg, L. D. L., Wolfe, B. T., Birami, B., Ruehr, N. K., Detto, M., … Anderegg, W. R. L. (2019). Climate and plant trait strategies determine tree carbon allocation to leaves and mediate future forest productivity. *Global Change Biology*, *25*, 3395–3405.

Trugman, A. T., Detto, M., Bartlett, M. K., Medvigy, D., Anderegg, W. R. L., Schwalm, C., … Pacala, S. W. (2018). Tree carbon allocation explains forest drought-kill and recovery patterns. *Ecology Letters*, *21*(10), 1552–1560.

Trugman, A. T., Medvigy, D., Mankin, J. S., & Anderegg, W. R. L. (2018). Soil moisture stress as a major driver of carbon cycle uncertainty. *Geophysical Research Letters*, *45*(13), 6495–6503.

Tyree, M. T., & Alexander, J. D. (1993). Plant water relations and the effects of elevated CO_2: A review and suggestions for future research. *Vegetatio*, *104*(1), 47–62.

Venturas, M. D., Sperry, J. S., & Hacke, U. G. (2017). Plant xylem hydraulics: What we understand, current research, and future challenges. *Journal of Integrative Plant Biology*, *59*(6), 356–389.

Venturas, M. D., Sperry, J. S., Love, D. M., Frehner, E. H., Allred, M. G., Wang, Y., & Anderegg, W. R. L. (2018). A stomatal control model based on optimization of carbon gain versus hydraulic risk predicts aspen sapling responses to drought. *New Phytologist*, *220*(3), 836–850.

Voelker, S. L., Brooks, J. R., Meinzer, F. C., Anderson, R., Bader, M. K. F., Battipaglia, G., … Wingate, L. (2016). A dynamic leaf gas-exchange strategy is conserved in woody plants under changing ambient CO_2: Evidence from carbon isotope discrimination in paleo and CO_2 enrichment studies. *Global Change Biology*, *22*(2), 889–902.

Walker, A. P., Beckerman, A. P., Gu, L., Kattge, J., Cernusak, L. A., Domingues, T. F., … Woodward, F. I. (2014). The relationship of leaf photosynthetic traits–V_{cmax} and J_{max}–to leaf nitrogen, leaf phosphorus, and specific leaf area: A meta-analysis and modeling study. *Ecology and Evolution*, *4*(16), 3218–3235.

Walker, A. P., Hanson, P. J., De Kauwe, M. G., Medlyn, B. E., Zaehle, S., Asao, S., … Norby, R. J. (2014). Comprehensive ecosystem model-data synthesis using multiple data sets at two temperate forest free-air CO_2 enrichment experiments: Model performance at ambient CO_2 concentration. *Journal of Geophysical Research: Biogeosciences*, *119*(5), 937–964.

Wang, Y., Sperry, J. S., Venturas, M. D., Trugman, A. T., Love, D. M., & Anderegg, W. R. L. (2019). The stomatal response to rising CO_2 concentration and drought is predicted by a hydraulic trait-based optimization model. *Tree Physiology*, *39*, 1416–1427.

Wolf, A., Anderegg, W. R. L., & Pacala, S. W. (2016). Optimal stomatal behavior with competition for water and risk of hydraulic impairment. *Proceedings of the National Academy of Sciences*, *113*(46), E7222–E7230.

Yamori, W., Evans, J. R., & von Caemmerer, S. (2010). Effects of growth and measurement light intensities on temperature dependence of CO_2 assimilation rate in tobacco leaves. *Plant, Cell & Environment*, *33*(3), 332–343.

Yang, J., Cao, M., & Swenson, N. G. (2018). Why functional traits do not predict tree demographic rates. *Trends in Ecology & Evolution*, *33*(5), 326–336.

Young, V. R., & Pellett, P. L. (1994). Plant proteins in relation to human protein and amino acid nutrition. *The American Journal of Clinical Nutrition*, *59*(5), 1203S–1212S.

Yu, K., Goldsmith, G. R., Wang, Y., & Anderegg, W. R. L. (2019). Phylogenetic and biogeographic controls of plant nighttime stomatal conductance. *New Phytologist*, *222*(4), 1778–1788.

Zhou, S., Medlyn, B., Sabaté, S., Sperlich, D., & Prentice, I. C. (2014). Short-term water stress impacts on stomatal, mesophyll and biochemical limitations to photosynthesis differ consistently among tree species from contrasting climates. *Tree Physiology*, *34*(10), 1035–1046.

Zhou, S., Medlyn, B. E., & Prentice, I. C. (2016). Long-term water stress leads to acclimation of drought sensitivity of photosynthetic capacity in xeric but not riparian *Eucalyptus* species. *Annals of Botany*, *117*(1), 133–144.

Table 5.1: List of important symbols and their default values and units.

Symbol	Description	Default value (unit)
	Leaf gas exchange	
A	Gross photosynthetic rate per LA	(μmol CO_2 m^{-2} s^{-1})
C_i	Leaf internal [CO_2]	(ppm)
D	Leaf-to-air vapor pressure deficit relative to atmospheric pressure	(unitless)
E	Tree transpiration rate per BA	(kg H_2O m^{-2} h^{-1})
E_{crit}	Maximal E at given soil moisture	(kg H_2O m^{-2} h^{-1})
G_C	Leaf diffusive conductance for CO_2 per LA	(mol m^{-2} s^{-1})
G_H	Leaf diffusive conductance for H_2O per LA	(mol m^{-2} s^{-1})
R	Leaf respiration per LA	(μmol CO_2 m^{-2} s^{-1})
	Tree traits	
B	Weibull parameter for tree vulnerability curve	2 (MPa)
BA	Tree basal area	1 (m^2)
C	Weibull parameter for tree vulnerability curve	5
G_{max}	Maximal G_H at 25 °C	0.8 (mol m^{-2} s^{-1})
H_{root}	Root depth	2 (m)
$invest_C$	Leaf biomass cost factor	2.0 (mol m^{-2})
$invest_N$	Leaf nutrient supply cost factor	0.04 (mol s μmol^{-1})
J_{max}	Maximal electron transport at 25 °C, 1.75 times V_{cmax}	(μmol CO_2 m^{-2} s^{-1})
k_{root}	Root hydraulic conductance per BA	5000 (kg H_2O h^{-1} m^{-2} MPa^{-1})
k_{sla}	Leaf hydraulic conductance per LA	2.0 (kg H_2O h^{-1} m^{-2} MPa^{-1})
k_{stem}	Stem hydraulic conductance per BA	10000 (kg H_2O h^{-1} m^{-2} MPa^{-1})
K	Soil-plant hydraulic conductance per BA	(kg H_2O h^{-1} m^{-2} MPa^{-1})
K_{max}	Maximal K when $E = 0$	2500 (kg H_2O h^{-1} m^{-2} MPa^{-1})
LA	Leaf area	1500 (m^2)
LCBM	Leaf biomass costs per BA	(mol m^{-2})
LCC	Leaf construction cost per BA	(mol m^{-2})
LMA	Leaf dry mass per area	(kg m^{-2})
NS	Leaf nutrient supply cost per BA	(mol m^{-2})
N_N	Nutrient investment per LA	(μmol CO_2 m^{-2} s^{-1})
T_{LL}	Leaf life span	(day)
V_{cmax}	Maximal carboxylation rate at 25 °C	(μmol CO_2 m^{-2} s^{-1})
V_{limit}	Anatomical limit to V_{cmax} due to chloroplasts self-shading	100 (μmol CO_2 m^{-2} s^{-1})
	Site traits	
C_a	Atmospheric [CO_2]	400 (ppm)
CNPP	Canopy net primary productivity per BA	(mol m^{-2})
GA	Ground area per tree	500 (m^2)
GCP	Growing season canopy profit per BA	(mol m^{-2})

Table 5.1: continued

Symbol	Description	Default value (unit)
LAI	Leaf area index, LA:GA	3
PAR	Photosynthetically active radiation	(μmol m^{-2} s^{-1})
T_{GS}	Growing season length	(day)
VPD	Atmospheric vapor pressure deficit	(kPa)

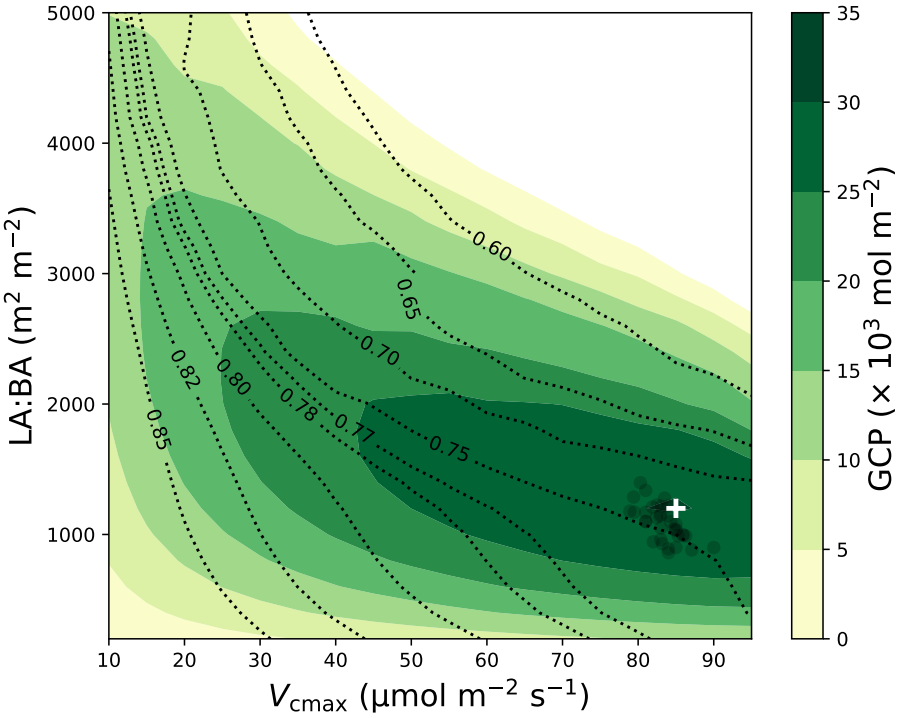

Figure 5.1: Growing season canopy profit (GCP, colored contour) and C_i/C_a ratio (dotted lines) at different leaf area per basal area (LA:BA) and photosynthetic capacity (measured by maximal carboxylation rate, V_{cmax}) for default model settings. The simulation was run for the weather data of year 2005. The color bar plots the GCP per BA, and the inline numbers represent photosynthetically weighted C_i/C_a ratio. The white plus identifies the global optimal LA:BA and V_{cmax} combination that yields highest GCP at year 2005. The gray circles plot the rest 34 optimal LA:BA + V_{cmax} combinations for weather data from year 1971 to 2004.

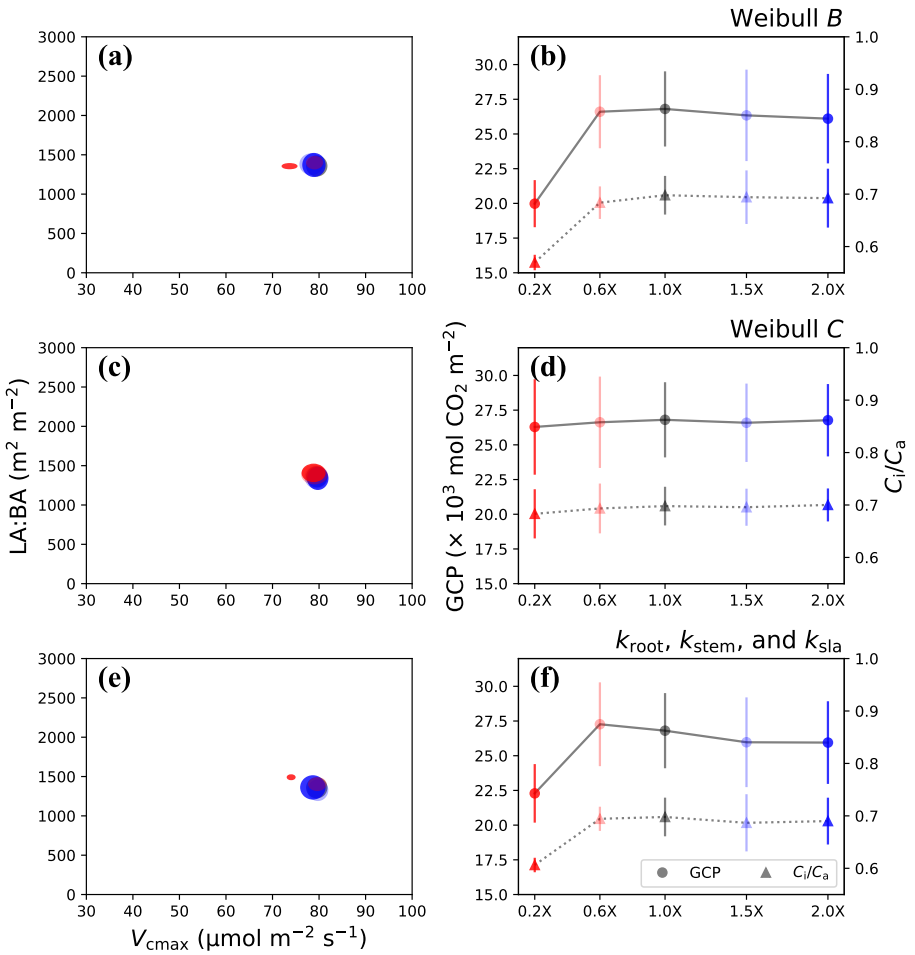

Figure 5.2: The influence of hydraulic traits on the optimal leaf area per basal area (LA:BA, y-axis of left panels) and photosynthetic capacity (V_{cmax}, x-axis of left panels) combination. Also shown is the gross canopy profit (GCP, circles, left y-axis of right panels) and photosynthetically weighted C_i/C_a ratio (triangles, right y-axis of right panels) at the leaf investment optimum. (a) Optimal LA and V_{cmax} when varying Weibull B to 20% (red), 60% (shaded red), 100% (gray), 150% (shaded blue), and 200% (blue) of the default value. The semiaxes of the ellipses represent the standard deviation (SD, N = 35) of the optimal V_{cmax} horizontally and the SD of optimal LA:BA vertically. (b) The GCP and average C_i/C_a at different Weibull Bs (color scheme same as (a)). The error bars plot the SD of the GCP and C_i/C_a. (c) and (d) Sensitivity to the Weibull C from 20% to 200% of the default value, which influences the rate of xylem cavitation with xylem pressure. (e) and (f) Sensitivity to k_{root}, k_{stem}, and k_{sla}, which determines the plant's hydraulic conducting efficiency, from 20% to 200% of their default values.

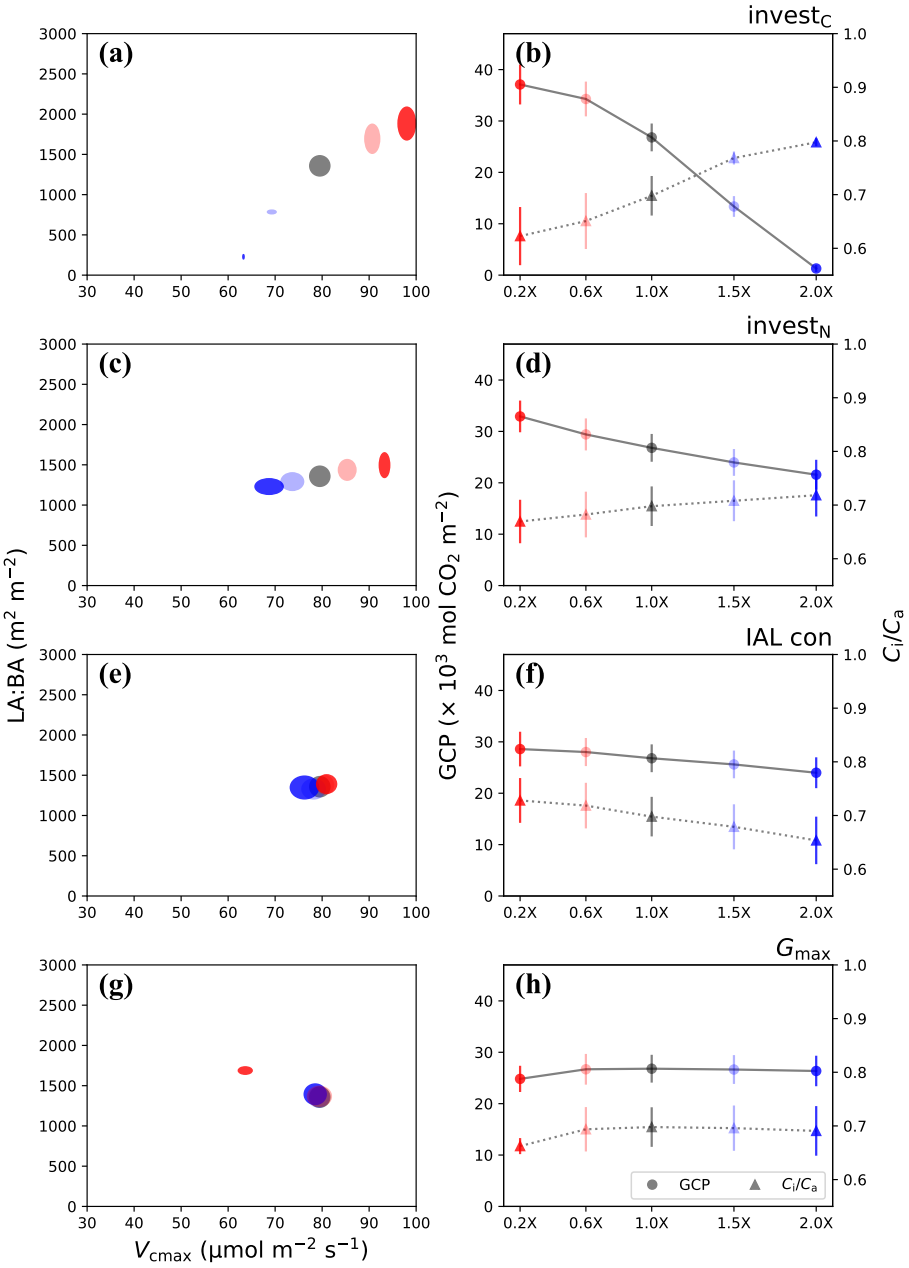

Figure 5.3: The influence of leaf traits on the optimal leaf area per basal area (LA:BA, y-axis of left panels) and photosynthetic capacity (V_{cmax}, x-axis of left panels) combination. Also shown is the gross canopy profit (GCP, circles, left y-axis of right panels) and photosynthetically weighted C_i/C_a ratio (triangles, right y-axis of right panels) at the leaf investment optimum. (a) Optimal LA and V_{cmax} when varying leaf biomass cost factor (invest$_C$) to 20% (red), 60% (shaded red), 100% (gray), 150% (shaded blue), and 200% (blue) of the default value. The semiaxes of the ellipses represent the standard deviation (SD, N = 35) of the optimal V_{cmax} horizontally and the SD of optimal LA:BA vertically. (b) The GCP and average C_i/C_a at different invest$_C$s (color scheme same as (a)). The error bars plot the SD of the GCP and C_i/C_a. (c) and (d) Sensitivity to the nutrient supply cost factor (invest$_N$) from 20% to 200% of the default value, which influences the rate of xylem cavitation with xylem pressure. (e) and (f) Sensitivity to intercellular airspace limitation (via IAL con) from 20% to 200% of their default values. (g) and (h) Sensitivity to maximal leaf diffusive conductance (G_{max}) from 20% to 200% of their default values.

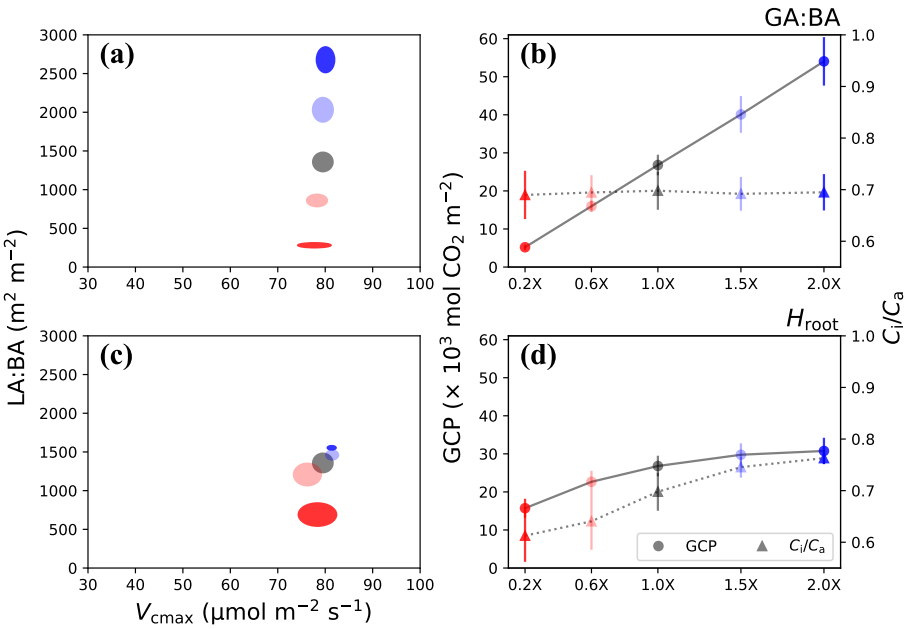

Figure 5.4: The influence of water supply on the optimal leaf area per basal area (LA:BA, y-axis of left panels) and photosynthetic capacity (V_{cmax}, x-axis of left panels) combination. Also shown is the gross canopy profit (GCP, circles, left y-axis of right panels) and photosynthetically weighted C_i/C_a ratio (triangles, right y-axis of right panels) at the leaf investment optimum. (a) Optimal LA and V_{cmax} when varying ground area per BA (GA:BA) to 20% (red), 60% (shaded red), 100% (gray), 150% (shaded blue), and 200% (blue) of the default value. The semiaxes of the ellipses represent the standard deviation (SD, N = 35) of the optimal V_{cmax} horizontally and the SD of optimal LA:BA vertically. (b) The GCP and average C_i/C_a at different GA:BAs (color scheme same as (a)). The error bars plot the SD of the GCP and C_i/C_a. (c) and (d) Sensitivity to the root depth (H_{root}) from 20% to 200% of the default value, which influences the rate of xylem cavitation with xylem pressure.

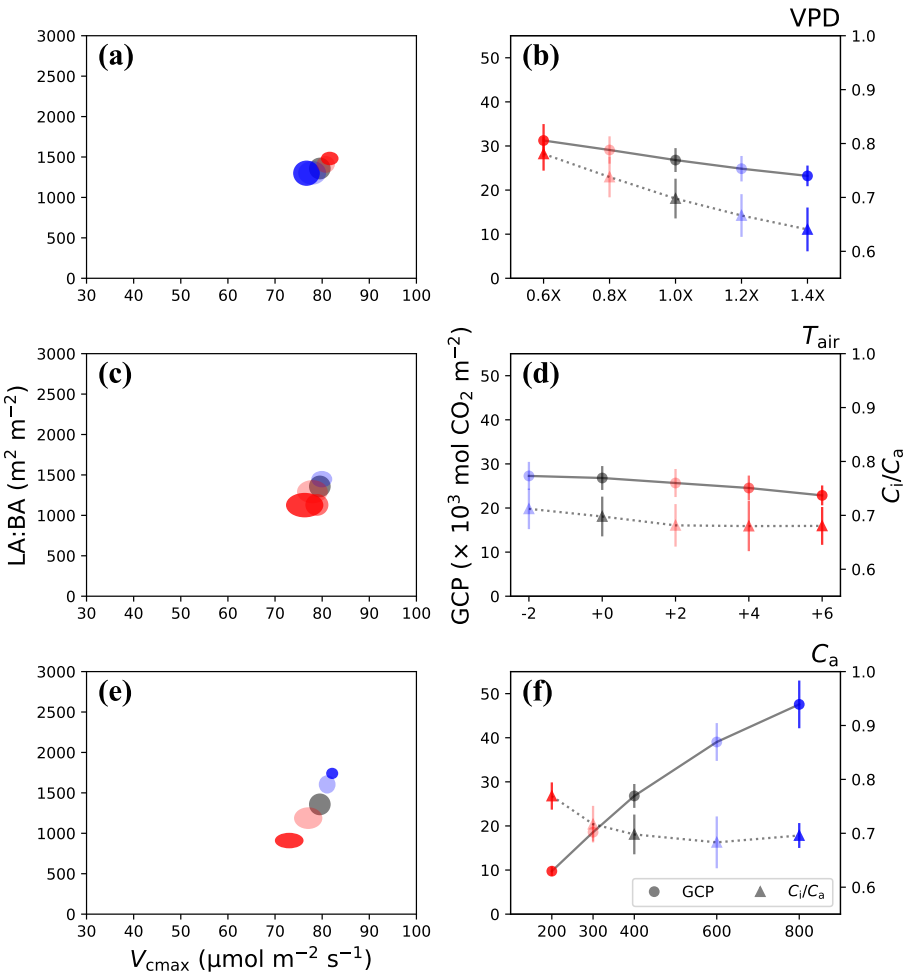

Figure 5.5: The influence of environmental conditions on the optimal leaf area per basal area (LA:BA, y-axis of left panels) and photosynthetic capacity (V_{cmax}, x-axis of left panels) combination. Also shown is the gross canopy profit (GCP, circles, left y-axis of right panels) and photosynthetically weighted C_i/C_a ratio (triangles, right y-axis of right panels) at the leaf investment optimum. (a) Optimal LA and V_{cmax} when varying hourly atmospheric vapor pressure deficit (VPD) to 60% (red), 80% (shaded red), 100% (gray), 120% (shaded blue), and 140% (blue) of the default value. The semiaxes of the ellipses represent the standard deviation (SD, N = 35) of the optimal V_{cmax} horizontally and the SD of optimal LA:BA vertically. (b) The GCP and average C_i/C_a at different VPDs (color scheme same as (a)). The error bars plot the SD of the GCP and C_i/C_a. (c) and (d) Sensitivity to the atmospheric [CO_2] (C_a) from 200 to 800 ppm (from red to shaded red, gray, shaded blue, and blue). (e) and (f) Sensitivity to the photosynthetically active radiation (PAR) from 20% to 100% the default value (from lighter to darker gray).

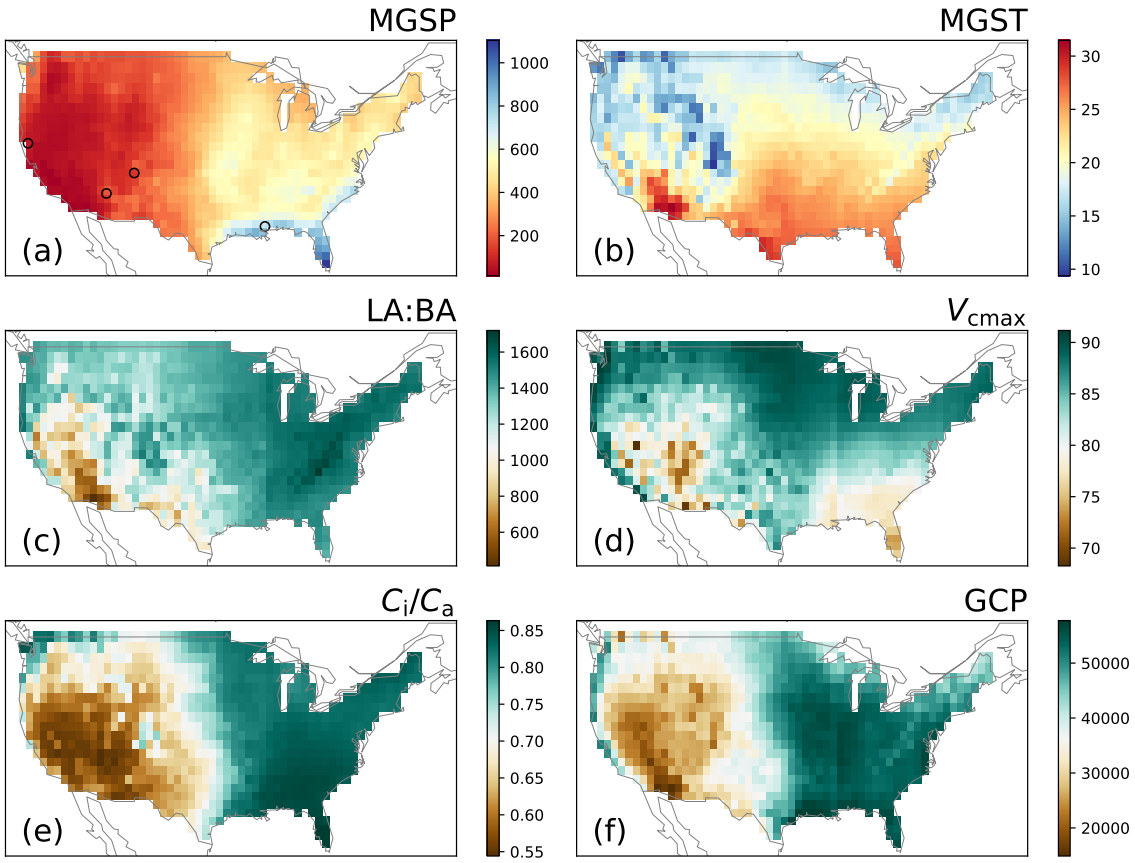

Figure 5.6: Spatial patterns of environment and leaf investment in the lower 48 states of the United States. (a) Spatial pattern of mean growing season precipitation (MGSP, unit see Table 5.1). (b) Mean growing season temperature (MGST). (c) Optimal leaf area per basal area (LA:BA) when we hold the tree traits at the default settings. (d) Optimal leaf photosynthetic capacity (measured by maximal carboxylation rate at 25 °C, V_{cmax}). (e) Growing season photosynthesis weighted C_i/C_a at optimal leaf investment. (f) Growing season canopy profit (GCP).

5.7 Supporting Information

5.7.1 Supplemental figures

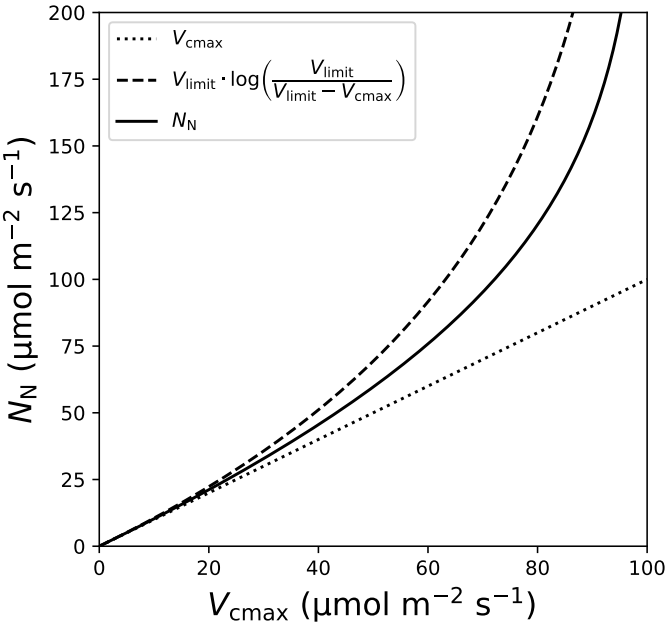

Figure 5.S1: Correlation between leaf nutrient investment (N_N) and maximal carboxylation rate (V_{cmax}) at 25 °C. The N_N (solid line) is the average of V_{cmax} (dotted line) and $V_{limit} \cdot \log\left(\frac{V_{limit}}{V_{limit} - V_{cmax}}\right)$ (dashed line, where V_{limit} is the anatomical limitation to V_{cmax} due to chloroplast self-shading).

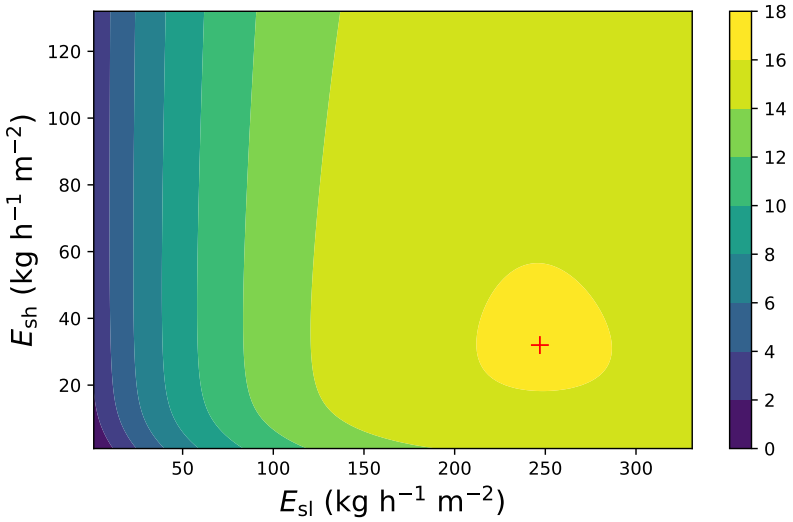

Figure 5.S2: Example of optimal transpiration partition between the sunlit layer (E_{sl}) and shade layer (E_{sh}). The colored contours plot the maximization criterion (equation 5.12 in main text, unit: μmol CO_2 m^{-2} s^{-1}), and the red symbol plots the optimal combination of E_{sl} and E_{sh}.

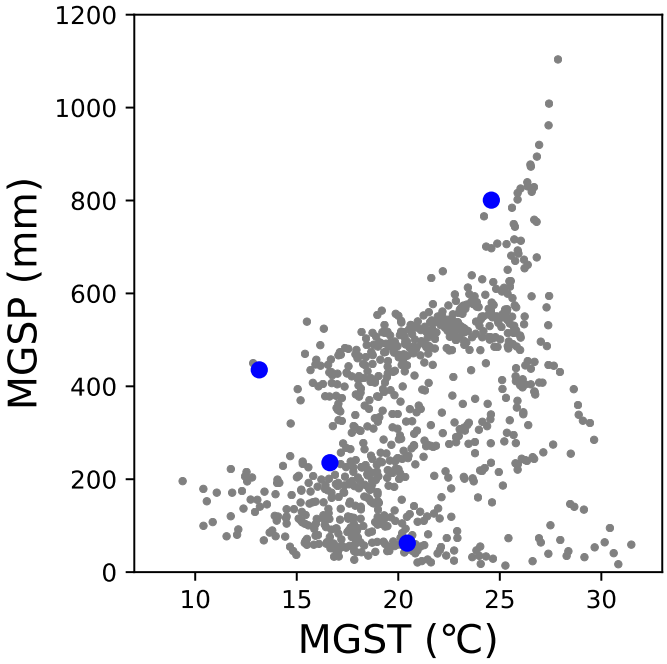

Figure 5.S3: Climate information for the sites used in the present study. The x-axis and y-axis each plots the mean growing season temperature (MGST) and precipitation (MGSP). Each gray point represents a gridded site in the lower 48 states of the United States. The blue circles are the sites used for sensitivity analysis, and they are Durango, Flagstaff, Trinity, and Hattiesburg (from left to right).

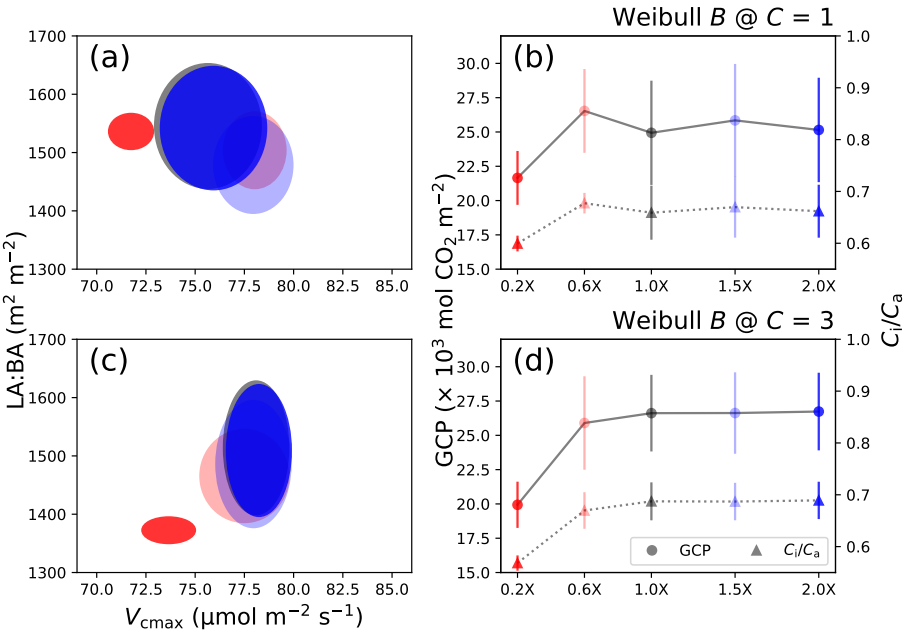

Figure 5.S4: The influence of Weibull parameter combination on the optimal leaf area per basal area (LA:BA, y-axis of left panels) and photosynthetic capacity (V_{cmax}, x-axis of left panels) combination. Also shown is the gross canopy profit (GCP, circles, left y-axis of right panels) and photosynthetically weighted C_i/C_a ratio (triangles, right y-axis of right panels) at the leaf investment optimum. (a) Optimal LA and V_{cmax} when varying Weibull B to 20% (red), 60% (shaded red), 100% (gray), 150% (shaded blue), and 200% (blue) of the default value at a Weibull C of 1. The semiaxes of the ellipses represent the standard deviation (SD, N = 35) of the optimal V_{cmax} horizontally and the SD of optimal LA:BA vertically. (b) The GCP and average C_i/C_a at different Weibull Bs (color scheme same as (a)). The error bars plot the SD of the GCP and C_i/C_a. (c) and (d) Sensitivity to the Weibull B a Weibull C of 3.

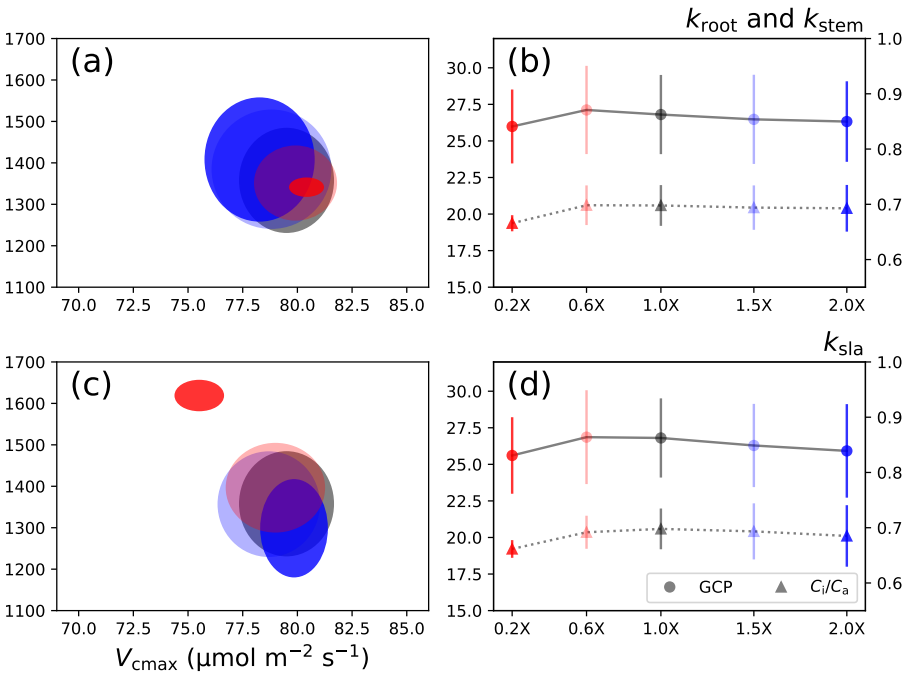

Figure 5.S5: The influence of hydraulic segmentation on the optimal leaf area per basal area (LA:BA, y-axis of left panels) and photosynthetic capacity (V_{cmax}, x-axis of left panels) combination. Also shown is the gross canopy profit (GCP, circles, left y-axis of right panels) and photosynthetically weighted C_i/C_a ratio (triangles, right y-axis of right panels) at the leaf investment optimum. (a) Optimal LA and V_{cmax} when varying the root and stem hydraulic conductance (k_{root} and k_{stem}) to 20% (red), 60% (shaded red), 100% (gray), 150% (shaded blue), and 200% (blue) of the default value. The semiaxes of the ellipses represent the standard deviation (SD, N = 35) of the optimal V_{cmax} horizontally and the SD of optimal LA:BA vertically. (b) The GCP and average C_i/C_a at different k_{root}s and k_{stem}s (color scheme same as (a)). The error bars plot the SD of the GCP and C_i/C_a. (c) and (d) Sensitivity to the leaf area specific conductance (k_{sla}) from 20% to 200% of the default value.

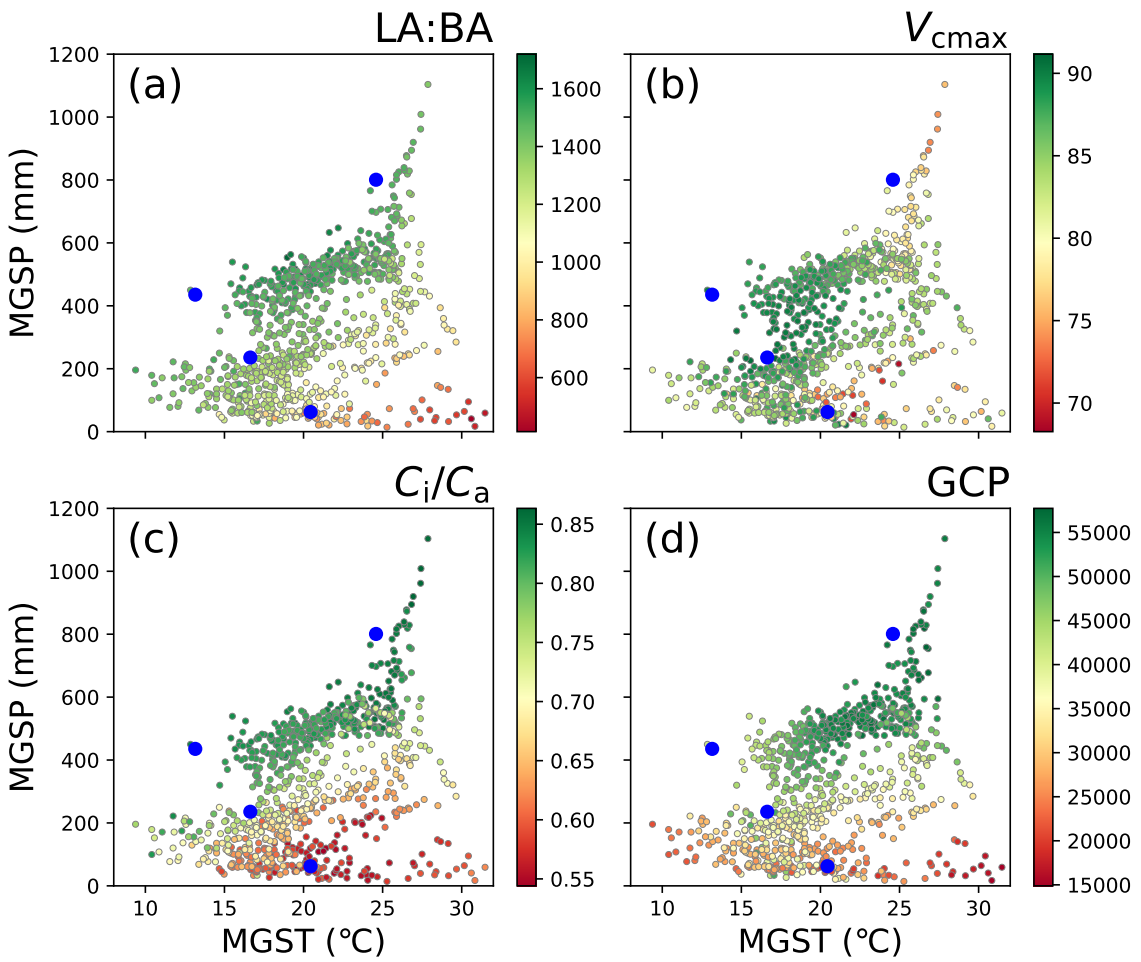

Figure 5.S6: Optimal leaf investment at different climatic conditions for the default plant traits. The x-axis and y-axis plot the mean growing season temperature (MGST) and precipitation (MGSP). Each small scatter point represents a gridded site in the lower 48 states of the United States. The blue circles are the sites used for sensitivity analysis, and they are Durango, Flagstaff, Trinity, and Hattiesburg (from left to right). (a) Pattern of optimal leaf area per basal area (LA:BA) as shown in the color bar next to it. (b) Optimal leaf photosynthetic capacity measured by the maximal carboxylation rate at 25 °C (V_{cmax}). (c) The growing season photosynthesis weighted C_i/C_a ratio at optimal leaf investment. (d) The growing season canopy profit (GCP) at optimal leaf investment.

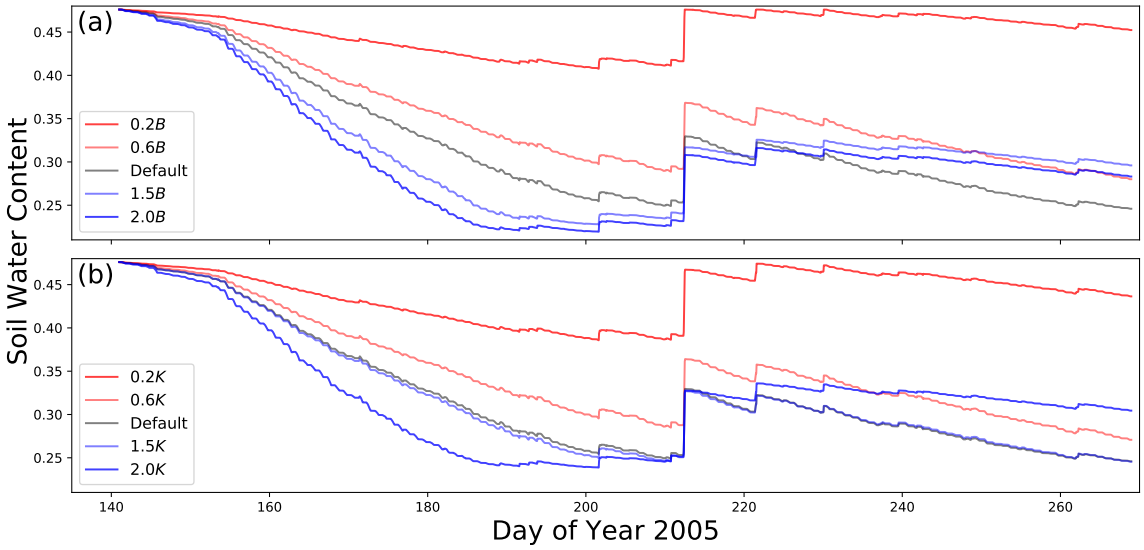

Figure 5.S7: Examples of hourly soil water content curves in the year 2005 at different hydraulic traits: (a) vulnerability curve Weibull B and (b) hydraulic efficiency K. Dark red, light red, gray, light blue, and dark blue each plots the soil water content curve at 20%, 60%, 100%, 150%, and 200% of the default value of B and K. Leaf area and photosynthetic capacity are optimized at the given setting. Decreased soil water content is due to evapotranspiration, and increased soil water content is due to precipitation.

5.7.2 Figure 5.2–5.5 for Durango, Hattiesburg, and Trinity

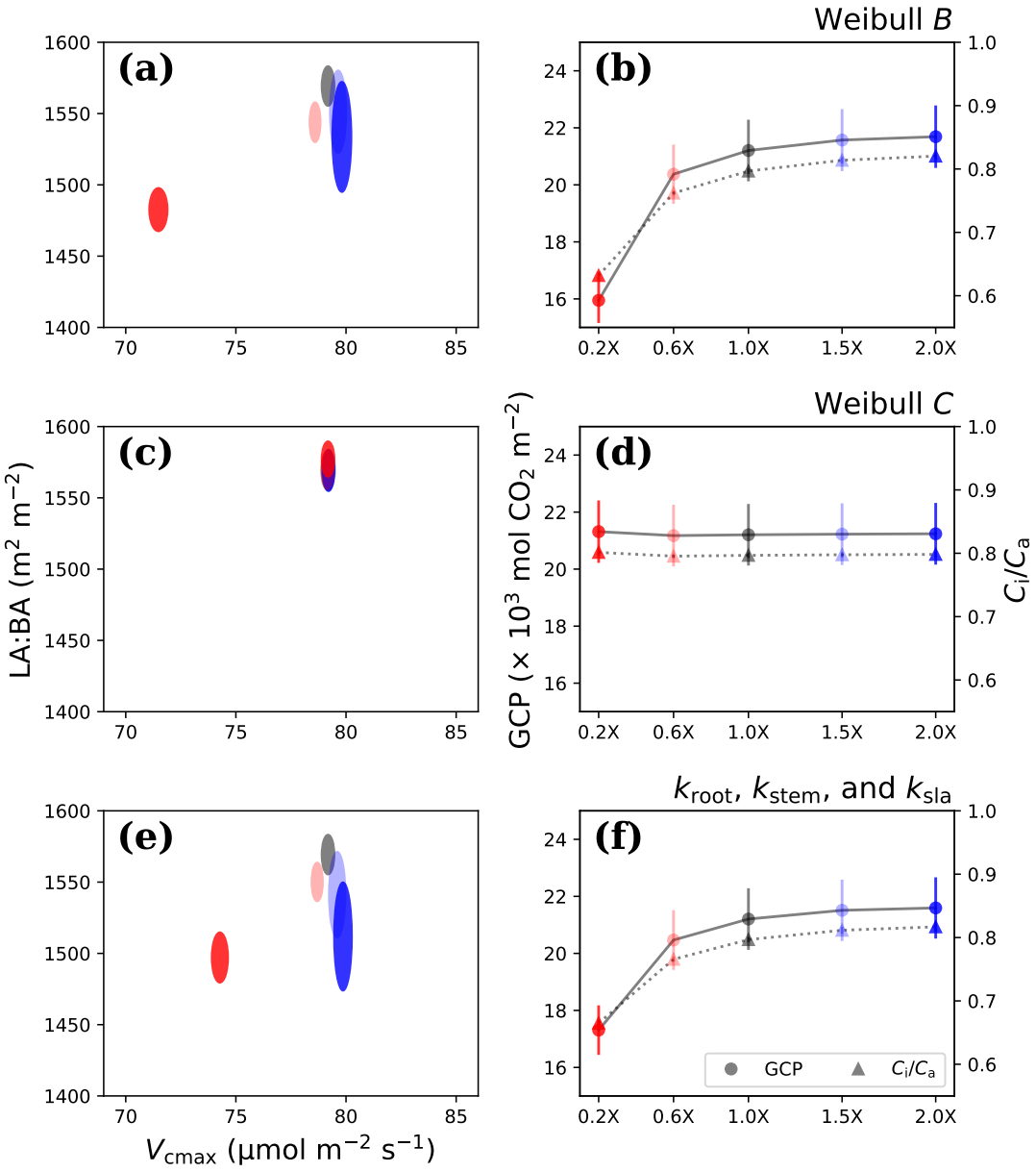

Figure 5.S8: Fig. 5.2 for Durango.

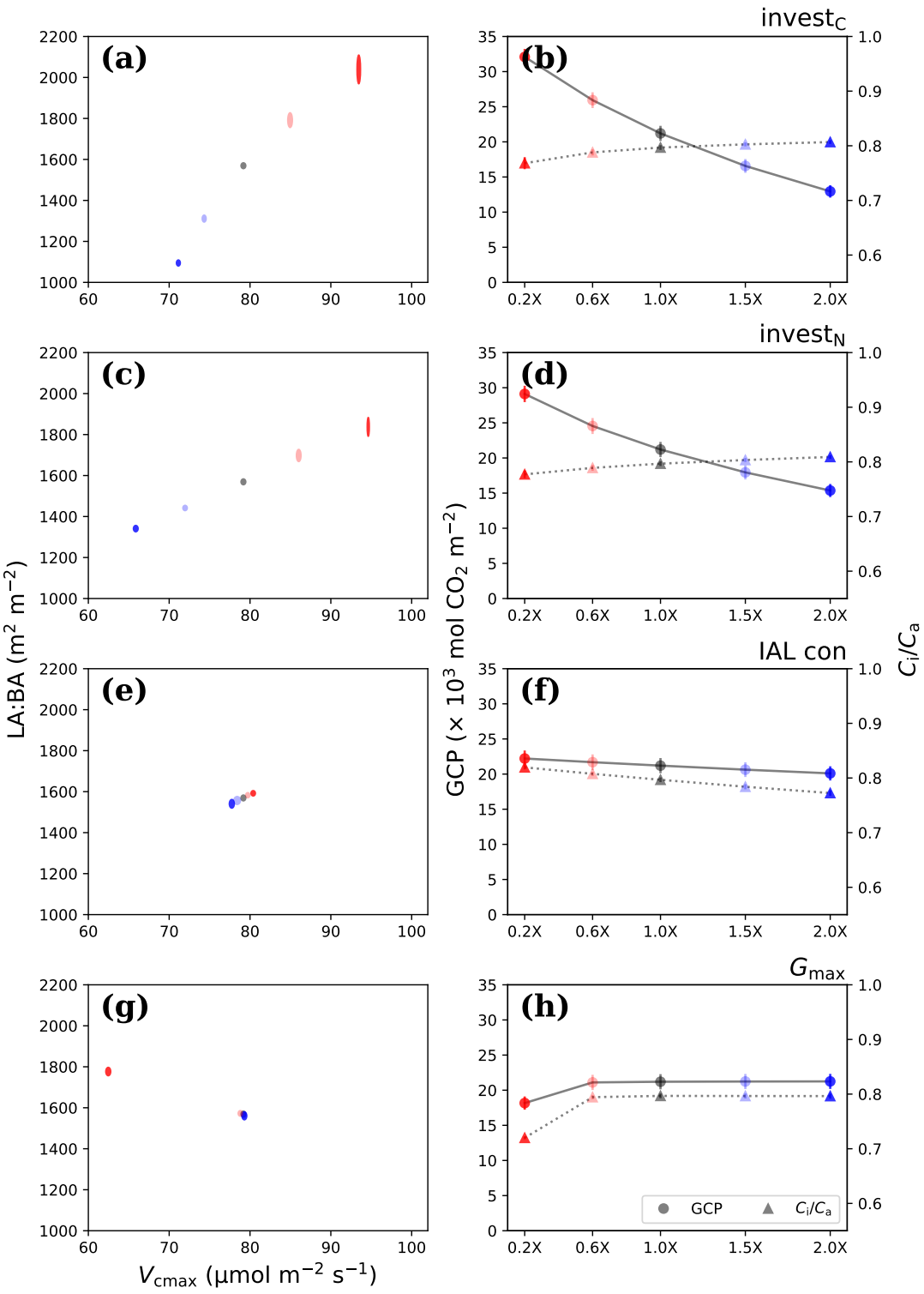

Figure 5.S9: Fig. 5.3 for Durango.

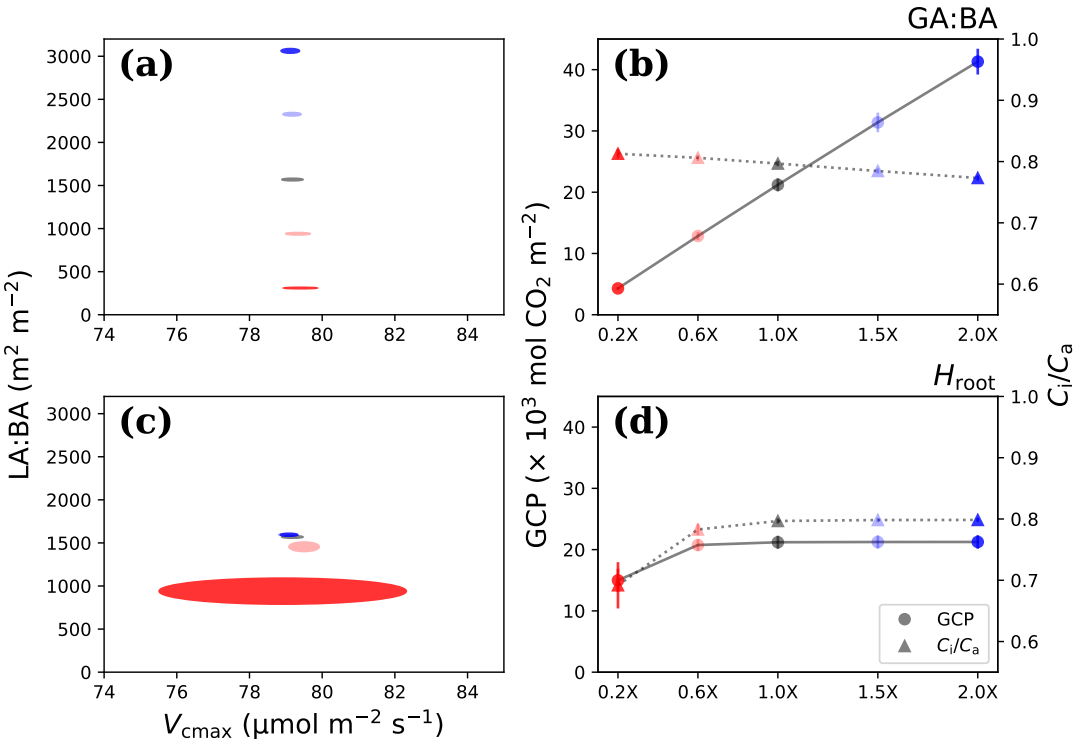

Figure 5.S10: Fig. 5.4 for Durango.

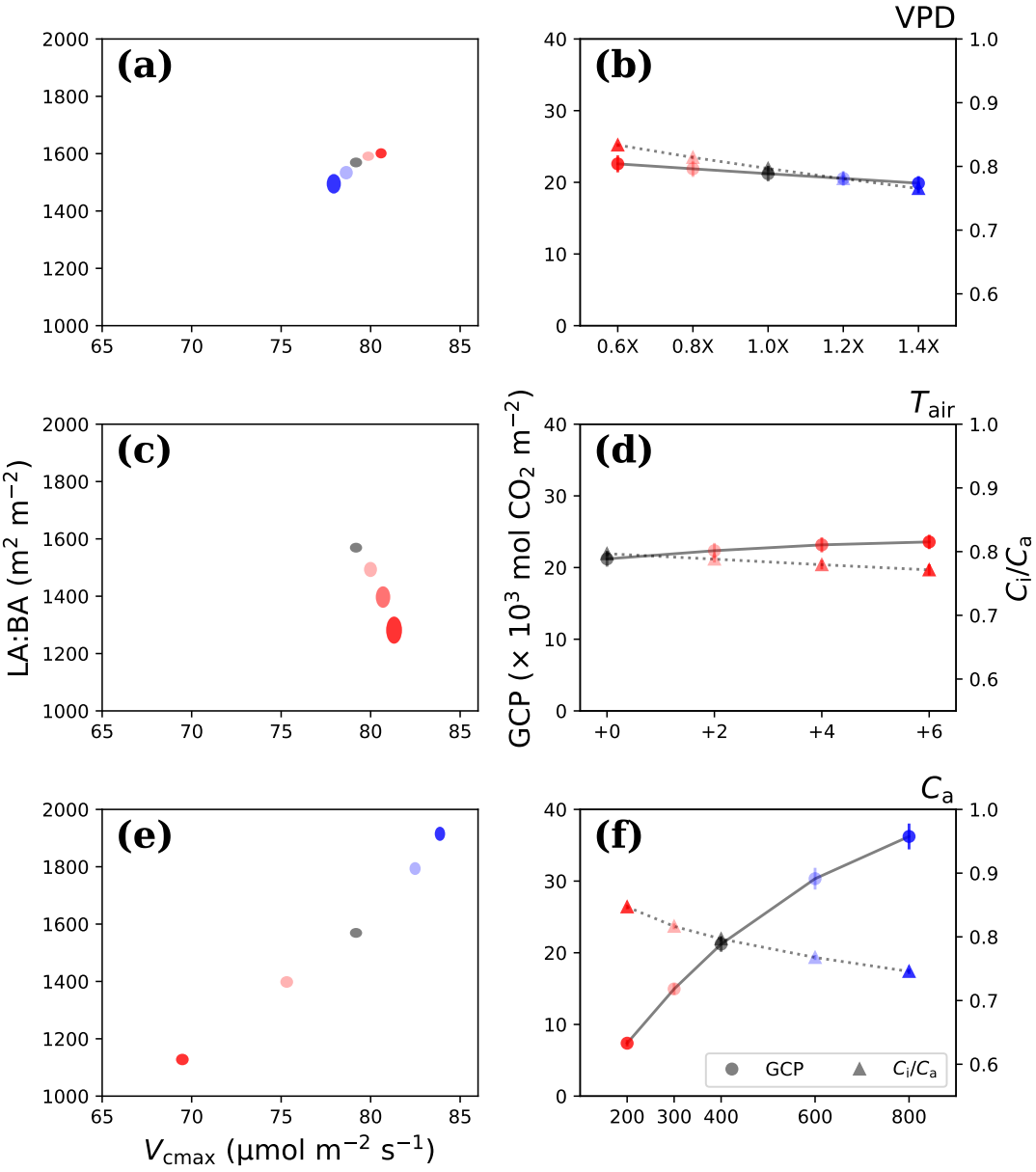

Figure 5.S11: Fig. 5.5 for Durango.

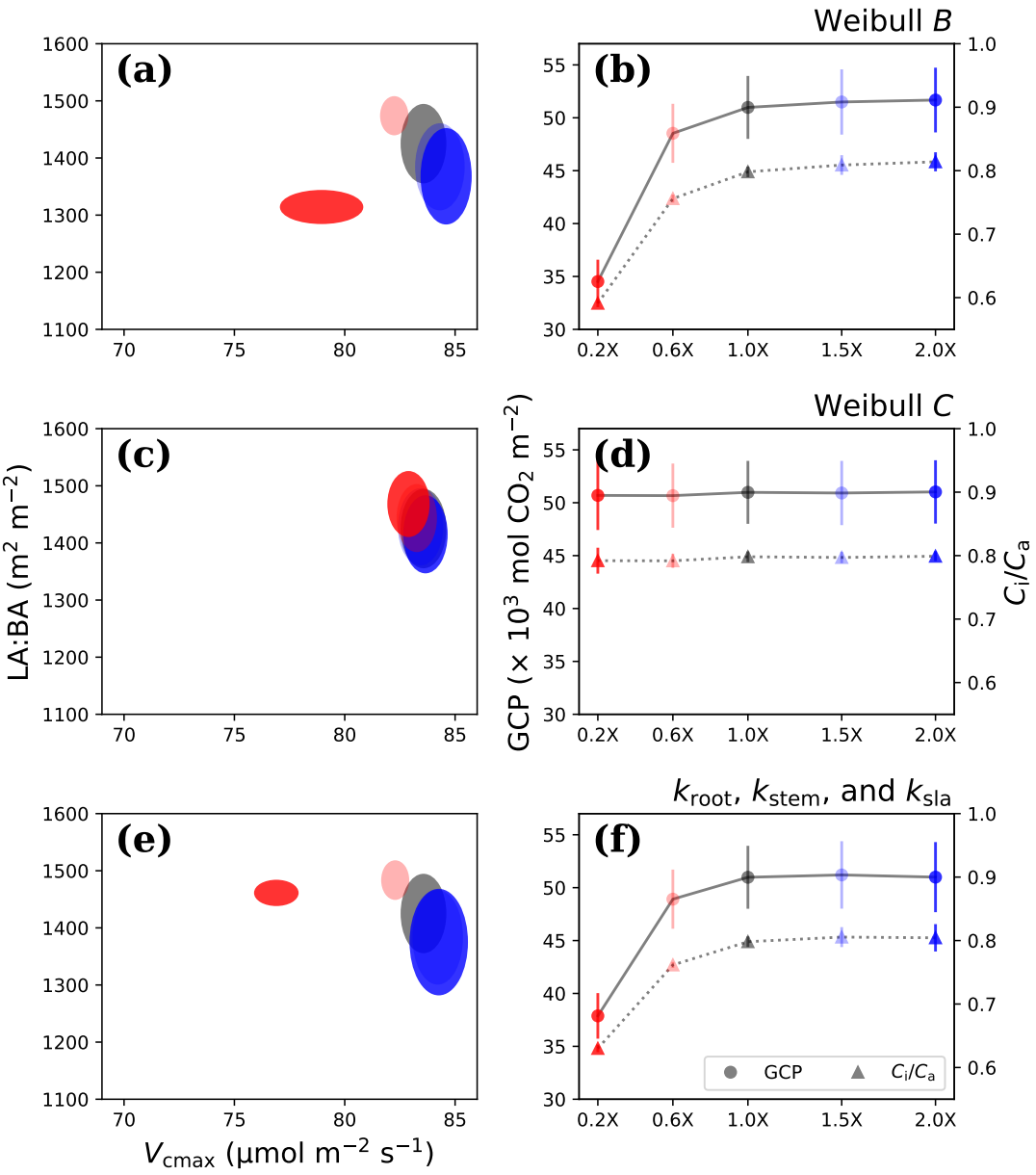

Figure 5.S12: Fig. 5.2 for Hattiesburg.

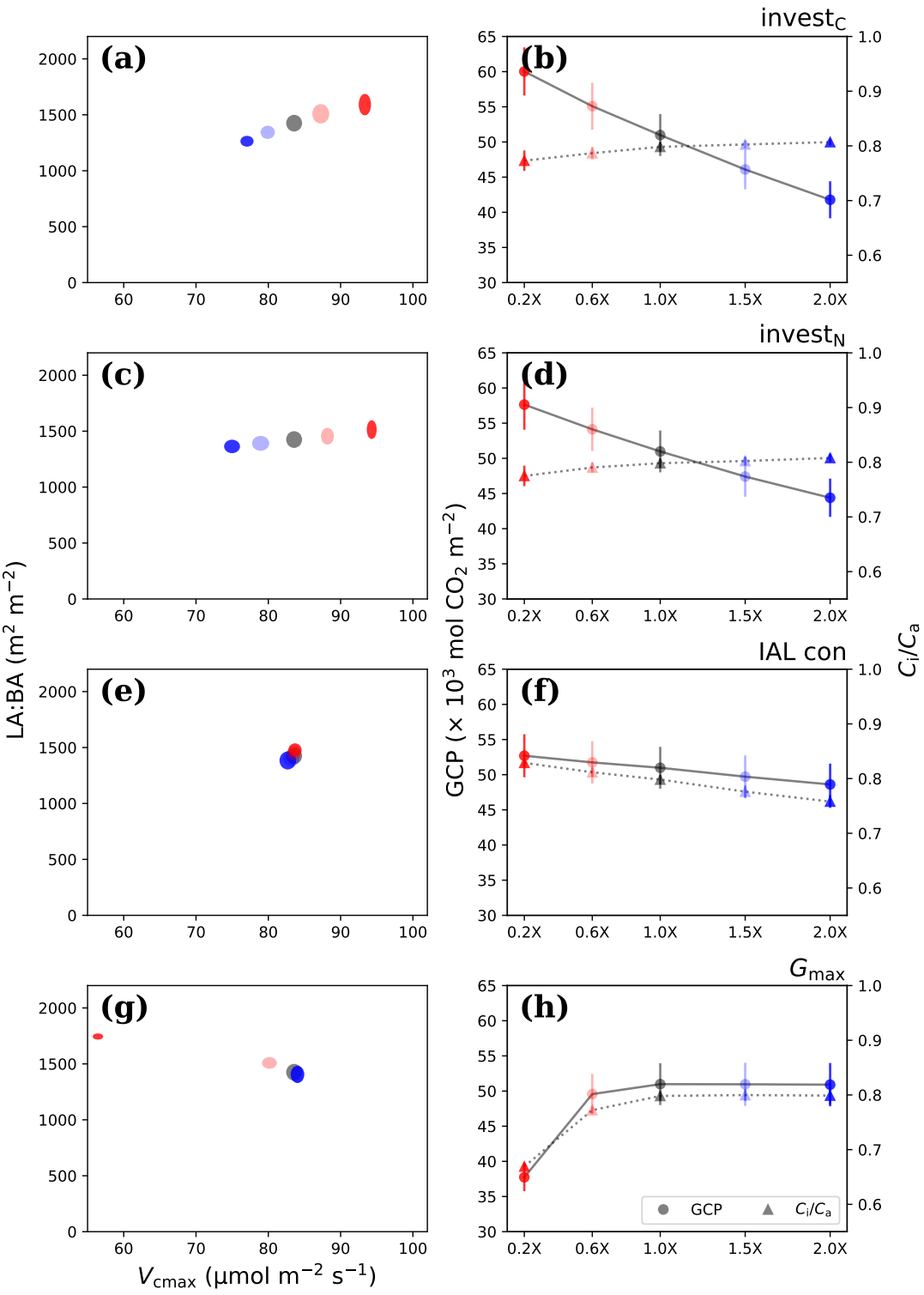

Figure 5.S13: Fig. 5.3 for Hattiesburg.

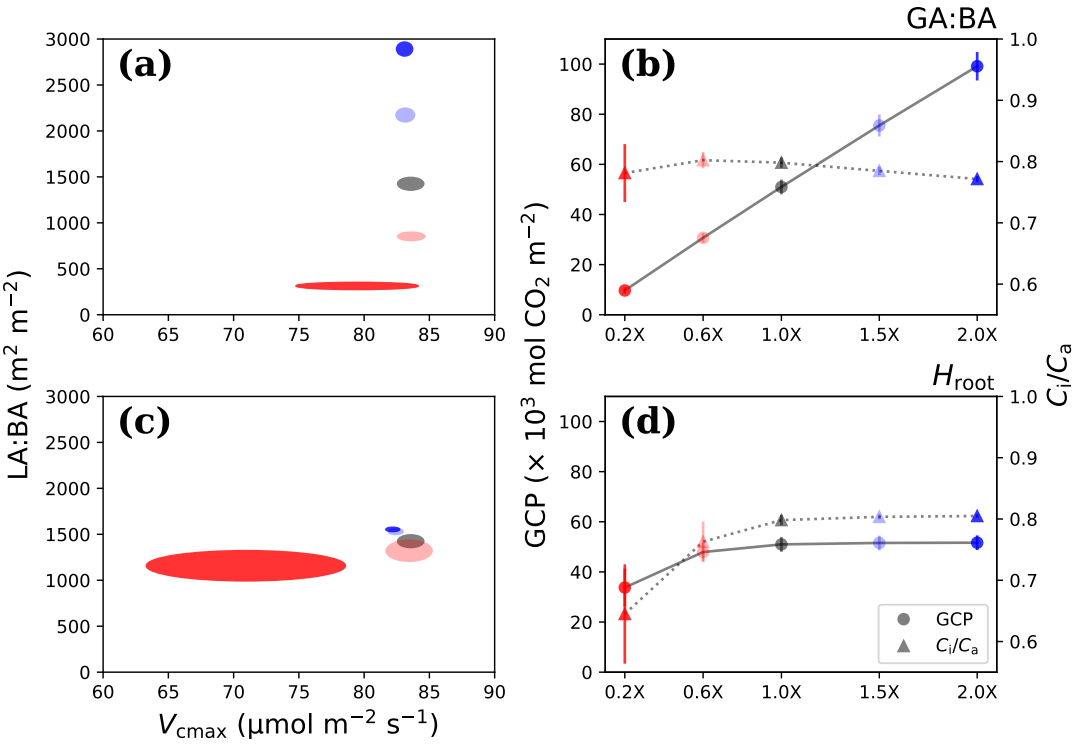

Figure 5.S14: Fig. 5.4 for Hattiesburg.

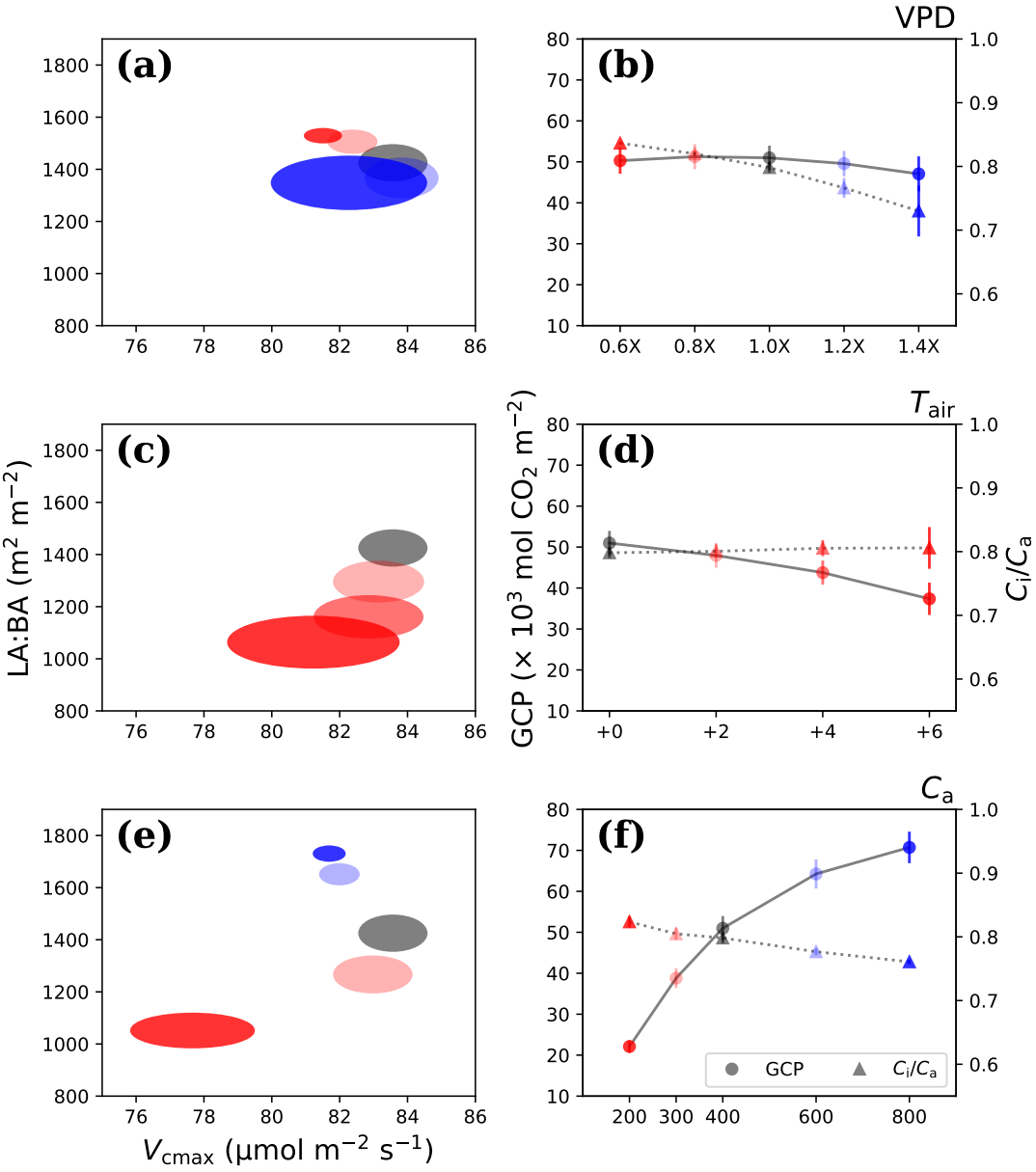

Figure 5.S15: Fig. 5.5 for Hattiesburg.

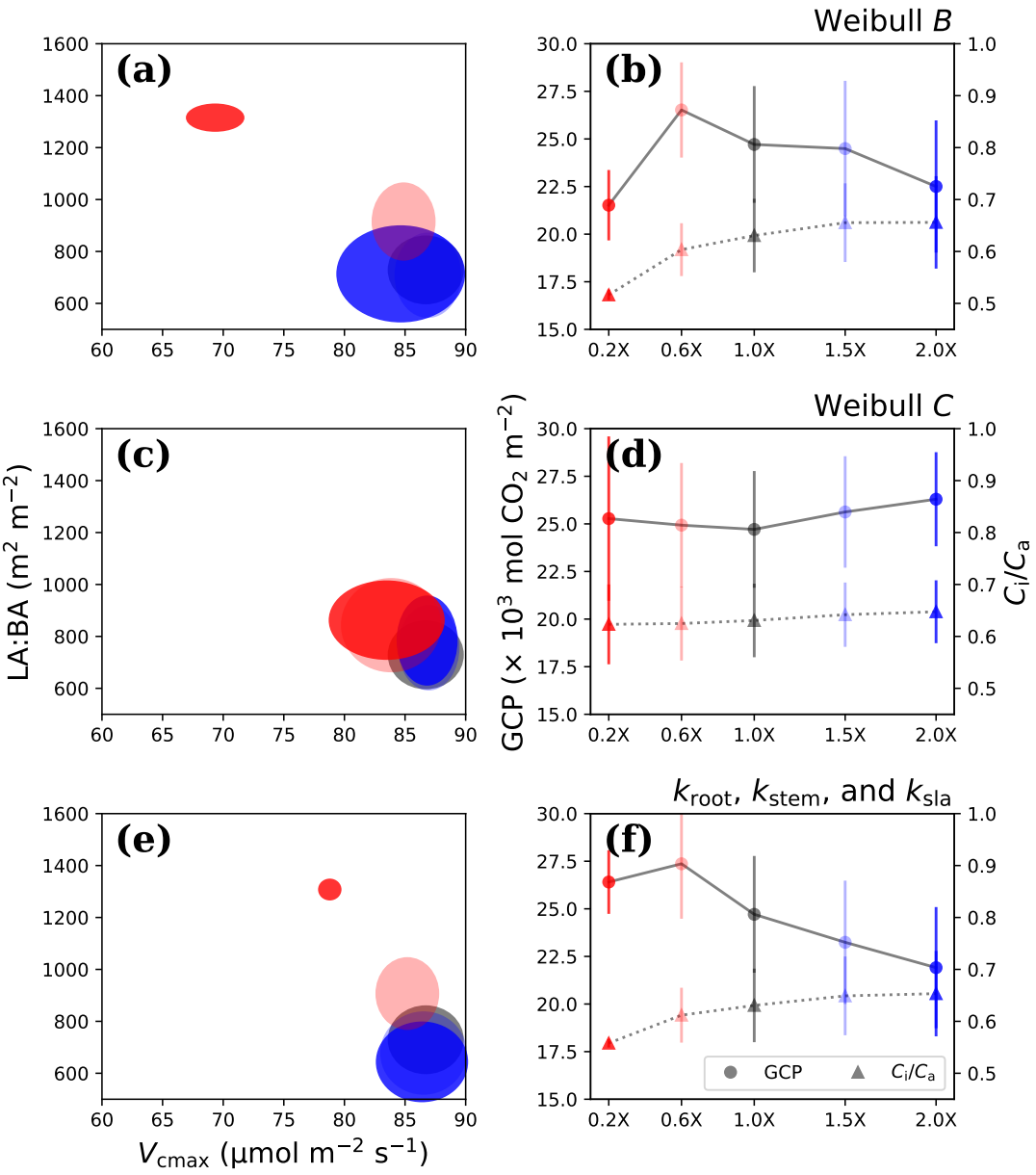

Figure 5.S16: Fig. 5.2 for Trinity.

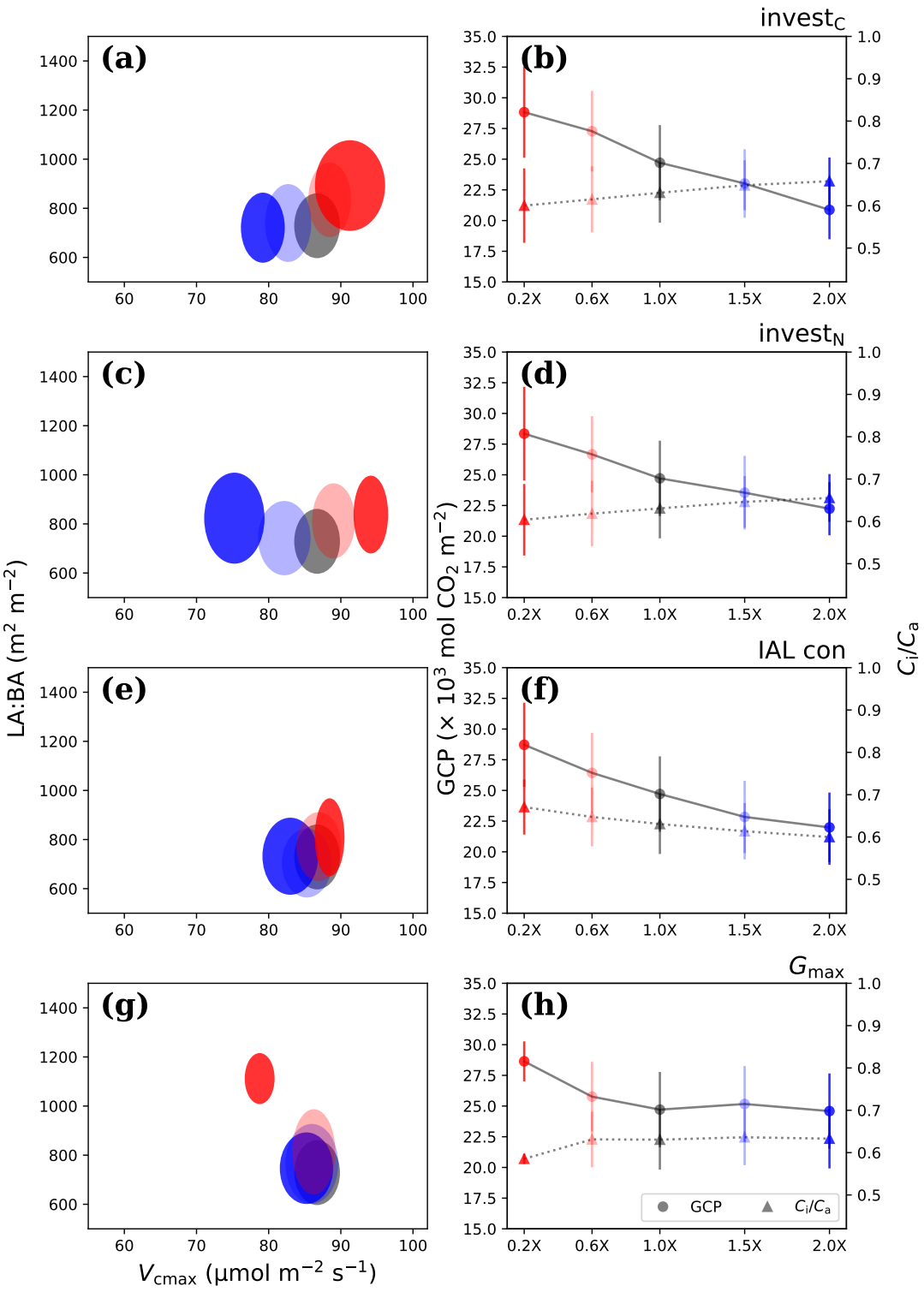

Figure 5.S17: Fig. 5.3 for Trinity.

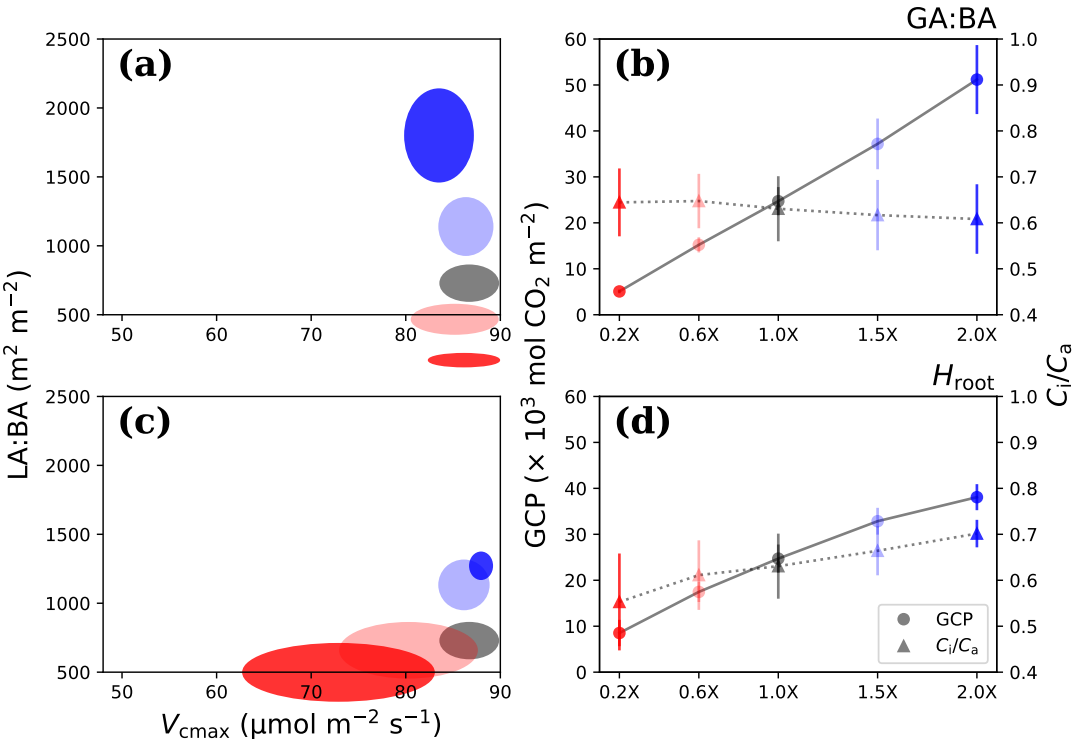

Figure 5.S18: Fig. 5.4 for Trinity.

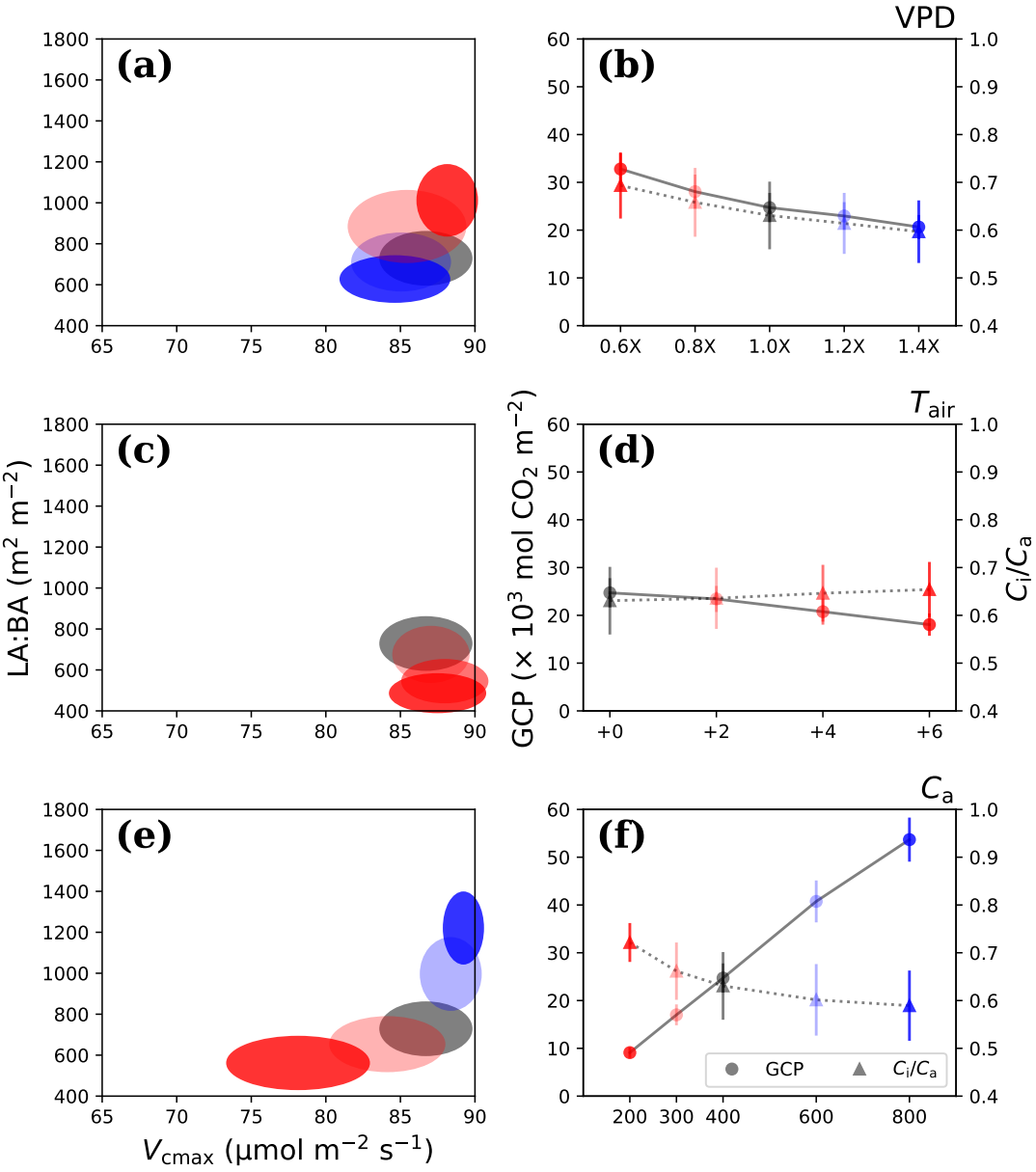

Figure 5.S19: Fig. 5.5 for Trinity.